

**A STUDY ON THE ROLE OF THERMOKINETIC  
MEASUREMENTS AND MODELLING IN  
MATERIALS DESIGN**

*By*

**S. RAJU**

Enrolment No.: ENGG 02 2007 04004

Indira Gandhi Centre For Atomic Research

Kalpakkam 603102, India

*A thesis submitted to the  
Board of Studies in Engineering Sciences  
In partial fulfillment of requirements*

For the Degree Of

**DOCTOR OF PHILOSOPHY**

*Of*

**HOMI BHABHA NATIONAL INSTITUTE  
MUMBAI, INDIA**



**August 2013**

# HOMI BHABHA NATIONAL INSTITUTE

## Recommendations of the *Viva Voce* Board

As members of the *viva voce* board, We certify that we have read the dissertation prepared by Mr. S. RAJU, entitled: “**A Study on the Role of Thermokinetic Measurements & Modelling in Materials Design**” and recommend that it may be accepted as fulfilling the dissertation requirement for the degree of Doctor of Philosophy.

\_\_\_\_\_  
Chair Person – **Dr. T. Jayakumar** Date:

\_\_\_\_\_  
Guide/Convener – **Dr. M. Sai Baba** Date:

\_\_\_\_\_  
Member 1 - **Dr. A. K. Bhaduri** Date:

\_\_\_\_\_  
Member 2 – **Dr. Saroja Saibaba** Date:

\_\_\_\_\_  
Date:

The final approval and acceptance of this dissertation is contingent upon the candidate’s submission of the final copies of dissertation to HBNI.

I, hereby certify that I have read this dissertation prepared under my direction and recommend that it may be accepted as fulfilling the dissertation requirement.

Date:

Signature of Guide

Place: IGCAR, Kalpakkam

## STATEMENT BY AUTHOR

This dissertation has been submitted in partial fulfillment of requirements for an advanced degree at Homi Bhabha National Institute (HBNI) and is deposited in the library, to be made available to borrowers under rules of the HBNI.

Brief quotations from this dissertation are allowed without special permission, provided that accurate acknowledgement of source is made.

Requests for permission for extended quotation from or reproduction of this manuscript in whole or in part may be granted by the competent authority of HBNI, when in his or her judgment, the proposed use of the material is in the interest of scholarship. In all other instances, permission must be obtained from the author.

(S. Raju)

Kalpakkam

Aug, 2013.

## DECLARATION

I, hereby certify that the investigation presented in the thesis has been carried out by me. The work is original and has not been submitted earlier as a whole or in part for a degree/diploma at this or any other Institution / University.

(S. Raju)

Kalpakkam

Aug., 2013.

## LIST OF PUBLICATIONS ARISING FROM THESIS

1. **S. Raju**, Arun Kumar Rai, B. Jeya Ganesh, M. Vijayalakshmi, T. Jayakumar and Baldev Raj, Characterisation of High Temperature Phase Stability and Evaluation of Metallurgical Compatibility with SS 304L, of Indigenously Developed Alternate Shielding Material Ferro-Boron for Fast Reactor Applications, *Energy Procedia*, **2011**, 7, 264-272.
2. **S. Raju**, Arun Kumar Rai, , B. Jeya Ganesh, G. Panneerselvam, M. Vijayalakshmi, T. Jayakumar and Baldev Raj , Investigation of high temperature phase stability, thermal properties and evaluation of metallurgical compatibility with 304L stainless steel, of indigenously developed ferroboration alternate shielding material for fast reactor applications, *Nucl. Engg. Design*, **2011**, 241, 2787–2801.
3. **S. Raju**, B. Jeyaganesh, Arun Kumar Rai, R. Mythili, S. Saroja and Baldev Raj, A study on martensitic phase transformation in 9Cr-1W-0.23V-0.063Ta- 0.56Mn-0.09C-0.02N reduced activation steel using differential scanning calorimetry, *J. Nucl. Mater.*, **2010**, 405, 59-69.
4. **S. Raju**, B. Jeya Ganesh, Arun Kumar Rai, S. Saroja, E. Mohandas, M. Vijayalakshmi and Baldev Raj, Drop Calorimetry Studies on 9Cr–1W–0.23V–0.06Ta–0.09C Reduced Activation Steel, *Int. J. Thermophys.*, **2010**, 31, 399-415.
5. **S. Raju** and E. Mohandas, Kinetics of solid state phase transformations: Measurement and Modelling of some basic Issues, *J. Chem. Sci.*, **2010**, 122, 83-89.
6. **S. Raju**, B. Jeya Ganesh, Arun Kumar Rai, R. Mythili, S. Saroja, E. Mohandas, M. Vijayalakshmi, K.B.S. Rao and Baldev Raj, Measurement of transformation temperatures and specific heat capacity of tungsten added reduced activation ferritic–martensitic steel, *J. Nucl. Mater.*, **2009**, 389, 385-393.

(S. Raju)

*Dedicated*  
*To The*  
*Lotus Feet of*  
*Bhagawan*

## *Acknowledgements*

Despite the candidate's pronounced reluctance to defend a degree at an advanced stage of his career, this thesis has eventually materialized, thanks to the persistent interest and affection shown by Dr. *Smt.* Saroja Saibaba and Dr. M. Sai Baba, the latter doubling his role as the thesis advisor. They moved the rock of Gibraltar, and I remain ever thankful to them.

I received immense encouragement from both Dr. T. Jayakumar and Dr. A. K. Bhaduri. Their faith in me and in my scholarship, despite my forthright interaction at times, has been a source of motivation to contribute something to fast reactor materials development. Dr. TJK's support to my involvement in RAFM steel and Dr. R. S. Keshavamurthy's coordination in Ferroboron related work is gratefully acknowledged.

My heartfelt acknowledgements go to my colleagues and research scholars at CMMS. The help rendered by Dr. Jeyaganesh and Dr. G. Panneerselvam at various stages are thankfully remembered.

In a subtle manner, my teachers at IISc., Bangalore and my association with late, Prof. P. Ramachandra Rao of BHU, have spurred my interest in physical metallurgy and materials thermodynamics. Besides, my brief contacts with many a seasoned practitioner of modern physical metallurgy at the Department of Atomic Energy (DAE), have contributed to sustaining my professional interest in this field. I am grateful to them all. It is only at DAE that the scientist in me sprouted and has been in the path of growth since then. My humble thanks are due to all Chairmen of DAE, and in particular, to the Directors of IGCAR, since my entry in 1986.

Finally, Dhana, Chandru, and Viji. It is only upon seeing the romantic pursuit of logic by Dhana and the dogged persistence of gifted Chandru in unscrambling the nuances of algebraic number theory, that I am still motivated to prospect for some more research. I have been virtually relieved of shouldering any genuine domestic responsibility, thanks to Viji. It is a God given privilege to have her as my wife. Both my mother in law and sister in law are a source of great domestic support to us at all times. To all of them, I remain as ever bound by their affection.

## CONTENTS

Abstract of Synopsis	xv
List of Figures	xvi-xxiii
List of Tables	xxiv-xxv

### Chapter 1

#### Alloy Design for Energy Systems: Role of Thermo-Kinetic Studies

		1-18
1.0	Introduction: Alloy Design as Systems Engineering Science	1
2.0	Top Down and Bottom Up Approaches to Materials Design	2
3.0	Materials Design for Nuclear Applications	6
4.0	Genesis of this study	9
5.0	Selection of Research Problem & Experimental Technique	9
6.0	Scope of this study	10
7.0	Materials of this study	10
7.1	Reduced Activation Ferritic Martensitic Steel	10
7.2	Ferroboron	12
8.0.	Organization of Thesis	13
	Conclusions	15
	References	16

### Chapter 2.

#### Experimental Methods: Drop Calorimetry, Differential Scanning Calorimetry and Supporting Metallography Techniques

		19-60
1.0	Introduction	19
2.0	Importance of Calorimetry in Phase Stability Characterisation	20
3.0	Calorimetry: General Principles	22

3.1	Principle of Drop Calorimetry	24
3.2.	Inverse Drop Calorimetry	26
3.3	Instrument Details	28
3.3.1	High Temperature Furnace	28
3.3.2	Measurement Head – Drop Transducer	28
3.3.3	Multi-Sample Introducer and the Drop Tube	29
3.3.4	Gas, Vacuum, Chill-water Circuit and Controller	29
3.4	Experimental Procedure	29
3.4.1	Working Crucible Loading	30
3.4.2	Calibration of Drop Calorimeter	30
3.5	Performing Drop Calorimetry Experiment	32
3.6	Enthalpy Estimation	34
4.0.	General Observations on Drop Calorimetry Data	35
4.1	Limitations of Drop Calorimetry	36
5.0	5.0 Dynamic or Differential Scanning Calorimetry	38
5.1	Principle of Heat Flux DSC	38
5.2	High Temperature Furnace	41
5.3	Measurement Head – DSC Probe	41
5.4	Vacuum Circuit, Gas Circuit, Chill water Cooling circuit	42
6.0	DSC Experimental Procedure	42
6.1	Determination of Phase Transformation Temperature	44
6.2	Calibration of Temperature in DSC	45
6.3	Determination of Phase Transformation Enthalpy	47
6.4	Determination of Apparent Specific Heat	49
6.5	Accuracy of Heat Capacity Measurements using DSC	51
7.0	Optical Metallography	52
7.1	Grain Size Measurement	52
7.2	Carbide Particle Density Measurement	53

7.3	Microhardness Measurements	53
7.4	Scanning Electron Microscopy (SEM) Study	54
8.0	X-Ray Diffraction (XRD) Study	54
8.1	High Temperature X-ray Diffraction (HTXRD)	55
	References	58-60

### Chapter 3

#### Thermodynamic Interrelationship Between Thermal and Elastic Properties: Development of Some Useful Approximations For Data Estimation & Assessment

		61-79
1.0	Introduction	61
2.0	Theoretical Development	63
2.1	Estimation of thermoelastic constants $\delta_s$ and $\xi_s$ from standard values of reference temperature thermal properties	66
3.0	Physical meaning of $\xi_s$	67
4.0	A Case Study on $\alpha$ -Plutonium	68
5.0	Discussion	73
6.0.	Summary	76
	References	77-79

### Chapter 4

#### Phenomenological Description of Phase Transformation Kinetics

		80-115
1.0.	Introduction	80
2.0	Isothermal <i>versus</i> Non-isothermal Processes: Influence of Heating and Cooling rates	82
2.1	Isothermal Phase Change	82
2.2	Non isothermal Phase Change	85
3.0.	Modelling of Nonisothermal transformation kinetics: Additivity approximation	87
3.1	Additivity and Isokinetic approximations: Nonlocal nature	89

4.0	Estimation of Apparent Activation Energy by Model	96
	Free Isoconversion Methods	
4.1	Integral Methods	98
4.2	Friedman Method	99
5.0	Application of KJMA Model	100
6.0	Physical meaning of $Q_{eff}$	104
7.0	DSC Profile Modelling	106
8.0.	Martensitic Transformation: Koistinen-Marburger Relation	110
9.0.	Summary	112
	References	113-115

## Chapter 5

### High Temperature Drop Calorimetry Measurements of Enthalpy and Heat Capacity Estimation of Reduced Activation Ferritic-Martensitic Steel

		116-140
1.0	Introduction: Necessity to generate Thermochemical Data on RAFM	116
1.1	Drop versus Dynamic Calorimetry Measurements	118
2.0	Material and Experimental Details	118
2.1	Drop Calorimetry Details	119
2.2	Accuracy of Data	120
3.0	Results	123
3.1	Enthalpy Increment versus Temperature Data	123
3.2	On-heating Phase Changes	126
3.3	Energetics of $\alpha$ +carbide $\rightarrow\gamma$ transformation	127
4.0	Discussion	130
4.1	Analytical description of $\Delta^{\circ}HT(T)$ Data	130
4.2	Comparison of Drop Calorimetry and DSC Data	133
4.3	General aspects	135
5.0	Summary	137
	References	138-140

## Chapter 6

## High Temperature Thermal Stability, Heat Capacity and Kinetics of $\alpha \rightarrow \gamma$ Diffusional Phase Transformation in Reduced Activation Ferritic Martensitic (RAFM) Steel

		141-181
1.0	Introduction	141
1.1	Necessity to develop RAFM steels for fusion applications	141
2.0	RAFM steel specification	143
3.0	Basic Microstructure Characterization	145
4.0	DSC Experiments	145
4.1	Transformation Temperature Measurements	145
5.0	Results	147
5.1	Microstructure	147
5.2.	DSC Thermogram upon slow heating and Cooling	151
6.0	Specific Heat Determination	159
6.1	Discussion on Thermal Stability and Specific heat	162
7.0.	Kinetics of $\alpha \rightarrow \gamma$ Phase Transformation	166
8.0	Mechanistic aspects of $\alpha \rightarrow \gamma$ Phase Transformation	171
9.0	Continuous Heating Transformation (CHT) Diagram	175
10.0	Summary	177
	References	178-181

## Chapter 7

### Characterisation of Martensitic Phase Transformation in RAFM steel

		182-215
1.0	Introduction	182
2.0	Experimental plan	183
3.0	Results	185
3.1	Martensitic Microstructure	185
3.2	DSC Results: Critical Cooling Rate Determination	187
3.3	Effect of holding time and temperature	191
3.4	Carbide Dissolution	194
4.0	Discussion	200

4.1	General remarks	200
4.2	Enthalpy of martensite formation, $M_s$ temperature and grain size effect	201
4.3	Critical cooling rate, carbide dissolution and grain size effect	203
4.4	Martensitic transformation kinetics	205
5.0	Summary	208
	References	210-215

## Chapter 8

### High Temperature Phase Stability, Thermal Properties and Metallurgical Compatibility of Ferroboron with SS 304L

		216-257
1.0	Introduction	216
2.0	Chemical composition and Characterisation	217
3.0	Experimental Measurements	218
3.1	Thermal stability of Fe-B alloy and combined Fe-B + 304L SS reaction couple	218
3.2	Enthalpy, heat capacity and lattice thermal expansion measurements	219
3.3	Estimation of the high temperature metallurgical compatibility between 304L stainless steel and Fe-B alloy	220
3.4	Reaction Diffusion Couple experiments	221
4.0	Results	223
4.1	Basic structural and microstructural characterisation	223
4.2	Thermal stability of Ferroboron alloy	225
4.3	Thermal stability of Ferroboron+ SS304LSS composite	229
4.4	SS304L-Ferroboron Diffusion couple	235
4.5	Estimation of reaction layer formation kinetics	239
4.6	Thermal Property Measurement: Specific heat	241

4.7	High Temperature Lattice Expansion of Ferroboron	244
5.0	Discussion	247
6.0	Summary	253
	References	255-257
Chapter 9		
Avenues for Further Research		258
	List of Publications	259

## Abstract of Synopsis

This synopsis describes in nutshell, the genesis, scope and organization of various components of this study. The importance of thermodynamic and kinetic investigations in facilitating the knowledge driven design of materials is exemplified by taking two case study materials. The comprehensive metallurgical aspects of high temperature phase stability of an indigenous variety of reduced activation ferritic-martensitic steel are investigated using isothermal drop and dynamic scanning calorimetry. Highly accurate experimental estimates of both energetic and kinetic quantities of  $\alpha$ -ferrite+carbide $\rightarrow\gamma$ -austenite phase transformation have been obtained. The systematics of martensite formation upon cooling from high temperature  $\gamma$ -austenite phase has been extensively probed. Further, drop calorimetry based values of enthalpy and heat capacity, and their variation with temperature have been presented, probably for the first time for any RAFM steel.

In case of Ferroboron, a novel and economical shielding candidate for future Indian fast reactors, the high temperature thermal stability, thermal properties, such as heat capacity and anisotropic lattice expansion and its metallurgical compatibility with SS 304L clad *etc.*, have been characterized, again by a combination of calorimetry, metallography and modelling.

In addition, a rigorous thermodynamic analysis of the interrelationship between various thermodynamic quantities, such as molar volume, enthalpy, entropy and bulk modulus has been presented. The potential use of such a thermodynamic modelling apparatus is illustrated by presenting a comprehensive assessment of thermophysical data of  $\alpha$ -Pu, a highly radioactive element. In a similar vein, a critical appraisal of various popular models of diffusional solid state transformations has been made, and a proposal for the consistent physically based analysis of the role of heating and cooling rates in altering the kinetics, has been presented.

## List of Figures

- Fig. 1.1 Basic architecture of a knowledge based material design protocol. Note that in the case of materials for strategic applications, such as nuclear, the input design requirements themselves form a complex matrix, for some of which the required *high maturity* knowledge base may not exist. The decision making process in such cases still calls for substantial experiential input
- Fig. 1.2 Multi-tiered nature of present day Materials Science, Engineering and Technology is schematically shown. Each level or tier is ideally suited for understanding materials behavior within the reach of its phenomenological constructs. The multi-scale modelling attempts to knit or make use of tools and information pertaining to different tiers into a coherent framework or knowledge base for the particular material design issue at hand
- Fig. 1.3 Top Down phenomenological approach to materials design
- Fig. 1.4 Different databases that constitute the comprehensive nuclear materials design knowledge base and their interrelated nature are graphically portrayed
- Fig. 1.5 Typical unit processes of a standard thermomechanical processing schedule of advanced engineering materials are shown. The microstructure is continuously modified at each one of this step. The microstructure, and hence the resulting properties at each stage and final in-service performance are actually governed by thermo-kinetics considerations that are appropriate to each stage of overall materials processing
- Fig. 2.1 Schematic of enthalpy increment variation with temperature. This is referred to as 'drop curve' in this study
- Fig. 2.2 (a) High temperature furnace with cabinet (b) Measurement head
- Fig. 2.3 Illustration of the temperature variation of Q for a typical experimental schedule and Calibration constant (inset)

- Fig. 2.4 The experimental setup of drop calorimeter
- Fig. 2.5 Snapshot of the drop calorimeter signal output
- Fig. 2.6 The experimental set up of heat flux DSC
- Fig. 2.7 (a) Setaram high temperature DSC furnace; (b) Heat flux DSC Plate – rod
- Fig. 2.8 Typical on-heating DSC profile showing two transformation thermal arrests
- Fig. 2.9 Temperature calibration with Al and Cu
- Fig. 2.10 Illustration of the thermocouple response under identical heating rate ( $10 \text{ K min}^{-1}$ )
- Fig. 2.11 Set of DSC profiles obtained during typical  $C_p$  measurement
- Fig. 2.12 Room temperature XRD profile of RAFM steel
- Fig. 3.1 Linear relationship between bulk modulus and enthalpy, for  $\alpha$ -Pu
- Fig. 3.2 Temperature variation of predicted enthalpy, compared to assessed experimental data of Ward [32]
- Fig. 3.3 Estimated molar volume variation with temperature is compared with experimental data
- Fig. 3.4 Linear relationship between molar volume and enthalpy for  $\alpha$ -Pu
- Fig. 4.1 A schematic of different kinetic path ways offered by three different cooling histories is shown. Paths A and B stand for transformations occurring under isothermal and linear cooling conditions, where as the path C represents a step wise cooling with small incremental isothermal holds. Note that in all the three paths A, B and C the net reduction in Gibbs energy  $\Delta^0G$  is the same
- Fig. 4.2 A graphical portrayal of the isothermal transformation diagram is shown. Note the sigmoidal nature of the transformation profiles and also the dependence of incubation time on reaction temperature
- Fig. 4.3 A schematic of TTT diagram for the formation of the low temperature stable  $\alpha$  phase from the high temperature polymorph,  $\beta$  is shown. The horizontal lines parallel to the time axis represent the time to reach fixed extent of transformation. Note the C-type nature of this

isotransformation contours. The upper portion of this contour, indicated in red is however absent for the reverse  $\alpha \rightarrow \beta$  phase change. Refer to text for further details

- Fig. 4.4 The isochronal or continuous heating transformation plot is graphically illustrated. Note that increasing the heating rate pushes up the transformation start temperature. Also, for fixed temperature, the transformation is more advanced at lower heating rates
- Fig. 4.5 The continuous heating transformation (CHT) diagram for the  $\alpha \rightarrow \beta$  transformation in uranium is shown. The dotted lines represent various heating rates, on to which the measured transformation start ( $T_S$ ), peak ( $T_P$ ) and finish ( $T_f$ ) temperatures are marked. Note the increased width of the  $\alpha+\beta$  two phase domain at higher heating rates. Data adapted from [9].
- Fig. 4.6 The influence of heating and cooling rates on the  $\alpha \leftrightarrow \beta$  structural transformations in titanium is graphically depicted. Note that compared to  $T_S$ , the  $T_f$  temperature exhibits a higher degree of nonlinearity in its variation with  $\beta$ . The non-linear model suggested here fits better the transformation start temperature dependence on scan rate
- Fig. 4.7 The exponential decay of the characteristic transformation time  $\tau$  with cooling rate  $\beta$ , for the  $\beta \rightarrow \alpha$  phase transformation in titanium is illustrated
- Fig. 4.8 The linear scaling of the quantity  $\ln(\tau - \tau_0)$  with  $1/\beta RT_p$  is shown for the  $\beta \rightarrow \alpha$  phase transformation in titanium
- Fig. 4.9 Isoconversional linearization schemes yielding physically unrealistic  $Q$  values, for the  $\alpha \rightarrow \gamma$  transformation in RAFM steel
- Fig. 5.1 The optical micrograph of the reduced activation steel in the quenched condition showing lath martensite
- Fig. 5.2 The temperature variation of the enthalpy increment values for the RAFM steel is graphically portrayed. The line through the points is guide to the eye only. Note the distinct inflections marked by arrows

that characterize the onset of various phase changes. The dotted line at 793 K refers to the extrapolated linear behaviour of the ferrite phase, if no microstructure changes accompany the heating process. The dotted line drawn from  $Ae_1$  is the empirically extrapolated variation of the enthalpy sum of ferrite and austenite two phase mixture. Refer to text for details

- Fig. 5.3 A comparison of drop calorimetry based  $C_p$  values obtained in the present study (lower line) with the ones measured using DSC (upper curve; Chapter 4)
- Fig. 5.4 A comparison of  $C_p$  of the reduced activation steel (RAFM) estimated in this study using the present drop calorimetry enthalpy measurements with the literature data on Eurofer 97 and F82H [30-32].
- Fig. 6.1 (a) Optical micrograph of the RAFM steel in the as received condition showing a highly deformed structure  
 (b) Optical micrograph of the sample normalised at 1253K / 2h, showing martensite structure  
 (c) Optical micrograph of the sample normalised at 1453 K showing coarser austenite  
 (d) Optical micrograph of the sample water quenched from 1553 K showing the presence of some  $\delta$  - ferrite (marked by arrows) in addition to martensite.  
 (e) Optical micrograph of the sample normalised at 1253K / 2h, followed by tempering at 1033 K for 30 min showing a tempered martensite structure  
 (f) Optical micrograph of the sample normalized at 1253 K followed by tempering at 1033K for 120 min showing the presence of carbides in the tempered martensite  
 (g) Optical micrograph of the sample normalized at 1253 K followed by tempering at 1033 K for 300 minutes showing the presence of carbides in the ferrite matrix

- Fig. 6.2 (a) Typical DSC thermogram of RAFM steel  
(b) The expanded view of the DSC profile around the melting region
- Fig. 6.3 (a) Temperature variation of specific heat for RAFM steel in different normalized conditions  
(b) The temperature variation of specific heat for RAFM steel in different tempered conditions. Note that in figure (a), the y-axis scale is compressed in order to bring out the very small differences among different martensites
- Fig. 6.4 The  $C_p$  of martensite, tempered martensite and their difference with temperature are plotted
- Fig. 6.5 DSC peak profiles for the  $\alpha + \text{carbides} \rightarrow \gamma$  transformation in RAFM
- Fig. 6.6 Variation of  $\alpha + \text{carbides} \rightarrow \gamma$  transformation temperature with heating rate
- Fig. 6.7  $\alpha \rightarrow \gamma$  transformation plots for different heating rates
- Fig. 6.8 Heating rate dependence of the kinetic constant  $k$  for the  $\alpha + \text{carbide} \rightarrow \gamma$ , transformation in RAFM steel
- Fig. 6.9 Continuous Heating Transformation (CHT) diagram for RAFM steel
- Fig. 7.1 (a) The optical micrograph of the 1253 K/15 minutes normalised sample showing packets of lath martensite and well delineated prior austenite grain boundaries. (b) The bright field TEM micrograph of the 1253 K/15 minutes normalised sample showing lath martensite and a carbide particle marked by arrow; (c) The optical micrograph showing the effect of tempering at 1033 K for 30 minutes
- Fig. 7.2 The DSC profile recorded at  $30 \text{ K min}^{-1}$  scan rate, showing clearly marked endothermic and exothermic transformation arrests during heating and cooling cycles respectively
- Fig. 7.3 The collage of exothermic transformation peak profiles obtained for lower range of cooling rates. The austenitising conditions are 1253 K/15 minutes. Fig. 7.3(b): Same as figure 7.3(a) with peak profiles obtained for higher range of cooling rates
- Fig. 7.4 Variation of  $M_s$  and  $M_f$  temperatures with cooling rate for 1253 K

solution annealed samples

- Fig. 7.5 The DSC profile pertaining to  $1 \text{ K min}^{-1}$  cooling rate. Note the absence of the highly exothermic martensitic transformation peak
- Fig. 7.6 The variation of microhardness of with cooling rate. Note the sudden increase in the hardness values at the critical cooling rate due to martensite formation
- Fig. 7.7 Effect of holding time at 1253 K on martensite peak profile, for a constant cooling rate of  $99 \text{ K min}^{-1}$ . Martensite forms in all cases, but  $M_s$  increases with holding time
- Fig. 7.8 Variation of  $M_s$  and  $M_f$  temperatures with holding time at 1253 and 1323 K. The vertical arrows placed at 120 minutes holding indicate the overall martensitic transformation temperature interval
- Fig. 7.9 A stack of baseline compensated isothermal DSC traces recorded at 1253 K indicating small endothermic peaks arising from discrete time dependent carbide dissolution events
- Fig. 7.10 Variation of martensite hardness with holding time in the austenite region for two different austenitising temperatures, 1253 and 1323 K respectively
- Fig. 7.11 Variation of austenite grain size with holding time at 1253 and 1323 K respectively
- Fig. 7.12 Variation of  $M_s$  temperature with austenite grain size at 1253 and 1323 K respectively
- Fig. 7.13 Fraction of martensite formed as a function of undercooling below  $M_s$  for samples that are subject to austenitisation treatment at 1253 K for (a): 1-30 minutes (top panel) and (b) 30 – 120 minutes (bottom panel). The line through the curves represents the Koistinen-Marburger fit (Eq. 2) to the transformation data
- Fig. 7.14 The rate of martensite formation is plotted as a function of martensite fraction for samples that are solution treated at 1253 K for different durations
- Fig. 8.1 Schematic diagram of the diffusional jig used for simulating the high

temperature metallurgical interaction between ferroboron powder and 304L stainless steel. Dimensions are given in mm

- Fig. 8.2 XRD pattern of the as-received Fe-B alloy powder
- Fig. 8.3 Optical micrograph of the as received Fe-B alloy. The irregular shape and size of the individual powder particle mounted onto the epoxy base is worth noting
- Fig. 8.4 DSC thermogram of Fe-B alloy obtained during heating and cooling at 10 K min<sup>-1</sup> in pure argon atmosphere. The occurrence of phase transformation events are marked by arrows
- Fig. 8.5 Fe-B binary phase diagram taken from the recent assessment of Okamoto [34]
- Fig. 8.6 (a) DSC profile obtained during heating of SS 304L + Fe-B alloy composite. The gradual time dependent pre-melting of SS304L in molten Fe-B is clearly evident. The series of thermal arrests witnessed during cooling is due to the formation complex boride phases  
(b) DSC profile of SS 304L showing thermal arrests due to melting and solidification
- Fig. 8.7 Variation in the onset of pre-melting or liquation temperature as a function Fe-B to 304L mass ratio: Couple (1):1:1/4; Couple (2): 1:2/5; Couple (3): 1:2 and Couple (4): 1:3. Note that independent of the mass ratio, the pre-melting of 304L in Fe-B is initiated at a constant temperature of 1471 K
- Fig. 8.8 XRD profile of the fused product of Fe-B alloy powder and 304L stainless steel
- Fig. 8.9 (a). Back scattered electron image of the high temperature Fe-B+304L stainless steel melt product. (b). Pseudo colour image obtained by x-ray mapping represents the matrix region rich in Fe; (c). Cr-rich boride phase embedded in matrix, and (d) the Ni-rich intergranular phase
- Fig. 8.10 Microstructural collage of the reaction layer formed at the interface

between 304L stainless steel and Fe-B powder for various time durations at 973 K

- Fig. 8.11 Microstructural collage of the reaction layer formed at the interface between 304L stainless steel and Fe-B powder at various temperatures for 600 h exposure
- Fig. 8.12 The progressive variation in the Ni and Cr concentration across the reaction interface for 1073 K/5000h diffusion anneal
- Fig. 8.13 Time temperature variation of the penetration layer depth
- Fig. 8.14 Variation of reaction rate constant  $k(T)$  with temperature in the range 823-1073 K
- Fig. 8.15 Enthalpy increment values as a function of temperature obtained in this study are compared with literature assessments for  $\text{Fe}_2\text{B}$  and FeB phases
- Fig. 8.16 Specific heat for Fe-B alloy obtained in this study is compared with literature estimates for FeB and  $\text{Fe}_2\text{B}$  borides
- Fig. 8.17 8.17(a). Variation of the lattice parameter of orthorhombic FeB phase with temperature. (b). Thermal expansivity along 'a' 'b' and 'c' directions are plotted with estimated volume thermal expansivity. (c). Lattice parameter variation with temperature of tetragonal  $\text{Fe}_2\text{B}$  phase (d). Thermal expansivity variation with temperature along 'a', and 'c' axes

## List of Tables

- 5.1 Listing of the experimental enthalpy increment  $\Delta^{\circ}H = H_T - H_{298}$  values for the  $\alpha$ -ferrite phase obtained in the present study. The data are given only up to about 1000 K only. For comparison, the values obtained by fitting the experimental data to Eq. (2) and the percentage deviation of the fit values from experimental estimates are also presented. The temperature and enthalpy values are rounded off to one decimal point
- 5.2 Listing of the values of fit-coefficients in Eq. (2) used in the analytical representation of the temperature variation of the enthalpy increment ( $H_T - H_{298} / J.g^{-1}$ ) data. For comparison, the coefficients obtained for the DSC based enthalpy values are also listed
- 5.3 A comparison of various transformation temperatures obtained in the present study using drop calorimetry with the corresponding estimates based on differential scanning calorimetry [16]
- 6.1 The chemical composition in weight percent of the RAFM steel
- 6.2 Heat treatment details adopted in the present study
- 6.3 Microstructural and Microhardness details corresponding to various heat treatments outlined in Table 6.2
- 6.4 Listing of  $Ac_1$  and  $Ac_3$  temperatures for differently treated RAFM samples
- 6.5 The on-heating transformation temperatures for RAFM steel as measured by DSC. The heating rate adopted is  $5 \text{ K min}^{-1}$ . The starting microstructure is derived from the normalisation treatment at 1253 K
- 6.6 Listing of fitting parameters of the measured specific heat data to expression given by Eq. (2). The  $T_C$  used in fitting is 1015 K for all samples. The overall temperature range of the data chosen for fitting is 480 to 1020 K, except for three cases, for which the presence of wiggles in the low temperature region adversely affected the quality of the fit. Hence a slightly restricted temperature range is adopted for these three cases
- 6.7 A comparison of  $C_p$  of martensite with that of tempered martensite

- 6.8 Listing KJMA kinetic parameters for  $\alpha \rightarrow \gamma$  transformation in RAFM steel
- 7.1 Listing of the parameters of the Koistinen - Marburger fit (*Eq. 2*) to the experimental data
- 8.1 Chemical composition of Ferroboron
- 8.2 Details regarding the co-melting experiments of Fe-B alloy powder with SS 304L. Four different reaction couples with the following Fe-B to 304L mass ratios: 1:1/4, 1:2/5, 1:2 and 1:3 are melted, at  $15 \text{ K min}^{-1}$  heating rate with the exception of couple I which is melted at  $3 \text{ K min}^{-1}$ . The corresponding data set obtained with separate experiments carried out on SS 304L and Fe-B powder is given for comparison
- 8.3 X-ray diffraction details of Fe-B+304L stainless steel co-melted product

## ALLOY DESIGN FOR ENERGY SYSTEMS: Role of Thermo-Kinetic Studies

### 1.0. Introduction: Alloy Design as Systems Engineering Science

Alloy or Materials design in its core is a decision making process. As a highly valued interdisciplinary topic of materials science, engineering and technology, it stands for the quintessential synthesis of a wide spectrum of information into a wholesome knowledge base that can facilitate the final choice of material(s), and in

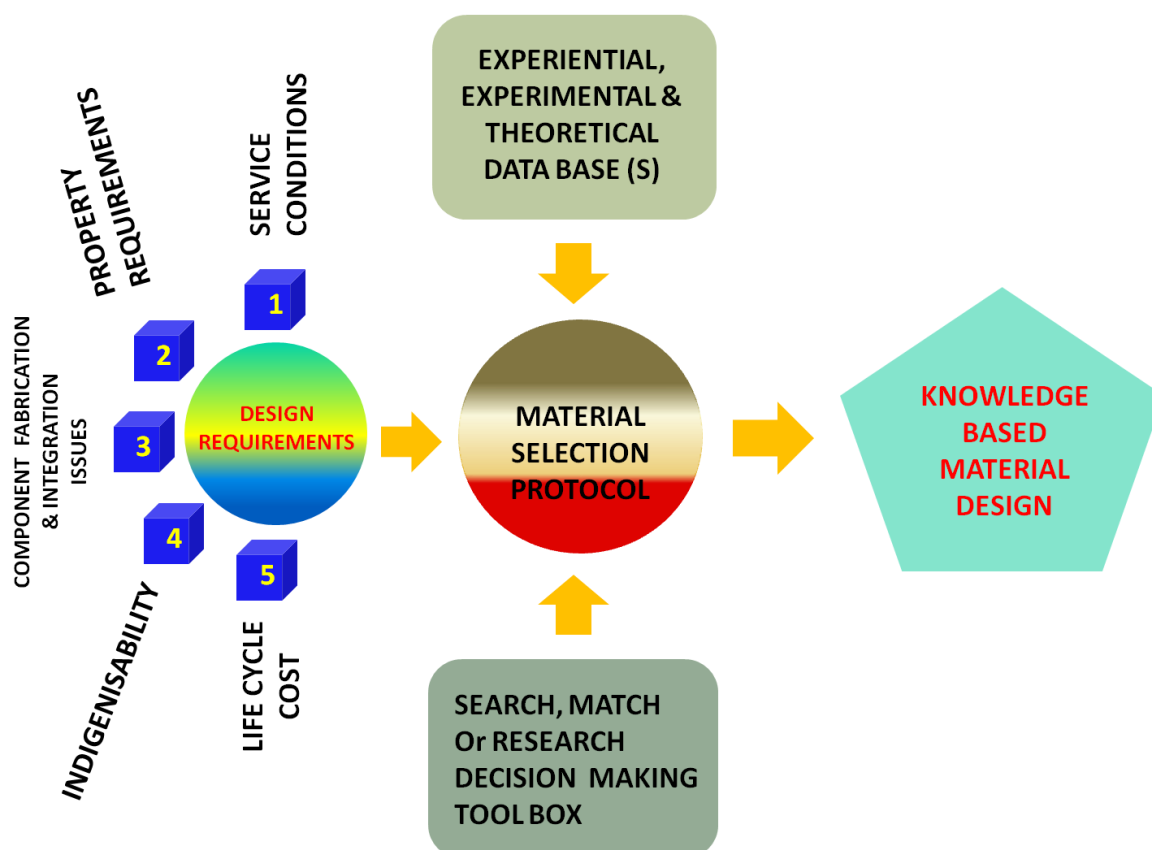


Fig. 1.1. Basic architecture of a knowledge based material design protocol. Note that in the case of materials for strategic applications, such as nuclear, the input design requirements themselves form a complex matrix, for some of which the required *high maturity* knowledge base may not exist. The decision making process in such cases still calls for substantial experiential input.

all probability with associated details of processing, component fabrication and testing procedures, for the chosen high end engineering application. The application could be anywhere in power, aerospace, automotive or nuclear industries. From obvious grounds, it is clear that every single bit of reliable and critically assessed data on materials:-their structure, properties, processing, degradation in service, recycling, waste disposal *etc.*, when knitted adroitly into carefully structured decision enabling algorithmic protocol(s), (often called material informatics) go on to constitute what may be called, **Modern Materials Design Expert System**. A good example is the ALADIN materials design protocol, developed in the case of aluminium alloys for automotive industries [1].

When viewed in the above mentioned perspective, any material design protocol should contain two basic modules: (i) structured data or knowledge base(s) and (ii) decision making tool box. The latter in effect, does the sophisticated search-match type functional mapping of design engineer's requirements against the available materials knowledge base. The basic architecture of a knowledge based materials design protocol having these components is illustrated in **Fig. 1.1**.

Modern materials design is a multidisciplinary job in nature. On a broader canvas, designing of materials for energy production and delivery systems spread over three areas: Science, Technology and Management. The relevance of former two being obvious, the third one is somewhat latent, yet omnipresent. Under the prevailing situation, especially in developing nations faced with huge energy deficit, complex socio, political and ecological imperatives often have to be weighed in together with the plant design choices that are advocated out of scientific considerations. Materials design has therefore to be pursued on a systems engineering basis.

## **2.0. Top Down and Bottom Up Approaches to Materials Design**

A question may arise at this point. Is it possible or not to design materials as well as their processing routines purely on an *ab-initio* or theoretical basis? Putting it plainly, can alloys be designed using ‘Bottom-Up’ approach, using basic theoretical and calculation tools of materials science ? [2-8]. At present, the answer to this question is

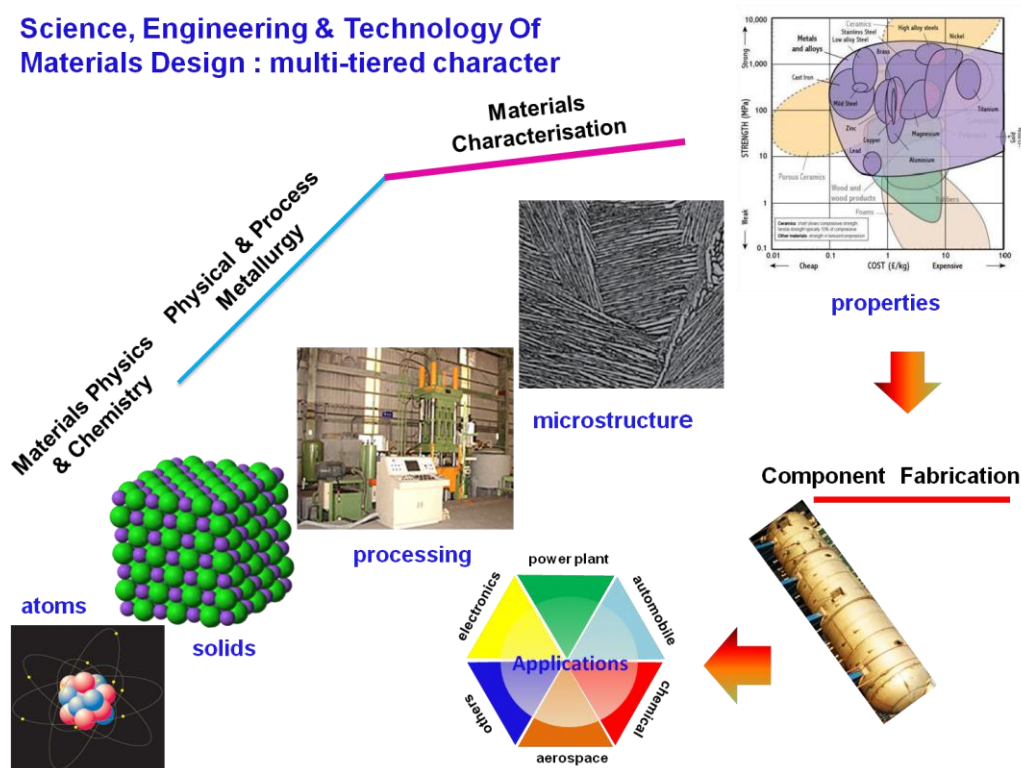


Fig. 1.2 Multi-tiered nature of present day Materials Science, Engineering and Technology is schematically shown. Each level or tier is ideally suited for understanding materials behavior within the reach of its phenomenological constructs. The multi-scale modelling attempts to knit or make use of tools and information pertaining to different tiers into a coherent framework or knowledge base for the particular material design issue at hand.

a mix of Yes and No [3]. Numerous as well as diverse developments taking place at the basic tiers of materials physics, chemistry and mechanics [3,4,7-16] together with rapidly advancing computing power do in fact serve to calculate a lot about materials, such as crystal structure, chemical bonding, phase stability, physical properties, and behavior under varied external conditions [3-20]. Computational Materials Science

has contributed richly to the successful building up of materials knowledge base or genome [21]. Yet, notwithstanding all this progress, it is somewhat early to expect that design of alloys, especially their processing methods to achieve the desired end properties for demanding engineering applications can be realized through theory alone. The reason is the current multi-tiered nature of materials knowledge base, which is graphically illustrated in **Fig. 1.2**.

The spectrum of materials behavior is understood only in a compartmentalized manner as of now (**Fig. 1.2**) [7]. Thus, for example, both structure and bonding are unambiguously dealt with at the atomic level, first principles - density functional, or *ab-initio* potential based methods [9, 10]. However, the physical properties to a large extent are only reasonably amenable for *ab-initio* theoretical estimation [2, 8, 17], save a few exceptions of well understood materials [4,7]. The plastic strength and plastic deformation aspects of metallic alloys are gainfully tackled, not at the interatomic level; but at a coarser sub-micron or mesoscopic level by continuum mechanics tools [14-16]. The Constitutive Equations of Plasticity, unlike their counterparts in condensed matter physics, namely Equations of State (EoS) rely on macroscopic concepts like dislocations, slip and twin systems and their response to external stimuli [15-16]. The calculation of equilibrium and kinetic phase diagrams of complex multicomponent alloys are routinely done by a hybrid approach involving a judicious combination of *Calphad* methodology [11, 18] and theoretical total energy methods [2,9,10]. The component fabrication procedures such as casting, thermomechanical treatment and welding are better understood by physical and process metallurgy tools [8]. Thus, in a nutshell, the knowledge base of materials is a sprawling one spanning many length scales. Therefore, it is better represented by a host of hierarchically sequenced distinct themes that range in complexity from atomic

physics/chemistry to solid state theory at the lower end to macroscopic phenomenological constructs of metallurgy and materials engineering at the other extreme.

The *top down* or what may be called the *phenomenological* approach to alloy design is schematically illustrated in **Fig. 1.3**. A quick appraisal of **Fig. 1.3**, suggests that the top down approach is more apt to be adapted when designing materials from functional requirements point of view. In this approach, the task of materials selection originates right at the component designer's table, rather than from the bottom of material's theorists bench [21]. The success of this approach lies in building up reliable material informatics, which could be both generic and specific in nature [22]. The information content for these databases could be gathered from the results of both

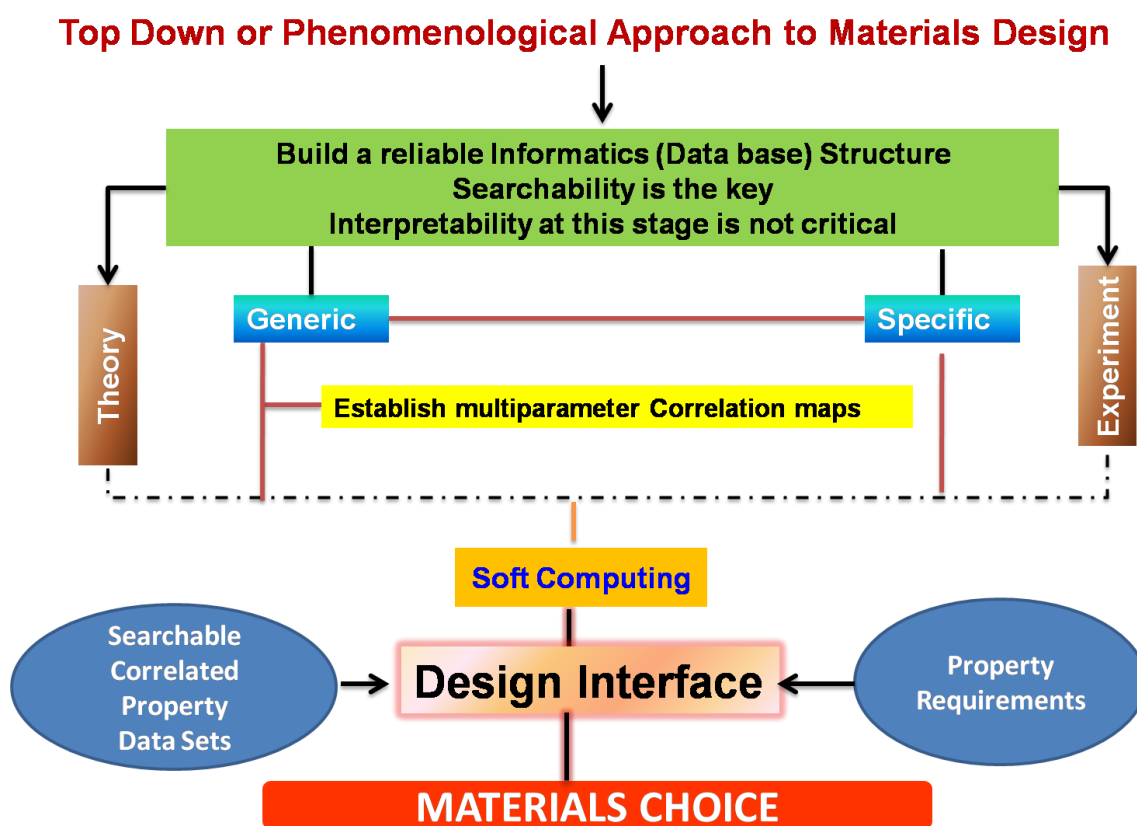


Fig. 1.3 Top Down phenomenological approach to materials design.

experimental and theoretical studies, after critical assessment. The information contents are finally cast in the form of multiparameter correlation maps through established data regression methods (neural network, genetic algorithms and the like) that are amenable for their extensive search-match capability [1, 23]. Ability to interpret the statistically arrived at multiparameter correlations is not important at this stage, although this may restrict the extrapolating capability of the database, beyond the purview of its validity range with any degree of confidence. This aspect of computational materials design is often known as soft computing [23], the purpose of which is to provide structured materials informatics into a materials design interface. The building up of a successful design interface marks the major milestone of the top-down approach to materials design, for which again, continuous data generation and assessment forms an important organ.

### **3.0. Materials Design for Nuclear Applications**

The problems faced in the selection of materials for nuclear applications are considerably more complex [24] than the ones involved in materials design for other advanced conventional energy systems [25]. The selection of materials for nuclear applications has to be made in the backdrop of a composite matrix of input parameters or constraints, some of which stem from safety and regulatory concerns [21], the others due to optimization of overall material life cycle cost, amenability to indigenization etc. These, *beyond normal functional requirements* of materials are very specific of nuclear industry. These nuclear specific constraints operate over and above the standard functional requirements, which include good high temperature strength under neutron irradiation, swell resistance, minimal activation while in-service (for fusion applications), compatibility with coolant (liquid metal cooled fast reactors) and fuel under typical operating conditions [26]. Most of these requirements

are implicitly covered in the often used phrase in nuclear materials community, namely, *radiation damage tolerant materials* [21, 24, 26].

*The real challenge for a nuclear material scientist in developing appropriate radiation damage tolerant materials for diverse nuclear components is that he has to perform his job in the midst of severe lack of appropriate (high maturity) material database, appropriate computational or simulation tools and even well articulated design codes, especially for advanced FBR and fusion applications.*

Quite contrary to what it is often believed to be, Nuclear Materials is an all-

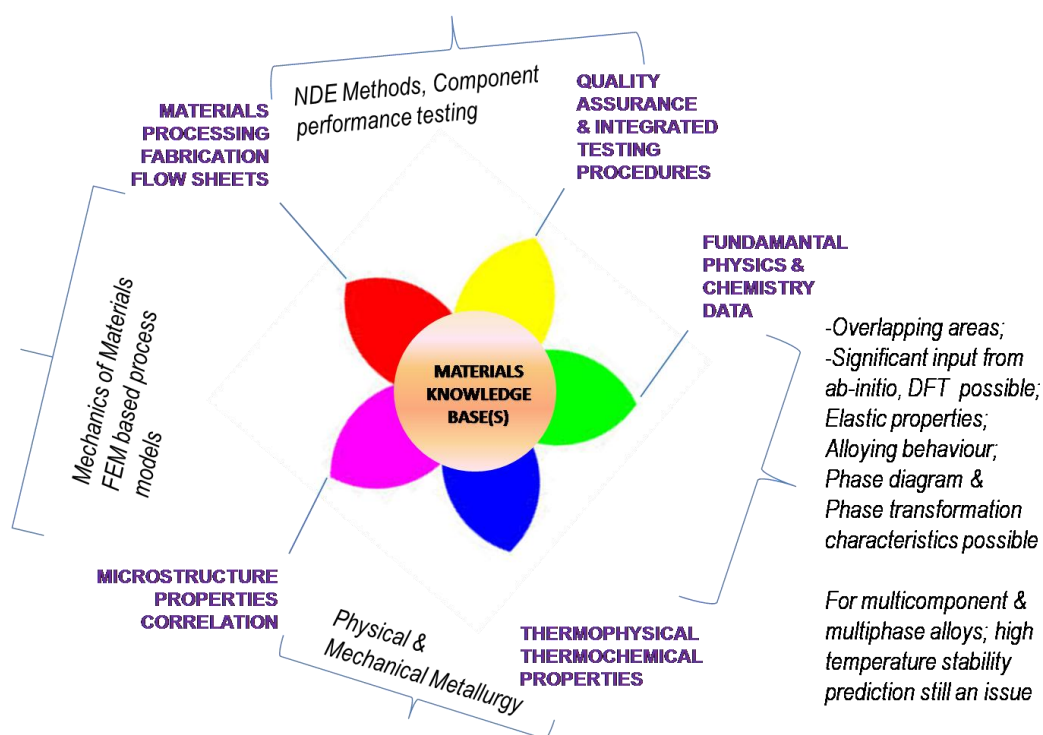


Fig. 1.4 Different databases that constitute the comprehensive nuclear materials design knowledge base and their interrelated nature is graphically portrayed.

inclusive and expansive domain. A truly broad spectrum of materials knowledgebase is required to understand, model and design a radiation damage tolerant material [24] that is also acceptable on environmental and commercial grounds. In **Fig. 1.4**, a survey of several different databases that are required to build a materials design

knowledgebase for nuclear energy systems is graphically portrayed. It is clear that there is ample scope for research on both basic and applied technology fronts in nuclear materials domain. Thus, for an example, the task of predicting the stability of materials under typical in-reactor and or anticipated transient conditions, calls for continuous updating of both thermodynamic and kinetic databases. The in-pile behavior of both fuel and clad especially needs to be understood in terms of basic nuts

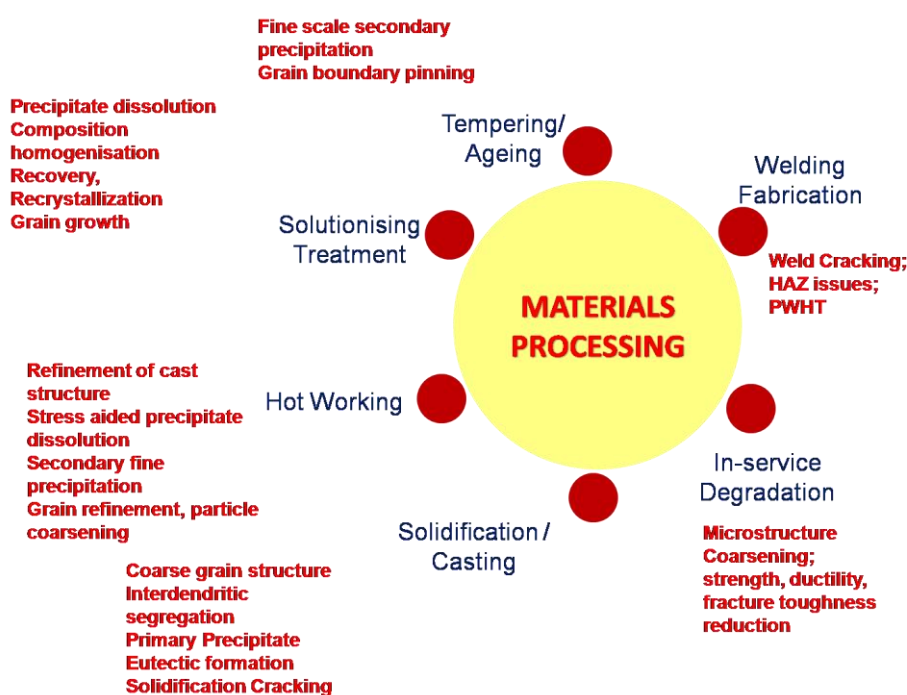


Fig. 1.5 Typical unit processes of a standard thermomechanical processing schedule of advanced engineering materials are shown. The microstructure is continuously modified at each one of this step. The microstructure, and hence the resulting properties at each stage and final in-service performance are actually governed by thermo-kinetics considerations that are appropriate to each stage of overall materials processing.

and bolts. This problem is better served by a combination of new key experiments and extensive modelling and simulations at the level of fundamental materials physics and physical metallurgy [20, 24]. On the other extreme, assuring component integrity for longer service and extended performance levels requires innovative R&D at the

design engineering level. Thus, viewed from either perspective, nuclear materials is a fertile breeding base for ushering in many a new paradigm in materials design philosophy

#### **4.0 Genesis of this study**

It is amidst this background, the theme of present research has originated. India has plans for a sizeable expansion in its nuclear power share, through a combination of both thermal and fast reactors in that order. Fast reactors are one of the means to exploit the native Th-reserves, so that long term fuel sustainability issues are adequately taken care of. Materials Challenges in fast reactors are plenty to say the least; and even more so, if large scale indigenizing of materials chain is to be aimed at in the long run, out of strategic imperatives. In this milieu, it is also noteworthy that India is a signatory to participating in the international fusion reactor development program, ITER.

Both fast fission and fusion materials research has opened up immense prospects for carrying out basic materials research, set in an applied context. Thus, active materials research towards developing indigenous variants of low or reduced activation version of high Cr-base ferritic steels, Oxide Dispersion Strengthened ferritic alloys (ODS Ferritics) *etc.*, has been initiated in the recent past. The present investigation constitutes a small component in an otherwise sprawling Nuclear Materials R&D work, being pursued at IGCAR, Kalpakkam, India.

#### **5.0 Selection of Research Problem and Experimental Techniques**

Having explained the contextual basis of present research, a brief explanation needs to be made about the choice of the research problem. The candidate, working in the discipline of physical metallurgy and specializing in calorimetry, the natural inclination would be to apply calorimetry techniques to investigate the high

temperature phase stability. It is well known that this aspect is at the interface of physical metallurgy and physical chemistry. *In reality however, the evolution of microstructure of an alloy during the course of its journey from being a cast ingot into a finished component and even during its performance, is decided by the synergy of thermodynamics and transformation kinetics*, both of which are amenable for calorimetry investigation. Although thermodynamics and kinetics may be viewed as two separate disciplines, we take the view, that it is practically advantageous to treat them as a single composite topic, for describing and modelling phase stability of engineering alloys. The importance of materials thermodynamics and kinetics of solid state transformations is illustrated in **Fig. 1.5**. This figure is rather self explanatory.

## **6.0. Scope of this study**

In view of the importance of Thermodynamic and Kinetic considerations in influencing the high temperature phase and microstructure stability of materials, the present study has focused on the following theme:

### **“The Role of Thermo-Kinetic Measurements and Modelling In Materials Design”**

In truth, this study is concerned with the *Calorimetric investigation of high temperature phase stability and thermal properties* of two indigenous nuclear materials that are of interest to Indian nuclear power program. This study has both experimental and modelling components, which will be outlined while enumerating the scope of each chapter. But before proceeding further, a brief familiarizing account of materials of this study is given below.

## **7.0. Materials of Study**

### **7.1 Reduced Activation Ferritic-Martensitic (RAFM) steel**

The principal material of this study is the Indian version of “ **Reduced Activation Ferritic Martensitic Steel (RAFM)**”, that is being developed by a consortium of three Indian research organizations (Indira Gandhi Centre for Atomic Research, Kalpakkam, Bhabha Atomic Research Centre, Mumbai and Institute of Plasma Research, Ahmedabad) and one industry (MIDHANI, Hyderabad) dedicated to developing structural materials for Indian nuclear and advanced ultra supercritical power plant applications. RAFM is an advanced version of Fe-based low carbon (~0.09 wt.%) and high Cr (~9wt.%) steel containing V, Ta, and W as principal substitution alloying elements. The amounts of B, N, S and P as impurities are kept under tight control. RAFM steel, but for its end applications is quite similar to modern 9Cr-based power plant steels, such as Gr. 91 or 92.

There are quite few excellent reviews surveying the metallurgy of modern power plant steels [29-30]; and their preeminent importance in nuclear applications is highlighted by Klueh [31]. In view of this, and further in deference to maintaining brevity, a comprehensive description of the physical metallurgy of ferritic steels is not attempted here. However, in general terms, one can say that the physical metallurgy of high Cr steels is one of  $\alpha$ -ferrite+carbides $\rightarrow\gamma$ -austenite transformation, which occurs during heating and the reverse,  $\gamma\rightarrow\alpha'$ -martensite formation upon cooling. Thus, in this sense, it is no more special than a low alloy carbon steel, except for the fact, that the presence of mutually interacting substitutional alloying additions like Ni, Mn, Mo, Nb, V, Ta, Si, Co etc, exerts a non trivial influence on the thermo-kinetic aspects of phase transformations. Nevertheless, their presence lends an excellent degree of tailorability to final microstructure, through adroit thermomechanical processing. This will become amply clear, when discussing the calorimetry results on RAFM steel.

The steel under study came from MIDHANI, and was made by vacuum induction melting, followed by vacuum arc refining, and hot forging cum rolling of the ingot into plates. Obviously RAFM steel is an advanced ferrous alloy, the successful use of which for fusion first wall and blanket applications in ITER concept, required reliable physical metallurgy and thermophysical property database. In the present study, calorimetry is the chosen experimental technique, as it gives information on both energetics and kinetic quantities of phase stability. Besides, it can also be used to measure high temperature heat capacity. However, it must be added that RAFM steel is a complicated material for performing accurate calorimetry, especially the analysis of results, as multiple phase transformations with overlapping temperature domains constitute its phase diagram. In the present study, careful dynamic calorimetry studies were employed to unravel the high temperature phase stability of RAFM steel up to its melting range. In particular, data on transformation kinetics of diffusional and displacive phase transformations are also detailed.

## 7.2. *Ferroboron: A Potential Neutron Shield Material*

The second material of this study is a **Ferroboron** alloy, which is still under development as an alternate, commercially viable fast neutron shield material. Unlike, the INRAFM steel, which has enough overseas predecessors like Eurofer, F82H, CLAM, *etc.*, [31], the genesis of Ferroboron as a India-specific nuclear material merits special mention. The story of the development of Ferroboron shield subassembly and its ongoing in-pile testing has been presented recently by Keshavamurthy *et al.*[32]. The aspects related to characterization of high temperature phase stability are summarized in Ref. [33, 34].

Being a new candidate material for nuclear applications, Ferroboron (Fe with 15 wt.% B) required extensive characterization on all counts. The present

investigation has contributed to the characterization of high temperature thermal stability, heat capacity and thermal expansion of this indigenous neutron shield material, using both static and dynamic calorimetry techniques, high temperature x-ray diffraction, besides diffusion couples for probing its long term, high temperature metallurgical compatibility with SS304L clad tubes, which is the proposed outer shield clad material in PFBR.

Further description of materials, has been presented at appropriate places in this thesis report.

## **8.0. Organization of thesis**

This thesis report consists of nine (9) chapters in all. Of these, the present inaugural chapter sets the tone of the thesis, by elaborating the scope of this study in the milieu of nuclear materials design.

*Chapter 2* deals with experimental methods. In particular, the principles of drop and dynamic calorimetry techniques together with the salient details of carrying out good reproducible calorimetry measurements are described in this chapter.

*Chapter 3* is concerned with the description of a thermodynamic theoretical apparatus that is useful in thermoelastic property data estimation and assessment. Starting from simple straight forward definitions of basic thermodynamic quantities, a systematic building of various thermodynamic interrelationships between enthalpy (H), molar volume (V) and bulk modulus (Bs) is made. Few useful scaling relationships between thermal and elastic quantities that would enable the prediction of elastic quantities from heat capacity data or *vice versa* are also provided in this chapter.  $\alpha$ -Pu has been taken up as an illustrative case study material, for demonstrating the validity of the theoretical framework developed in this study.

*Chapter 4* deals with the phenomenological framework of kinetics of diffusional and displacive martensitic transformations. The purpose of this chapter is to provide the necessary theoretical basis for the analysis of the dynamic calorimetry results obtained on RAFM steel.

*Chapter 5* deals with drop calorimetry measurements of enthalpy increment data on RAFM steel. Drop calorimetry measurements give (near) equilibrium values of  $\alpha(\text{ferrite})+\text{Carbide}\rightarrow\gamma(\text{austenite})$  transformation start ( $A_{c1}$ ) and finish ( $A_{c3}$ ) temperatures, together with associated enthalpy. Further, the measured enthalpy data over a range of temperature have been treated to get the much needed heat capacity data on RAFM steel. *Chapter 5* contains probably the first ever reported results of drop calorimetry based enthalpy and heat capacity data for a RAFM steel.

*Chapter 6* deals with the dynamic calorimetry measurements of the on-heating transformation sequence encountered in RAFM steel, during slow heating, so that the results can be cross corroborated with equilibrium predictions. In this chapter, the effects of heating rate variation in influencing the kinetics of diffusional  $\alpha(\text{ferrite})+\text{Carbide}\rightarrow\gamma(\text{austenite})$ , transformation is quantitatively analysed and a continuous heating transformation (CHT) diagram has been proposed for RAFM steel.

*Chapter 7* is concerned with the displacive martensitic transformation in RAFM steel that occurs upon cooling from single phase austenite. The kinetic characteristics of martensite formation, as affected by the austenitisation temperature, holding time in the austenite domain and the cooling rate are investigated by differential scanning calorimetry. The cooling rate to form nearly 100% martensite has also been estimated as a part of this study. The role of undissolved carbides in influencing the martensite propagation kinetics is also critically reviewed in this chapter.

*Chapter 8* deals exclusively with the results of comprehensive characterization study on Ferroboron. This chapter contains the results of static and dynamic calorimetry based thermal stability estimates of Ferroboron. The anisotropic thermal expansion behavior has been quantified using high temperature x-ray diffraction (HTXRD). But more importantly the high temperature metallurgical compatibility of Ferroboron with SS304L has been investigated using diffusion couple experiments.

In the light of research findings reported in this study, *Chapter 9* identifies some of the potential avenues for further research.

**Conclusions:** This introductory chapter sets the tone of the thesis report. It begins with the brief highlighting of the issues involved in both top-down and bottom-up approach to nuclear materials design. The synergy between various linkages is brought out in designing materials knowledge base for nuclear applications. This is followed by the enumeration of the scope of this study, which is to investigate the thermokinetic aspects of high temperature phase stability in two indigenous materials, namely RAFM steel and Ferroboron alloy. A brief familiarizing account of these two materials, followed by a succinct summary of the organization of this thesis into different chapters, constitutes the rest of this chapter.

## References

1. Ingemar A. E. Hulthage, Mark S. Fox, Michael P. Rychener and Martha L. Farinacci, *The architecture of ALADIN: a knowledge based approach to alloy design*, IEEE Expert, Aug. (1990) p.56.
2. D. Raabe, B. Sander, M. Fria'k, D. Ma, and J. Neugebauer, *Acta Mater.*, 55 (2007) 4475.
3. J. A. Elliott, *Int. Mater. Rev.*, 56 (2011) 207.
4. Z. X. Guo, D. G. Pettifor, L. Kubin and G. Kostorz, Selected papers of the 1st International Conference on Multiscale Materials Modelling – London, United Kingdom 17–20, July 2002 – Preface, *Mater. Sci. Eng. A*, A365, (2004) 1.
5. P. E. J. Flewitt: ‘The use of multiscale materials modelling within the UK nuclear industry’, *Mater. Sci. Eng. A*, A365, (2004) 257.
6. A. M. Stoneham, *Mater. Sci. Eng. C*, C23, (2003), 235.
7. A. Gonis, P.E.A. Turchi, and J. Kudrnovsky, (eds.), *Stability of Materials*, Vol. 746 of NATO Advanced Study Institute, Series B: Physics (New York: Plenum, 1996).
8. H. R. Shercliff, *Modelling of materials and processes*, CUED/CMATS/TR243, Cambridge University Engineering Department, Cambridge, UK, (1997).
9. M. Asta, V. Ozolins, and C. Woodward, *JOM*, Sep. 2001, p.16.
10. A. Zunger, *MRS Bulletin*, 22 (1997), p.20.
11. N. Saunders and A. P. Miodownik, *CALPHAD: Calculation of Phase Diagrams: A Comprehensive Guide*, Oxford, U.K, Pergamon Press, (1998).
12. L. Q. Chen, *Annu. Rev. Mater. Res.*, 32, (2002) 113.
13. K. Thornton, J. Agren and P. W. Voorhees, *Acta Mater.*, 51, (2003), 5675.
14. I. Steinbach, *Model. Simul. Mater. Sci. Eng.*, 15 (2009) 17.

15. B. Devincere and L. P. Kubin, *Mater. Sci. Eng.*, A234, (1997) 8.
16. W. A. Curtin and R. E. Miller, *Model. Simul. Mater. Sci. Eng.*, 11, (2003), R33.
17. Yan Song, Rui Yang, Dong Li, Zhuangoi Hu and Zhengxiao Guo, *J. Comp-Aided Mat. Design*, 6, (1999) 355.
18. Ai Wu Zhu, Gary J Shiflet and E. A. Starke., Jr., *Mat. Sci. Forum*, 519-521, (2006) 35.
19. J. M. Rickman and R. LeSar, *Annu. Rev. Mater. Res.*, 32 (2002) 32.
20. D. J. Bacon and Y. N. Osetsky, *Int. Mater. Rev.*, 47, (2002) 233.
21. S. Sharafat, G. R. Odette and J. Blanchard, *J Nucl. Mater.*, 386-388 (2009) 896.
22. G. B. Olson, *Acta mater.*, 61 (2013) 771.
23. Krishna Rajan, *Data mining & Material Informatics: a primer*, lecture notes, available from: [www.tms.org/pubs/journals/jom/0703/rajan.pdf](http://www.tms.org/pubs/journals/jom/0703/rajan.pdf)
24. M. Samara, W. Hoffelner, Chu Chun Fu, M. Guttman and R. E. Stoller, *Proceedings of ICAPP*, Nice, France (2007), paper # 7207; see also; S. Zinkele's paper in this proceedings.
25. R. Viswanathan, J. Sarver, and J. M. Tanzosh, *J. of Materials Engineering and Performance*, 15, (2006) 255.
26. B. D. Wirth, K. Nordlund, D. G. Whyte, and D. Xu, *MRS Bulletin*, 36 (2011) 216.
27. F. Masuyama, *ISIJ Inter.*, 41 (2001) 612.
28. K. Maruyama, K. Sawada and J. Koike, *ISIJ Inter.*, 41 (2001) 641.
29. H. K. D. H. Bhadeshia, *ISIJ Inter.*, 41 (2001) 626.
30. F. Abe, M. Taneike and K. Sawada, *J. press. vessels & piping*, 84 (2007) 3.
31. R. L. Klueh and D. R. Harris, *High Chromium Ferritic and Martensitic Steels for Nuclear Applications*, ASTM, PA (2001).

32. D. Sunil Kumar, R. S. Keshava Murthy, P. Mohanakrishnan and S. C. Chetal, *Nucl. Eng., Design*, 240 (2010) 2972.
33. S. Raju, A. K. Rai, B. Jeyaganesh, M. Vijayalakshmi, T. Jayakumar and Baldev Raj, *Energy Procedia*, 7 (2011) 264.
34. A. K Rai, S. Raju, B. Jeya Ganesh, G. Panneerselvam, and M. Vijayalakshmi, *Nucl. Eng. and Design*, 241 (2011) 2787.

## Experimental Methods: Drop, Differential Scanning Calorimetry and Supporting Metallography

### 1.0. Introduction

The main experimental technique that is adopted in this study for making thermodynamic and kinetic measurements is calorimetry, in its static and dynamic variants. In the former category, the inverse drop calorimetry (IDC or simply DC) has been chosen for the measurements of high temperature enthalpy increments ( $H_T - H_{298.15}$ ). This is an isothermal calorimetry experiment, yielding values of enthalpy increment at the selected experimental temperature. The enthalpy data thus obtained over a range of temperature constitutes the basic thermodynamic or thermochemical information, from which other thermodynamic quantities like specific heat, entropy and Gibbs energy can be estimated by standard procedures. If performed carefully and over a reasonable range of temperature with as close a temperature interval ( $\Delta T$ ) as can be adapted under prevailing situation, drop calorimetry data offer reliable means of getting good high temperature heat capacity data. In the present study, SETARAM MultiHTC96<sup>®</sup> type calorimeter is employed in its 'inverse drop mode' for high temperature enthalpy measurements.

The dynamic calorimetry, as the name suggests, is performed under nonisothermal conditions. In the present study, a differential scanning calorimeter, of SETARAM Setsys1600<sup>®</sup> heat-flux type is used for studying both energetic, and in particular, the kinetic aspects of phase transformations that occur during heating and cooling cycles from fixed set temperatures, at usually predetermined scan rates ( $\beta$ ). Both calorimetry

techniques are complementary, although, the scanning calorimetry owing to its relative ease and speed of measurement appears to be the most popular one in use.

At this point, it may be said in general terms, that by virtue of the scanning mode, the measurements of differential scanning calorimetry (DSC) often pertain, not to true thermodynamic *equilibrium* conditions, - a fact that obliterates the value of DSC based thermodynamic data to an extent. It is possible to operate DSC under isothermal conditions as well; however, the temperature stability to a high level of desire is still a question mark in many commercial DSC equipments. The drop calorimetry on the other hand is implicitly designed for better thermal stability, but makes a relatively huge demand on experimental time and other requirements. It is obvious that preference among the two is dependent on the problem under investigation. In tune with the scope of this study as outlined in the opening chapter, both techniques are employed. Accordingly, a brief description of important details of both drop and DSC techniques are presented in this chapter.

Besides, it should also be mentioned that the present study though primarily oriented towards calorimetry as the major investigation tool, has also made extensive use of supporting metallography tools like x-ray diffraction, microhardness measurements, optical and scanning electron microscopy techniques. These supplementary techniques support the basic calorimetry data by the way of providing useful microstructural characterization of the calorimetry samples.

## **2.0. Importance of Calorimetry in Phase Stability Characterisation**

At the outset, it must also be mentioned that there exists in open literature, very little critically assessed thermodynamic data for many of the advanced power plant ferritic steels, which are essential from the point of view of understanding and predicting thermal and microstructural stability at typical operating temperatures for

extended service times. In case of special grade ferritic alloys meant for nuclear fission and fusion applications, this requirement is even more critical, as phase stability estimation and alloy design are required to meet more stringent design specifications and demanding service conditions [1-10].

*It may be added that drop calorimetry based enthalpy data are not available in open literature for RAFM steel. The present study constitutes the first such set of measurements, performed on indigenously developed reduced activation ferritic-martensitic steel. These data when taken together with accurate estimates of transformation temperatures, transformation enthalpy values obtained by dynamic calorimetry measurements constitute a very valuable basis towards generating a self consistent thermodynamic database on RAFM. A similar argument holds good for the other material of this study, namely Ferroboron, a possible alternate neutron shielding candidate material. In both cases, the research is conceived as an integral part of providing the necessary physical metallurgy support to indigenous alloy development initiative, and has therefore focused on performing accurate characterization of the thermal stability of these indigenous compositions.*

Although laborious and time consuming, phase stability characterization through dedicated experiments is an established research program for obtaining valuable information on time and temperature dependent evolution of microstructure. On the other hand, thanks to recent developments in computational power and theoretical methodologies, it is also possible to predict phase stability with reasonable degree of confidence, if accurate (optimal) thermochemical data on various phases are available, both as functions of composition and temperature. This requirement of having optimal database is considered essential from the point of view of validating the predictions. Thus, the availability of information on fundamental quantities like enthalpy, entropy

and Gibbs energy as a function of temperature and composition for different phases and their change while undergoing phase transformation plays a crucial role in the fundamental thermodynamic characterization of high temperature materials.

### 3.0. Calorimetry: General Principles

A calorimetry measurement in its essence is nothing but accurate thermometry, with the important *caveat* that the measurement of temperature or its differential is accurately quantified in terms of the *effective* heat transacted between a sample and a suitable reference medium under full thermal equilibrium. This calorific quantification is realized by employing suitable calibration procedures [11].

The basic principle of calorimetry is easy to understand: When two bodies, initially at different temperatures are brought into thermal contact, heat is transferred from body with higher temperature to one at lower temperature. This heat transfer if ensured to happen in a loss free or loss minimized ambience, such as the one prevailing in a good, properly insulated calorimeter; - can be quantified as being directly proportional to the driving temperature difference, with the temperature dependent (also instrument dependent in practice) proportionality constant  $C(T)$ , embodying the complex interplay of many different factors. The relationship between the heat ( $Q$ ) that is transferred and the change in final and initial temperature ( $T_f - T_i$ ) is given as

$$Q = C(T) \times (T_f - T_i) \quad (2.1)$$

Different calorimeters differ in the manner in which the heat transport between the objects involved in energy transaction and the sensor device is ensured. The proportionality constant  $C$  appearing in *Eq. (2.1)* is therefore a superposition of the apparent heat capacity of the sample producing heat and also the heat transfer characteristics of the entire calorimetry cell, including ambience details, like gas

pressure, gas flow rate, thermal characteristics of the crucible *etc.* Although it is theoretically possible to model the heat transfer phenomenon that occurs in a given type of calorimeter under a set of well defined experimental conditions, so that the calorimetry constant  $C(T)$ , can be estimated on an *ab-initio* basis [12]. But in general practice, it is preferred to estimate  $C(T)$ , by performing the experiment with a suitable standard under well defined conditions, for which the amount of  $Q$  or enthalpy that is transacted is accurately known *a priori*. In this way, the transferability of  $C$  is ensured between the calibrant and the actual sample, *if indeed the experiments are performed under identical and reproducible conditions*. So calibration of a calorimeter is of paramount importance.

Apart from this general principle, the actual methodology employed in calorimetry calibration is dependent on the type of calorimeter used, which in turn is decided by the choice of materials systems, and the temperature range of interest and the nature of physical problem studied [13,14]. While there are many designs of static calorimeters, in which the experiment and measurement are done under constant temperature or probably at *near-equilibrium* conditions, there are also techniques in which the thermal response of a system is monitored as a function of time, during which the temperature of the furnace and thereby the sample is continuously changed. This dynamic or scanning technique, as mentioned earlier in introduction, has one remarkable feature, in that the measurement is often carried out under *non-equilibrium* conditions [14]. By virtue of this possibility, which is both an advantage and limitation in its own respect, the dynamic calorimetry technique can be put to effective use for studying a variety of non equilibrium phenomenon, such as phase transitions, relaxataion phenomenon especially their onset temperatures as a function of heating (cooling) rate, together with the associated heat effects [14].

The static calorimetry technique on the other hand is useful in studying the time dependent stability at a fixed temperature under close to ideal thermal equilibrium conditions. Such a set up is ideally suited for making equilibrium thermodynamic property measurements of a stable phase as a function of temperature. The major characteristics of many different versions of static and dynamic calorimetry techniques are adequately summarized in the compendium authored by Cezairliyan *et al* [15]. In deference to the limited space and keeping in focus the major techniques used in this study, the present description is confined to only drop and scanning calorimetry techniques. In what follows, the drop calorimetry technique is taken up first for detailed discussion

### 3.1. Principle of Drop Calorimetry

Enthalpy increment, that is relative enthalpy at a chosen temperature  $T$  with respect to its value at the reference temperature, usually taken as 298.15 K, is measured in a direct drop calorimeter by heating a sample to the desired temperature at suitable heating rate and after equilibration at this temperature for some fixed time is dropped in to a well-equilibrated calorimeter block or bed that is maintained at fixed reference temperature. Driven by the temperature differential, the measured rise in the temperature of the calorimeter substance due to heat transfer under externally insulated conditions is used to obtain the enthalpy of the sample, knowing its mass and the heat capacity of the calorimetry fluid or solid. The experiment is usually repeated by dropping the reference or calibrating sample of known mass and known enthalpy under identical experimental conditions. In an actual schedule of drop calorimetry measurements, temperature of sample is varied in discreet closely spaced steps and the experiments are repeated afresh at each new temperature with *new* sample. Despite the possibility that the successive drops can be performed at fairly

closely spaced temperature intervals; the drop calorimetry offers only a set of closely spaced discrete data points. *One does not obtain a continuous enthalpy increment versus temperature data through drop calorimetry. This has important bearing in the precise fixation of the transformation temperatures, although the enthalpy change accompanying phase changes are accurately given in drop calorimetry.* The measurement of phase change enthalpy using drop calorimetry is given below (see, **Fig. 2.1**).

The measuring block in the calorimeter consists of a well-insulated calorimeter substance (liquid or solid) usually contained in a alumina crucible surrounded by circumferential arrays of B-type thermocouples which serve to accurately measure the change in temperature upon dropping a hot sample into the cold block [17]. This temperature difference  $\Delta T$  arises due to the transfer of heat (thermal energy) from the hot sample to the calorimeter substance, under ideally speaking, adiabatic conditions. In practice, there are invariably present in any calorimetry set up, some thermal loss mechanisms, such as due to radiation. In actual practice, the output of the thermopile  $\Delta V$  (normally in microvolts) is continuously monitored with time until the thermal equilibration ( $\Delta T \sim 0$ ) is completely obtained. This may take anywhere between 20 to 30 minutes, depending upon the experimental parameters.

The net heat change  $Q$  (inclusive of losses in a strict sense; but which is kept minimal in a good calorimeter design) is determined as

$$Q = C(T) \Delta V \times \Delta t \quad (2.2)$$

where  $C(T)$  is the usual calibration constant.  $C(T)$  is determined by calibration with known enthalpy standards like  $\alpha$ -alumina. By determining  $Q(T)$  as a function of temperature  $T$ , the curve of enthalpy versus sample temperature is readily obtained. A schematic of one such enthalpy curve or drop curve, as it will be referred to in this thesis report, is shown in **Fig. 2.1**. This curve is obtained for a simple substance,

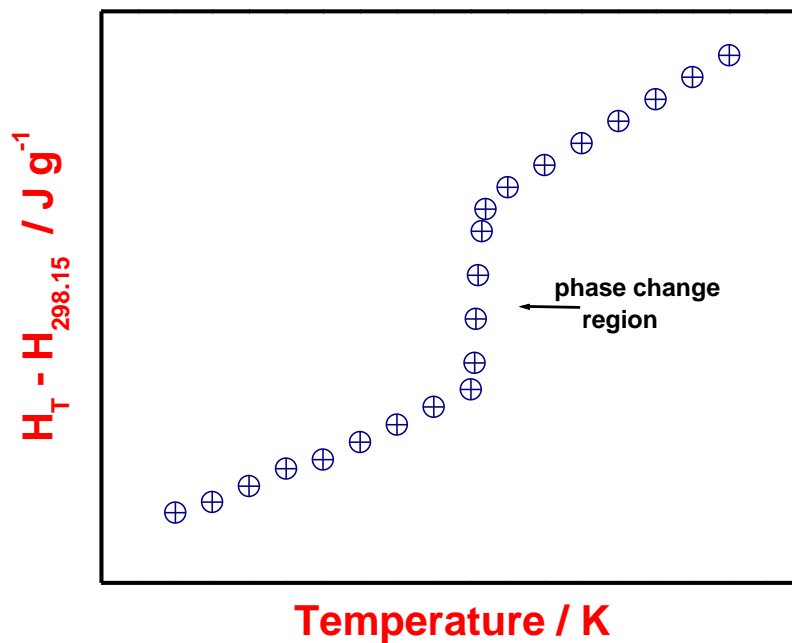


**Fig. 2.1** Schematic of enthalpy increment variation with temperature. This is referred to as 'drop curve' in this study

which exhibits a phase change at fixed temperature. Usually, there will be an enthalpy jump that is associated with a phase transformation event; this however may not be as dramatic as the one that is portrayed in Fig 2.1. However, if the transformation is continuous, that is occurring over a temperature domain, then the enthalpy exhibits a gradual change of slope. This is often the case with the  $\alpha$ -ferrite to  $\gamma$ -austenite phase transformation that occurs in many ferritic steels.

### 3.2. Inverse Drop Calorimetry

In the inverse drop calorimeter mode, measurements are made in the inverse manner, namely the cold sample is dropped onto the hot calorimeter bed. The principal advantage of this inverse drop mode over the normal one is that the heat losses that are accrued in the normal mode of dropping the hot sample are minimized by resorting to dropping of cold samples. In accordance with this change, the instrument is also tailored in its design in the appropriate manner [17]. Inverse drop

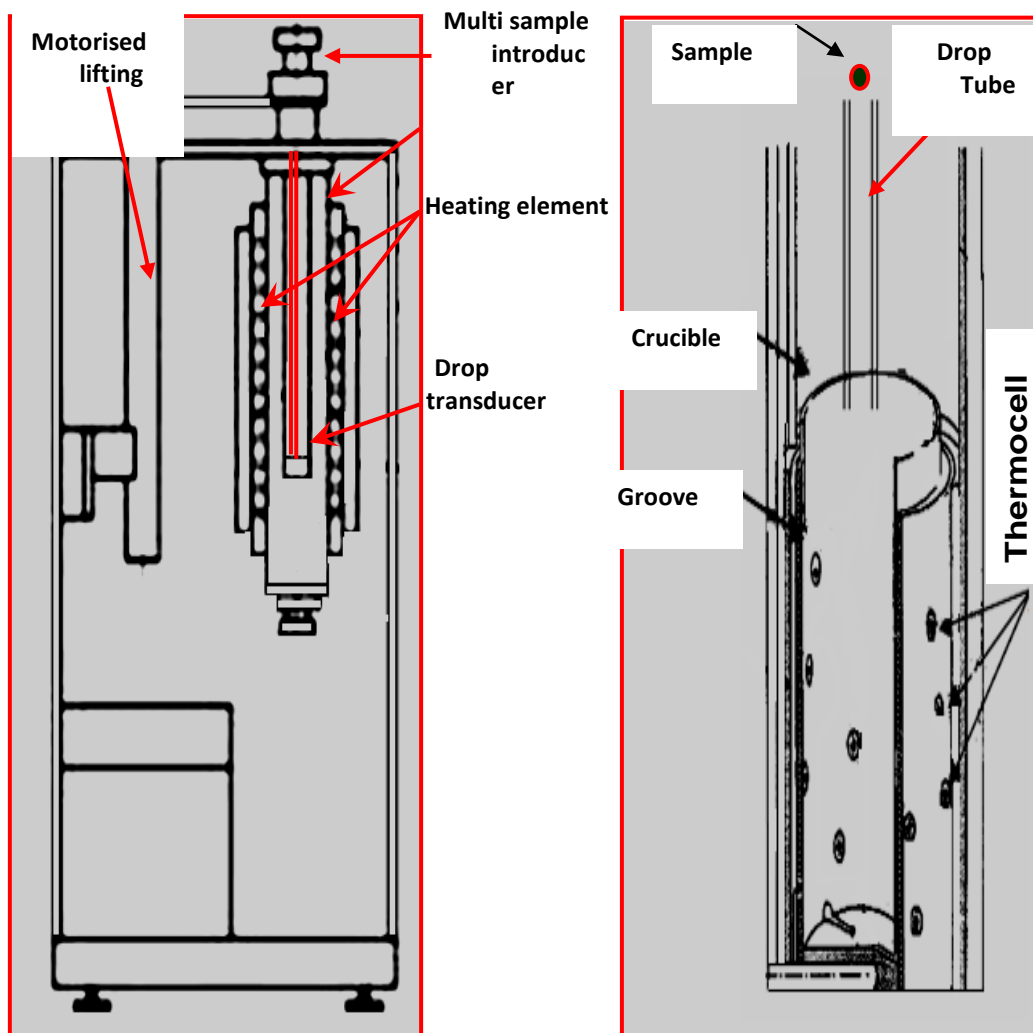


**Figure 2.2** (a) High temperature furnace with cabinet (b) Measurement head [17]

calorimetry has some advantages; namely it can easily adopt small sample size, avoid any metastable phase retention from high temperature excursion, ability to study

many different types of chemical reactions *etc* [15]. But, there is also a significant limitation, in that strongly displacive transitions like martensitic ones that take place almost instantaneously in power plant ferritic alloys upon cooling from high temperature austenite phase, are not readily studied in the inverse drop mode. This is because, martensite forms upon cooling of high temperature austenite phase beyond a threshold or critical cooling rate. It is obvious that dropping of hot austenite sample is not feasible in inverse mode of drop calorimetry.

### 3.3. Instrument Details

The drop calorimeter used in this study is manufactured by *Setaram*, France; - the actual model is the “Multi Detector *HTC Drop Calorimeter – 96 type*, functioning in inverse drop mode. The instrument details are pictorially depicted in **Fig. 2.2** [17].

#### 3.3.1. High Temperature Furnace

The high temperature furnace, supported by the drop calorimeter cabinet's top plate is displayed in **Fig. 2.2 (a)**. The furnace is made out of graphite tube which acts as the heating element (1) that surrounds the experimenting chamber containing the calorimeter. A sealed alumina tube (2) running from the top portion of the furnace into the bottom separates the experimental chamber from the furnace atmosphere.

#### 3.3.2. Measurement Head – Drop Transducer

The experimental chamber containing the transducer is usually called the drop transducer or detector whose cross sectional view is displayed in **Figure 2.2(b)**. This measurement head itself is an integrated structure made of a cylindrical recrystallized alumina tube in which two grooves are cut at its bottom to introduce the sample crucible. The crucible has a working volume of  $6.25 \text{ cm}^3$  with dimensions 16.20 mm in diameter and 44.50 mm in height. The measuring crucible's temperature is monitored by a thermocell made up of 28 B-type thermocouples distributed over the

bottom and all over the side surface of the crucibles. Similarly a dummy reference crucible having an identical thermocell arrangement is kept underneath the sample crucible. This vertically aligned arrangement of both the sample and reference crucible is placed in the uniform temperature zone of the graphite furnace. Measurement of the sample and furnace temperatures is undertaken by two thermocouples of B type (PtRh-6% / PtRh-20%).

### 3.3.3. *Multi-Sample Introducer and the Drop Tube*

The multi sample introducer equipped at the top portion of the experimental chamber shown in **Figure 2.2(a)** provides 23 slots to load samples in to it. Normally four to six samples are loaded for each measurement. For each sample, a reference sample is also loaded in to the adjacent slot. The drop tube called sample-guiding tube shown in **Figure 2.2(b)**, guides the sample to fall exactly in to the sample crucible during the course of the experiment.

### 3.3.4. *Gas, Vacuum, Chill-water Circuit and Controller*

The equipment contains two separate gas circuits, one for the furnace and another for the analysis chamber to maintain the required inert gas atmosphere. An external rotary vacuum pump (EDWARDS) supplied by *Setaram* is used for evacuating both the experimental and furnace chambers before starting the experiment. An external chill water supply with controlled flow (Julabo FC 1600 T) is provided for the furnace cooling. The heating schedule programming, the data acquisition and storage are performed through the CS 32 controller interfaced with the personal computer. In the following section, the procedure for performing inverse drop calorimetry experiment is discussed.

## 3.4. *Experimental Procedure*

The samples for drop calorimetry are cut from slices of steel by slow speed diamond wire saw. After cutting, they are cleaned thoroughly with methanol and dried before weighing. The sample mass is kept around 50 – 75 mg with a dimension of 2-3 mm square with 2 mm height. The cuboidal sample is loaded in to the respective specimen slots of the multi sample introducer of *Setaram* multi HTC inverse drop calorimeter. Along with samples, the standard alumina ( $\alpha$ -Al<sub>2</sub>O<sub>3</sub>) samples weighing 66.8 mg and supplied by Setaram are also loaded in to respective vacant slots.

#### 3.4.1. Working Crucible Loading

This is usually done by lifting the whole measurement head column by pressing motor lifting switch (**Figure 2.3a**). The working crucible is the one which contains the high pure alumina powder called the calorimeter substance onto which the sample is dropped during each experiment. The working crucible together with the alumina powder is called the alumina bed. Once the alumina powder is filled to 3/4<sup>th</sup> of the crucible capacity, it is loaded in to the measurement head. Similarly the working crucible can be unloaded after each experiment using the motor lifting switch.

#### 3.4.2. Calibration of Drop Calorimeter

The temperature of the calorimeter has been calibrated periodically (every 3 months) with melting of pure element standards such as In, Sn, Al, Ag, Au, Cu. The heat change (Q) calibration is made by dropping the  $\alpha$ -alumina standard reference material. The performance of the thermocell has also been monitored by repeatedly observing the standard deviation of the value of heat change (Q) of the standard  $\alpha$ -alumina in the temperature range 460 to 1373 K. For example, the temperature variation of Q measured over one typical experimental schedule is graphically shown in **Fig. 2.3**. In this figure, an inset is shown for a typical sensitivity curve used for enthalpy evaluation. The polynomial fit expression used is:  $a + bT + cT^2 + dT^3$  and the

fit coefficients obtained are:  $a=0.248\pm0.078$ ,  $b=7.84\pm2\times10^{-4}$ ,  $c=8.795\pm3\times10^{-8}$ ,  $d=-2.5\pm1\times10^{-10}$ .

In this figure, different symbols correspond to different sets of data obtained at different instances of time with standard  $\alpha$ -alumina. The individual data points of Q quoted here are taken from different experimental runs (more than 10) that have been carried out on alumina when used as the standard during enthalpy measurement. It is found that the standard deviation of Q is less than 5 up to 810 K and is less than 13 for higher temperatures. It must be mentioned that in each experiment, the filling level of

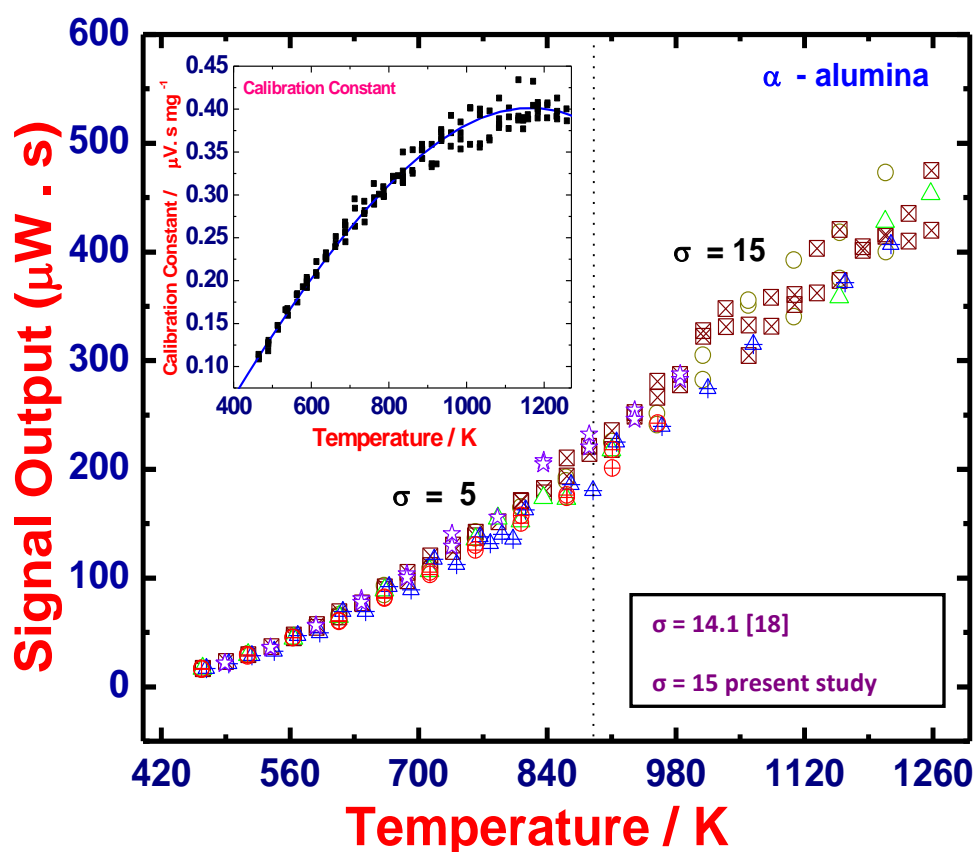


**Fig. 2.3** Illustration of the temperature variation of Q for a typical experimental schedule and Calibration constant (inset)

alumina powder in the sample crucible is nearly the same, although it could not be claimed that it was maintained at an absolutely constant level throughout.

### 3.5. Performing Drop Calorimetry Experiment

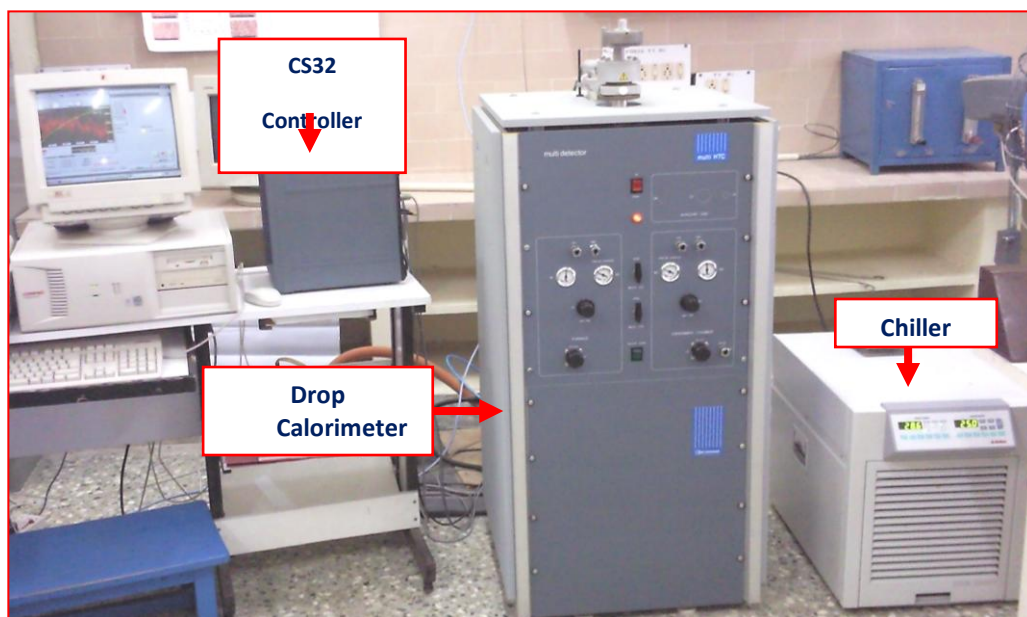


**Fig. 2.4.** The experimental setup of drop calorimeter

The present drop calorimetry experimental setup is displayed in **Fig. 2.4**. After loading the samples and setting the working crucible in its position, the experimental as well as the furnace chambers are evacuated. This is followed by flushing both the chambers with high purity argon gas (Iolar grade II) a few times, and continuing the process of evacuation and controlled argon gas leaking in an alternate manner. When the argon gas pressure level reaches one atmospheric pressure in both chambers, the chill water supply is switched on. Then the furnace is gradually heated to a desired experimental temperature at a rate of about  $3\text{--}5\text{ K min}^{-1}$ . Once the pre-set value of the temperature of the alumina bed is attained to within the accuracy of  $\pm 0.1\text{ K}$ , the respective samples are dropped from the corresponding slots in to the hot alumina bed through the guiding ceramic drop tube (**Fig. 2.3b**). The heat absorbed by the sample upon dropping produces a sudden change in the temperature of the alumina bed. The thermocell measures the temperature difference between the sample and reference and

the typical integrated output is given as  $\Delta V$  vs. time (t) is shown in **Fig. 2.5**. The RS 232 controller serially interfaced with the computer provides for this digital conversion. An identical experiment is carried out at the same temperature by dropping the known mass of calibration standard to quantify the heat flux, which is measured as area under the  $\Delta V$  vs. time curve [19].

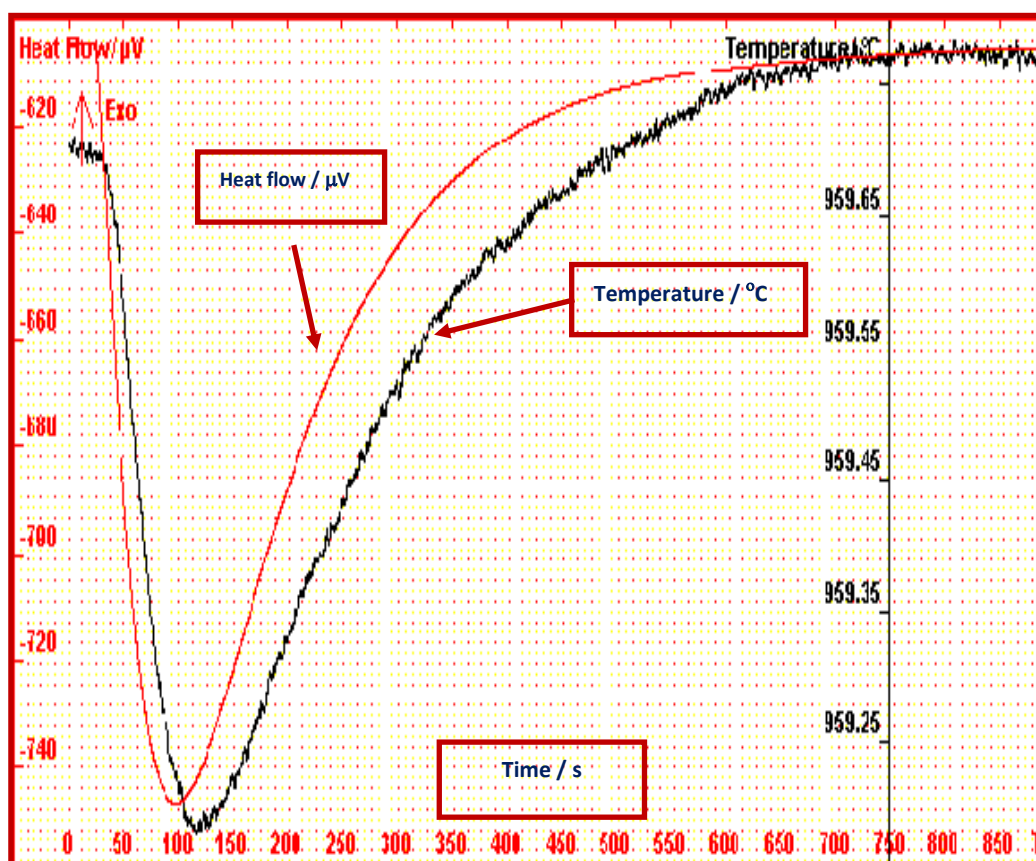


**Fig. 2.5** Snapshot of the drop calorimeter signal output

The elaborate methodology of converting the raw signal into effective enthalpy is outlined in detail Ref. [20]. A brief description of essentials is provided here. The typical time for the data acquisition is maintained between 20 and 25 minutes for each drop. Once the data acquisition is completed for one drop experiment, quite a sufficient time is allowed for the alumina bed to retain its thermal equilibrium for the next drop. This time gap between the successive drops must be adequate so that no

spurious data by the way of non equilibrium character of the alumina bed are collected by the subsequent drop measurements.

In the present study, a time of about 20 minutes is allowed to elapse between successive drops. *Finally, it must also be mentioned that new, nearly identical samples are used for each successive drops.* The mass of the dropped samples are measured after the experiment to gauge any loss or gain due to reaction with the bed or due to oxidation. Normally, about four drops are performed for each temperature; this is done in order to assess the intrinsic scatter associated with the experiment at one temperature and with the particular experimental methodology chosen. Once a satisfactory degree of reproducibility has been established, the number of repeat drops has been kept to three, as this resulted in considerable saving of time.

A total of three experimental schedules covering the temperature range 400 to 1400 K are conducted. The upper temperature range is varied according to the requirements. Each experimental schedule consists of a series of successive drop experiments performed at prefixed discrete temperature steps (approximately 25 K) so that the entire region of stability of the  $\alpha$ -ferrite phase, besides some limited incursion into the  $\gamma$ -austenite domain of 9Cr-1W based RAFM steel is included in the final analysis. In addition, a few more additional runs are also performed at select temperatures on a nonregular basis to frequently check the deterioration in reproducibility. Apart from a few stray data points, which are identified to be clear outsiders to the generally observed data trend, all the rest of data points obtained in this manner are used in the final analysis. The samples after the drop experiment are carefully preserved for further metallographic characterization.

### 3.6. *Enthalpy Estimation*

As mentioned before, the raw signal ( $\mu\text{V}\cdot\text{s}$ ) for both sample and the reference are measured under identical conditions. Following established procedures, it is assumed that negligible heat loss due to radiation and quasi-adiabatic conditions are sustained in the experimental chamber [18, 21].  $Q_S(T)$ , the heat energy transported from the hot alumina bed to the cold sample can be written as [18, 21]

$$Q_S(T) = C(T) \times (m_S/M_S) \times (H_T - H_{298.15})_S \quad (2.3)$$

In the above expression,  $m_S$  is the mass of the sample,  $M_S$  its molecular weight and  $(H_T - H_{298.15})_S$  is the measured enthalpy increment with respect to 298.15 K (25<sup>0</sup>C) the reference temperature and  $C(T)$  is the temperature dependent calibration constant. The calibration constant can be obtained from the heat change  $Q_R(T)$  recorded with the standard alumina reference drop, whose critically assessed enthalpy values are known from literature [22]. Thus

$$Q_R(T) = C(T) \times (m_R/M_R) \times (H_T - H_{298.15})_R \quad (2.4)$$

In this equation,  $m_R$  is the mass of the reference sample,  $M_R$  its molecular weight which is taken to be 101.96 Kg m<sup>-3</sup> [22]. It is worth noting that  $C(T)$  remains the same in both expressions. Considering Eq. (2.3) and (2.4) together, it is clear that the quantities  $Q_S(T)$ ,  $Q_R(T)$ , (heat flux transferred between the sample, reference and the alumina bed) are measured at each temperature, as the respective area under the peak (see **Fig. 2.5**). The quantity  $C(T)$ , the calibration constant is obtained by substituting in Eq. (2.4) the known enthalpy value  $(H_T - H_{298.15})_R$  of standard reference for each temperature. This calibration constant,  $C(T)$  is subsequently used to determine the unknown enthalpy  $(H_T - H_{298.15})_S$  of the sample at each temperature.

#### 4.0. General Observations on Drop Calorimetry Data

It is generally assumed that the drop calorimetry measurements are carried out at thermally equilibrium conditions. As a result, reliable and consistent thermodynamic

data are obtained with static calorimetric measurements. The enthalpy variation with temperature measured at discrete temperature increments is used to derive specific heat, by fitting the temperature variation of enthalpy to a suitable analytical representation. In principle, it is desirable to have as large a number of data points as is possible for obtaining reliable conversion of enthalpy into specific heat. This is especially true for characterizing the thermal property variation in the phase transformation domain. In drop calorimetry, when adequate precautions are ensured, it is possible to achieve reproducible experimental data points, especially since a high level of accuracy in measuring and maintaining temperature stability is possible. In the present study, we have allowed enough equilibration time so as to achieve a temperature stability of  $\pm 0.1$  K. The accuracy of temperature measurement is  $\pm 2$  K. In order to avoid or minimize the effect of thermal gradients in the sample affecting the attainment of true equilibrium, a slow heating rate of  $5 \text{ K min}^{-1}$  and a reasonable sample mass of 75 to 100 mg are adopted in this study. Too large a sample mass, while contributing to signal strength also add up to data scatter as the noise level is also raised in general. It is the general experience of the present investigation, that starting from about 300 K, it has taken about 5 hours to reach 1000 K and at this fixed temperature, the furnace is equilibrated for about 2 more hours to achieve a temperature stability of  $\pm 0.1$  K. This is the typical of experimental schedules for high temperature measurements. The measured enthalpy is accurate to  $\pm 5\%$ . (see, Fig. 2.3) In view of such careful measures adopted in the present study, it is sincerely believed that drop calorimetry technique has yielded reliable estimates for basic thermodynamic quantities. However, drop calorimetry has certain limitations, which are briefly discussed below.

#### *4.1. Limitations of Drop Calorimetry*

There is one major limitation associated with drop measurements. It comes from the discrete nature of the measurements. In essence drop technique is an isothermal experiment. As mentioned before, it is necessary to perform such isothermal measurements at closely spaced temperature intervals. But there is a practical limit to this achievement. Thus for example, it is not possible for obvious reasons to obtain drop measurements at every one or even five Kelvin interval. The time requirements for one such drop curve is really too large. Besides, the actual temperature reached between successive samples is also a function of its mass, hence identical attainment of the same temperature in the repeat experiment is strictly not possible. However, it is possible to gather reliable drop calorimetry data points at 20 to 25 K intervals, which is practical from the point of view of labour as well.

Moreover, no matter how close a temperature step is desired, a continuous enthalpy versus temperature curve is not traced in the drop calorimetry. It is for this reason, a precise measurement of transformation temperatures is not generally realized in the drop calorimetry; nevertheless it is possible to obtain a fair estimate of the transformation domain from the drop curve, if appropriate close sampling of data points is adopted around the transformation domain. In the present study, this aspect has been dedicatedly taken care of by conducting separately few repeat runs with less than 25 K step in the transformation domain alone. In this sense, it is possible to derive a fairly reliable estimate of the jump or change in enthalpy that is witnessed in the transformation region. It is needless to stress the fact that measurement of transformation enthalpy under near thermal equilibrium conditions constitutes a very valuable addition to thermodynamic database.

The other major limitation of inverse drop calorimetry is the fact that this technique is not suited for studying the energetics of martensitic transformation as this

metastable phase forms under non equilibrium conditions during rapid cooling. The inverse drop calorimetry on the other hand records the thermodynamic manifestation of events as they unfold during the heating cycle. Thus for example, it is possible to study the relaxation kinetics of martensite, precipitation of various secondary phases etc., using inverse drop calorimetry. But what is the most attractive part of drop calorimetry is that this technique permits such relaxation behavior to be studied under near thermal equilibrium conditions. It is in this sense that drop calorimetry as an isothermal technique differs significantly from dynamic or scanning calorimetry technique.

It is precisely the void that is left open by drop technique is filled by its dynamic counterpart, namely the differential scanning calorimetry (DSC). In the present study, both these techniques are employed keeping in mind their respective innate advantages to study the issue of phase stability in RAFM steel. In what follows, the dynamic or differential scanning calorimetry is described in detail.

## **5.0. Dynamic or Differential Scanning Calorimetry**

### *5.1. Principle of Heat Flux DSC*

The principle behind DSC is the comparison of the heat flow to the sample and to an inert reference material when both are heated or cooled at a fixed rate. Phase changes that are associated with heat absorption or evolution induce a commensurate change in the differential heat flow between sample and reference, which in effect appears as an uncompensated temperature differential  $\Delta T$ , spread over the transformation event. The basic output of a heat flux DSC is therefore the time dependent variation of  $\Delta T$ . The differential scanning calorimetry is hence a dynamic method where the experiments are carried out at a constant heating or cooling rate. The use of a twin crucible cradle with a single heating source (containing individual

housing for the sample and reference in DSC) is advantageous because it cancels out or compensates for the heat leakage and the temperature disturbances that are common to both housings.

The heat flux DSC used in the present study (Setaram® Setsys 1600) is displayed in **Fig. 2.6**. The heat flux calorimeter consists of two pans, one for sample and the other for reference. The two pans are connected by a low resistance heat flow path, with the thermocouple meant to sense the differential temperature positioned exactly

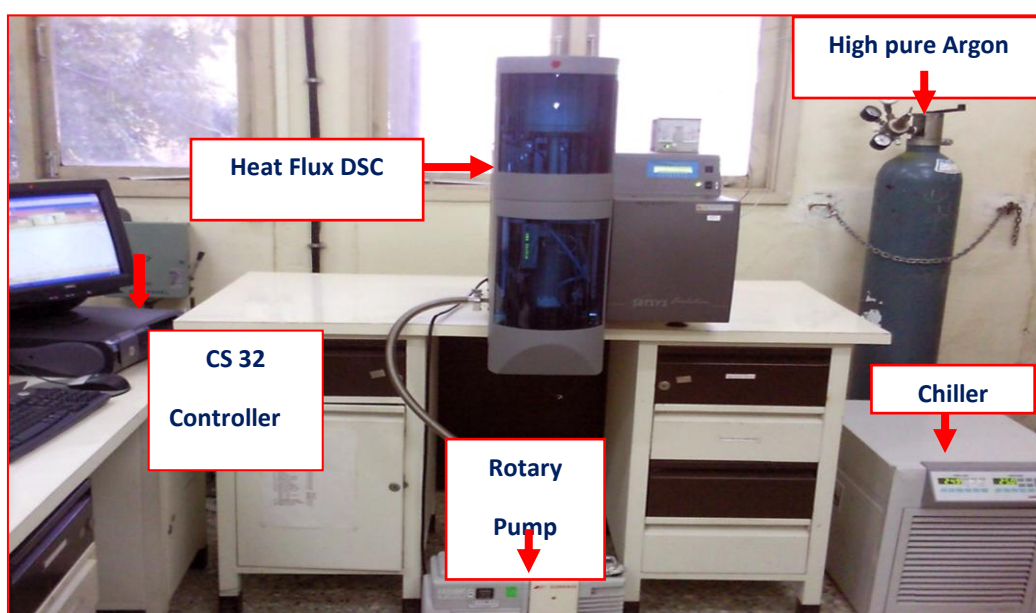


**Fig. 2.6.** The experimental set up of heat flux DSC

underneath and midway connecting sample and reference. Such an arrangement is very critical to ensuring good heat flux thermal analysis sensor, if it were to satisfy the purpose of serving as DSC. In a heat flux calorimeter, the sample and the reference pan are heated or cooled by a single furnace, while in a power compensating setup, these are heated separately.

A heat flux DSC relies on good calibration methodology for obtaining reproducible results. While, at high temperatures exceeding about 1273 K, it is altogether impossible to avoid heat loss due to radiation, nevertheless it is possible to

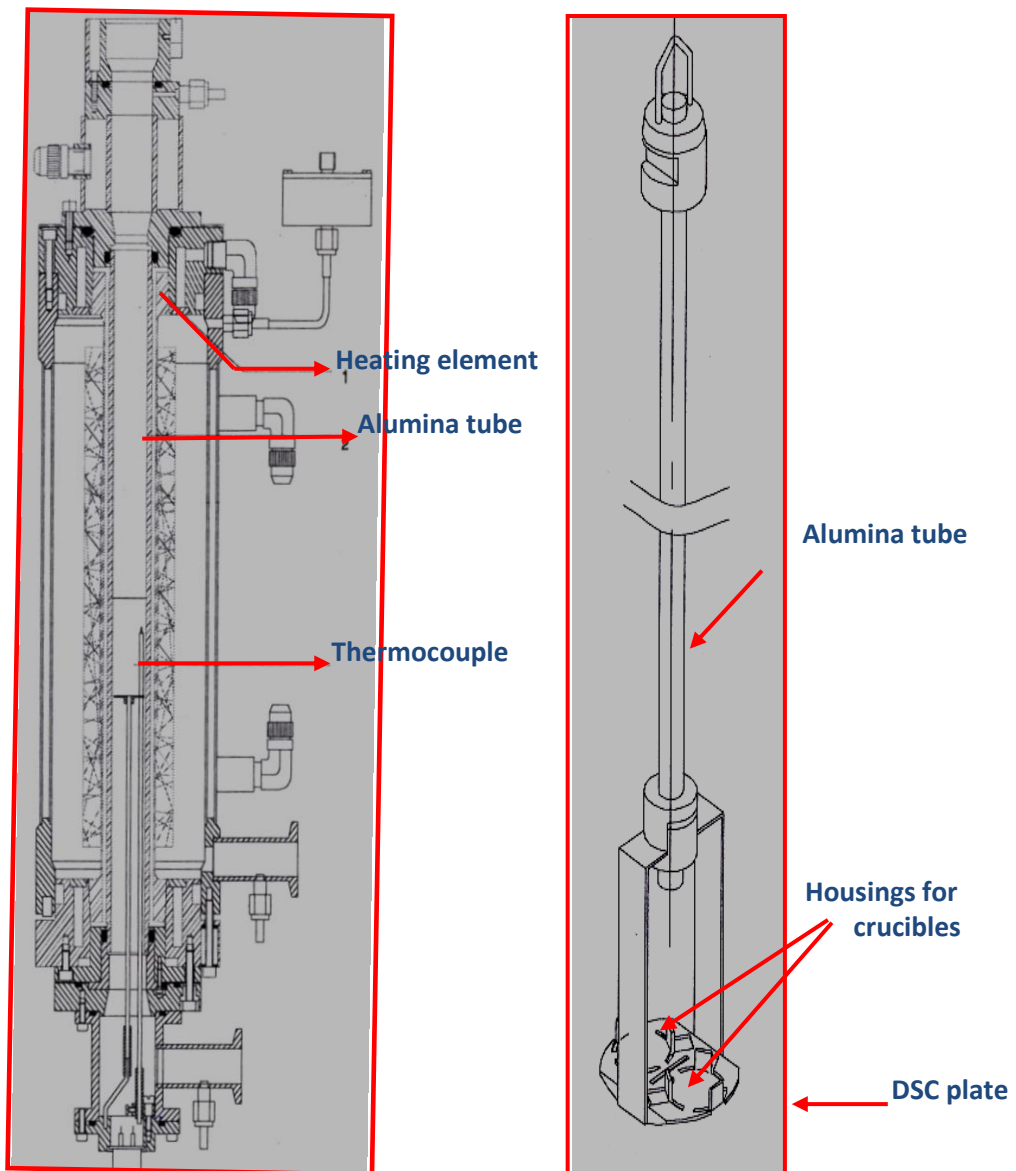


**Fig. 2.7** (a) Setaram high temperature DSC furnace  
(b) Heat flux DSC Plate – rod

minimize by careful design of the DSC, and to take further care of it by suitable calibration. The accuracy of results obtained with DSC is slightly inferior at high temperature, notwithstanding the possibility of ensuring adequate experimental precaution [23].

The *Setaram Setsys 1600* heat flux differential scanning calorimeter is basically a single structure integrated unit, wherein furnace, measurement head, mass flow controller, gas circuits and the controller are housed on a single mount. A separate

chiller (*Julabo FC 1600 T*) for water circulation is connected to cool the instrument furnace, which is made of graphite. The control of equipment is made through the proprietary software that is interfaced with the equipment. The essential components of this DSC are as follows [24]:

### 5.2. *High Temperature Furnace*

As shown in **Fig. 2.7(a)**, the furnace is of cylindrical shape and its heating element is made up of a graphite tube. An inert gas atmosphere is always maintained at the furnace chamber to avoid carbon evaporation at higher temperature. A thermocouple of B-type (PtRh6% /30%) is placed in the analysis chamber and furnace chamber for respective temperature measurement.

### 5.3. *Measurement Head – DSC Probe*

The DSC – plate is called the measurement head which is displayed in **Fig. 2.7(b)**. This is a machined metallic plate made of platinised copper-constantan containing two housings for the sample and reference crucible fitted to a narrow alumina rod. The sample and reference crucibles are made of recrystallised alumina having nearly identical mass of about 240–250 mg and a volume of about 100  $\mu\text{L}$ . The metallic plate consists of an embedded thin wire of highly conductive platinum that serves the purpose of *heat resistor* between sample and the reference. The differential thermocouple of B-type (PtRh 6%/PtRh 30%) is positioned exactly below the DSC plate and the gap between them is less than 2 mm. In addition, the central section of the DSC plate sensor contains a thermocouple of B- type that measures the sample temperature directly. The whole set up comprising DSC plate, sample and reference crucibles, thermocouples, guiding alumina tube together make up the heat flux DSC probe which is hung from the top balancing plate. The DSC probe is always kept within the uniform temperature zone of the water cooled graphite furnace.

#### 5.4. Vacuum Circuit, Gas Circuit, Chill water Cooling Circuit

A rotary vacuum pump serves the purpose of evacuating both analysis and furnace chamber. A separate chill water supply is provided by the Julabo FC 1600 unit for the furnace. The vacuum and the water supply operations are done through an electro valve command option. The programming and temperature control of the furnace is done by the controller which is integrated with the CPU.

#### 6.0. DSC Experimental Procedure

Samples for DSC study are cut using a diamond saw where care is taken to reduce the mechanical damage and stress introduction into the sample. The sample mass is kept nearly identical to about 50-55 mg with a dimension of about  $2 \times 2 \times 1$  mm dimension. These samples are polished to obtain a flat surface to ensure better heat conduction. In the present study, an empty alumina crucible is taken as a reference and the other identical crucible is loaded with the sample. Before starting the experiment, the experimental chamber consisting DSC probe and the furnace chamber is evacuated and purged with pure argon gas (Iolar grade II). A steady argon flow of about 50 ml per minute is maintained by means of electronic mass flow controller (MFC) throughout the experiment. An argon pressure of about 1300 mbar is maintained in the graphite furnace chamber.

The DSC experiments performed in the present study consist of following heating and cooling schedules: In the initial step, the furnace temperature is gradually raised up to 473 K at a heating rate of 5 or 10 K min<sup>-1</sup> and is allowed to stabilize at this temperature for about 15 minutes. This preconditioning leads to a smooth non-wavy baseline signal which is essential before the start of any quantitative DSC experiment. This step is programming the devise console to adopt preplanned heating, holding and

cooling schedules, which are typical of a planned DSC experiments. A typical schedule goes as follows:

Heating from 473–1273 K under various heating rates in the range 1-100 K min<sup>-1</sup> in case of experiments for studying the ferrite to austenite transformation kinetics. It should be added that the actual choice of the heating rate(s) varied depending on the requirement; but the instrument capability exists for adopting any value from 0.01 to 100 K min<sup>-1</sup>. For heat capacity measurements, a slow scan rate of 5 or 10 K min<sup>-1</sup> is more ideal, while a faster heating at 100 K min<sup>-1</sup> is adopted for quickly taking the sample to the pre designated aging temperature. In the case of recording the sequence of various diffusional on-heating phase changes that a ferritic steel experiences, as it is heated from room temperature to its melting range, (~1823 K) a slow heating scan at the rate of 1 to 3 K min<sup>-1</sup> is normally adopted. Besides these, the steel samples are often heated to various temperatures in the high temperature  $\gamma$ -austenite region under varying heating rates and held at these temperatures for varying time durations ranging from 1 to 120 minutes. The samples after ensuring homogenization in the austenite region are cooled with different thermal history, 1 to 100 K min<sup>-1</sup>, so as to determine the critical cooling rate required for martensite formation. These experiments also allow for studying the effect of heating rate and also the holding period thereof in the austenite region on the martensite formation propensity in 9Cr-steels. These experiments are possible to be carried out *in-situ* in the DSC cell and follow the thermal response accompanying the martensite formation. In general DSC is employed for following studies:

- (i) Accurate determination of phase transformation temperatures
- (ii) Estimation of heat effects accompanying phase changes
- (iii) Estimation of the kinetic parameters of phase transformation

## (iv) Estimation of specific heat

The details regarding the above mentioned experiments are given below.

## 6.1. Determination of Phase Transformation Temperature

A standard DSC thermogram is shown in **Fig. 2.8**. The difference in heat flow between the sample and reference is plotted along the y- axis and the temperature or time along the x- axis. When the sample experiences no phase change, the basic DSC signal is a smooth baseline without any characteristic features; in the ideal case the heat flow is parallel to the x- axis, a straight line should be obtained.

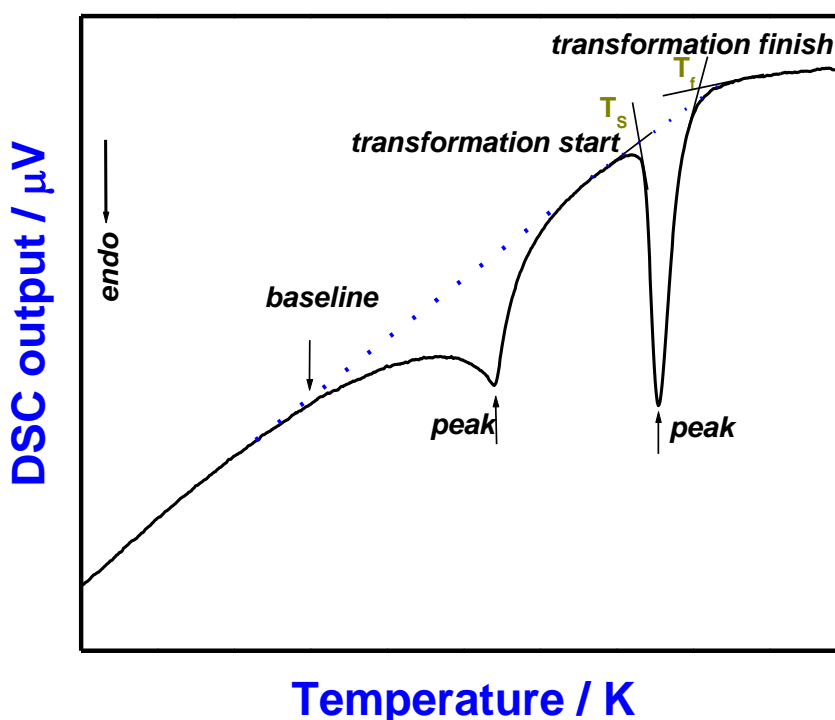


**Fig. 2.8** Typical on-heating DSC profile showing two transformation thermal arrests

However, in a heat flux DSC, the heat flux compensation between sample and reference is far from being exact, especially at high temperatures, due to the non-identical thermal character of apparently the same set of crucibles. A mild deviation from horizontal base line is what is often obtained, which constitutes the base response of the equipment + sample under no phase change conditions. However,

when there occurs a phase transformation in the sample, the differential heat flow due to the latent heat of transformation which is transported across the heat flux resistor results in the production a distinct thermal arrest, often evident as a peak in the otherwise featureless baseline plot. This is illustrated in **Fig. 2.8**.

The phase transformation onset (start) and finish temperatures are determined by drawing a tangent to the baseline from the point of maximum inclination (inflection point of the peak); - their intersection is taken as the transformation temperature. This construction is also illustrated in **Fig. 2.8**. Throughout this study,  $T_S$  is taken to represent the start of the phase transformation,  $T_p$  the peak and  $T_f$  the finish of the phase transformation.

#### 6.2. Calibration of Temperature in DSC

The temperature calibration is very important in DSC. It is done using the melting points of pure aluminium, zinc, tin, copper, silver, gold, and iron standards [25]. The onset value  $T_S$  of the melting point has been determined, based on the procedure

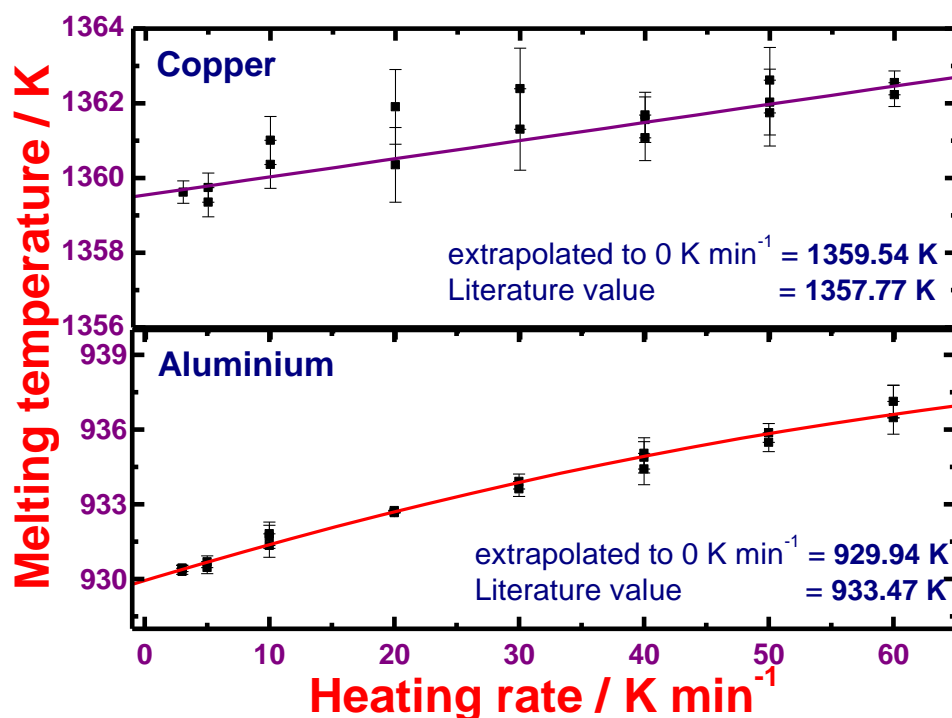


**Fig. 2.9** Temperature calibration with Al and Cu.

explained above. These onset temperatures are determined for various heating rates such as 1, 3, 5, 7, 10, 15, 20, 30 K min<sup>-1</sup> etc., and the resulting data are plotted in **Fig. 2.9**.

In general, the heating rate dependence of transformation temperatures is nonlinear to varying degrees depending on the dynamics of the phase change. However in a standard calorimetry experiment, the widely and generally adopted procedure is to extrapolate the plot to hypothetical 0 K min<sup>-1</sup> limit to arrive at the so-called equilibrium onset temperature [26, 27].

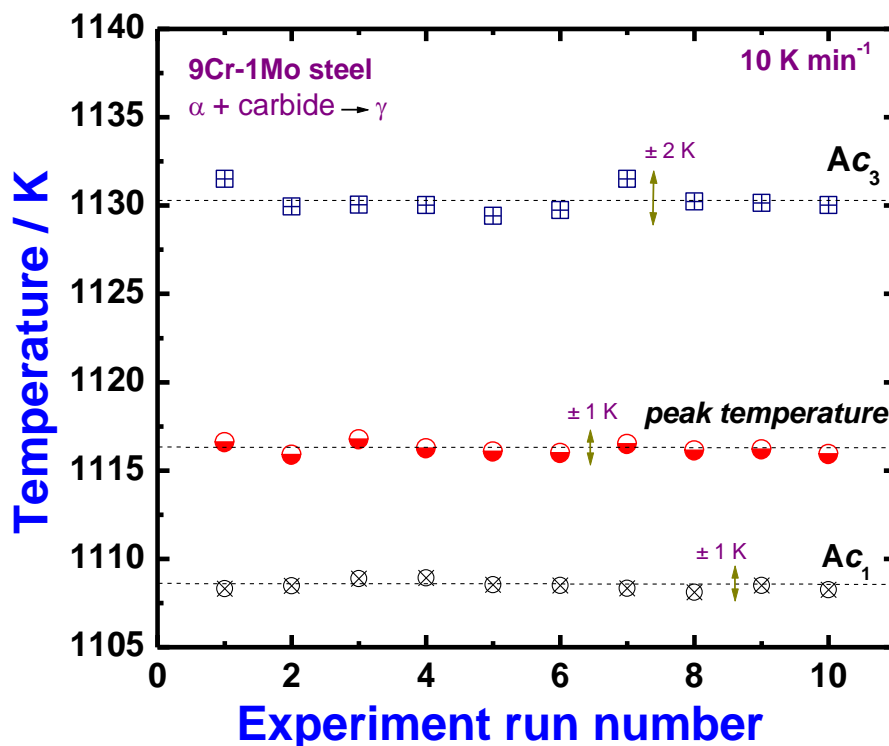


**Fig. 2.10** Illustration of the thermocouple response under identical heating rate (10 K min<sup>-1</sup>)

These values are compared with the standard literature values in order to estimate the correction to be employed for obtaining the true transformation temperatures. This calibration chart is illustrated in **Figure 2.9** for aluminium and copper. The temperature accuracy in case of low heating rate experiments (1–30 K min<sup>-1</sup>) is found

to be  $\pm 2$  K for samples of mass up to 50–100 mg; while, it is  $\pm 4$  K for high heating rates ( $99 \text{ K min}^{-1}$ ). The extrapolated melting temperature of Cu and Al is compared with literature values and the deviation is found to be within  $\pm 4$  K. The degree of reproducibility of repeat runs is  $\pm 1$  K (**Fig. 2.10**). In this figure, the measured transformation temperatures of ferrite to austenite transformation occurring in a standard 9Cr-1Mo steel and obtained with several samples of nearly same mass are compared. The variation of the measured start ( $A_{c1}$ ), peak and finish ( $A_{c3}$ ) temperatures recorded at a fixed  $10 \text{ K min}^{-1}$  heating rate is found to be about  $\pm 2$  K. Reliable and reproducible calibration of DSC for the cooling cycle is comparatively difficult as samples with known extent of undercooling are difficult to get in the temperature range of our interest. Nevertheless, for slow cooling rates, an acceptable degree of reproducibility is still possible, by employing appropriate standards. In the present study, pure iron (Fe with 99.99 mass % purity; Aldrich chemicals, UK) is often employed as the calibration standard for steels.

### 6.3. Determination of Phase Transformation Enthalpy

From a standard nonisothermal DSC scan exhibiting a peak due to distinct phase transformation, it is generally assumed that the heat of phase transformation is directly proportional to the peak area after suitable baseline normalization. Thus,

$$\Delta H_{tr} = k(T) \times \text{Peak Area} \quad (2.5)$$

$\Delta H_{tr}$  is the enthalpy change accompanying phase transformation,  $k(T)$  is the temperature dependent calibration constant. Peak area is the total area under the transformation peak or trough as the case may be, which is readily obtained by the data processing software after appropriate baseline construction [27-30]. The conversion factor  $k(T)$  is obtained by measuring the peak area recorded with the melting or fusion reactions of known enthalpy primary or secondary standards like

pure aluminium, zinc, tin, copper and iron etc [27-30]. It must be added that the calibration constant is a function of the heating or cooling rate, besides the hydrodynamic nature of the ambience. Thus factors like argon or any other carrier gas flow rate, the type of crucibles used etc., have a crucial bearing on the sensitivity of the calibration constant determination. Normally, it is preferable to employ the melting or solidification reactions of pure metals for calibrating the heat effects of unknown transformation events. In case of metals that solidify with large undercoolings, the actually measured enthalpy will exhibit a deviation from the literature value which pertains to equilibrium solidification. It is for this reason the calibration constants are quite reliably estimated for small heating rates. In addition, it is also desirable to employ a calibrant that shares similar thermophysical characteristics with the alloy under investigation so that spurious effects arising from the disparate conduction characteristics are generally avoided. Thus for example, it is better to employ pure iron or iron with small but known amount of carbon as the calibrant for characterising accurately the enthalpy effects of steels. It is even preferable to employ a known member derived from the same family as that of the alloy under investigation as a secondary calibrant. Thus, we employ plain 9Cr-1Mo steel with 0.07 mass percent carbon as the secondary calibrant for all studies concerning ferritic steel. This plain 9Cr-ferritic steel is calibrated using pure iron.

Another frequent source of error in the estimation of the enthalpy calibration constant arises from the uncertainty associated with the measured peak area. Although in modern calorimeters this is not a serious issue, it is yet possible to overlook this aspect by the way of not properly setting the transformation onset and offset temperatures. In such cases, it is quite likely that the measured area might not be a true representative of 100% phase change or else, it could be an overestimate as well

by the selection of wrong baseline. In the present study, we have minimized this extraneous source of error by going in for accurate baseline calibration by subtracting a nil sample empty run signal from the actual run recorded with the sample in position. Also, identical pair of crucibles, gas flow rate and scanning rate conditions is employed to minimize spurious factors from affecting the accuracy.

#### 6.4. *Determination of Apparent Specific Heat*

It is now established that with proper ordinate calibration, a DSC can be effectively used to get reliable estimates of specific heat [27-30]. The basic principle is simple and is one of comparing the carefully obtained signal outputs from three consecutive runs that are recorded under identical experimental conditions which includes the same set of crucibles and heating-holding-cooling schedules. In a strict sense these three runs must be performed without switching off the machine so as not to disturb the thermal equilibrium that is rather difficult to ensure reproducibly in dynamic calorimetry. For this reason, usually slow heating rates like 3, 5, 10 K min<sup>-1</sup> are preferred, with slower the better. In **Fig. 2.11**, these aspects are graphically illustrated. The three runs are as follows.

- i. baseline run which consists of using identical empty crucibles on both sides of the DSC plate
- ii. reference or calibration run with the sample crucible containing the known mass of standard sample, whose  $C_p$  is known before hand

- iii. sample run with a known mass of ferritic steel or any other sample as the case may be loaded onto the sample crucible.

In the present study, one more additional baseline run is done in order to ensure the

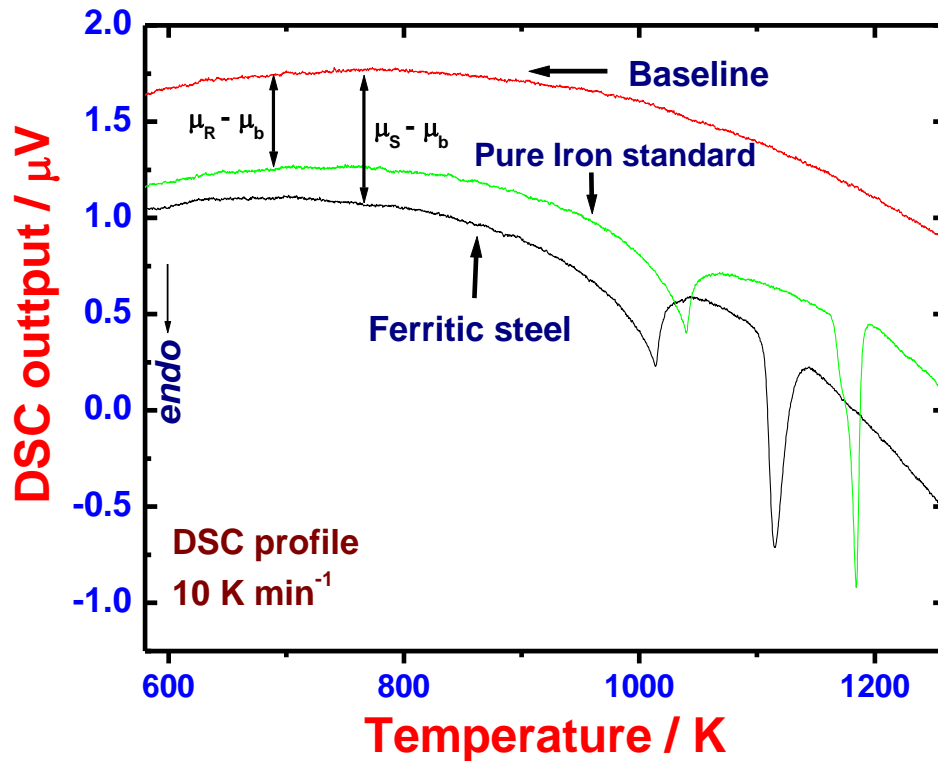


Fig. 2.11 Set of DSC profiles obtained during typical  $C_p$  measurement

extent of the base line reproducibility at the end of each experimental schedule. A good agreement between the start and finish baselines is suggestive of the stable thermal dynamics of the entire DSC module and the temperature sensor. Once accurate DSC output have been obtained for the above mentioned three runs, the following formula, based on the method of ratios can be employed to calculate  $C_p$  [12,28-30].

$$C_p^S = C_p^R \times (m_R / m_S) \times \{(\mu_S - \mu_b) / (\mu_R - \mu_b)\} \quad (2.6)$$

In the above expression,  $C_p^S$  and  $C_p^R$  represent the specific heat of the sample and the reference whose masses are given by  $m_S$  and  $m_R$  respectively.  $\mu_S$  is the DSC signal

(usually microvolt) obtained with the sample,  $\mu_R$  is the corresponding signal obtained with the reference or standard material and  $\mu_b$  is the baseline signal obtained with empty crucibles. In the present study, both 5 and 10 K min<sup>-1</sup> heating/cooling rates have been tried with good reproducibility. Thus, the sample is heated to 1273 K (1000 °C), at 10 K min<sup>-1</sup> followed by an isothermal hold of about 15 minutes at this temperature. Subsequently, the sample is cooled to 473 K at 10 K min<sup>-1</sup> and is allowed a resident time of about 15 minutes at this temperature, before it is finally cooled to room temperature.

#### 6.5. Accuracy of Heat Capacity Measurements using DSC

The accuracy of  $C_p$  and its reproducibility depend on several factors that are mentioned before in the context of enthalpy calibration. Additionally, we may also add that factors such as even positioning of crucibles in the measurement stage (this has to be absolutely flat), purge gas flow rates, its stability over longer durations of time, crucible contamination, sample inhomogeneity etc., affect the reproducibility of the base line, which is an important factor in getting accurate heat capacity measurement. In the current set of experiments, accuracies do vary depending on the temperature range. It is found that up to about 973 K (700 °C), an accuracy of about  $\pm 5\%$  is obtained with multiple attempts and taking the best set of data among them. But exceeding about 1000 °C, the exact reproducibility of baseline suffers gradually due to various counts; a mild drift between successive baselines suggest that random sources of uncertainty creeping in the experiment at high temperatures. This is especially so, under very slow scan rates like 1 K min<sup>-1</sup>. The stability of mass flow controller for very long sustained durations with 50 to 100 ml min<sup>-1</sup> flow rate suffers a little in typical tropical coastal conditions. Somewhat erratic open-closure of MFC nozzle is encountered under rainy conditions in our lab, which results in significant

variation of Ar-gas flow rate. As each significant change in the hydrodynamic balance of the whole setup affects base line reproducibility, very long experimental timings are usually avoided. Unfortunately, no attempt to quantify this random phenomenon is made in this study. It is for this reason that we adopt  $10 \text{ K min}^{-1}$  when measuring  $C_p$  up to about 1273 K, though a slower scan rates would be advised otherwise.

## **7.0. Optical Metallography**

The optical microscopy studies are carried out with the *Leica MeF4A*® optical microscope fitted with a Leica digital camera and associated proprietary software for image acquisition and treatment. The sample for optical metallography has been prepared using established procedures [31]. Due care has been taken to ensure that it contains all the representative features present in the investigated material. Low speed diamond wire saw has been used for sample cutting to minimize the damage. Mounting of sample is usually done using cold setting resin (epoxy resin) and some samples through hot mounting press (thermosetting plastic – phenolic resin). Mounted specimens are ground with rotating discs of abrasive papers such as wet silicon carbide paper. Samples are systematically ground from coarser to finer emery grades. The final grinding is done with 1200 mesh, after which the samples are alumina and diamond polished. This step is followed by washing in soap solution followed by methanol. Etching is done by gently swabbing the surface of the specimen with cotton bud soaked with the appropriate etchant. Etched samples are immediately washed with distilled water and methanol to protect from any further chemical attack. In this study the polished RAFM samples are given a mild initial etch with 2% Nital solution, followed by swabbing with Vilella's reagent (10 ml HCl, 90 ml ethanol / methanol, 2 gm picric acid).

### *7.1 Grain Size Measurement*

The average linear intercept method is used to measure the grain size. It is obtained by drawing a set of line segments on the microstructure and counting the number of times the line segments are intersected by grain boundary and finding the ratio of the intercepts to line length. Thus it is written as,

$$\text{Average grain size} = \text{line length} / N \times M. \quad (2.7)$$

where N = number of intercepts and M = magnification.

The statistical scatter in grain size quantification from 50 measurements is of the order of  $\pm 10\%$ .

### 7.2 Carbide Particle Density Measurement

The number of carbide particles present per unit area in case of thermally aged samples has been counted manually in many locations (more than 50 times) and it is used to arrive at the particle density. The relative difference of the particle density is only semi quantitatively mapped as a function of tempering time, realizing fully well that absolute measures in such cases are not meaningful besides difficult to obtain experimentally from 2D serial sectioning.

### 7.3. Microhardness Measurement

The hardness measurements have been carried out with *Leitz* Vickers micro hardness tester. All the measurements are taken with 50 and 100 g load which lies in the load independent region of the load vs. diagonal length plot made for 9Cr steels. About eight to ten measurements are taken for each sample and the average value is reported here. A standard test block of known hardness with prescribed load of 100 g is used for calibration. The probable error calculated by taking 15 indentation measurements on the standard sample is found to be within  $\pm 2\%$ . The Vickers number (HVN) is calculated using the following formula

$$\text{HVN} = 1.854 \times (F/D^2). \quad (2.8)$$

with  $F$  being the applied load (measured in kilograms-force) and  $D^2$ , the area of the indentation (measured in square millimeters). The applied load is also specified when HVN is cited.

#### 7.4. Scanning Electron Microscopy (SEM) Study

The scanning electron microscopy studies are carried out with *Philips XL30 ESEM* attached with *EDAX* facility. Secondary electron and back scattered electron modes are used for the microstructural observations. The sample preparation procedure for SEM studies is similar to the one employed for optical microscopy studies. In order to prevent the electrostatic charge formation, samples are gold coated and when required, conducting carbon tapes are also used for the purpose of charge grounding. The magnification calibration is made with standard cross grating samples of 20 lines/mm and 2160 lines/mm. The high resolution calibration test is performed on a carbon film embedded with gold nanoparticles, whose spacing is of the order of 20 Å. Energy dispersive X-ray analysis is carried out using energy dispersive spectrometer for qualitative identification of elements with atomic number greater than 10. Energy calibration is carried out with a detector resolution of 132 eV at Mn- $K_{\alpha}$ .

#### 8.0. X-Ray Diffraction (XRD) Study

The X-ray characterization is performed with *Inel XRG 3000* -X-Ray Diffractometer which makes use of a curved position sensitive X-ray detector for detecting diffracted the X-ray intensity. Such type of detectors can measure up to 120 degrees of  $2\theta$  simultaneously and have high speed of data acquisition, especially during high temperature measurements. Thin slices of samples have been cut from respective steels with a dimension of 10 mm×10 mm and thickness of about 2 mm using diamond saw. The sample is cut in such a way that it is easily leveled flat in a

sample stage to avoid the height problem. Before loading, the samples have been ground well with 1000 grit paper to remove any unwanted particles sticking in to it. The voltage and the current level in X-ray tube are set as 40 kV and 30 mA. The wavelength used is of 1.5406 Å (Cu-K $\alpha$ ) fitted with nickel filter. The diffraction pattern for each sample is recorded for 1h duration. The diffractometer has been calibrated with annealed silicon powder supplied by NPL, India. The particle size of

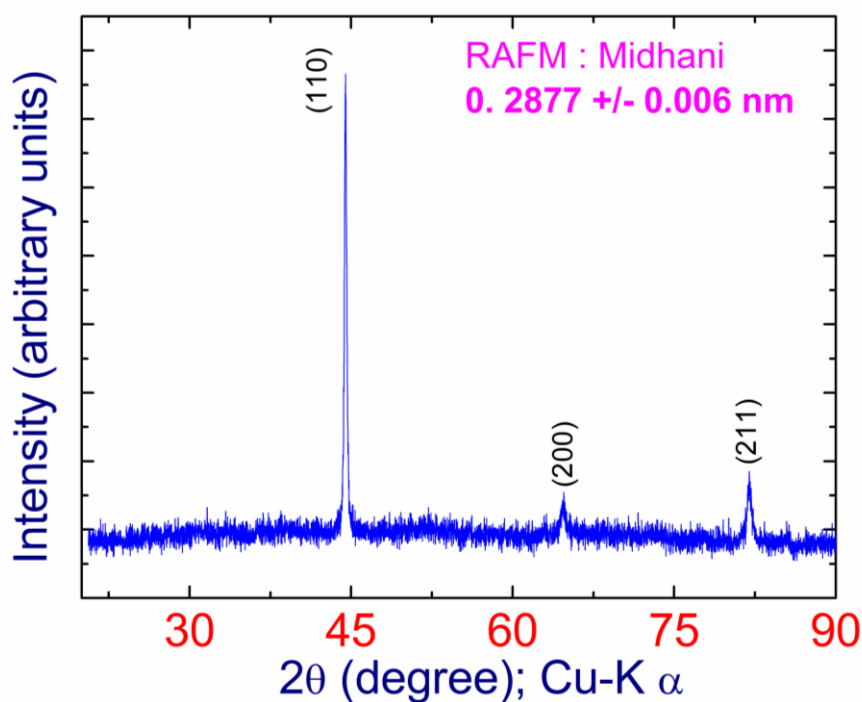


Fig. 2.12. Room temperature XRD profile of RAFM steel

the silicon powder is about 5000 Å. The peak positions, the full width at half maximum, and the  $d$ -spacings are recorded with this machine and are compared with the standard values suggested by NPL. A sample XRD profile obtained for RAFM steel is shown in **Fig. 2.12**.

### 8.1 High Temperature X-ray Diffraction (HTXRD) study

HTXRD study has been carried out on Ferroboron for characterising its anisotropic thermal expansion. Since, the details of HTXRD experiments have already

been reported in some of our recent thermal expansion studies [32-34], we skip here an elaborate account. These experiments are performed in a Philips-MPD<sup>®</sup> x-ray diffraction system equipped with a high vacuum (better than  $10^{-5}$  mbar) high-temperature stage consisting of a tantalum resistance heater (Buhler high temperature stage). The temperature is monitored by a Pt-Pt/Rh thermocouple that is spot welded to the bottom of the tantalum heater. Experiments are carried out with nickel filtered Cu-K $\alpha$  radiation in the  $\theta$ - $\theta$  geometry. The heating stage is flushed with argon before the start of each experimental run. A heating rate of 1 K per minute with a soaking time of 60 minutes at each temperature step is followed. Individual runs are taken at every 50 K interval. For calibration purposes, HTXRD studies have been carried out on pure iron.

During the course of this experiment, we have also co-recorded the reflections arising from the substrate tantalum heater. This is done in order to account for the temperature drop between the bottom portion of the tantalum heater and the thin foil sample placed on it. This temperature difference arises due to the finite thickness of the sample foil and any attempt to go in for very thin foils resulted in sample buckling and thereby a distortion of diffraction geometry as well. Since effecting a rigorous correction factor to these effects is rather difficult, we resorted to an empirical correction procedure [32]. This is achieved by comparing the lattice parameter data of tantalum calculated from the co-recorded heater reflections against the critically assessed lattice parameter data on tantalum by Reeber and Wang [35].

These individual HTXRD scans are processed subsequently to obtain accurate lattice parameter estimates for ferroboron, only three high angle reflections corresponding to Fe<sub>2</sub>B and FeB phases are considered and the average of the lattice parameters pertaining to these principal reflections is taken to be the representative

value. This is because of the fact that at high temperatures, certain difficulty is encountered with respect to the precise peak fixation of low intensity iron reflections.

## References

1. V. K. Sikka, C. T. Ward and K. C. Thomas, Proc. on '*Ferritic Steels for High-Temperature Applications*', (ed. A. K. Khare), ASM, Metals Park, OH, 65-84, (1983).
2. S. J. Sanderson, Proc. Int. Conf. on '*Ferritic Steels for fast reactor steam generators*', (ed. S.F.Pugh, E.A. Little), BNES, London, 120-123, (1978).
3. W. L. Bell, T. Lauritzen, and S. Vaidyanathan: Top. Conf. on '*Ferritic alloys for use in nuclear energy technologies - Ferritics for breeder reactor in-core applications*', (ed. J. W. Davis and D. J. Michel), ASM, Met. Soc. AIME, Warrendale, PA, 113-124, (1983).
4. Baldev Raj, H.S. Kamath, R. Natarajan and P.R. Vasudeva Rao, *Prog. Nucl. Energy*, 47 (2005) 369.
5. S. Raju, B. Jeya Ganesh, Arun Kumar Rai, R. Mythili, S. Saroja and Baldev Raj, *J. Nucl. Mater.*, 405 (2010) 59.
6. Baldev Raj, K. Bhanu Sankara Rao and A.K. Bhaduri, *Fusion Engg. Des.*, 85 (2010) 1460.
7. Baldev Raj and K. Bhanu Sankara Rao, *J. Nucl. Mater.*, 386-388 (2009) 935.
8. AC spark emission spectrometer, (JY132F), JOBIN YVON Emission and ICP-OES JOBIN YVON (U2 SIMULTANE), France.
9. B. Jeya Ganesh, S. Raju, Arun Kumar Rai, E. Mohandas, M. Vijayalakshmi, K B.S Rao and Baldev Raj, *Mater. Sci. Technol.*, 27 (2011) 500.
10. S. K. Albert, C. R. Das and A. K. Bhaduri, *Specifications for modified 9Cr-1Mo welding electrodes*, IGCAR internal report, PFBR, 33010 SP 1006 (2002).
11. Lee D. Hansen and Richard S. Criddle, *Thermochim. Acta.*, 160 (1990) 173.

12. W. Hemminger and G.W.H. Höhne, *Calorimetry — Fundamentals and Practice*, Weinheim, Verlag Chemie, (1984).
13. Michael E. Brown, *Introduction to Thermal Analysis, Techniques and Applications*, second edition, Kluwer Academic Publishers, The Netherlands. (2001).
14. P. K. Gallagher, *Handbook of Thermal Analysis and Calorimetry*, 1, (Ed. M.E. Brown), Elsevier, Amsterdam, (1998).
15. K. D. Maglic, A. Cezairliyan, V. E. Peletsky (Eds.), *Compendium of Thermophysical Property Measurement Techniques*, vol. 2, Plenum Press, New York, (1992).
16. <http://www.setaram.com/MHTC-96-Accessories.htm>.
17. Multi HTC-96, Setaram Installation Guide and Manual (1997).
18. M. Nevrieva, D. Sedimidubsky and J. Leitner, *Thermochim. Acta.*, 347 (2000) 123.
19. Yoichi Takahashi and Yuji Kohsaka, *J. Nucl. Mater.*, 130 (1985) 109.
20. S. Raju, B. Jeya Ganesh, Aritra Banerjee and E. Mohandas, *Mater. Sci. Engg.*, 465A (2007) 29.
21. J. Leitner, A. Strejc, D. Sedimidubsky, and K. Ruzicka, *Thermochim. Acta.*, 401 (2003) 169.
22. D. G. Archer, *Thermodynamic Properties of Synthetic Sapphire ( $\alpha$ -Al<sub>2</sub>O<sub>3</sub>), Standard Reference Material 720 and the Effect of Temperature Scale Differences on Thermodynamic Properties*, *J. Phys. Chem. Ref. Data*, 22 (1993) 1441.
23. S. M. Sarge, E. Gmelin, G. W. H. Hohne, H. K. Cammenga, W. Hemminger, W. Eysel, *Thermochim. Acta*, 247 (1994) 129.
24. <http://www.setaram.com/SETSYS-Evolution-DTA-DSC.htm>.

25. R. Sabbah, An Xu-wu, J.S. Chickos, M.L. Planas Leitão, M.V. Roux , L.A. Torres, *Thermochim. Acta*, 331 (1999) 93.
26. L. Richardson, E. L. Charsley; "Calibration and Standardisation in DSC", in *Handbook of Thermal Analysis and Calorimetry. Vol. 1: Principles and Practice*, M. E. Brown (editor), Elsevier Science B.V. (1998).
27. E. Gmelin and St. M. Sarge, *Pure Appl. Chem.*, 67 (1995) 1789.
28. B. Wunderlich, *Thermal Analysis*, San Diego, CA, Academic Press, (1990).
29. M. Brown, *Introduction to Thermal Analysis*, London, Chapman and Hall, (1988).
30. G.W.H. Höhne, W. Hemminger, and H.-J. Flammersheim, *Differential Scanning Calorimetry: An Introduction for Practitioners*, Berlin, Springer-Verlag, (1996).
31. L. E. Samules, *Metallographic Polishing by Mechanical Methods*, IV<sup>th</sup> edition, ASM International, Materials Park, USA (2003).
32. R. Jose, S. Raju, R. Divakar, E. Mohandas, G. Panneerselvam, M. P. Antony and K. Sivasubramanian, *J. Nucl. Mater.*, 317 (2003) 54.
33. G. Panneerselvam, S. Raju, R. Jose, K. Sivasubramanian, R. Divakar, E. Mohandas and M. P. Antony, *Mater. Letters*, 58 (2003) 216.
34. S. Raju, K. Sivasubramanian, R. Divakar, G. Panneerselvam, A. Banerjee, E. Mohandas, and M. P. Antony, *J. Nucl. Mater.*, 325 (2004) 18.
35. R. R. Reeber and K. Wang, *Mater. Sci. Engg.*, R23 (1998) 101.

## Thermodynamic Interrelationship Between Thermal and Elastic Properties: Development of Some Useful Approximations For Data Estimation & Assessment

### 1.0. Introduction

A rigorous thermodynamic description of condensed phases in terms of pressure ( $P$ ), volume ( $V$ ) and temperature ( $T$ ) coordinates, namely the equation of state (EoS) suggests that there must exist certain well-defined interrelationship between thermal and elastic properties, especially with regard to their temperature and pressure dependencies [1, 2]. A good example to illustrate this point is the relatively temperature independent nature of the (thermal) Grüneisen parameter  $\gamma_G$ , which contains rather implicitly the compensating or synergetic influence of temperature on different thermal and elastic quantities, such as volume thermal expansivity ( $\alpha_V$ ), molar specific heat ( $C_P$ ), molar volume ( $V$ ) and adiabatic bulk modulus ( $B_S$ ) [3]. In a similar context, it can also be proven from basic thermodynamic principles that the isothermal pressure dependence of volume thermal expansivity  $(\partial\alpha_V/\partial P)_T$ , is identically related to the isobaric temperature variation of bulk modulus  $(\partial B_T/\partial T)_P$  [2]. In reality, it is possible to establish different linkages or approximations connecting the temperature and or pressure dependencies of different thermodynamic quantities, purely by invoking the self-consistent phenomenological framework of classical thermodynamics, if phase transitions are not involved [4-6]. Incidentally, phase transitions are marked by discontinuity in the temperature or pressure variation of appropriate thermodynamic quantities. However even here, an adroit application of

thermodynamics can yield useful information about the nature and quantum of jump in basic thermal quantities at phase transformation.

Despite such theoretical possibilities, it is not always easy to decipher the existence of a particular thermodynamic linkage entirely from first principles [1]. This is so, because the measured thermal and elastic quantities often take *apparently* diverse functional representations with regard to their temperature and pressure variations [1, 6]. However, the experimental data on many thermophysical quantities of condensed phases, in particular their pressure and temperature variations, when taken and analyzed together, reveal certain surprisingly simple relations over a reasonable range of temperature and or pressure [6-14].

*Although appearing to be empirical or phenomenological at first sight, such experimentally deduced correlations or systematics reflect certain underlying physical basis, which if correctly identified and exploited judiciously, can lead to a versatile thermodynamic framework that will help the cause of a self-consistent interpolation cum prediction of thermal quantities from limited, inhomogeneous or even partial data sets [10, 11].*

It is with this intent that we analyse in this chapter the thermodynamic implications of a linear relationship connecting molar volume ( $V$ ) with enthalpy increment ( $H_T - H_0$ ) and bulk modulus under constant pressure conditions. *The relevance of this basic thermodynamic study in the present context should be obvious: it is designed to serve as a useful conceptual framework for a critical self-consistent appraisal of the calorimetry data, in conjunction with other related information reported in literature.*

In the present chapter, an attempt is made to derive a set of useful approximations, relating enthalpy increment with other thermodynamic quantities.

The practical utility of some of the thermodynamic relations developed here is demonstrated by taking on  $\alpha$ -plutonium as the case study material. It may be interesting to note that Plutonium is a difficult to work with material in real world. Yet, there is a good amount of experimental information, accrued over a period due to path breaking research under hot-cell conditions by pioneers in nuclear materials. Moreover, Pu is also a difficult choice for first principles total energy calculations, owing to its peculiar character of 5f-electrons. All this, plus IGCAR's resident interest in metal fuelled fast reactors, have made Pu as the case study material. But, we hasten to add that thermodynamics being system independent, the approximations developed here have extended validity for many types of materials, provided, they are employed well within their domain of their validity.

## 2.0. Theoretical development

The starting point of our analysis is the following linear relation proposed originally by Anderson [6, 12], for characterizing the relative variation of adiabatic bulk modulus ( $B_S$ ) with respect to the corresponding enthalpy increment ( $H_T-H_0$ ) under constant pressure.

$$B_S = B_0 - \xi_S (H_T-H_0). \quad (1)$$

In the above expression,  $B_S$  and  $B_0$  stand respectively for the adiabatic bulk modulus values at temperatures  $T$  and  $T_0$  respectively.  $T_0$  is an appropriately chosen reference temperature, which can be preferably (but not always) above  $\theta_D$ , the Debye characteristic temperature.  $H_T-H_0$  represents the corresponding incremental enthalpy, with  $H_0$  being the enthalpy at the reference temperature.  $\xi_S$  is a temperature independent thermoelastic constant. A detailed discussion on the physics of this expression is deferred to another section in this chapter. In what follows, the attention

is focused on enlisting some of the important thermodynamic implications of this approximation. *Eq. (1)* can be rewritten as follows.

$$H_T = H_0 + (B_0/\xi_S)\{1-(B_S/B_0)\}. \quad (2)$$

Now, the temperature dependent bulk modulus ratio  $B_S(T)/B_0$ , may be expressed in terms of the corresponding ratio of molar volume ( $V_T/V_0$ ), by appealing to the concept of temperature independent adiabatic Anderson-Grüneisen parameter,  $\delta_S$  [6, 13]. Thus one may write,

$$B_S/B_0 = (V_T/V_0)^{-\delta_S}. \quad (3)$$

The Anderson- Grüneisen parameter  $\delta_S$  is given by the following expression [6,13]

$$\delta_S = - (1/\alpha_V B_S) \times (\partial B_S / \partial T)_P = -(\partial \ln B_S / \partial \ln V)_P. \quad (4)$$

The negative sign on the right hand side implies that as the volume increases with temperature at constant pressure, the bulk modulus exhibits a decrease, so that  $\delta_S$  assumes a positive value. Substituting for  $B_S/B_0$  from *Eq. (3)* into (2), we obtain the following relation connecting directly the enthalpy with molar volume.

$$H_T = H_0 + (B_0/\xi_S)\{1- (V_T/V_0)^{-\delta_S}\}. \quad (5)$$

It is useful to recall that apart from invoking the validity of *Eq. (1)*, the only other assumption that has gone into deriving *Eq. (5)* is the temperature independent nature of  $\delta_S$ . Following the example of temperature independent thermal Grüneisen parameter,  $\gamma_G$  [14], it is often assumed that at high temperatures ( $T \geq \theta_D$ ),  $\delta_S$  is only *mildly* temperature sensitive and that for all *practical* purposes, a temperature independent constant value  $\delta_0$  may be used in *Eq.(5)* [6, 13].

On the contrary, it is also possible to improve the technical sophistication of this simple approximation (*Eq.5*), by taking recourse to some models that characterize the temperature variation of  $\delta_S(T)$  itself. It may be inferred from *Eq. (4)* that models

for the temperature variation of  $\delta_S$  translate effectively into models that account for the isobaric volume variation of bulk modulus [6,11,13]. Thus for example, we may invoke the following empirical relation proposed recently by Jacobs and Oonk for expressing the isobaric volume dependence of bulk modulus [9].

$$B_S/B_0 = \exp\{-\delta_0[(V_T-V_0)/V_0]\}, \quad (6)$$

Using *Eq. (6)* in *Eq. (2)*, we may derive

$$H_T = H_0 + (B_0/\xi_S)\{1 - \exp(-\delta_0 [(V_T-V_0)/V_0])\}. \quad (7)$$

Incidentally, it must be mentioned that *Eq. (6)* presupposes the fact that in place of temperature independent  $\delta_S$ , the composite quantity  $(\delta_S/V)$  is taken as temperature independent [15]. Since the argument inside the exponential function on the right hand side of *Eq. (7)* is rather small, that is,  $\delta_0[(V_T-V_0)/V_0] \ll 1$ , we may approximate the exponential function as a series expansion in  $(V_T-V_0/V_0)$  and retaining only the linear term in such an expansion, we obtain after some algebraic manipulation, the following linear correlation between enthalpy and molar volume.

$$H_T = H_0 + (B_0\delta_0/V_0\xi_S)(V_T-V_0). \quad (8)$$

It is clear that *Eq. (8)* is a less sophisticated approximation than *Eq. (7)*; nevertheless it is a simple and useful one, as we will see soon.

Alternately, one may also adopt the Chopelas and Boehler approximation for expressing the volume dependence of  $\delta_S$  [16]. In this approximation, a composite quantity  $A$ , defined by the following expression

$$A = (1+\delta_S)/V_T = (1+\delta_0)/V_0, \quad (9)$$

is taken to be temperature independent. That is in place of  $(\delta_S/V)$ , the composite quantity  $(1+\delta_S)/V_T$  is assumed to be temperature independent. With this assumption,

the corresponding expression for the isobaric volume dependence of bulk modulus takes the following form.

$$B_S/B_0 = (V_T/V_0) \exp\{-A(V_T-V_0)\}. \quad (10)$$

Substituting for  $B_S/B_0$  from Eq. (10) in (2), we get the following fourth approximation connecting enthalpy variation with volume.

$$H_T = H_0 + (B_0/\xi_S) \times \{1 - (V_T/V_0) \exp[-A(V_T-V_0)]\}. \quad (11)$$

### 2.1. *Estimation of thermoelastic constants $\delta_S$ and $\xi_S$ from standard values of reference temperature thermal properties*

The expressions given in (5),(7), (8) & (11) provide for a ready estimation of enthalpy from molar volume data, if values of  $B_0$ ,  $V_0$ ,  $\xi_S$  and  $\delta_0$  are known. Of these,  $B_0$  and  $V_0$  are standard quantities corresponding to the reference temperature  $T_0$ . Reliable estimates these quantities may be considered as readily available input for many materials. Additionally, the values of thermoelastic constants  $\xi_S$  and  $\delta_0$  need be known at the reference temperature. As evident from the definition of  $\delta_S$  vide Eq. (4),  $\delta_0$  is uniquely determined, if the temperature derivative of bulk modulus  $(\partial B_S/\partial T)_0$  and volume thermal expansivity  $(\alpha_0)$  at the reference temperature  $(T_0)$  are known. *For a good number of materials, the bulk modulus data may be available over a small range of temperature in the low to moderate temperature region. But in general, the extensive availability of temperature dependent elastic property data is still rather scarce for many solids of practical interest (this is so far many nuclear materials). If information regarding  $(\partial B_S/\partial T)_0$  is also lacking for a solid of specific interest, we may employ the following relation suggested by Ledbetter for obtaining a first order estimate of this quantity [17].*

$$(\partial B_S/\partial T)_P = -(\alpha_V B_S)\delta_S = -(C_P \gamma_G/V)\delta_S = -3R \gamma_G (\gamma_G + 1)/V. \quad (12)$$

The above relation gives basically the high temperature constant limit value of  $(\partial B_S/\partial T)_P$ . It is useful to recall that  $\gamma_G$  is the popular Grüneisen parameter. Thus after defining all the quantities, the only remaining thermoelastic parameter that remains to be explained in detail is  $\xi_S$ . This point is addressed in the following section.

### 3. Physical meaning of $\xi_S$

Upon differentiating *Eq. (1)* with respect to temperature, we get,

$$(\partial B_S/\partial T)_P = - \xi_S C_P. \quad (13)$$

Now, by substituting for  $(\partial B_S/\partial T)_P$  in the above expression in terms of  $\delta_S$  from *Eq. (4)* and in addition, employing the following basic definition of the thermal Grüneisen parameter  $\gamma_G$  [3, 6]

$$\gamma_G = \alpha_V B_S V / C_P, \quad (14)$$

in effectively replacing the product of thermal expansivity and bulk modulus ( $\alpha_V B_S$ ), we finally arrive at the following expression for  $\xi_S$

$$\xi_S = \gamma_G \delta_S / V. \quad (15)$$

*Note that in the above definition of  $\xi_S$ , we have not assumed the temperature independence of either  $\gamma_G$  or  $\delta_S$ . In fact, their individual temperature sensitivities are implicitly subsumed or compensated in the overall temperature independent nature of  $\xi_S$ . In this sense,  $\xi_S$  represents a higher order thermoelastic quantity. It must further be added that in general the temperature sensitivities of  $\gamma_G$  and  $\delta_S$  in themselves are generally small [6] and besides are formidable issues to be resolved on a rigorous thermodynamic basis. Nevertheless, in proposing an empirical linear scaling relation between two thermal properties, such as *Eq. (1)*, the intricacies of the temperature variations of two complex thermoelastic parameters like  $\gamma_G$  and  $\delta_S$  are adequately*

taken care of. *In hindsight, this is one of the remarkable advantages of the linear scaling approximation given in Eq. (1).*

As the first simplifying step, the temperature dependence of both  $\gamma_G$  and  $\delta_S$  may be set to zero [6, 14]. Such an approximation may be valid only at high temperatures ( $T > \theta_D$ ). Under such case, one can estimate  $\xi_S$  as

$$\xi_0 = \gamma_0 \delta_0 / V_0. \quad (16)$$

The other important point to note from Eq. (16) is that by substituting for  $\xi_0 = \gamma_0 \delta_0 / V_0$  in Eq. (8), we can further simplify the enthalpy dependence of molar volume in the following manner.

$$H_T = H_0 + (B_0/\gamma_0)(V_T - V_0). \quad (17)$$

The above linear approximation suggests that  $(\partial H/\partial V)_P = (B_S/\gamma_G)$ , is another temperature independent composite quantity. In what follows, we present an illustrative application of the thermodynamic framework developed in this study by estimating the thermal properties of  $\alpha$ -plutonium.

#### 4.0. A Case Study on $\alpha$ -Plutonium

A study on  $\alpha$ -plutonium is interesting on two counts. In the first, it is rather difficult to carry out extensive experimentation on plutonium and its alloys on account of its highly radioactive and self-damaging nature [19]. Secondly, a fundamental understanding of the physics of plutonium is indeed a challenging task, as it is one of a delicate balance between a typically delocalised *versus* localised descriptions of the dynamics of bonding electrons [20]. It is believed that the physicochemical characteristics of  $\alpha$ -Pu, the first among the six allotropes, must in some way derive from this intricate physics. Notwithstanding the experimental difficulties, a fair amount of experimental information on thermal and physical properties exist for  $\alpha$ -

plutonium [21-32]. Thanks to the availability of fairly pure crystals of  $\alpha$ -Pu with reasonable mass in the recent past, some of its physical properties have been redetermined [33-36]. Recently, Ledbetter *et al* [36] have accurately determined the temperature variation of the elastic properties of  $\alpha$ -Pu by resonant ultrasound spectroscopy in the temperature range of 18 to about 385 K, thus offering a complete set of values for most part of the existence domain of  $\alpha$ -Pu. The interesting part of their work is the finding that notwithstanding the subtleties of  $f$ -electron physics, the measured temperature dependence of the adiabatic bulk modulus can be adequately characterised by the classical Varshni's model, as given below [37].

$$B_S(T) = B_S(0) - S/[\exp(\theta_E/T) - 1]. \quad (18)$$

In the above expression,  $S$  is a temperature independent constant and  $\theta_E$  is the characteristic Einstein temperature. Strictly speaking they are to be treated as fit-constants. However, as shown by Ledbetter [17], the above model may be derived by assuming the Einstein single oscillator model of specific heat ( $C_V$ ), besides implicitly invoking the *ansatz* that  $(\partial B_S/\partial T)_P = -\xi_S C_P$ . In fact, it can be shown that within the spirit of the linear correlation between enthalpy and bulk modulus (*Eq. 1*), the constant  $S$  is given by the relation [17]

$$S = (3R \theta_E) \xi_S, \quad (19)$$

and the slope  $(\partial B_S/\partial T)_P$  by the expression

$$(\partial B_S/\partial T)_P = -\{S/\theta_E \times 1/3R\} C_P. \quad (20)$$

$C_P$  is given by the Einstein approximation [3]

$$C_P = 3R (\theta_E/T)^2 \exp(\theta_E/T)/[\exp(\theta_E/T) - 1]^2. \quad (21)$$

In normal course of investigation,  $\theta_E$  the Einstein characteristic temperature is a material dependent quantity, characterizing optic modes; but in general, one may use

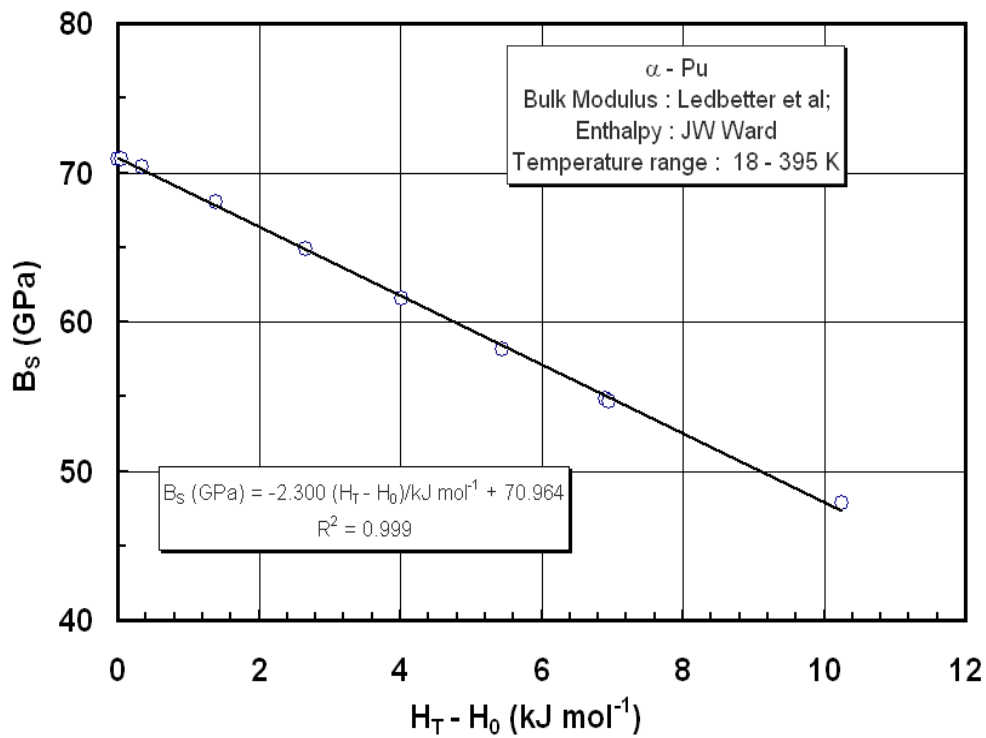


Fig. 3.1. Linear relationship between bulk modulus and enthalpy, for  $\alpha$ -Pu

a Debye model as well with  $\theta_D \approx \theta_E/0.77$ , as for example suggested by Ledbetter. It is also useful to note that  $\theta_D$ , the Debye characteristic temperature may be estimated from known estimates of averaged sound velocity and density. In the present case,  $\theta_E$  is basically treated as a fit parameter. Its resemblance to actual Einstein model based temperature is inconsequential to ensuing discussion.

In **Fig. 3.1**, we present the linear correlation observed between the experimental values of enthalpy [38] and adiabatic bulk modulus [36]. The slope  $\xi_S$ , of the best-fit line is found to be  $2.3 \times 10^6 \text{ mol m}^{-3}$ . This experimental value for  $\xi_S$  compares rather well with the theoretically estimated value of  $2.85 \times 10^6 \text{ mol m}^{-3}$ . This theoretical estimate is obtained from *Eq. (19)* using Varshni's model fit parameters, namely  $S = 11.3 \text{ GPa}$  and  $\theta_E = 158.8 \text{ K}$ . In fact, using this latter theoretical value of  $2.85 \times 10^6 \text{ mol m}^{-3}$  for  $\xi_S$ , and making a back calculation of

enthalpy in terms of experimental  $B_S$  data using *Eq. (1)*, it is found that the calculated values are within  $\pm 5\%$  of the assessed experimental data [38]. This is reflected in **Fig. 3.2**, where the original experimental and back calculated enthalpy values are compared for  $\alpha$ -plutonium.

Although, we could not estimate the uncertainty associated with the theoretical estimate of the thermoelastic constant  $\xi_S$ , (the corresponding uncertainty in the empirical fit parameters  $S$  and  $\theta_E$  are not known), it appears that experimental enthalpy values themselves are generally no better than  $\pm 5\%$  level of accuracy [29]. As a further cross check, one can also estimate  $\xi_S$ , using the definition given in *Eq. (16)* in terms of  $\gamma_0$ ,  $\delta_0$  and  $V_0$ .

Taking the required data for  $\alpha$ -plutonium ( $\gamma_0 = 2.87$  (*extrapolated*),  $\delta_0 = 8.91$ ,  $V_0 = 11.712 \times 10^{-06} \text{ m}^3 \text{ mol}^{-1}$ ) from the work of Wallace *et al* [39], a value of  $2.18 \times 10^{06}$  has been deduced for  $\xi_0$ . It is again noteworthy that this value is fairly close to  $2.3 \times 10^{06}$ , that is obtained from the slope of the straight-line fit that is given in **fig. 3.1**.

In summary, it may be noted that notwithstanding the uncertainties inherent of the experimental data, there is a genuine linear correlation between bulk modulus and enthalpy (*Eq. 1*) for  $\alpha$ -plutonium.

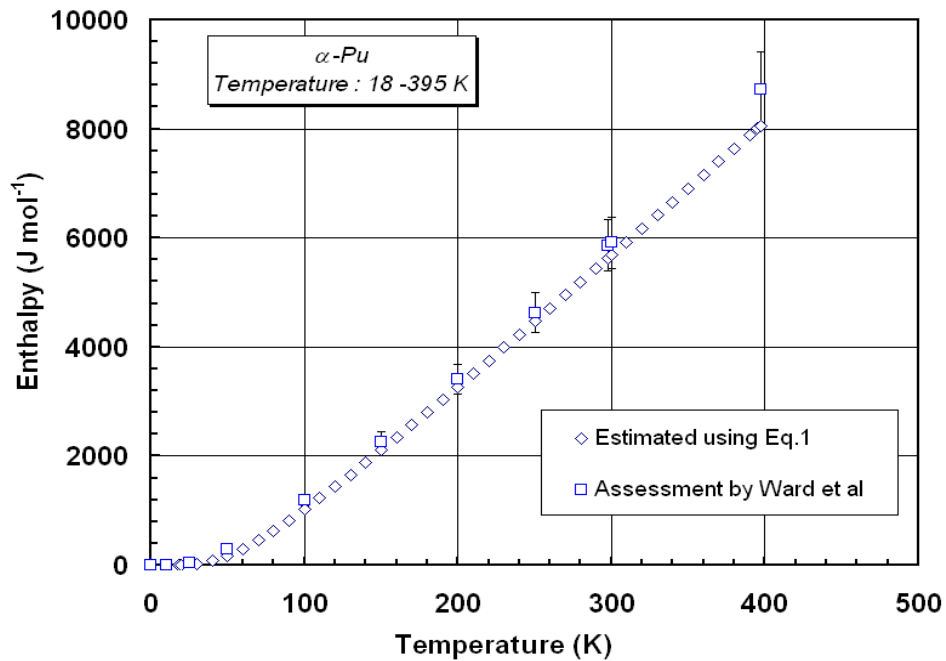


Fig. 3.2. Temperature variation of predicted enthalpy, compared to assessed experimental data of Ward [38]

In the next step, we attempt to estimate the temperature variation of molar volume using experimental enthalpy data. Among various approximations developed in this study, we chose the simplest of approximations given by *Eq* (17). The values of  $V_0 = 11.712 \times 10^{-06} \text{ m}^3 \text{ mol}^{-1}$ ,  $\gamma_0=2.87$  and  $B_0=54.4 \text{ GPa}$ , needed for this purpose are taken respectively from the work of Wallace [39] and Ledbetter *et al* [36]. In **Fig. 3.3**, the estimated and experimental values of molar volume as a function of temperature are compared. As can be seen from this figure, the estimated values are only slightly higher than the experimental estimates. In view of the uncertainty that is invariably associated with lattice parameter measurements, and also considering the fact that *Eq.* (17) is basically a linear approximation, this level of agreement can be considered as good.

## 5.0. Discussion

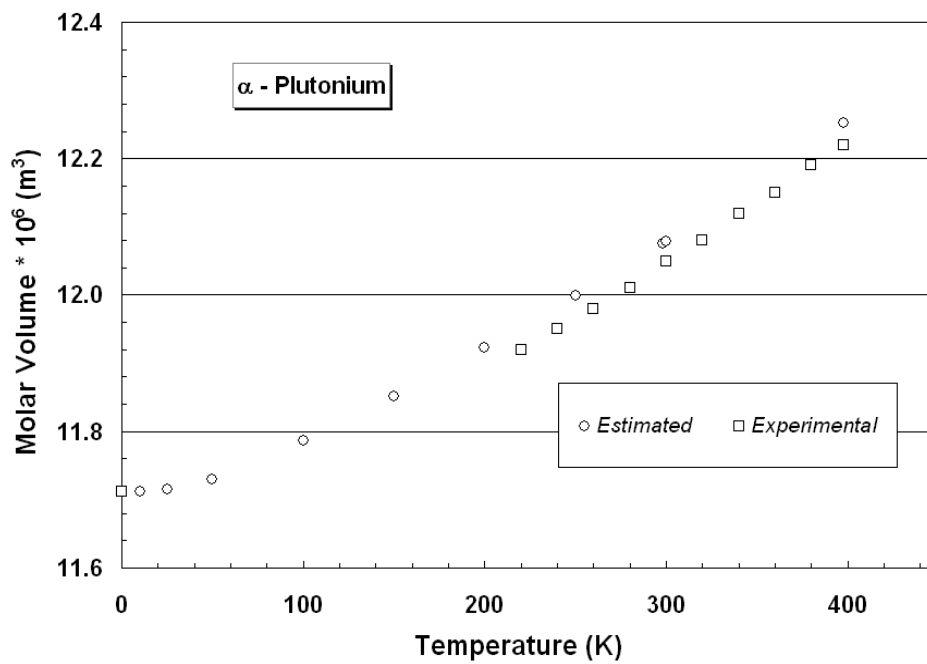


Fig. 3.3. Estimated molar volume variation with temperature is compared with experimental data

A study on the interrelationship between thermophysical quantities is in fact not new. In all probability, the early and a well-noted thermodynamic treatment of the interrelationship between thermal and elastic quantities had been provided by Grüneisen himself [40]. By proposing a temperature independent parameter  $\gamma_G$  (Eq. 14), he had issued a compact statement with regard to the compensating influence of temperature on  $(\alpha_V/C_P)$  *vis a vis* the product  $(B_S V)$ . In a recent study, we further probed this topic of interrelationship between thermal and elastic properties from the standpoint of one of the Grüneisen hypotheses, namely the ratio  $\lambda = \alpha_V/C_P$ , is temperature insensitive [10, 41]. When viewed in a broader perspective, this assumption translates into following relation between molar volume and enthalpy at constant pressure [10].

$$V_T = V_0 \exp(\lambda_0 \Delta H). \quad (22)$$

$\lambda_0$  is the value of the Grüneisen ratio at the reference temperature [10]. If in the above approximation, we further assume that  $\exp(\lambda_0\Delta H) \approx (1 + \lambda_0\Delta H)$ , then we recover a linear relation connecting  $V_T$  with  $\Delta H$ .

That is,

$$V_T = V_0 + \lambda_0 V_0 \Delta H. \quad (23)$$

It is instructive to note the similarity between *Eq. (23)* and *Eq. (17)*. In other words, the present linear approximation can be traced to Grüneisen's exponential relationship (*Eq. 22*). In **Fig. 3.4**, the graphical depiction of the linear correlation between enthalpy and molar volume in case of  $\alpha$ -plutonium is portrayed.

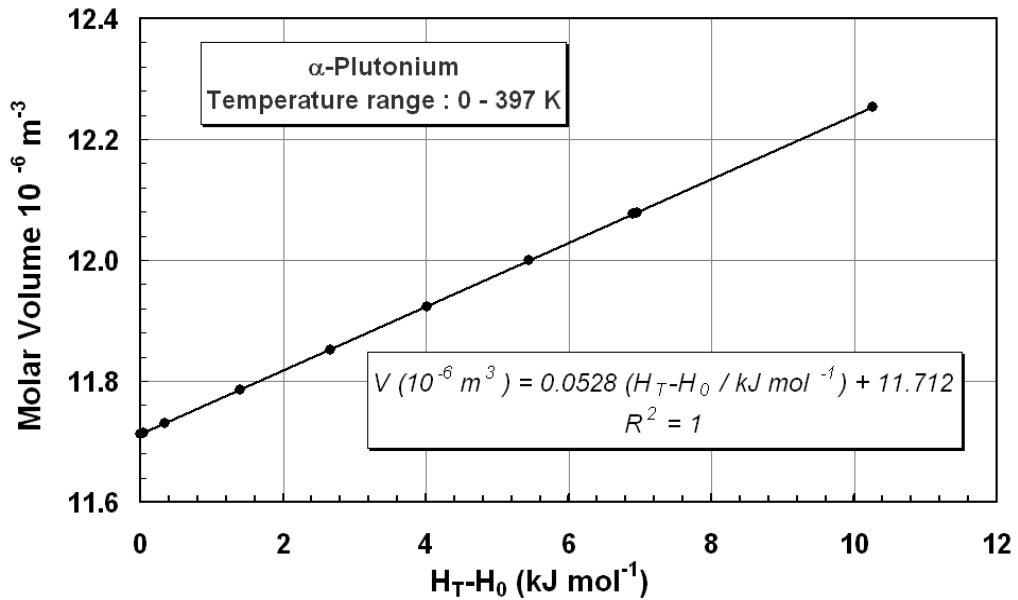


Fig. 3.4. Linear relationship between molar volume and enthalpy for  $\alpha$ -Pu

It emerges from the comparison of these two linear relations (*Eq. 17 & 23*) that  $\lambda_0 V_0 = \gamma_0 / B_0$ , which otherwise also follows from the definition of  $\gamma_0$ , as given in *Eq. 14*. By making use of this fact in the thermodynamic definition of  $\xi_0 = \gamma_0 \delta_0 / V_0$ , we obtain

$$\xi_0 = \lambda_0 \delta_0 B_0. \quad (24)$$

In view of the above, *Eq. (1)* may now be rewritten in the following equivalent form.

$$B_S = B_0 (1 - \lambda_0 \delta_0 \Delta H). \quad (25)$$

The other important point with regard to the applicability of the approximations developed in this study is concerned with the *true* constancy of various thermoelastic parameters invoked for the purpose. As a general remark, it may be said that all thermoelastic quantities are in principle sensitive to temperature variation and a rigorous theoretical quantification of this dependency is difficult. It is generally found that for many solids, and for temperatures exceeding the Debye characteristic temperature,  $T \gg \theta_D$ , the temperature variation of thermoelastic quantities may be considered as negligible [6]. It is in this light, that the proposition of a second order thermoelastic parameter like  $\xi_S$ , which implicitly incorporates the temperature dependence of primary or first order thermoelastic quantities, such as  $\gamma_G$ ,  $\lambda$ ,  $\delta_S$  etc. assumes practical significance. As amply demonstrated by the results obtained for  $\alpha$ -plutonium, the self-consistency of approximations suggested in this study is quite obvious. In this sense, the invocation of a constant  $\xi_S$  can offer fairly reliable predictions for molar volume from bulk modulus data or *vice versa*. Further, it may also be said that in proposing empirical correlations like Eq. (1), (17) or (23) involving measurable thermodynamic quantities, a consistent description of the interrelationship between them has also been enabled. This fact will be of use in analyzing the internal thermodynamic consistency among diverse data sets. The other point that must be kept in mind while using the approximations derived in this study is with regard to the onset of phase transformations. For obvious reasons, the various thermodynamic quantities suffer continuous or discontinuous changes in the domain of phase transformations and as a result of this, the temperature independent character of various thermoelastic parameters is lost in the phase transition region. In view of

this, the validity of the thermoelastic relations suggested in this study is lost, when the system under study evinces phase instability.

Finally, it is instructive to have a brief mention of uncertainty about fit parameter, such as  $\theta_E$  and  $S$ , entropy, which is a derived quantity from  $C_p$ . At first, it is useful to recall that these are not primary estimated quantities here, especially the former. Use is made of assessed literature data on thermodynamic properties of alpha Pu by Oetting [29, 30] and by Ward [38]. In Oetting's general compilation, the uncertainty for  $C_p$  is about  $\pm 8\%$ ; which would translate as 5% for an integral quantity like enthalpy and almost of the same order for entropy (actually  $TS$ ). As for  $\theta_E$ , the estimated value is about 158 K; which going by  $R^2$  value of about 0.99 for the fit, is of high accuracy. However, a corresponding experimental estimate is still lacking for alpha plutonium. Throughout the discussion, the emphasis is more on the outcome of the linear scaling than in the analysis of error bars of experiment supplied quantities. In fact, the soundness of linear correlation sets the lower limit for the inaccuracy involved in any estimation.

## 6.0. Summary

A comprehensive thermodynamic analysis of the linear isobaric relationship between bulk modulus and enthalpy has been presented. By invoking a hierarchy of approximations for representing the volume dependence of bulk modulus, a set of self-consistent relations connecting molar volume and enthalpy increment has been deduced. The applicability of the thermodynamic framework derived in this study has been demonstrated in case of  $\alpha$ -plutonium by successfully predicting its molar volume as a function of temperature using enthalpy data.

## References

1. S. Raju and E. Mohandas, *Z. Metallkd.*, 89 (1988) 527.
2. C. B. P. Finn, *Thermal Physics*, Second edition, Chapman Hall, London (1993).
3. G. Grimvall, *Thermophysical Properties of Materials*, North-Holland, Amsterdam, (1986).
4. R. E. Barker, *J. Appl. Phys.*, 34 (1963) 107.
5. D. B. Sirdeshmukh, P. G. Krishna and K. G. Subhadra, *J. Mater. Sci.*, 38, (2003) 2001.
6. O. L. Anderson, *Equations of state of solids for geophysics and ceramic science*, Oxford University press, New York (1995).
7. J. L. Tallon, *J. Phys. Chem. Solids*, 41 (1980) 837.
8. R. Grover, I. C. Getting and G. C. Kennedy, *Phys. Rev.*, B7 (1973) 567.
9. M. H. G. Jacobs and H. A. J. Oonk, *Phys. Chem. Chem. Phys.*, 2 (2000) 2641.
10. S. Raju, K. Sivasubramanian and E. Mohandas, *Scripta mater.*, 44 (2001) 269.
11. C. Bina and R. Helffrich, *Annual Rev. Earth and Planet Sci.*, 20 (1992) 527.
12. O. L. Anderson, *Phys. Chem. Minerals*, 16 (1989) 559.
13. O. L. Anderson, *Phys. Rev.*, 144 (1966) 553.
14. D. J. Steinberg, *J. Appl. Phys.*, 52 (1981) 6415.
15. S. Raju, K. Sivasubramanian and E. Mohandas, *Phys. Chem. Chem. Phys.*, 3 (2001) 1391.
16. A. Chopelas and R. Boehler, *Geophys. Res. Lett.*, 19 (1992) 1983.
17. H. Ledbetter, *Phys. Stat. Solidi*, B181 (1994) 81.
18. S. Raju, K. Sivasubramanian and E. Mohandas, *J. Alloys Compounds*, 416 (2006) 58.
19. R. D. Baker, S. S. Hecker and D. R. Harbur, *Los Alamos Science*, (1983) 142.

20. A. M. Boring and J. L. Smith, *Los Alamos Science*, 26 (2000) 90.
21. M. Rosen, G. Erez and S. Shtrikman, *J. Phys. Chem. Solids*, 30 (1969) 1063.
22. T. M. Sandenaw, *J. Phys. Chem. Solids*, 23 (1962) 1241.
23. J. E. Gordon, R. O. A. Hall, J. A. Lee and M. J. Mortimer, *Proc. R. Soc., London., Ser. A*, 351 (1976) 179.
24. R. O. A. Hall, J. A. Lee and M. J. Mortimer, *Cryogenics*, 15 (1975) 156.
25. *Plutonium Handbook : A Guide to Technology*, edited by O. J. Wick, Gordon and Breach Science Publ., NY (1967) 31.
26. G. Rob, C. E. Olsen and J. F. Andrew, *J. Nucl. Mater.*, 199 (1992) 6.
27. C. A. Calder, E. C. Draney and W. W. Wilcox, *J. Nucl. Mater.*, 97 (1981) 126.
28. R. Lallement, *Phys. Letters*, 5 (1963) 182.
29. F. L. Oetting, M. H. Rand and R. J. Ackermann, *The chemical thermodynamics of Actinide elements and compounds*, Part I : The Actinide Elements, IAEA, Vienna (1976).
30. F. L. Oetting, R. O. Adams, *J. Chem. Thermodynamics*, 15 (1983) 537.
31. C. E. Rollon and G. F. Gallegos, *J. Therm. Anal.*, 21 (1981) 159.
32. J. R. Cost and R. A. Salzar, *J. Alloys and Compounds*, 206 (1994) 103.
33. M. Boivineau, *J. Nucl. Mater.*, 297 (2001) 97.
34. J. C. Lashley, J. Singleton, A. Migliori, J. B. Betts, R. A. Fisher, J. L. Smith and R. J. McQueeney, *Phys. Rev. Lett.*, 91 (2003) 205901 (1-4).
35. T. G. Zocco, D. S. Schwartz and J. Park, *J. Nucl. Mater.*, 353 (2006) 119.
36. H. Ledbetter, A. Migliori, J. Betts, S. Harrington and S. El-Khatib, *Phys. Rev.*, B71, (2005) 172101(1-3).
37. Y. Varshni, *Phys. Rev.*, B 2 (1970) 3952.

38. J. W. Ward, P. D. Kleinschmidt, and D. E. Peterson, in: *Handbook on the Physics and Chemistry of the Actinides*, edited by A. J. Freeman and C. Keller (Elsevier, Amsterdam, 1986), 309.
39. D. C. Wallace, *Phys. Rev.*, B 58 (1998) 15433.
40. E. Grüneisen, in: *Handbook der Physik*, Vol. 10, Springer-Verlag, Berlin (1926), 1-52; as cited in *Ref.* [6].
41. S. Raju, K. Sivasubramanian and E. Mohandas, *Mater. Lett.*, 57 (2003) 3793.

# Phenomenological Description of Transformation Kinetics

## 1.0. Introduction

A study of phase transformations that occur in solid state is of interest on both basic and applied grounds. Since phase transformations represent the explicit manifestation of thermodynamic instability, a comprehensive mapping of the evolutionary character of different phase fields in terms of appropriate intensive thermodynamic variables is extremely useful in constructing phase diagrams, the use of which in the design of materials is only too obvious [1]. While thermodynamic considerations decide the ultimate stability of condensed systems, it is the *time scale* marking the *rate* of attainment of this true thermodynamic equilibrium, which decides the potential of a solid as a practically useful engineering material. Testimonies to this fact abound in materials literature, especially in the realm of metals and alloys. While thermodynamics classifies phase changes in terms of the nature of discontinuity in appropriate free energy susceptibility functions, the kinetic considerations serve to broaden this classification even further [2]. This arises, because the number of *kinetic paths* available in general for solid state phase transformations are many, and these can be realised by manipulating appropriate *kinetic path* variable [3]. **Fig. 4.1** schematically illustrates this viewpoint with respect to one kinetic variable, namely heating or cooling rate ( $\beta$ ) that can be easily manipulated in a dynamic calorimetry experiment. The other possible kinetic path variables include: starting grain size ( $d$ ) or other microstructure morphology index of the material, stress state ( $\sigma$ ), irradiation

level, magnetic field *etc.* All these are extremely well known in physical metallurgy; however, what is less commonly appreciated is that these could act either singly or in combination to decide the overall kinetics of transformation.

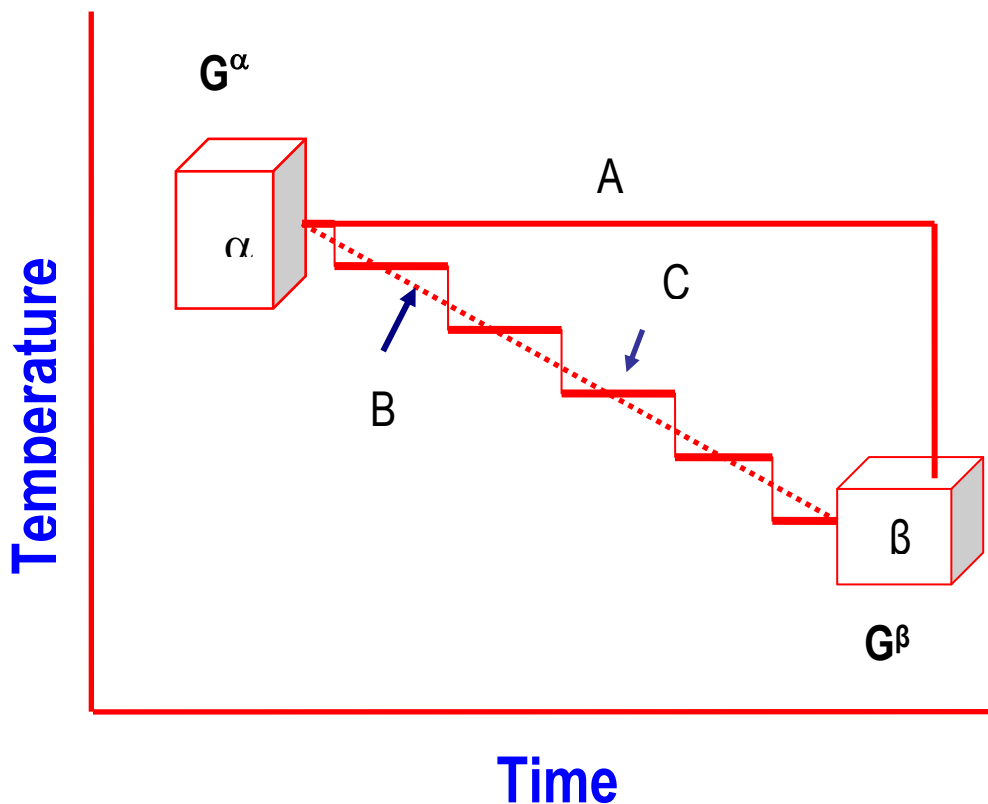


Fig. 4.1. A schematic of different kinetic path ways offered by three different cooling histories is shown. Paths A and B stand for transformations occurring under isothermal and linear cooling conditions, whereas the path C represents a step wise cooling with small incremental isothermal holds. Note that in all the three paths A, B and C the net reduction in Gibbs energy  $\Delta^0G$  is the same

In the survey undertaken in this chapter, an attempt is made to highlight the role of one important kinetic variable, namely the role of heating and cooling rate, in decisively altering the kinetics of diffusional and displacive phase transformations that occur in metals and alloys. The choice of this variable is based on the pre-eminent status that *thermal history* as a process parameter enjoys in dictating the final microstructure of many engineering alloys used in strategic applications. The other

reason is that relevant experimental kinetic data with sufficient degree of accuracy are easily generated by taking recourse to high resolution thermal analysis techniques, the results of which are rather easily processed to obtain information on transformation temperatures, transformation velocity, especially their dependence on thermal history. In what follows, we highlight some interesting, but somewhat less well-known kinetic aspects of phase transformations through select examples drawn from this research. It is submitted that this is a classical field, well served by many authoritative works, as the peculiarities in phase changes encountered in metals and alloys, glasses, polymers and in composites have drawn their own specialty (often somewhat less transparent) descriptions of transformation kinetics. It is an awesome task to describe these multifarious developments in a unified manner. However, in what follows, a simple, and brief, yet transparent conceptual description of the essence of the kinetic issues, irrespective of their domain of relevance, is attempted.

## **2.0. Isothermal *versus* Non-isothermal Processes: Influence of Heating and Cooling rates**

### *2.1. Isothermal phase change*

As illustrated in **Fig. 4.1**, a phase transformation between two phases  $\alpha$  and  $\beta$  can be realised under varying time ( $t$ )–temperature (T) combinations, known under the generic name of thermal history. In the purely isothermal case, the sample is held at a fixed temperature (*path A in Fig. 4.1*) the magnitude of which decides effectively the available chemical driving force ( $\Delta^\circ G$ ) and diffusional mobility (D) of atoms. Apart from temperature, the time duration of isothermal holds decides the extent of transformation. For the case of  $\alpha \rightarrow \beta$  transformation, which is promoted by an increase of temperature, both  $\Delta^\circ G$  and the diffusional mobility D of atoms increase

with the extent of overheating,  $T - T_{tr}$ .  $T_{tr}$  is the equilibrium transformation temperature at which  $\Delta^{\circ}G$  goes identically to zero. The temperature dependent Gibbs energy difference to a first order approximation may be given as [4]

$$\Delta^{\circ}G(T) \approx \Delta^{\circ}H_{tr} \Delta T / T_{tr}. \quad (4.1)$$

$\Delta^{\circ}H_{tr}$  is the latent heat associated with the phase change at  $T_{tr}$ , and  $\Delta T = |T - T_{tr}|$  is the degree of overheating (or undercooling, if  $\beta \rightarrow \alpha$  reverse transformation is considered).

The fraction transformed is recorded as a function of time  $X(t)$ , for time spans that are greater than a minimum threshold known as the incubation time,  $\tau_{inc}$  (**Fig. 4.2**).

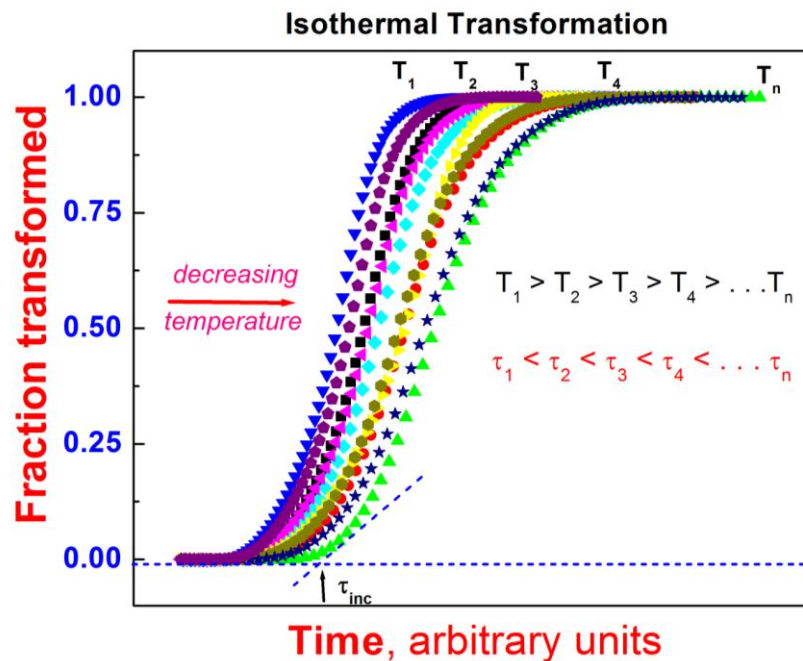


Fig.4.2. A graphical portrayal of the isothermal transformation diagram is shown. Note the sigmoidal nature of the transformation profiles and also the dependence of incubation time on reaction temperature

It is clear that for  $t < \tau_{inc}$ ,  $X(t) = 0$ .  $\tau_{inc}$  is a characteristic kinetic quantity, the magnitude of which is decided by both  $\Delta^{\circ}G(T)$  and diffusivity [5]. Apart from temperature and pressure,  $\tau$  depends on stress, magnetization *etc.*

The basic isothermal experimental kinetics data are therefore  $\{X, t\}_T$  and  $(\partial X/\partial t)_T$ ; both of which are obtainable by a combination of thermal analysis and metallographic techniques. Besides the standard transformation plots (**Fig. 4.2**), a most popular way of representing  $\{X, t\}_T$  data is by means of isotransformation fraction  $X\{T, t\}$  contour plots, which are often called TTT (time, temperature, transformation) diagrams in metallurgy. One such diagram is schematically sketched in **Fig. 4.3** for an arbitrary  $\beta \rightarrow \alpha$  cooling induced transformation.

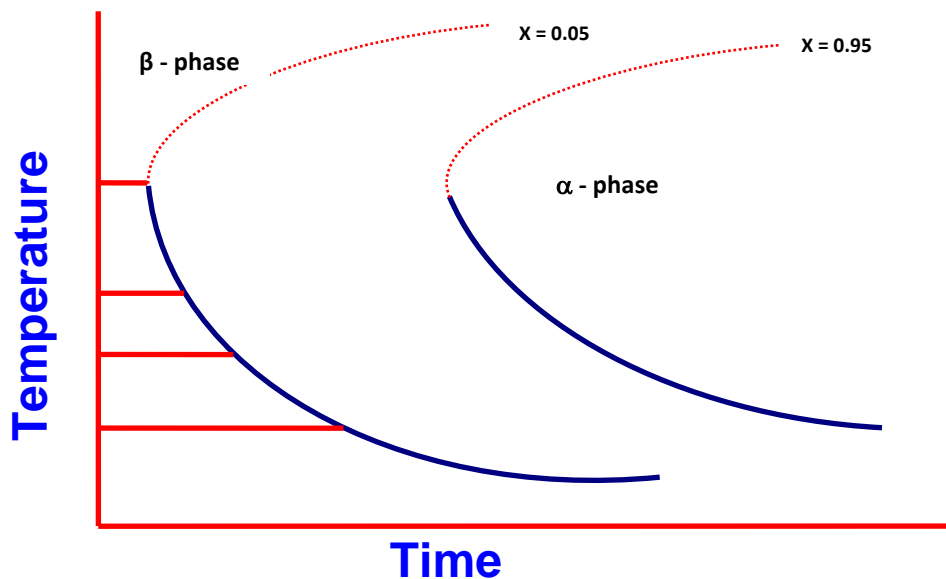


Fig.4.3. A schematic of TTT diagram for the formation of the low temperature stable  $\alpha$  phase from the high temperature polymorph,  $\beta$  is shown. The horizontal lines parallel to the time axis represent the time to reach fixed extent of transformation. Note the C-type nature of this isotransformation contours. The upper portion of this contour, indicated in red is however absent for the reverse  $\alpha \rightarrow \beta$  phase change. Refer to text for further details

It is useful to note that the C-type nature of the isotransformation contour is intrinsic to diffusive phase changes occurring during cooling and is generally absent for the corresponding  $\alpha \rightarrow \beta$  on-heating phase change. The obvious reason is that although  $\Delta^\circ G$  increases with undercooling  $|T - T_{tr}|$ , this is accompanied by reduced atomic mobility which in turn retards the transformation [3]. But such a simplistic outlook

does not consider the influence of hard impingement effects on the physical advance of transformation front.

## 2.2. Non isothermal phase change

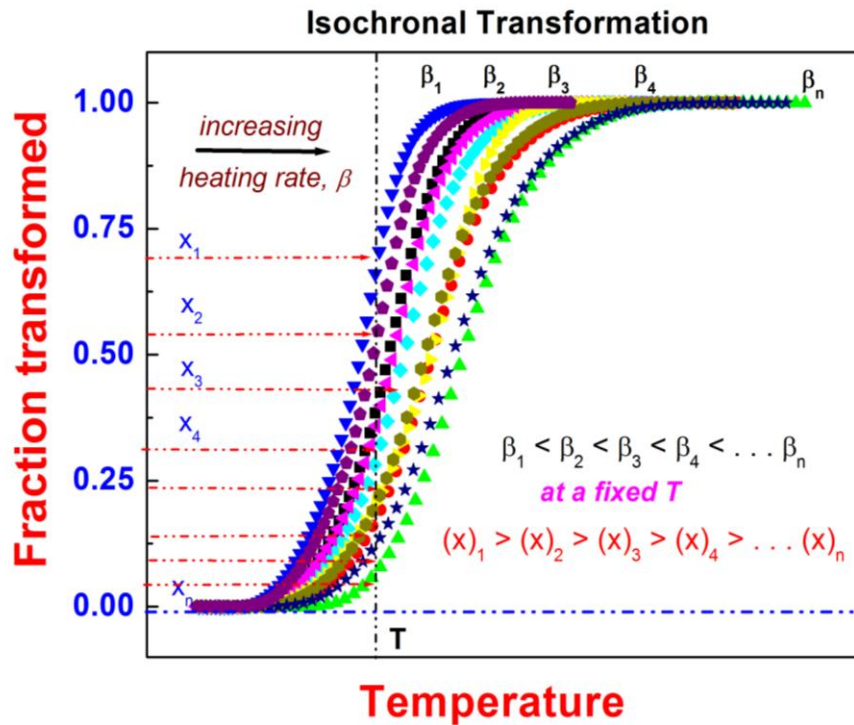


Fig.4.4. The isochronal or continuous heating transformation plot is graphically illustrated. Note that increasing the heating rate pushes up the transformation start temperature. Also, for fixed temperature, the transformation is more advanced at lower heating rates.

The isochronal process involves continuous heating or cooling as a function of time (*path B* in Fig. 4.1) or with interrupted isothermal holds (*path C* in Fig. 4.1). To avoid unnecessary complexity, we shall consider in the present analysis only linear heating and cooling processes. A typical continuous heating transformation plot is portrayed in **Fig. 4.4**. It is clear that higher heating rates push the transformation onset temperatures ( $T_S$ ) to successively higher values; stated in equivalent terms, for a fixed temperature  $T$ , the transformation is *more advanced* for *slower* heating rates. A

corollary of this deduction is that the adoption of successively higher heating rates takes the transforming system *increasingly away from equilibrium*. The case of equilibrium in this case pertains to the asymptotic limit,  $\beta \rightarrow 0$ . Incidentally, the symbol  $\beta$  is used to represent the heating and cooling rate in this chapter and elsewhere in this report, although, it is usually reserved for phase designation. Thus, although the system is physically taken to successively higher temperatures in quick succession in isochronal heating experiments, it is done so without realising the *equilibrium* extent of transformation slated for that temperature. This lagging behind the equilibrium, means a pileup of *unspent* driving force  $\Delta^{\circ}G(T)$  which is only waiting to be dissipated through *alternate* modes of phase transformation. There is enormous evidence in metallurgical literature, which suggests that on rapid heating or cooling conditions, classical nucleation and growth mediated phase changes are inhibited and yield way to *martensitic* or *displacive* types [6, 7]. From an experimental point of view, the heating or cooling rate dependence of transformation temperatures, in addition to the transformed fraction  $X(T)$ , offer a valuable wholesome kinetic dataset. It is generally the case that the variation of transformation temperatures is highly nonlinear with respect to heating or cooling rate, and this tendency is exhibited more remarkably by the transformation finish ( $T_f$ ) temperatures [8]. An example to this effect is provided in **Fig. 4.5**, which incidentally represents a continuous heating transformation (CHT) diagram for the  $\alpha \rightarrow \beta$  structural change in uranium, taken from our own earlier work on Uranium [9].

It is interesting to note that the temperature interval of the two phase domain  $\alpha+\beta$  increases at higher heating rates, a feature which is unique to kinetic phase diagrams. Such examples will be encountered later in this report, while discussing the results on diffusional phase transformation in RAFM steel.

### 3.0. Modelling of Nonisothermal transformation kinetics: Additivity approximation

It is generally the case that nonisothermal experiments are easily performed with minimal expenditure of time; but their results are the difficult ones to understand

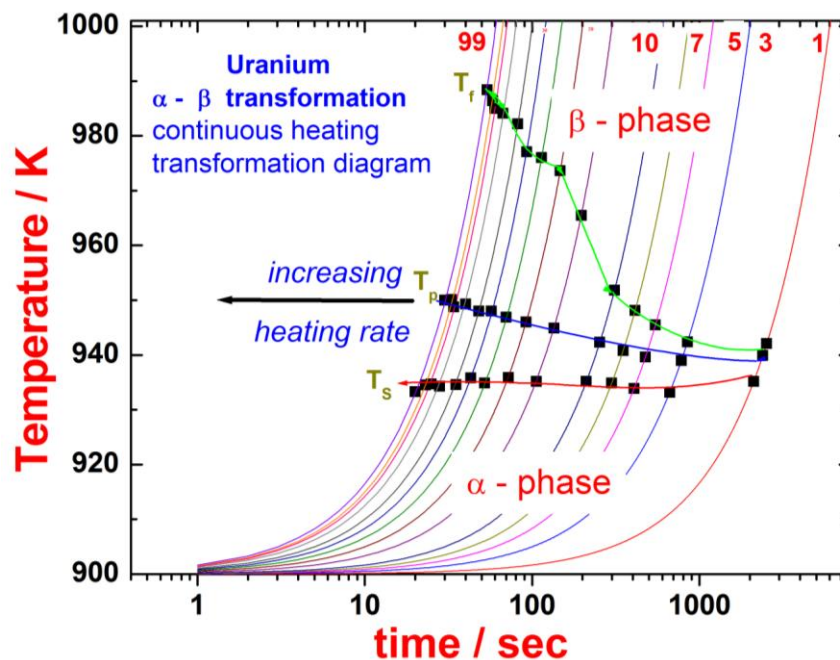


Fig. 4.5. The continuous heating transformation (CHT) diagram for the  $\alpha \rightarrow \beta$  transformation in uranium is shown. The dotted lines represent various heating rates, on to which the measured transformation start ( $T_s$ ), peak ( $T_p$ ) and finish ( $T_f$ ) temperatures are marked. Note the increased width of the  $\alpha+\beta$  two phase domain at higher heating rates. Data adapted from [9].

and interpret in concrete terms. The isothermal experiments, while more involved in terms of labour, offer fundamental results that may be tested in terms of transparent theoretical descriptions [10-13]. From an applied context, most of the industrial heat

treatments are done under *complex* thermal history, thereby necessitating a holistic understanding of both isothermal and nonisothermal phase transformation kinetics. In literature, there are very few rigorous treatments aimed primarily at tackling the problem of phase evolution under varying time-temperature history [14-16], and generally their mathematical complexity comes in the way of their widespread practical appeal.

Traditionally, and quite usefully as well, the problem of nonisothermal transformation kinetics is modelled as a sum of short isothermal steps; this approximation is popularly called the Scheil's additivity rule in metallurgy [17], which, even as of now, is extensively used in modelling the solidification kinetics of alloys, high temperature homogenisation treatment as well as particle dissolution upon heating and precipitate formation reactions under cooling etc. [18-20]. The essence of the additivity approximation is illustrated in *path C* in **Fig. 4.1**. Basically, the total time span,  $t = (T_f - T_s)/\beta$ , spent between the two temperature intervals  $T_f$  and  $T_s$  under a fixed scan rate  $\beta$ , is divided into  $n$  number of small isothermal steps with time interval  $\Delta t$ . Mathematically, the total fraction transformed  $X(T)$  at any particular temperature  $T$  ( $T_s \leq T \leq T_f$ ) which is reached after a finite time interval  $t = T - T_s/\beta$ , is approximated as,

$$X(T) = X(T_s + \beta t) = \sum x_i; (i = 1, n). \quad (2)$$

Further,

$$t = \sum \Delta t_i, \text{ for } i = 1, n. \quad (3)$$

The individual  $x_i$  ( $\Delta t_i$ ), the isothermally transformed fractions are determined normally by adopting a well behaved *isothermal* rate equation to model the progress of transformation. There are no firm guidelines as to the correct choice of the isothermal

rate equation, but the one proposed by Kolmogorov, Johnson, Mehl and Avrami for diffusional phase changes [21] is most extensively used in metallurgy. Without going into derivational details, the isothermal KJMA model may be given as follows.

$$X(t) = 1 - \exp\{-((k(T)t)^n)\}. \quad (4)$$

$k(T)$  represents the isothermal rate constant, which as a matter of convenience is taken to be of the Arrhenius form.

$$k(t) = k_0 \exp(-Q_{eff}/RT). \quad (5)$$

$n$  is the (overall) or *pseudo* transformation exponent.  $k_0$  and  $Q_{eff}$  assume standard implications. In principle, the rate constant  $k$  and the transformation exponent  $n$  are sensitive to transformation path variable, such as heating or cooling rate, to varying degree of sensitivity. This fact is often overlooked in many simplistic modelling approaches however [22]. But in our humble opinion, the major issue of modelling (not developing a theory for) nonisothermal transformation kinetics does not lie in evolving a proper nonisothermal analogue of KJMA [23], since more serious technical limitations arise from the use of the additivity principle itself. As this is an important issue, we shall dwell upon this in a little more detail here.

### 3.1. Additivity and Isokinetic approximations: Nonlocal nature

In invoking the linear superposition of isothermal events, it is implicitly assumed that the *jump* from one isothermal hold to the next one is *instantaneous*, and hence *no* phase formation is allowed or expected during this jump. It is nevertheless obvious that instantaneous jump is practically meaningless. The error accrued by this assumption may be minimised by going in for smaller  $\Delta t_i$ . The other assumption that is implicit in the additivity approximation is that different isothermal events are *isokinetic*, a preposition which is generally not obeyed by many solid state phase changes, especially during the later stages of growth [24]. *The core of nonisokinetic*

*nature stems from the fact that the starting configuration given to each individual isothermal transformation step is just not the same, as for example, in a single shot isothermal phase change.* Since transformation kinetics are a strong function of the instantaneous configuration, each successive isothermal step has somewhat altered kinetic imperatives and hence as a rule, solid state phase changes under nonisothermal conditions are nonisokinetic in nature.

A practical implication of the above reasoned arguments is that the adoption of rate expressions that are originally developed for isothermal phase changes, for modelling of isochronal transformation kinetics is technically incorrect, if the nonlocal nature of the *motivation* for phase change is not incorporated. This is notwithstanding of the successful numerical fitting of the experimental data by many isokinetic descriptions.

Thus for an example, the classical isothermal rate equations are mostly the variable separable type, in the sense that  $(dX/dt)$  is expressed as a product of two functions, one each for characterising the T and X dependence.

$$(dX/dt) = f(X) k(T). \quad (6)$$

$f(X)$  is an empirical reaction model and  $k(T)$  is the rate constant as mentioned before. But such a separable representation is conceptually incompatible with the basic premise of isochronal transformation kinetics [16], despite the fact that they are extensively patronised in data analysis (including the present author), basically because of their simplicity.

On the other hand, a conceptually transparent alternative would be to start from the basic fact that for small range of  $\beta$  ( $10^0$  to  $10^2$  K min<sup>-1</sup>) usually encountered in controlled thermal analysis experiments, the transformation start temperature is found to vary in a linear manner with  $\beta$ . That is,

$$T_s(\beta) = T_{eq} + \beta\tau. \quad (7)$$

$T_{eq}$  is the ideal thermodynamic equilibrium transformation temperature corresponding to the static case,  $\beta \rightarrow 0$ . In practice,  $T_{eq}$  can also be treated as a fit parameter.  $\tau$  is a characteristic time of the nonisothermal phase change kinetics, which is somewhat akin to the incubation time,  $\tau_{inc}$  proposed for the isothermal case. At this stage, an amplification of the meaning of  $\tau_{inc}$  is not needed for proceeding further.

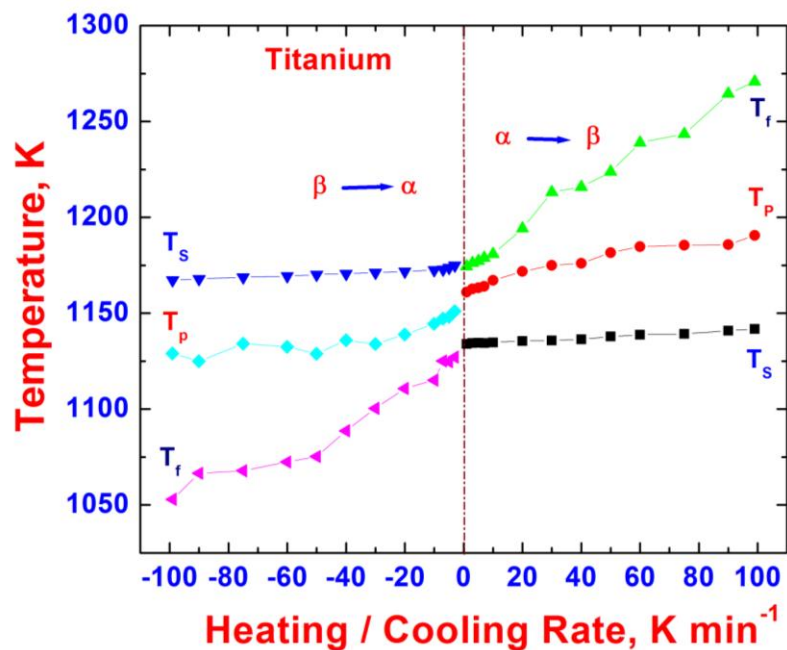


Fig. 4.6. The influence of heating and cooling rates on the  $\alpha \leftrightarrow \beta$  structural transformations in titanium is graphically depicted. Note that compared to  $T_s$ , the  $T_f$  temperature exhibits a higher degree of nonlinearity in its variation with  $\beta$ . The non-linear model suggested here fits better the transformation start temperature dependence on scan rate.

The physical basis of Eq. (7) is rather straight forward. Given adequate time  $t$  greater than  $\tau_{inc}$ , the reaction would certainly start at  $T_{eq}$ ; however, in a continuous heating experiment, (depending on heating rate) the *mandatory* expenditure of a minimum of  $\tau_{inc}$  seconds after having reached  $T_{eq}$  would alter the temperature to a higher value, namely  $T_{eq} + \beta\tau$ . So the first traces of the transformation product are

observed not at  $T_{eq}$ , but only at  $T_{eq} + \beta\tau$ . Certainly this is a conservative, linear approximation. The actual time delay involved in realising advanced transformation stages (not the early nucleation step) is even more than what is given by the linear model. This deficiency can be partly accounted for by now making  $\tau$  itself a function of  $\beta$ , although, the physical justification for this not straight forward. Thus, by using a second tier of approximation,

$$\tau(\beta) = \tau_0 + \tau' \beta; \quad (8)$$

the nonlinear variation of  $T_S$  with  $\beta$  is readily obtained. The experimental validity of this model is amply borne out by the measured  $\alpha \leftrightarrow \beta$  transformation temperature of titanium as a function of  $\beta$  (**Fig. 4.6**). A similar argument has also been used in the explaining the heating rate dependence of  $\alpha \rightarrow \beta$  transformation temperature in uranium [9]. After accounting for the nonlinear variation of transformation temperature with heating/cooling rate, we shall propose in the next phase a general analytical rate expression for  $(\partial X/\partial t)_\beta$  that is valid for both isothermal and nonisothermal conditions. This model dates back to the earlier work of Leblond and Devaux, who proposed it on an axiomatic basis [16].

$$(\partial X/\partial t)_\beta = X_{eq}(T) - X(t) / \tau. \quad (9)$$

Equation (9) is based on the basic deduction that the instantaneous rate of transformation  $(\partial X/\partial t)_\beta$  for a chosen  $\beta$ , is dependent on the extent of deviation of the (actual) transformation extent  $X(t)$  from its corresponding equilibrium value at  $T$ ,  $X_{eq}(T)$ . This latter quantity is thermodynamic in nature and may be obtained from equilibrium phase diagram (lever rule in a binary) or may be set as an internal reference value that is estimated under very slow heating or cooling conditions. This latter methodology is more apt to be followed in slow scan DTA experiments. A

rough estimate of  $\tau$  (assumed to be  $\beta$  independent in the trial case) can be obtained from the experimental data using Eq. (7). Thus  $(\partial X/\partial t)_\beta$  is readily obtained. *But what is more appealing is that Eq. (9) can be used in an inverse manner to obtain  $X_{eq}(T)$ , the equilibrium fraction transformed from experimental data measured under dynamic conditions.* But the actual caveat in realising this possibility lies in measuring accurately the  $X(t)$  values; this method works better for larger values of  $X_{eq}(T) - X(t)$ , which means that experiments need be performed under considerably large heating or cooling rates. Further, metallography based estimates of  $X(t)$  often do not yield highly accurate values of transformation extent. Again caution is the watchword in making such generalization.

*The essential theoretical import of Eq.(9) is that under nonisothermal conditions,  $X(t)$  approaches  $X_{eq}$  with a time constant given by  $\tau$ .* For the sake of maintaining analogy with the isothermal case, we term this  $\tau_\beta$  as a dynamic incubation time. It can be logically argued that  $\tau_\beta$  exceeds  $\tau$ -static by a margin which is actually the time delay introduced because of kinetic considerations. An accurate knowledge of the difference,  $\tau_\beta - \tau$ -static is very useful in interrelating the isothermal and nonisothermal transformation data, as for example argued by Rios [25]. At present, the generalised functional dependence of  $\tau_\beta$  with  $\beta$  is not known. Nevertheless, an attempt is made to model the  $\tau(\beta)$  behaviour through an exponential relaxation model. Again this is purely empirical at this stage; an exponential relaxation is favoured in terms of its ubiquitous popularity.

$$\tau = \tau_0 + A \exp(-m/\beta). \quad (10)$$

In the above description,  $\tau$  approaches  $\tau_0$ , when  $\beta \rightarrow 0$ .  $m$  is an empirical parameter having the same dimension as that of  $\beta$  and is characterising the exponential decay of

$\tau$  with  $1/\beta$ . Further,  $\tau = \tau_0 + A$  for  $\beta \rightarrow \infty$ . Thus, a limiting time is found to operate for very high heating rates as well. *All these inferences assume that  $\tau$  versus  $\beta$  is a continuous function; any abrupt change in the behaviour is suggestive of the operation of a different transformation mechanism.* At present the theoretical justification for this linear+exponential model is not clear, but it is motivated by a similar experimental finding made with respect to the heating rate dependence of the rate constant  $k$  for the structural transformation in uranium [9]. Further, we also found that this model is found to fit the experimental data well for the  $\beta \rightarrow \alpha$  transformation in pure titanium as well [26].

For the sake of relating the exponential decay model of  $\tau$  with a kinetic coefficient ( $Q_{eff}$ ) of the transformation process, an empirical modification of Eq. (10)

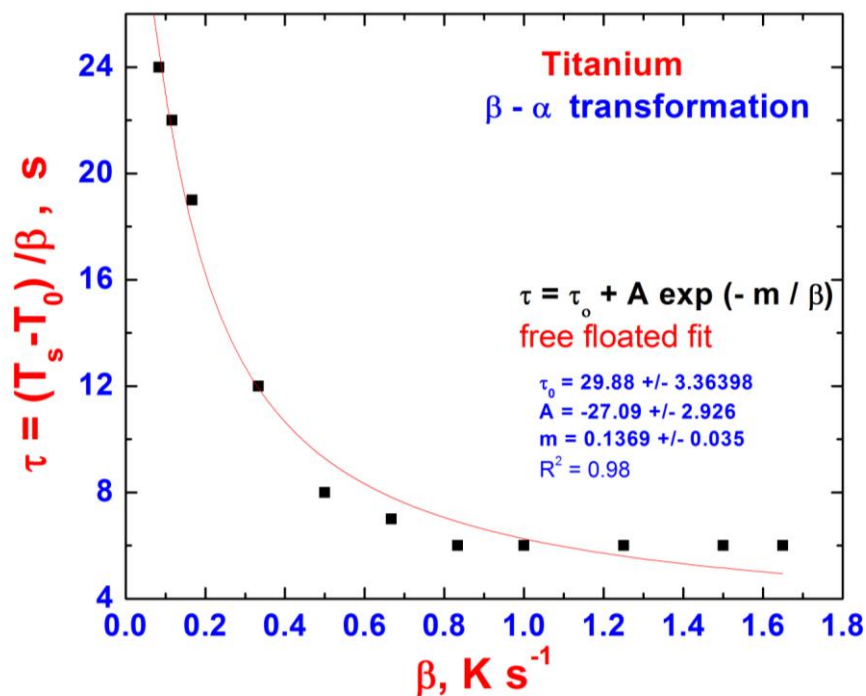


Fig. 4.7 The exponential decay of the characteristic transformation time  $\tau$  with cooling rate  $\beta$ , for the  $\beta \rightarrow \alpha$  phase transformation in titanium is illustrated

in the following manner is attempted.

$$\tau = \tau_0 + A \exp(-m'Q_{eff}/\beta RT_p). \quad (11)$$

Note, that  $Q_{eff}/RT_p$  is a dimensionless quantity. Both *Eq.* (10) and (11) are really the same and work well for the polymorphic structural changes in uranium and titanium [9,26] In **Fig. 4.7**, the exponential relaxation model (*Eq.* 10) for  $\tau$  is illustrated using results obtained on  $\beta \rightarrow \alpha$  structural transformation in a dilute titanium alloy [26].

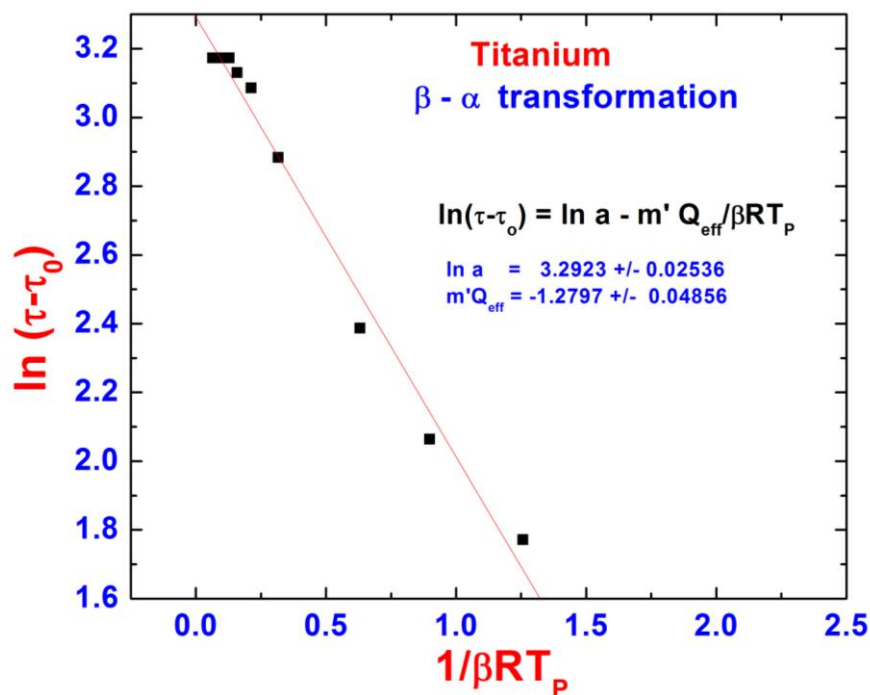


Fig. 4.8. The linear scaling of the quantity  $\ln(\tau - \tau_0)$  with  $1/\beta RT_p$  is shown for the  $\beta \rightarrow \alpha$  phase transformation in titanium

Before ending this section, it is very instructive to note that *Eq.* (11) serves to pseudo linearise the  $\beta$ -dependence of experimental transformation temperature data. By taking logarithm on both sides of *Eq.* (11) and after a mild rearrangement, we get

$$\ln(\tau - \tau_0) = \ln A - m'Q_{eff}/\beta RT_p. \quad (12)$$

It is interesting to note that *Eq.* (12) bears interesting similarity with the Ozawa, Kissinger like linearization schemes often used in the estimation of apparent

activation energy values from thermal analysis data [27, 28]. The utility of Eq. (12) in obtaining a linear correlation is again illustrated in **Fig. 4.8** for the case of titanium. But now, the separation of  $m'Q_{eff}$  into independent parameters namely  $m'$  and  $Q_{eff}$  is a nontrivial task; it is clear that both  $m$  and  $m'$  are related, as it has been found in case of uranium where  $m' \approx m/10$ . This appears to be true for the  $\alpha \rightarrow \gamma$  transformation in pure iron as well as in 9Cr-1Mo ferritic steel. But we are not certain about the general transferability of this finding. Nevertheless, using this scaling factor between  $m$  and  $m'$ , a plausible estimate of about  $100 \text{ kJ mol}^{-1}$  for the  $Q_{eff}$  of  $\beta \rightarrow \alpha$  transformation for titanium is obtained.

As a further remark, it must be added that the present scheme is intrinsically capable of mirroring the kinetic asymmetry associated with forward and reverse transformations. This quite often found in many forward and reverse diffusional transformations, but the incorporation of other path variables like grain size and the effect of strain is yet to be worked out. The role of internal and external stress in modifying  $\tau$ , the characteristic time scale is a fundamental problem in physical metallurgy, which requires analytical expansion of the meaning of  $\tau$  on a physically based model of nucleation and growth stages. These developments, when incorporated correctly can make this scheme a fully physically based one.

#### **4.0. Estimation of apparent activation energy by model free isoconversion methods**

A majority of theoretical methods adapted at present for analyzing the kinetics of temperature programmed solid state transformations take recourse to the following functional form connecting the instantaneous scan rate dependent reaction rate  $(\partial x / \partial T)_\beta$  with a suitable empirical function  $f(\alpha)$  that is characteristic of the

transformation model through a temperature dependent effective rate constant  $k(T)$  [29-32]. Thus

$$(\partial x / \partial T)_\beta = f(x) k(T) (1/\beta). \quad (13)$$

In the above expression  $\beta = (dT/dt)$ , is the heating scan rate, from which it obtains that

$$t(T) = (T - T_S) / \beta. \quad (14)$$

$k(T)$  is often assumed to follow the standard Arrhenius form

$$k = k_o e^{-Q/RT}. \quad (15)$$

$k_o$  is the temperature independent frequency factor,  $Q$  is the apparent activation energy for the whole process under consideration and  $R$  is the universal gas constant.

Further, it is generally assumed that at the peak temperature  $T_P$ , the transformation rate  $(\partial x / \partial T)_\beta$  is at its maximum [29-32]. Hence at  $T_P$ , the first and second derivatives of  $x(T)$  with respect to temperature vanishes, implying thereby that  $T_P$  is an inflection point in the  $\alpha$  versus  $T$  curve. Thus, by differentiating Eq.(13) with respect to temperature twice and taking in the process due account of the temperature dependence of  $k(T)$ , one obtains

$$(\partial^2 x / \partial T^2)_\beta = \beta^{-1} \{ (\partial f(x) / \partial x) (\partial x / \partial T) k + f(x) k Q / RT^2 \} \quad (16)$$

At  $T = T_P$ ,  $(\partial^2 x / \partial T^2)_\beta = 0$ . Thus, from the above expression, after substituting for  $(\partial x / \partial T)_\beta$  from Eq. (13) and effecting some regrouping of terms, it emerges that

$$[-(\partial f(x) / \partial x)] \times (kR/Q) = \beta T_P^2. \quad (17)$$

Taking logarithm on both sides, we obtain

$$\ln\{\beta/T_P^2\} = \ln\{(-\partial f/\partial x)_{T_P}\} + \ln(k_o R/Q) - Q/RT_P. \quad (18)$$

Eq. (18) is the famous Kissinger-like expression obtained for estimating the apparent activation energy  $Q$  as the slope of the linear plot between  $\ln\{\beta/T_P^2\}$  and  $1/RT_P$ . The intercept gives  $k_o$  provided a suitable model for  $f(x)$  is assumed. In most instances of

application of Kissinger like formalism for extracting  $Q$ , it is assumed that  $\ln\{(\partial f/\partial x)_{T_p}\}$ , is negligible as this term is comparatively small in magnitude [32]. It must also be added that in the original Kissinger derivation, this relation was obtained for a specific reaction model  $f(x)$  [see, *ref.* 32 for a discussion]; however, as shown here, this is really not needed for extracting apparent activation energy  $Q$  from basic thermal analysis data.. We shall return to discuss this point at a latter juncture in this chapter.

#### 4.1 Integral Methods

There is another, what is known as the integral method of arriving at Kissinger like expression, in which one recasts *Eq.* (13) in the following manner.

$$\int_{0 \rightarrow \alpha} \{dx/f(x)\} = g(x) = k_0/\beta \int_{T_s \rightarrow T_E} (e^{-Q/RT}) dT \quad (19)$$

The temperature integral on the right hand side has no closed form analytical solution and hence a variety of approximations are invoked in the literature, depending on the magnitude of  $Q/RT$  [30]. Since this aspect is a subject of numerous technical discussions in thermoanalytical literature and besides is not within the scope of present study, we skip any further elaboration here. However, as a typical example, we take the case of  $Q/RT \gg 1$ . Under such situation, one may adopt the following simple approximation [31],

$$\int_{0 \rightarrow T} (e^{-Q/RT}) dT \approx R/Q \{T^2 e^{-Q/RT}\}. \quad (20)$$

Substituting this approximation for the integral in *Eq.* (19) and taking logarithm after suitable rearrangement, we obtain

$$\ln\{\beta/T_p^2\} \approx -Q/RT_p + \ln\{Rk_0/Q g(x)\}. \quad (21)$$

Both Eq. (18) and (21) reflect in spirit the standard Kissinger relation often employed to estimate  $Q$  from isochronal DSC experiments performed under constant heating rates. Again the value of the intercept is dependent however, on the nature of  $g(x)$ .

As a passing remark, it may be added that besides the popular Kissinger method, there are a few other procedures that are commonly employed for obtaining  $Q$  from the scan rate versus peak temperature data without invoking any functional form for  $f(x)$ . Following Starink [32], they may be given by the general expression

$$\ln\{\beta/T_P^S\} \approx -A Q/RT_P + \text{Constant}. \quad (22)$$

In the above expression,  $S$  is a variable exponent, which assumes different values for different linearisation schemes. Thus for example,  $S = 0$  stands for the Ozawa method [33];  $S = 1$  goes by the name of Boswell method [14]; Starink on the other hand suggests that  $S = 1.95$  or  $1.8$  may be adopted for getting accurate  $Q$  [32, 35].

Before concluding this section, it is instructive to bring into discussion another version of model free kinetic analysis that is due originally to Friedman [26]. If one has an accurate data set on  $(\partial x/\partial T)_\beta$  as a function of  $T$ , for various scan rates, then this method is very useful in obtaining the activation energy spectrum as a function of transformation extent ( $x$ ). This method is outlined briefly in the ensuing section, as this is popular still among solid state chemists.

#### 4.2. Friedman Method

This method is quite simple and direct in the sense that by taking logarithm of Eq. (13) one obtains

$$\ln\{(\partial x/\partial T)_\beta \times \beta\} = \ln [f(x)] + \ln(k_0) - Q/RT. \quad (23)$$

Now, from the data on  $(\partial x_i/\partial T)_\beta$ , the rate of transformation measured at a fixed  $x_i$  against the corresponding  $1/T_i$  for a series of constant scan rates  $\beta$ , a linear

isoconversional scaling of reaction kinetics is possible by plotting  $\ln\{(\partial x_i/\partial T)_\beta \times \beta\}$  against the corresponding  $1/RT_i$ . In fact, one may construct an array of linear plots for various values of fractions transformed ( $x_i$ ) so that pseudo ( $x_i$ ) dependent activation energies, that is  $Q(x_i)$  may be obtained from the respective slopes of these straight line plots. The absence of any significant dependence of the activation energy with respect to the extent of transformation may be taken to imply the *possibility* that the transformation is controlled by a *single* elementary step [37]. While drawing this conclusion, it must be borne in mind that in order to get reliable results out of Friedman's isoconversion scaling method, it is necessary that data on  $\{(\partial x_i/\partial T)_\beta$  are sufficiently accurate. In view of this requirement, the successful application of Friedman's model is restricted to an intermediate range of transformed fraction, say  $0.25 \leq x \leq 0.75$ , for at low and higher values of,  $x$ , many measured transformation curves exhibit deviation from true sigmoidal character.

### 5.0. Application of KJMA Model

Within the spirit of isoconversional formalism of treating the non isothermal DSC data as symbolized by Eq. (13), a description of kinetics is said to be formally complete, only with an appropriate specification of  $f(x)$  together with  $k$ , the rate constant. Although, it is in principle possible to estimate  $k_o$  from the intercept of a Kissinger plot (neglecting small contribution from  $f(x)$ ), a complete kinetic characterization necessitates the fitting of experimental data to a suitable reaction model.

A general survey of literature on thermoanalytical studies yields no firm guidelines for effecting the appropriate choice of  $f(x)$ . It appears however, that the use of Kolmogorov-Johnson –Mehl-Avrami (KJMA) kinetics is rather wide spread in the

area of kinetic analysis of metallic glass crystallization [38]. Although, the validity of KJMA kinetics is established only for select nucleation and growth mediated reaction schemes [39], we choose this model in the present study purely as an empirical construct for describing the crystallization kinetics. Therefore, no decisive interpretation should be sought for the KJMA parameters, if the model itself is not derived from sound physical reasoning. The governing expression for the non-isothermal version of KJMA kinetics is given as follows [38].

$$x(T) = 1 - \exp\{-[k(T-T_s)/\beta]^n\}. \quad (24)$$

As mentioned before,  $k$  in the above expression may be taken as the standard Arrhenius rate constant (*cf.* Eq. (26)). Note that  $k$  is taken inside the square brackets, so that  $kt$  ( $t(T) = T-T_s/\beta$ ) may be taken as a single composite path variable characterizing the progress of reaction with time under isochronal conditions [40].  $n$  is the KJMA exponent, taken here as a constant (temperature independent) for the reaction under consideration. In the general case however,  $n$  may vary with transformation extent.

Two points merit discussion when applying Eq. (24) for the analysis of isochronal DSC data. In the first, Eq. (24) is assumed to hold good for the entire span of the transformation. The apparent activation energy  $Q$  is taken here as independent of transformation extent, while applying the KJMA model to analyzing isochronal DSC data. This is only to simplify the portrayal of transformation kinetics. A similar consideration holds good for the Avrami exponent as well. Secondly, it must be stressed that Eq. (24) is not a true isoconversional type kinetic equation since it cannot be reduced to the form of Eq. (13), if  $k$ , the Arrhenius rate constant is taken as temperature dependent. In other words, Eq. (24) in the form that it is presented here is

a *not* a *bonafide* rate equation for representing non-isothermal kinetics, despite its widespread use. The justification for this conclusion may be presented as follows.

Differentiating Eq. (24) with respect to temperature, we obtain

$$(\partial x/\partial T)_\beta = n(1-x)(k\Delta T/\beta)^{n-1} \times \{(k/\beta) + dk/dT(\Delta T/\beta)\}. \quad (25)$$

In the above expression,  $\Delta T = (T-T_S)$ . Since,  $(k\Delta T/\beta) = \{\ln(1/(1-x))\}^{1/n}$ , and further,  $d\ln k/dT = Q/RT^2$ , we may simplify the above expression in the following manner

$$(\partial x/\partial T)_\beta = n(1-x) \{\ln[1/(1-x)]\}^{n-1/n} \times k/\beta \{1 + \Delta T Q/RT^2\}. \quad (26)$$

By neglecting  $\Delta T Q/RT^2$ , or in other words, setting  $d\ln k/dT = 0$ , we may approximate Eq. (26) in the following manner

$$(\partial x/\partial T)_\beta \approx (1/\beta)(1-x) \{\ln[1/(1-x)]\}^{n-1/n} k. \quad (27)$$

Upon comparing this expression with Eq.(13), it emerges that

$$f(x) = (n-1)(1-x) \{\ln[1/(1-x)]\}^{(n-1)/n}. \quad (28)$$

It is clear that  $\Delta T Q/RT^2 \approx Q/RT$ , only if  $\Delta T = T-T_S$ , is set equal to  $T$ , for  $T \gg T_S$  in many cases. For most solid-state transformations,  $Q/RT$  is many times greater than one and hence the term  $1 + \Delta T Q/RT^2$  in Eq. (26) never equals one. Thus, in the strict sense, the non-isothermal version of the KJMA model as given by Eq. (24) for the transformed fraction cannot be reduced to a true isoconversional type kinetic equation (*cf.* Eq. 24). This point is brought into current discussion, because in many treatments of non-isothermal transformation kinetics employing KJMA scheme, the temperature independence of  $k$  is implicitly assumed, while evaluating  $n$ , the Avrami exponent [41]. It is obvious that no firm theoretical interpretation of  $n$  is possible under such circumstances, even if the theoretical appropriateness of the KJMA model is otherwise held valid for the transformation mechanism under consideration [21]. The papers of Kruger [42], Ruitenber *et al.* [43] and Liu, Sommer and Mittemeijer [44]

may be consulted for further familiarization on the finer aspects of non-isothermal form of KJMA expression. We only wish to reiterate that in the present study, Eq. (24) is employed purely as a simple empirical model, but with due regard to the temperature variation of  $k(T)$  in estimating  $n$ . A straightforward algebraic manipulation of Eq. (24) gives,

$$\{\ln[1/(1-x)]\}^{1/n} = k(T-T_S)/\beta. \quad (29)$$

Taking logarithm on both sides, we get the following bi-logarithmic expression

$$\ln\{(\ln[1/(1-x)]^{1/n})/(T-T_S)\} = \ln(k/\beta) \quad (30)$$

Substituting for  $k = k_o e^{-Q/RT}$ , we in turn recast this expression to get

$$\ln\{(\ln[1/(1-x)]^{1/n})/(T-T_S)\} = \ln(k_o/\beta) - Q/RT. \quad (31)$$

Knowing  $T_S$  and the fraction transformed as a function of temperature for a fixed scan rate  $\beta$ , the bi-logarithmic term on the left hand side may be computed for each temperature interval  $T-T_S$ , if appropriate value of  $n$  is known *a priori*. Plotting of this quantity against  $1/RT$ , enables the determination of  $Q$  from the slope and  $k_o$  from the intercept. Since  $n$  is unknown in the present case, we use Eq. (31) in a reverse manner. By substituting the value of  $Q$  as well as  $k_o$  obtained from the Kissinger method for example, we determine the optimal value of  $n$  that best fits the experimental data. It must be added that this method presupposes an accurate knowledge of  $T_S$ , the transformation start temperature under a fixed heating rate. In principle, one may also obtain the best-fit  $\{T_S, n\}$  pair through a full nonlinear optimization of the  $\{x_i, T\}$  data with known values of  $Q$ . This is somewhat involved and to keep things simple, it is preferred to use the experimental  $T_S$  temperatures in obtaining a first order estimate of  $n$ . It must be said that in the present study, only a restricted range of data pertaining to the range,  $0.25 \leq x \leq 0.75$  have been considered for the estimation of  $n$ . This is because,

the cumulative errors associated with the  $(T_i, x_i)$  data in low  $\alpha$  regime is rather large, that it resulted in poor convergence of simulated and experimental values of the composite quantity  $\ln\{(\ln[1/(1-x)]^{1/n})/(T-T_S)\}$ . Once a selection of the suitable data range has been made, the estimated values of  $n$  revealed little scatter for various extent of  $x_i$ .

#### 6.0. Physical meaning of $Q_{eff}$

One other important issue that is related to the kinetic deconvolution of thermal analysis data by so-called iso-conversional methods has to do with the meaning of effective activation energy parameter,  $Q_{eff}$ . In the theoretical development presented above as well as in many of the model free kinetic approaches to processing DTA/DSC transformation temperature versus scan rate data, no explicit mention of the microscopic origin of activation parameter is invoked. Sometimes, the isoconversional methods lead to physically unrealistic  $Q$  values, although excellent linearization of the scan rate dependence of transformation temperature is readily obtained. As an illustrative example, the Kissinger, Ozawa, Boswell and Starink linear plots obtained in the present study on RAFM steel, but yielding physically unrealistic  $Q$  values for the  $\alpha \rightarrow \gamma$  transformation is shown in **Fig. 4.9**. The reason for this discrepancy is not clear and certainly not apparent from any of the formal treatments of isoconversional methods. However, as argued in Mittemeijer's work, for transformations that are occurring rather close to equilibrium, the isoconversional methods often yield high  $Q$  values [49]. This is because of small values of  $\Delta G$  of phase transformation, when it is taking place at close to equilibrium transformation temperature. This results in generally higher  $Q$  reported for lower scan rates (see, **Fig. 4.9**). In our view, this arises from the conceptual inadequacy of isoconversional

methods. A solution to this problem is the use of physically based transformation model for eliciting the kinetic quantities.

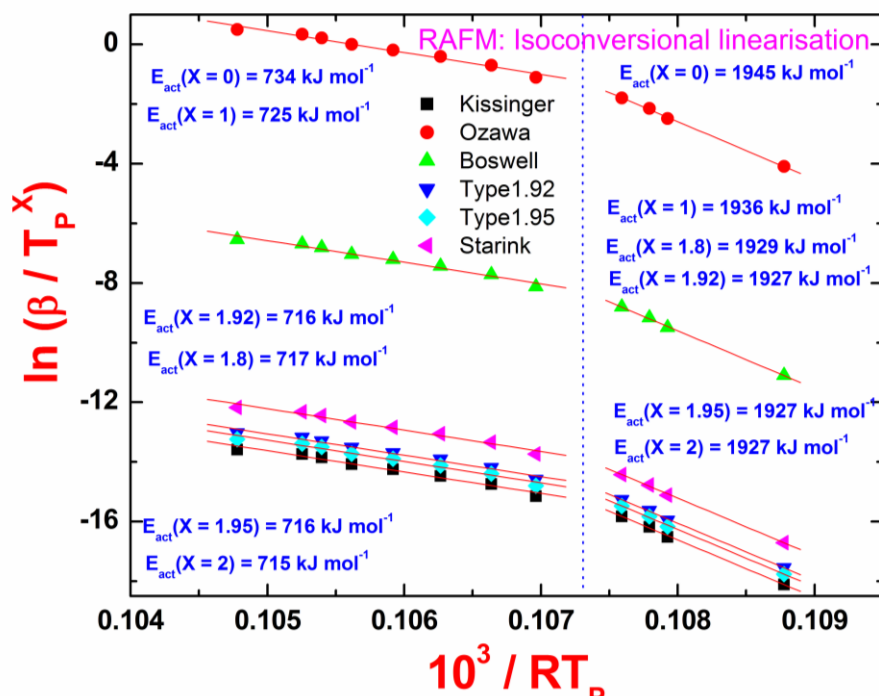


Fig. 4.9. Isoconversional linearization schemes yielding physically unrealistic Q values, for the  $\alpha \rightarrow \gamma$  transformation in RAFM steel

Although the discussion is centred around one representative or crude average of a time scale quantity  $\tau$ , which is nothing but  $\tau=1/k(T)$ , the inverse of rate constant, an attempt to derive  $\tau$  from a transparent physically based reasoning of the unit processes involved in the transformation process has not been made so far. This is the serious lacunae of the isoconversional and model free approaches to transformation kinetics, albeit quite useful as they prove to be in giving an empirical support to reaction kinetics. The reasoning of a justification for plausible values of Q, obtained *via*, an isoconversional formalism is better left to the latter development of what are known as modular models of transformation kinetics, a topic that is richly served by a series of papers from E. J. Mittemeijer, and F. Sommer's group [45-51]. In this approach,

discrete, tailorable models for treating the time and temperature dependence of both nucleation and growth rates are incorporated into the classical analytical description of diffusional transformation kinetics, pioneered by Kolmogorov, and Johnson Mehl and Avrami (KJMA).

In such treatments, a model based physical interpretation of both  $Q$  and  $n$ , *the overall transformation kinetics parameters* emerge in terms of energy barriers involved in the nucleation step and the activation energy involved in the diffusive propagation of transformation front. In actual practice, it is possible to do a robust analytical fit of the basic transformation data, such as  $\{X_t, \beta, \}$  or preferably, the normalised  $(\partial X/\partial t)_\beta$  transformation rate in terms of appropriate transformation modules, to obtain both temperature and transformation extent dependent  $Q$ , the activation energy values. This is the approach that is followed in this study for modelling the diffusional transformation kinetics of  $\alpha \rightarrow \gamma$  phase transformation that occurs in reduced activation ferritic-martensitic (RAFM) steel upon heating.

#### **7.0. DSC profile modelling**

A more appealing way of interpreting the transformation peak profiles obtained under both isothermal and nonisothermal conditions, is to adopt a suitable modular for KJMA model for direct profile modeling. Such an approach has been pioneered by Michelson and Dahms [52], which has since then been followed by many others [53]. The essential features of direct DSC profile fitting (actually suitably normalised one) goes as follows.

Assuming a site saturation nucleation situation, (which is the obvious starting point for a simple discussion,) that is all the nuclei are assumed to be present at the

start of the transformation and its number density remains invariant throughout, the volume fraction transformed,  $X_V$ , is given as

$$X_V = 1 - \exp(-CNr^n). \quad (32)$$

where  $r$  is the radius of the growing region,  $n$  is the Avrami exponent,  $C$  is a geometric constant, ( $=4\pi/3$  for spheres growing three dimensions;  $=1$  for unidirectional rod growth; in general,  $C = (4\pi/3)^{1/4-n}$ ) and  $N$  is the density of nuclei, i.e., the number of  $\gamma$ -austenite phase nuclei per unit volume. Since nucleation is not invoked in this model, the Avrami exponent  $n$  is exclusively a function of the growth dimensionality. The radius  $r$  can be rewritten as  $v \times t$ , where  $t$  is the transformation time and  $v$  is the growth velocity, given by

$$v = dr/dt = k \exp(-Q/RT). \quad (33)$$

$Q$  is the effective activation energy for the growth part and may be found by the Kissinger method, or any of the isoconversional equivalents.  $k$  is a preexponential rate constant. The growth velocity  $v$  is constant for any given temperature and is taken as independent of time for simplicity. The rate constant  $k = 1/\tau$ ; and hence may be related to a frequency  $\omega$  through the relation [52, 53].

$$\omega/k = (CN)^{1/n}. \quad (34)$$

The above relation follows from the basic isothermal form of the standard Avrami relation

$$X_V = 1 - \exp(-(t/\tau)^n). \quad (35)$$

Thus, the isothermal site saturation Avrami form is of the following type

$$X_V = 1 - \exp\{-\omega^n \exp(-nQ/RT)t^n\}. \quad (36)$$

In a more familiar form, Eq. (36) may be written as

$$X_V = 1 - \exp\{kNv^n t^n\}. \quad (37)$$

According to Michelson-Dahm model, if  $\phi$  is the heat flow recorded by DSC in  $\mu\text{V}$ , then it is related to  $dX_V/dt$ , the rate of transformation by the following expression [52],

$$\phi = \Delta H_{tr} \times dX_V/dt. \quad (38)$$

$\Delta H_{tr}$  is the total transformation enthalpy, measured directly as the total peak area after base line refinement. For anisothermal transformations, a similar expression incorporating  $\beta = dT/dt$ , the heating rate may be written.

$$\phi = \Delta H_{tr} \times (dX_V/dT) \times \beta \quad (39)$$

The above expression is germane to all profile modeling schemes; only the term  $(dX_V/dT)$  assumes suitable form depending on the details of nucleation and growth conditions. Thus, for a simple site saturation type Avrami, with growth controlled transformation, (many satisfy this requirement: polymorphic transitions occurring in fine grained material, grain boundary precipitation etc),  $(dX_V/dT)$  can be obtained by differentiating Eq. (32) with time. Notice that in differentiating,  $N$  is kept constant; if a differentiable  $N = N(t)$  function is chosen, then non site saturation case can also be simulated. In the final analysis, we get,

$$(dX_V/dt) = nCNr^{n-1} (dr/dt) \exp(-CNr^n). \quad (40)$$

$$(dX_V/dT) = nCNr^{n-1} (dr/dT) \exp(-CNr^n). \quad (41)$$

From above, it emerges that for isothermal case

$$\phi = \Delta H_{tr} \times dX_V/dt.$$

$$\phi = \Delta H_{tr} \times n\omega^n t^{n-1} \exp(-nQ/RT) \times \exp[-\omega^n \exp(-nQ/RT) t^n]. \quad (42)$$

And for non isothermal case, growth velocity,  $v$

$$v = dr/dT = k/\beta \exp(-Q/RT). \quad (43)$$

Integrating this,

$$\int dr = \int k/\beta \exp(-Q/RT) dT. \quad (44)$$

$r(t)$  can be determined. This integral cannot be solved exactly, but good approximations exist for this purpose. Skipping these mathematical details, one obtains,

$$\phi = \Delta H_{tr} \beta n (\omega/\beta)^n (RT^2/Q)^{n-1} \exp(-nQ/RT) \times \exp\{-(\omega/\beta)^n (RT^2/Q)^n \exp(-nQ/RT)\}. \quad (45)$$

Eq. (45) can be fitted to measured  $\phi$  DSC microvolt output for fixed  $\beta$  (K/s), for obtaining  $\omega$ , the frequency factor and  $n$ , the growth exponent.  $Q$  is estimated before hand from isoconversional or the Kissinger method.

It is not always the case that Kissinger or Kissinger like method gives plausible values of  $Q$ , (see., Ref. 49). Instead, one can assume some plausible values of  $Q$ , as equals to the bulk or grain boundary diffusion activation barrier for the slow diffusing species. This trial value can be refined as matter of optimizing collectively all the fit parameters.

In this simple scheme,  $k$ , the rate constant for growth velocity is related to constant  $\omega$ ; in reality however, growth velocity may be a function of time and temperature. The temperature dependence can be incorporated as,

$$k = a \times \omega \exp(\Delta S/R) (1 - \exp(-\Delta G/RT)). \quad (46)$$

$a$  = lattice parameter or jump distance,  $\Delta S$  is the entropy part of activation free energy  $\Delta G$ .  $\Delta G$  is often approximated by Eq, (1).

$$\Delta^\circ G(T) \approx \Delta^\circ H_{tr} \Delta T / T_{tr}. \quad (47)$$

In summary, by incorporating appropriate degree of sophistication in describing  $dX_v/dT$ , the profile fitting can be done on a parametric study of  $Q$ ,  $n$  etc. In place of calorimetry, the transformation extent can also be obtained from metallography,

dilatometry and high temperature lattice expansion *etc.* Further information on DSC profile modeling may be obtained by consulting the papers of Michaelson and Dahms [52] and Berry & Barmak [53].

### 8.0. Martensitic Transformation: Koistinen- Marburger Relation

The kinetics of martensitic transformation is modelled after the popular relation proposed by Koistinen and Marburger on empirical grounds [54]. In what follows, we use this relation in a slightly modified form, in order to incorporate explicitly the cooling rate in it.

$$X(T) = \exp \{-(b/\beta) (M_s-T)^n\}. \quad (48)$$

Here  $X(T)$  is the fraction of austenite remaining untransformed at each temperature. A slight recasting of this expression yields,

$$1-y(T) = \exp \{-(b/\beta) (M_s-T)^n\}. \quad (49)$$

Or,

$$y(T) = 1-\exp \{-(b/\beta)(M_s-T)^n\}. \quad (50)$$

$y(T)$  is the fraction of martensite formed at temperature  $T$ . In the above expression,  $\beta$  is the cooling rate in  $K \text{ sec}^{-1}$ ,  $M_s$  is the onset temperature in Kelvin and  $n$  is a constant. By setting  $(b/\beta)^n=b$ , a simple two parameter description of *martensitic* transformation after the well-known empirical framework of Koistinen and Marburger (K-M) is readily obtained [54]. It must be added that in the original K-M prescription,  $n$  is taken to be unity [54]; but we allowed it to vary here in order to get better numerical agreement. The results of fitting of the experimental data obtained on RAFM steel using *Eq. (50)* will be discussed later. However, it is useful to note that just as in the case of  $\alpha$ -ferrite  $\rightarrow \gamma$ -austenite, diffusional transformation wherein, the value of transformation rate constant,  $k$  is dependent on  $\beta$ , the heating rate, (variation of  $k/\beta$

with  $\beta$  assumes a power law), the values for  $b'$  also exhibit an increase with increasing cooling rate. Since Eq. (48-50) is empirical in origin, it is not possible to provide a physicochemical basis for the cooling rate variation of parameter  $b$ . The negative value of  $n$  arises from the fact that with positive values for the argument  $(T_s - T)$ , the transformation extent  $X(T)$  increases with decreasing temperature.

The K-M equation was justified by Magee on phenomenological grounds in the following manner [55]. Magee assumed that in a finite temperature drop  $dT$ , the number of new martensitic plates per unit volume of austenite  $dN$ , is proportional to the increase in chemical driving force,  $\Delta G_V^{\gamma \rightarrow \alpha}$ . That is,

$$dN = k_m \times d(\Delta G_V^{\gamma \rightarrow \alpha}). \quad (51)$$

$k_m$  is the proportionality constant for martensite transformation. If  $dy$  is the corresponding change in volume fraction of martensite in this temperature interval  $dT$ , then,

$$dy = V dN v. \quad (52)$$

$V$ , is the average volume of the newly formed plates, and  $dNv$  is the change in the number of plates per unit volume. Setting  $dNv/dN = 1-y$ , we get,

$$\begin{aligned} dy &= V dN v = V(1-y)dN. \\ &= V(1-y) k_m d(\Delta G_V^{\gamma \rightarrow \alpha}). \\ &= V(1-y) k_m \{ [d(\Delta G_V^{\gamma \rightarrow \alpha})/dT] \times dT \}, \\ &= V(1-y) k_m \Delta S_V^{\gamma \rightarrow \alpha} (\Delta T). \end{aligned} \quad (53)$$

In Eq. (53), we have used,  $d(\Delta G_V^{\gamma \rightarrow \alpha})/dT = \Delta S_V^{\gamma \rightarrow \alpha}$  the entropy of transformation.

Thus, in final analysis

$$\int dy/1-y = [V k \Delta S_V^{\gamma \rightarrow \alpha} \Delta T. \quad (54)$$

Integration by variable separable procedure, yields with the assumption that  $V k_m \Delta S_{\gamma \rightarrow \alpha}$  is a constant and that  $dT = \Delta T = M_s - M_f$ , the temperature interval between martensite start and finish temperatures. Thus,

$$\ln(1-y) = V k_m \Delta S_{\gamma \rightarrow \alpha} [M_s - M_f] \quad (55)$$

Thus, we get the K-M relation, with the tacit identification that  $V k_m \Delta S_{\gamma \rightarrow \alpha} = b$ , the K-M constant in the empirical equation. The effect of altering  $\beta$ , the cooling rate has to do with the constant  $k_m$ , since  $\Delta S_{\gamma \rightarrow \alpha}$  and  $V$  are independent of thermal history. But this aspect is not probed in this study any further.

## 9.0. Summary

A brief operative review of basic aspects of phase transformation kinetics has been presented in this chapter. Importance is given to highlighting less common aspects of interpreting the diffusional transformation kinetics by standard isoconversional procedures. The heating or cooling rate dependence of transformation kinetics, and its incorporation in an analytical treatment of dynamic calorimetry data have also been dealt with in this chapter. In addition, the role of profile modelling in terms of modular transformation kinetics, along the lines of KJMA formalism, has been highlighted. Finally, a very brief description of Koistinen-Marburger relation for describing the temperature dependent progress of martensite formation is also presented.

### References

1. F. Rhines, *Phase Diagrams in metallurgy, their development and applications*, McGraw Hill, NY (1951).
2. M. Hillert, *Phase equilibrium, phase diagrams and phase transformations: their thermodynamic basis*, Cambridge University Press, Cambridge (1998).
3. A. K. Jena and M. C. Chaturvedi, *Phase transformations in Materials*, Prentice-Hall, New Jersey (1992), p.414.
4. D. Turnbull, in: *Solid state physics: Advances in research and applications*, edited by F. Seitz and D. Turnbull, vol. 3, Academic Press, NY (1956), p. 226.
5. D. A. Porter and K. E. Easterling, *Phase transformations in metals and alloys*, Van Nostrand Reinhold, Workingham, (1981).
6. E. A. Wilson, *Met. Sci.*, **18** (1984) 471.
7. J. J. Rechten and R. D. Nelson, *Metall. Trans.*, **4A** (1973) 2755.
8. J. Burke and P. H. Dixon, *J. Nucl. Mater.*, **7** (1962) 38.
9. Arun Kumar Rai, S. Raju, B. Jeya Ganesh, E. Mohandas, S. Sudha and V. Ganesan, *J. Nucl. Mater.*, **383** (2009) 215.
10. M. J. Starink, *Thermochimica acta*, **404** (2003) 163.
11. F. Liu, F. Sommer, C. Bos and E. J. Mittemeijer, *Int. Mater. Rev.*, **52** (2007) 193.
12. B. Ya. Lyubov, *Kinetic theory of phase transformations*, Amerind Pub. Co., New Delhi (1978).
13. J. W. Christian, *The theory of transformations in metals and alloys*, 2<sup>nd</sup> edition, Pergamon Press, Oxford (1975).
14. T. Reti, M. Gergely and P. Tardy, *Mater. Sci. Tech.*, **3** (1987) 365.
15. M. T. Lusk and H. -J. Jou, *Metall. Trans.*, **28A** (1997) 287.

16. J. B. Leblond, G. Mottet, J. Devaux and J –C. Devaux, *Mater. Sci. Tech.*, **1** (1985) 815.
17. E. Scheil, *Archiv. fur das Eisenhüttenwesen*, **8** (1935) 565; as cited in Ref. 25.
18. P. Kruger, *J. Phys. Chem. Solids*, **54** (1993) 1549.
19. J. S. Ye, H. B. Chang and T. Y. Hsu, *Metall. Trans.*, **34 A** (2003) 1259.
20. R. G. Kamat, E. B. Hawbolt, L. C. Brown and J. K. Brimacombe, *Metall. Trans.*, **23 A** (1992) 2469.
21. F. L. Cumbreira and F. Sanchez Bajo, *Thermochimica acta*, **266** (1995) 315.
22. L. V. Meisel and P. J. Coate, *Acta Metall.*, **31** (1983) 1053.
23. J. Vasquez, C. Wagner, P. Villarez and R. Jieminez - Garay, *Acta mater.*, **44** (1996) 4807.
24. M. T. Todinov, *Acta mater.*, **48** (2000) 4217.
25. P. R. Rios, *Acta mater.*, **53** (2005) 4893.
26. J. Prabha, *Unpublished research* (2008).
27. G. Ruitenbergh, E. Woldt and A. K. Petford-Long, *Thermochimica acta*, **378** (2001) 97.
28. J. Baram and V. Erukhimovitch, *Thermochimica acta*, **291** (1997) 81.
29. H. J. Borchardt and F. Daniels, *J. Amer. Chem. Soc.*, **79** (1957) 41.
30. J.H. Flinn, *Thermochimica Acta*, **300** (1997) 83.
31. S. Vyazovkin and V. Goryachko, *Thermochim. Acta*, **194** (1992) 221.
32. M. J. Starink, *Int. Mater. Rev.*, **49**(2004) 191-226.
33. T. Ozawa, *J. Thermal analysis*, **2** (1970) 301.
34. P. G. Boswell, *J. Thermal Analysis*, **18** (1980) 353.
35. M. J. Starink, *Thermochim. Acta*, **404** (2003) 163-195.
36. H. L. Friedman, *J. Ploymer Sci.*, C **6** (1964) 183-195 (as cited in Ref. 32).

37. B. Roduit, in : *Advanced Kinetics and Technology Solutions, AKTS – Thermokinetics software*: <http://www.akts.com>.
38. F. L. Cumbreira and F. Sanchez- Bajo, *Thermochim. Acta*, **266** (1995) 315-330.
39. J. W. Christian, *Theory of Phase Transformation in Metals and Alloys*, Part I, (2<sup>nd</sup> edition) Pergamon, Oxford (1971).
40. E. J. Mittemeijer, *J. Mater. Sci.*, **27** (1992) 3977.
41. J. M. Criado and A. Ortega, *Acta Metall.*, **35** (1987) 1715-1721.
42. P. Kruger, *J. Phys. Chem. Solids*, **54** (1993) 1549.
43. G. Ruitenberg, E. Woldt and A. K. Petford-Long, *Thermochim Acta*, **378** (2001) 97.
44. F. Liu, F. Sommer, and E. J. Mittemeijer, *J. Mater. Sci.*, **39** (2004) 1621.
45. E. J. Mittemeijer, *J. Mater. Sci.* **27** (1992) 3977.
46. A. T. W. Kempen, F. Sommer and E. J. Mittemeijer, *J. Mater. Sci.* **37** (2002) 1321
47. F. Liu, F. Sommer, and E.J. Mittemeijer, *J. Mater. Sci.* **39** (2004) 1621.
48. F. Liu, C. Yang, G. Yang and Y. Zhou. *Acta Mater.* **55** (2007) 5255.
49. W. Baumann, A. Lieneweber and E. J. Mittemeijer, *J. Mat. Sci.*, **19** (2011) 526.
50. E. J. Mittemeijer and F. Sommer, *Z. Metallkd.* **93** (2002) 352.
51. F. Liu, F. Sommer and E. J. Mittemeijer, *Acta Mater.* **52**, (2004) 3207.
52. C. Michaelsen and M. Dahms, *Thermochim. Acta*, **288** (1996) 217.
53. D. C. Berry and K. Barmak, *J. Appl. Phys.*, **101** (2007) 014905.
54. D. P. Koistinen and R. E. Marburger, *Acta Metall.*, **7** (1959) 59.
55. C. L. Magee, in: *Phase Transformations*, ASM Metals Park, OH, (1968), p.118.

## High Temperature Drop Calorimetry Measurements of Enthalpy and Heat Capacity Estimation of Reduced Activation Ferritic-Martensitic Steel

### **1.0. Introduction: Necessity to generate Thermochemical Data on RAFM steel**

It is well-known that the availability of reliable and critically assessed thermodynamic data is essential for facilitating the knowledge driven approach to alloy-design [1]. There is at present an urgent need for generating accurate high temperature thermochemical and thermophysical property information on many advanced engineering alloys that are slated for applications in conventional and emerging power generation options [2]. The profitable understanding of factors that govern ultimately the materials selection and component design depends to a large extent on our ability to successfully model and simulate the degradation mechanisms that the chosen candidate material is expected to experience during its normal service or under hypothetical accident conditions [1]. While modelling of materials performance is veritably a daunting task if viewed in its entirety of scope and perspective, it is nevertheless useful to address this issue in a compartmentalised manner. This latter modular approach advocates the deployment of simple phenomenological models that are valid at different length scales, with the output stemming from each one of the modules serving as the input needed for exploring the problem at the next higher level of sophistication. In the area of such hierarchical, multi-tiered approach to materials modelling, there has been a sustained effort since the last decade towards developing successful thermodynamic and kinetics protocols which aim at rationalizing and predicting phase and microstructural stability of advanced engineering materials at the level of classical thermodynamics and

continuum mechanics. In such an approach, it is needless to over emphasize the pivotal role played by reliable material property data set [1, 2].

As discussed elsewhere in this thesis report, high chromium ferritic-martensitic steels containing about 9-10 wt.% Cr with specifically tailored composition limits for minor alloying additions like Mo, Nb, V, Mn, Ni, Si, N, S, P etc., are of interest in both conventional and nuclear power generation applications [3] owing to their attractive combination of physical and mechanical properties, compatibility with liquid metal coolant, resistance to swelling against fast neutrons and lower cost [4]. Despite the fact that there have been numerous studies devoted to exploring the microstructure- mechanical property and performance correlation of these materials as a function of several processing variables including melting practices [5-14], *there is a relative paucity of experimental data on basic thermodynamic and thermophysical properties*. It is in view of this situation that we have undertaken in the present study to measure the temperature variation of enthalpy increment of a low-carbon, nuclear grade 9 wt.% Cr- steel containing controlled amounts of W and Ta. The composition of this reduced activation ferritic–martensitic (RAFM) steel slated for possible application in fusion reactors [3,15] has been designed to minimize the induced radioactivity hazard arising from elements like Mo, Nb, N, Cu, Co, Al etc.,. This is realized by substituting these elements with the comparatively more benign homologous replacements such as W, Ta, and V [15, 16].

The present chapter deals with inverse drop calorimetry study of RAFM steel. Accurate estimates enthalpy increment and heat capacity as a function of temperature at close to thermodynamic equilibrium conditions are gathered from this study [17]. The results will be supplemented by differential scanning calorimetry investigation, which is described in the following chapter.

### 1.1. Drop versus Dynamic Calorimetry Experiments

It is generally held that the static or isothermal drop calorimetry measurements give more accurate values of enthalpy under equilibrium thermodynamic conditions, while in the case of dynamic or differential scanning calorimetry studies, the experiments by design yield data that are obtained under varying non-equilibrium conditions [17]. As a consequence, the dynamic calorimetry based transformation temperature and transformation enthalpy data require appropriate normalizing to account for finite heating/cooling rate effects [18]. In view of this fact, one of the objectives of the present investigation is to make a comparative assessment equilibrium transformation thermodynamic data with that obtained using scanning calorimetry technique [16]. The thermodynamic quantities investigated include, temperature variation of enthalpy increment and hence specific heat, the on-heating transformation temperatures besides an estimate of the latent heat associated with the  $\alpha$ -ferrite  $\rightarrow$   $\gamma$ -austenite transformation. The relevant experimental details of drop calorimetry are already discussed in chapter 2.

### 2.0. Material and Experimental Details

The composition of RAFM is already listed in previous chapters. The as melted ingot is processed by hot forging and hot rolling into plates with a finish temperature of about 1323 K (1050°C). In the present study, the steel is given an additional solution heat treatment at 1523 K (1250°C) for about 30 minutes followed by quenching to room temperature. This solutionising temperature is somewhat higher than the usually employed one namely 1323 K (1050°C), since the presence of highly cohesive Ta and W containing carbides necessitated a higher solutionising temperature for their complete dissolution in the high temperature  $\gamma$ -austenite phase. But it must be added that depending on the actual duration of this solutionising

treatment a small quantity of  $\delta$ -ferrite phase is also found in some samples [16; see chapter 4].

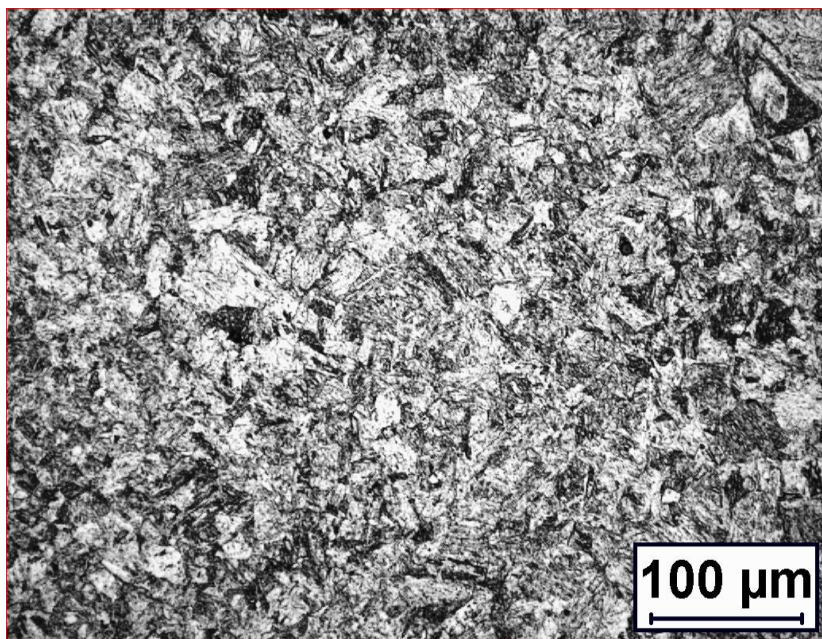


Fig. 5.1. The optical micrograph of the reduced activation steel in the quenched condition showing lath martensite

The optical micrograph of the typical solution-treated and water quenched sample is shown in **Fig. 5.1**. The copious presence of fine lath martensite is readily apparent. The average microhardness of the martensite microstructure measured with 50 & 100 g load is found to vary between 470 and 510 in the Vickers scale. The room temperature ( $\sim 293$  K) lattice parameter of the  $\alpha$ -ferrite phase, determined by x-ray diffraction (Cu- $K_{\alpha}$ ) is found to be  $0.2876 \pm 0.003$  nm. The bulk density of the sample, as determined using the standard immersion method is found to be  $7.67 \times 10^3$  Kg m<sup>-3</sup>. Using this bulk density value and the x-ray lattice parameter, the average atomic weight of this steel is estimated to be  $0.0548(5)$  Kg mol<sup>-1</sup>.

### 2.1. Drop Calorimetry: Specific Details

The inverse drop calorimetry measurements were performed using *Setaram multi* HTC 96<sup>®</sup> calorimeter in the drop mode. The description of the equipment, calibration

of heat flow into effective enthalpy and data analysis procedures have been presented in detail in chapter 3 and also in our publications [19, 20]. A typical data collection time of about 20 to 30 minutes is maintained in the present study. Considering the small mass ( $50$  to  $70 \pm 0.1$  mg) of the sample, this time is considered adequate to ensure the attainment of thermal equilibrium in the experiment. Highly pure  $\alpha$ -Al<sub>2</sub>O<sub>3</sub> pellet supplied by *Setaram* was used as the primary calibration standard. In addition, drop measurements were also made on OFHC grade copper samples [21], whose measured enthalpy increment values agreed to better than 2% with the reported literature estimates [22].

A total of three experimental schedules covering the temperature range 400 to 1273 K are conducted under highly pure argon (Iolar grade 2) atmosphere. Each schedule consists of a series of drop experiments performed at prefixed discrete temperature steps (approximately 25 K) so that the entire region of stability of the  $\alpha$ -ferrite phase, besides some limited incursion into the  $\gamma$ -austenite domain are covered in the present study. In addition, a few more runs were performed at select temperature intervals especially in the neighborhood of the transformation region, to assess the extent of reproducibility and the typical scatter of enthalpy increment data. Apart from a few stray data points, which are identified to be clear outsiders to the otherwise general trend, all other data points are used in the final analysis.

## 2.2. Accuracy of Data Measured in Drop Calorimetry

Before proceeding with the presentation of the results, it is rather useful to bring into discussion some pertinent facts associated with the measurement of transformation temperature and enthalpy data obtained using drop calorimetry technique. In the first, it must be reiterated that the technique of drop calorimetry by virtue of its experimental design offers only discrete enthalpy increment data points at

preselected temperature intervals. A continuous enthalpy curve as a function of temperature is not obtained by this technique. Hence, it is very likely that the exact or actual onset temperature of the phase transformation is either missed out or only crudely measured, if the choice of the temperature interval is kept rather large. In the present study, we have ameliorated this problem to some extent by maintaining approximately 25 K as the typical temperature interval between two consecutive drops. Further, by beginning each successive experimental run with different starting temperatures, say from 400 K in the first run and from 425 K in the next one etc., we could eventually gather multiple data points over the entire temperature range of interest with closer than 25 K temperature step. Thus, notwithstanding the fact that *discontinuous* drop calorimetry measurements yield only an approximate estimate of phase transformation temperature or domain, it is yet possible to detect and trace the effect of phase change on enthalpy in a definite manner using drop technique.

In addition, we may also note that the extent of temperature stability and the precision in each drop experiment are quite good in carefully conducted drop calorimetry studies. This is made possible by adopting a slow heating rate ( $5 \text{ K min}^{-1}$ ) to reach the set temperature and further by ensuring a fairly long resident time at each isothermal holding step, we could achieve a temperature stability of  $\pm 0.1 \text{ K}$  under a steady high pure argon (Iolar grade 2) flow. This level of thermal stability is vital to ensuring a high level of precision or reproducibility in temperature measurement.

The other important technical issue concerning drop calorimetry data is the unavoidable scatter in the enthalpy values, especially in the high temperature transformation range. It is our general experience, that in properly optimized runs, different data points measured at nominally the same temperature do not reveal a scatter that is larger than  $\pm 5\%$  of the measured enthalpy increment value itself.

Unfortunately, in some of the drops the scatter observed is somewhat more especially at the transformation region where successively dropped samples did *not* experience the same extent of phase transformation. This problem is ubiquitous to steel samples in which ensuring a very high level of sample homogeneity is rather difficult. Although, we could not do many drop measurements at each temperature, we did indeed carry out as many as three repeat runs at select temperatures with fresh samples and with maintaining almost similar, if not exactly identical experimental conditions. Only those data points which were clearly within the expected and acceptable scatter range of enthalpy increment values are taken into consideration. A few data points that deviated by more than 5 % scatter band of the enthalpy increment value due to various reasons like, the incomplete phase transformation and the dropped samples not fully penetrating into the bed or occasionally due to some mild oxidation etc., were disregarded. These data points were not considered for the final analytical treatment as well. Based on our previous experience obtained with stainless steel and pure copper samples [21], such procedure yielded quite satisfactory results. The transformation temperature reproducibility achieved in the three repeated drop experiments is in the range 2-5 K (5 K is the maximum observed), and this has been convincingly established from the measurements done using pure iron (Aldrich Chemicals, less than 80 mass ppm of combined impurities).

It can be argued that in case of high alloy steel with comparatively a poor thermal diffusivity, the scatter in the measured transformation temperature data can in principle be larger than that observed in case of pure iron. This may be so, since  $\alpha \rightarrow \gamma$  transformation kinetics in steel are expected to be somewhat sluggish due to reasons of slow solute diffusion. Thus, even for samples of the same mass, it would take longer time to complete the phase change in steels as compared to pure iron. This

point assumes considerable significance, if the  $\Delta T-t$  data collection time is kept short, since in which case the full transformation enthalpy would not be recorded. Strictly speaking, there is no fool-proof means of ascertaining this uncertainty in drop calorimetry measurements for a complex material like RAFM steel. However, it is yet possible that a credible estimate of the transformation temperature and transformation enthalpy can still be made by fixing an upper bound for the error bar based on experience obtained in measuring the transformation temperature of iron with 80 mass ppm carbon alloy. Based on this datum, we have assumed in the present study a maximum uncertainty of  $\pm 5$  K in reporting transformation temperature values. We hasten to add that this should not be confused with the error associated with temperature measurement using Pt(10%Rh)/Pt thermocouple, which is estimated to be about  $\pm 1$  K. With this background information, we shall next enumerate the different features of the enthalpy increment versus temperature curve.

### 3.0. Results

#### 3.1. Enthalpy increment versus temperature data

In **Fig. 5.2**, the measured enthalpy increment ( $H_T - H_{298}$ ) values are plotted with respect to temperature,  $T$ . In order to avoid undue clutter arising from many very closely spaced data points, only the data corresponding to two typical runs (filled squares and circles) are shown in the figure. The smooth line connecting the data points serves to delineate the observed trend and certain distinct features of the enthalpy–temperature curve. In **Table 5.1**, the experimental enthalpy increment data are listed for select temperature intervals. A quick perusal of **Fig. 5.2** reveals that starting from 400 K onwards enthalpy exhibits a steady almost a linear increase up to about 793 K. From this point onward, the enthalpy increment curve exhibits a distinct inflection with subsequent onset of a non linear behaviour. The dotted line emanating

from 793 K is drawn to indicate the probable extrapolated behaviour of enthalpy for the hypothetical case when the microstructure of the ferritic steel is assumed to remain unchanged during continued heating. In addition to this change of slope at 793 K, the presence of some other features in an otherwise smoothly increasing character of enthalpy is also clearly noticed in **Fig. 5.2**. These points are marked by arrows in **Fig. 5.2**.

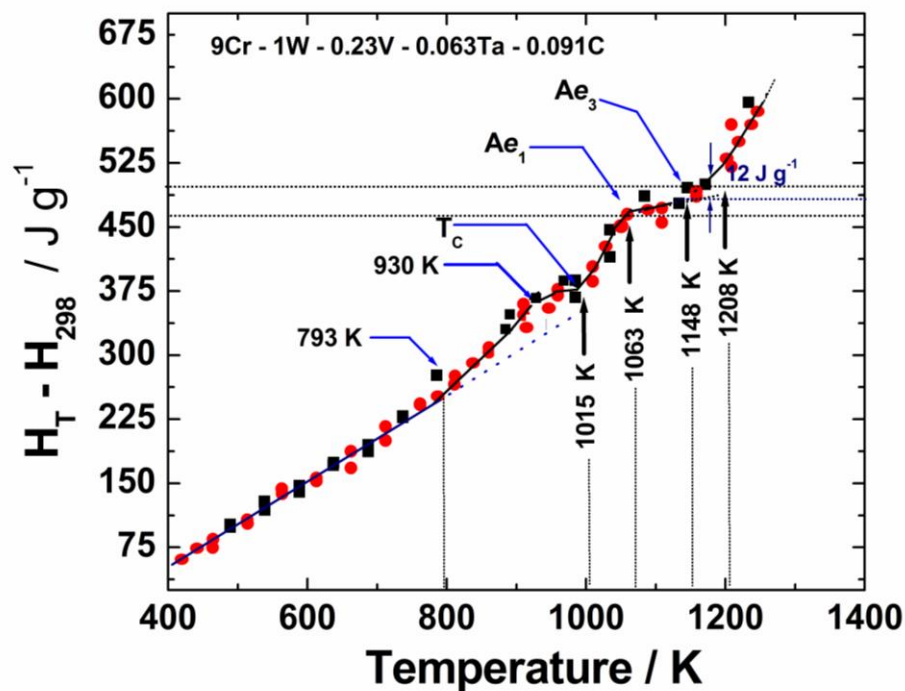


Fig. 5.2. The temperature variation of the enthalpy increment values for the RAFM steel is graphically portrayed. The line through the points is guide to the eye only. Note the distinct inflections marked by arrows that characterize the onset of various phase changes. The dotted line at 793 K refers to the extrapolated linear behaviour of the ferrite phase, if no microstructure changes accompany the heating process. The dotted line drawn from  $Ae_1$  is the empirically extrapolated variation of the enthalpy sum of ferrite and austenite two phase mixture. Refer to text for details

Interpreting these inflections in the enthalpy–temperature curve in the light of our findings on this steel using dynamic calorimetry [Chapter 6, See also, Ref. 16], it can be said that these inflections or plateau like characteristics in the enthalpy curve are

indicative of the occurrence of phase transformations as they are also accompanied by finite changes in the enthalpy content. These are discussed in the following section.

**Table 5.1.** Listing of the experimental enthalpy increment  $\Delta^{\circ}H = H_T - H_{298}$  values for the  $\alpha$ -ferrite phase obtained in the present study. The data are given only up to about 1000 K only. For comparison, the values obtained by fitting the experimental data to *Eq. (2)* and the percentage deviation of the fit values from experimental estimates are also presented. The temperature and enthalpy values are rounded off to one decimal point.

Temperature (K)	Experimental	Fit	Error (%)	Temperature (K)	Experimental	Fit	Error (%)
	Enthalpy Data (J g <sup>-1</sup> )	Enthalpy Data (J g <sup>-1</sup> )			Enthalpy data (J g <sup>-1</sup> )	Enthalpy data (J g <sup>-1</sup> )	
464.1	77.2	74.8	-3.18	736.8	228.2	226.9	-0.55
464.3	77.3	84.6	8.68	761.6	242.1	243.0	0.35
489.3	90.9	101.7	10.67	761.9	242.3	241.9	-0.15
489.4	90.9	98.5	7.66	785.9	255.9	276.3	7.39
513.8	104.3	107.4	2.84	786.1	256.0	229.8	11.4
513.9	104.3	102.8	-1.48	812.0	271.1	275.5	1.62
538.7	118.1	118.6	0.440	811.0	270.5	265.8	-1.74
538.7	118.1	128.7	8.28	835.8	285.1	315.7	9.68
563.4	131.8	143.7	8.24	835.9	285.2	256.4	11.24
563.5	131.9	137.7	4.24	860.4	300.2	308.8	2.80
588.4	145.7	147.1	0.95	860.5	300.2	303.3	1.03
588.5	145.8	139.7	-4.36	885.4	315.9	296.7	-6.44
612.9	159.4	152.7	-4.36	885.5	316.0	302.0	-4.61
613.0	159.4	156.2	-2.06	910.2	332.2	347.2	4.32
637.3	172.9	171.2	-1.04	910.2	332.2	359.9	7.71
637.7	173.1	174.0	0.49	935.1	349.3	336.0	-3.95
662.5	186.9	187.4	0.30	935.2	349.4	395.1	11.58
662.5	187.0	167.8	11.39	959.5	367.1	377.0	2.64
687.2	200.6	195.0	-2.89	959.6	367.1	369.9	0.77
687.2	200.6	186.9	-7.31	984.7	386.4	387.7	0.33
712.1	214.4	200.0	-7.23	984.8	386.5	367.4	-5.19
712.3	214.5	216.5	0.92	1009.3	406.6	403.8	-0.69

736.8          228.2          228.5          0.12          1009.3          406.6          386.5          -5.20

### 3.2. On-heating phase changes as reflected by the enthalpy – temperature curve

Starting from 400 K, the first major deviation from linearity is noticed around 793 K (520 °C). Since the starting microstructure in the quenched condition is one of lath martensite (*Fig. 5.1*) with high dislocation density, this marked deviation from the linear enthalpy change is taken to be associated with the possible thermally activated relaxation of the *strained* martensite substructure. The available literature on the tempering physical metallurgy of 9Cr-steels supports this view point [8]. With further increase in temperature, this martensite relaxation is followed by the occurrence of a gentle plateau at around 930 K (657 °C). Since the martensite in low carbon ( $\leq 0.1 \text{ wt.}\%$ ) steel is basically one of *bcc*-ferrite that is supersaturated with carbon and further the temperature of 930 K (657 °C) is sufficient enough to bring about appreciable mobility of carbon atoms in the  $\alpha$ -ferrite phase, it is possible that this second feature of the enthalpy curve is associated with the precipitation of  $M_{23}C_6$  or  $M_7C_3$  type carbides on prior austenite and inter - lath boundaries [8,23]. Thus, we attribute this second inflection feature in **Fig. 5.2** to carbide precipitation event.

Subsequent to carbide precipitation, the enthalpy rises steeply for a while, before exhibiting another cusp at about 1015 (742 °C). Judging by our previous DSC results [16], this temperature corresponds to the Curie point  $T_C$  which marks the onset of the ferromagnetic to paramagnetic transition in the  $\alpha$ -ferrite phase. The cusp at  $T_C$  is characteristic of only a small change in enthalpy, and hence is not reflected sharply by present drop measurements. The magnetic transformation is closely followed by another region, which persists up to 1063 K (798 °C). In fact, in the region bounded by 1063 to 1148 K (798-875 °C),  $\Delta^0H$  changes in a steady fashion. The lower end of

this range stands for the lower critical temperature designated as  $Ae_1$  in **Fig. 5.2**. This temperature marks the onset of  $\gamma$ -austenite formation from  $\alpha$ -ferrite + carbide mixture upon heating. The other temperature designated as  $Ae_3$  stands for the upper critical temperature which signifies supposedly the completion of austenite formation reaction. The region enclosed by  $Ae_1$  and  $Ae_3$  thus represents the  $\alpha$ -ferrite + carbides  $\rightarrow \gamma$ -austenite three phase inter-critical region [24]. Immediately after  $Ae_3$ , the enthalpy varies in an irregular manner for some small temperature interval, but from about 1208 K (935 °C) onwards, it again registers a steadily increasing trend that is characteristic of the  $\gamma$ -austenite phase. This latter onset temperature varied somewhat among different experimental runs and in the present study it ranges from 1208-1253 K (935-980°C). This temperature is suggestive of the possible realization of homogeneous austenite following complete carbide dissolution in the high temperature austenite [19]. It must be recalled that in high alloy steels during continuous heating, the alloy carbide dissolution does not necessarily go to completion immediately following the completion of austenite reaction at  $Ae_3$ . The sluggish nature of carbide dissolution requires some small superheating above  $Ae_3$ , to facilitate the realization of homogeneous austenite [25].

### 3.3. Energetics of $\alpha$ -ferrite + carbide $\rightarrow \gamma$ -austenite phase transformation

As discussed in the previous section and also brought out in our recent DSC study [16], the  $\alpha \rightarrow \gamma$  phase change takes place in the temperature domain  $Ae_1 \leq T \leq Ae_3$ . Further, as seen in **Fig.5.2**, the enthalpy also varies in a steady manner in this temperature interval. Since austenite formation is a nucleation and growth process, which involves a temperature dependent change in both composition and phase fraction of the respective constituents, a measurable heat effect follows as a consequence. Stating this in another manner, the observed total enthalpy in the  $Ae_1$ -

$Ae_3$  domain derives both from the change in specific heat of the constituents as a function of temperature as well as from the enthalpy change ( $\Delta^{\circ}H^{\alpha \rightarrow \gamma}$ ) associated with the  $\alpha \rightarrow \gamma$  phase transformation. This point has been amply elaborated upon in our previous drop calorimetry studies on plain 9Cr-steels [19]. Hence avoiding the repetition of a detailed explanation, we may write for  $H_T$ , the total enthalpy in the phase transformation regime ( $Ae_1 \leq T \leq Ae_3$ ), the following expression,

$$H_T = H_0 + \int \{ (x_{ferrite} C_{P,ferrite}) + (x_{carbide} C_{P,carbide}) + (x_{austenite} C_{P,austenite}) \} dT + \Delta^{\circ}H_{tr} \quad (1)$$

In the above expression,  $H_0$  is the reference enthalpy at transformation start temperature, taken after convention as  $Ae_1$ . The first contribution inside the curly brackets of Eq. (1) on the right hand side stands for the mole fraction weighted sum of ferrite and austenite enthalpies.  $x_i$  denotes the phase (mole) fraction of the constituent  $i$  and  $C_{P,i}$ , its molar specific heat. It must be reiterated that in the temperature range  $Ae_1 \leq T \leq Ae_3$ , both  $x_i$  and  $C_{P,i}$  are temperature dependent by virtue of the progress of  $\alpha$ -ferrite carbide  $\rightarrow \nu$ -austenite transformation. Thus for example, at  $T \leq Ae_1$ , the austenite phase fraction ( $x_\gamma$ ) equals zero; with increasing temperature, there is a gradual increase in its phase fraction and as the  $Ae_3$  temperature is approached  $x_\gamma \rightarrow 1$ . Therefore, in the temperature range  $T \leq Ae_1$ , the observed total enthalpy is governed by the specific heats of  $\alpha$ -ferrite and carbide only. But, if we choose to ignore the small contribution from the carbide phase, the enthalpy variation is fully decided by the specific heat variation of  $\alpha$ -ferrite alone. Similarly, for temperatures exceeding  $Ae_3$  point, the change in enthalpy is determined only by the specific heat of austenite; the small enthalpy effect due to austenite homogenization arising from the dissolution of any remaining trace of carbide is again discounted. In the intervening inter-critical region, the enthalpy is dictated by the dynamic course of the  $\alpha \rightarrow \gamma$  transformation. It

must be said that such a splitting of total enthalpy and hence  $C_p$  into two phenomenological components is driven by the necessity to understand the energetics of  $\alpha \rightarrow \gamma$  transformation in terms of simple and separable reaction steps. It may also be added that a rigorous calculation of the thermodynamics of highly alloyed steel such as the present one requires specific information on phase fractions of ferrite, carbides and austenite, as a function of temperature. More importantly, one also needs data on their individual specific heats, so that a brute force calculation of  $\Delta H_{tr}(T)$  using Eq. (1) can be attempted. While ferrite, austenite and carbide phase fractions, as a function of temperature can be calculated through CALPHAD methodology [26], only scanty experimental data are available for their actual temperature dependent specific heats  $C_p^\alpha(T)$  and  $C_p^\gamma(T)$ . In view of such practical difficulties, we have chosen to simply extrapolate the enthalpy of ferrite from its region of stability into the inter-critical domain as well. A fair idea about the extent of progress of the  $\alpha \rightarrow \gamma$  transformation or equivalently the volume fraction of ferrite remaining untransformed  $x_{ferrite}$ , at each temperature is obtained from our previous study of the transformation kinetics using differential scanning calorimetry [16]. In this study, the fraction of austenite formed as a function of temperature in the transformation temperature domain is empirically estimated by adopting the Kolmogorov-Johnson-Mehl-Avrami model of diffusional transformation kinetics [16]. The area under the DSC peak after due calibration is taken to reflect the full phase transformation enthalpy,  $\Delta^0 H_{tr}$ . This value is estimated to be  $14 \text{ J g}^{-1}$ .

From **Fig. 5.2**, it can be estimated that the total enthalpy difference between the two limiting points  $Ae_3$  and  $Ae_1$  is about  $35 \text{ J g}^{-1}$ . As explained in Ref. [19], and also implicitly portrayed by Eq. (1), not the entire of this  $35 \text{ J g}^{-1}$  is associated with phase change effect. In fact a good extent of it is associated with the weighted

enthalpy sum from untransformed fraction of ferrite and transformed austenite phase. This is actually the first term on the right hand side of Eq. (1). This sum is simply *approximated* by extrapolating the enthalpy behavior from  $Ae_1$ , the transformation starting point up to the transformation finish temperature  $Ae_3$ . This extrapolation is graphically sketched in dotted line in **Fig. 5.2**. The subtraction of this extrapolated value at  $Ae_3$  from the total enthalpy difference of  $35 \text{ J g}^{-1}$  yields about  $12 \text{ J g}^{-1}$  and this value is taken to be the rough measure of the phase change enthalpy. As mentioned in section 2.3, the measured total enthalpy difference between  $Ae_3$  and  $Ae_1$  is taken to be accurate to  $\pm 5\%$  in the present case. But the errors associated with the estimation of the fraction of austenite formed and also the uncertainty in  $C_p$  of ferrite and austenite will compound the final uncertainty only further. We have not made a systematic effort to evaluate this latter factor; but in spite of this the value obtained for the transformation enthalpy is in good agreement with the estimate of  $14 \text{ J g}^{-1}$ , which is based on our previous differential scanning calorimetry measurements [16].

#### 4.0. Discussion

##### 4.1 Analytical representation of $\Delta^0H(T)$ data

Since the enthalpy increment variation with temperature is basically non-linear in nature, it is not possible to fit these data by a single functional form that is valid throughout the temperature range of this study. Further, we have not gathered adequate data points in the  $\gamma$ -austenite phase field to warrant a rugged analytical characterization of data in this regime. Therefore the present analytical treatment of the data is restricted to the  $\alpha$ -ferrite region only. The following empirical expression is used to fit the data in the temperature interval  $400 \leq T \leq 1050 \text{ K}$ , for the  $\alpha$ -ferrite phase.

$$H_T - H_{298} / \text{J g}^{-1} = a/2 (T^2 - 298^2) + b/3 (T^3 - 298^3) + c/4 (T^4 - 298^4) + d \ln(T/298)$$

$$- e'(T_C-T)/T_C \times \{ \ln [(T_C-T)/T_C] - 1 \}. \quad (2)$$

The above expression basically empirical and is used from point of view of convenience. Besides it is consistent with the one that has been recently employed by us for representing the  $C_P(T)$  data obtained using differential scanning calorimetry [16]. Thus in consistence with *Eq.(2)*, we get for  $C_P(T)$  the following functional representation

$$C_P^\alpha(T) / J g^{-1} K^{-1} = aT + bT^2 + cT^3 + d/T + e \ln[(T_C-T)/T_C]. \quad (3)$$

The last term in the above expressions stand for the magnetic contribution to the total enthalpy and specific heat respectively of  $\alpha$ -ferrite phase.  $T_C$  is the magnetic transformation temperature taken to be 1015 K for the present RAFM steel. A non-linear least squares regression of the enthalpy increment data to *Eq. (2)* yielded the following values for the fit coefficients:

$$\left. \begin{aligned} a &= 0.00463; \\ b &= -8.492 \times 10^{-6} \pm 4.9754 \times 10^{-7}; \\ c &= 4.8104 \times 10^{-9} \pm 5.5425 \times 10^{-10}; \\ d &= -122.17084 \pm 23.5675, \text{ and} \\ e' &= 0.0325. \end{aligned} \right\} \quad (4)$$

It must be mentioned that the coefficient  $a$  is preset to the quoted value during the fitting procedure. While it is possible to treat this coefficient as a freely-floated parameter during fitting, it is found that fixing this quantity yielded a better fit ( $R^2 = 0.98$ ); more importantly this gave for  $C_P$  at 298 K a value, which agreed well with our previous differential scanning calorimetry based estimate for the same sample [Chapter 6; Ref. 16].

In **Table 5.2**, the percentage deviation of the fitted  $\Delta^{\circ}H(T)$  values from the corresponding experimental ones is listed. It can be seen that *Eq. (2)* provides a

satisfactory fit to the experimental data in the temperature range 400 to 1050 K. In **Table 5.3**, the values of the fit-coefficients appearing in *Eq. (2)* are compared for both the drop calorimetry based direct enthalpy values and the indirect ones obtained from DSC-  $C_p$  data [16]. As can be seen from this table, there is a fair degree of correspondence between these two sets of coefficients, notwithstanding the intrinsic differences in the manner the experiments are conducted in these two complementary calorimetry techniques. This aspect is addressed further in the following section.

**Table 5.2**

Listing of the values of fit-coefficients in *Eq. (2)* used in the analytical representation of the temperature variation of the enthalpy increment ( $H_T - H_{298} / J.g^{-1}$ ) data. For comparison, the coefficients obtained for the DSC based enthalpy values are also listed.

<b>Coefficient</b>	<b>Drop data</b>	<b>DSC data</b>
<i>a</i>	0.00463	$0.00491 \pm 0.14248 \times 10^{-3}$
<i>b</i>	$-8.49 \times 10^{-6} \pm 4.98 \times 10^{-7}$	$-8.47 \times 10^{-6} \pm 2.6 \times 10^{-7}$
<i>c</i>	$4.81 \times 10^{-9} \pm 5.54 \times 10^{-10}$	$4.66 \times 10^{-9} \pm 1.37 \times 10^{-10}$
<i>d</i>	$-122.17 \pm 23.5675$	$-171.90 \pm 11.51$
<i>e</i>	0.0325	$0.0325 \pm 1.25 \times 10^{-3}$
$R^2$	0.97	0.98

**Table 5.3**

A comparison of various transformation temperatures obtained in the present study using drop calorimetry with the corresponding estimates based on differential scanning calorimetry [16].

<b>Transformation</b>	<b>Drop calorimetry value (K)</b>	<b>DSC value (K)</b>
Martensite relaxation	793	Not clearly observed
$\alpha'$ (martensite) $\rightarrow$ $\alpha$ -ferrite + carbide	930	937
ferromagnetic $\alpha$ -ferrite $\rightarrow$ paramagnetic $\alpha$ -ferrite, $T_C$	1015	1018
$\alpha$ - ferrite + carbide $\rightarrow$ $\gamma$ -austenite + carbide	$Ae_1 = 1063$ $Ae_3 = 1148$	$Ac_1 = 1104$ $Ac_3 = 1144$
$\gamma$ -austenite + carbide $\rightarrow$ $\gamma$ -austenite (homogeneous austenite; completion of	1208 -1253	Not clearly observed

carbide dissolution)

#### 4.2. Comparison of drop and differential scanning calorimetry data

As mentioned in the introduction, it is important to note that drop calorimetry is essentially a static or isothermal technique performed under near thermal equilibrium conditions. By maintaining the drop bed at several different closely spaced temperature intervals and carefully calibrating the instrumental sensitivity parameter at these temperatures, it is possible to trace the enthalpy increment variation with temperature in a *quasi-continuous* manner. The enthalpy increment data thus collected at discrete temperature increments can also be used to calculate specific heat, provided the temperature variation of enthalpy is satisfactorily represented by a suitable functional form. *While a high level of accuracy in measuring temperature as well ensuring its stability is possible in drop calorimetry setup, it is however impossible to trace the enthalpy variation in a truly continuous manner, especially around regions of phase transformation.* This feature is in stark contrast to the dynamic or differential scanning calorimetry experiments, wherein continuous heating experiments are easily done, but at the cost of reduced accuracy in temperature measurement and heat-flux calibration [27]. Thus, it is clear that the thermochemical data generated by these two techniques are bound to have certain differences that are germane to their respective designs. In **Fig. 5.3**, the practical manifestation of this aspect is graphically portrayed by comparing the  $C_P$  values obtained in the present study (lower curve) with those of dynamic calorimetry technique [16]. The DSC estimates (upper curve) are seen to be systematically higher than the equilibrium drop calorimetry values. In this case, the DSC experiments are conducted at a heating rate of  $10 \text{ K min}^{-1}$ . In a strict sense, the DSC values need to be corrected for finite heating rate effects, so that a meaningful comparison can be made

against the heating rate independent static drop calorimetry values. This is a very involved process to perform rigorously and in view of this, we resorted to an empirical correction method based on our previous experience with the DSC – based measurements of the heat capacity of pure iron having 80 mass *ppm* of combined impurities [28]. Since fairly reliable and consistent values for the  $C_p$  of iron are available in literature [29], this data set is used to calibrate the relative overestimation of our heat capacity measurement through dynamic calorimetry method. This empirical temperature dependent adjustment is applied to the DSC–based  $C_p$  data of

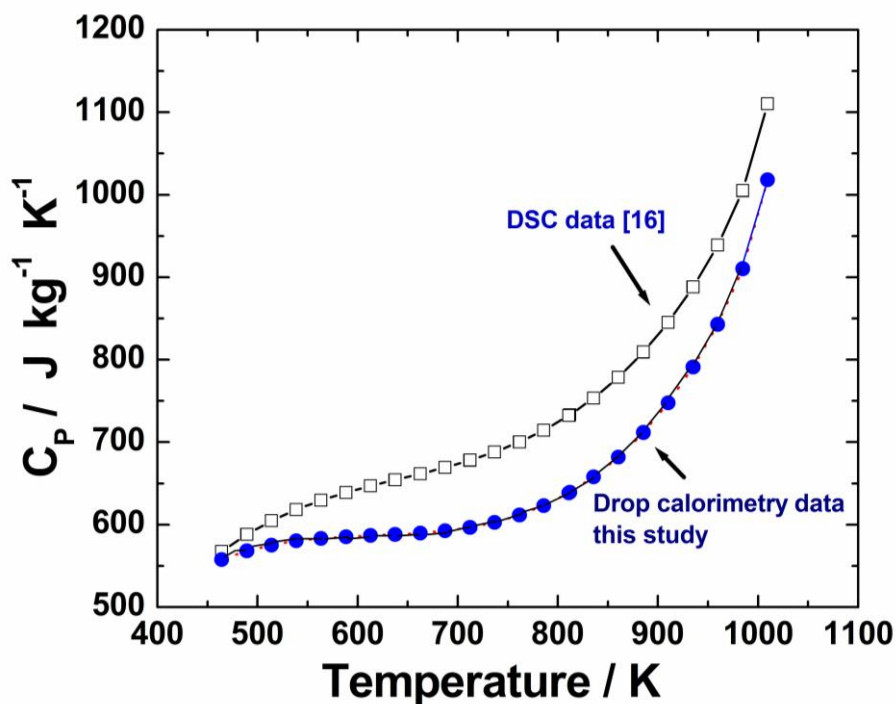


Fig. 5.3. A comparison of drop calorimetry based  $C_p$  values obtained in the present study (lower line) with the ones measured using DSC (upper curve; Chapter 4)

present RAFM steel as well [16].

In a similar manner, the various on-heating transformation temperatures obtained using DSC have also been corrected for the finite heating rate effects. These temperatures are compared with the present drop calorimetry based values in **Table**

**5.3.** Although, a fair degree of agreement is noticed among two sets of transformation temperatures, the value of  $Ae_1$  is considerably less than that of  $Ac_1$ , obtained using DSC. It must be admitted that as mentioned elsewhere in this chapter, there is some difficulty in precisely fixing the transformation onset point from merely studying the slope change or inflection associated with the enthalpy versus temperature curve; for as mentioned before, the drop experiments never traces the transformation event in a truly continuous fashion. It is quite likely that  $Ae_1$  in the present study is somewhat underestimated. However, this must also be weighed in together with the well-known limitation that is intrinsic to DSC, in that the onset of the diffusional transformation solvus is always overestimated here owing to the operation of finite heating rate effects [27]. Considering all these issues, we believe that the overall agreement between the drop and differential scanning calorimetry results for the transformation temperature is rather satisfactory.

#### *4.3. General points*

As mentioned in the introduction, it must be reiterated that to the best of present author's knowledge, not much data with regard to thermodynamic quantities of high chromium reduced activation steels are available in open literature [30-32]. In particular, we could not come across any drop calorimetry based steady state measurements of thermal quantities on this advanced fusion reactor material. However, in the recent past, there has been a renewed interest in the nuclear materials community in generating systematic property database on many an emerging nuclear structural material. Thus, two popular reduced activation steel grades, namely Eurofer 97 and F82H have been extensively researched in the past and recommendations have already been drawn for their physical and mechanical properties [30-32]. The chemical compositions of these two steels are fairly similar (but not identical) to the

RAFM steel used in this study. In **Fig. 5.4**, we have compared the recommended  $C_p$ -T data of both Eurofer 97 and F82H reduced activation steels with the present results. It is gratifying to note that the  $C_p$  values of the RAFM grade used in this investigation

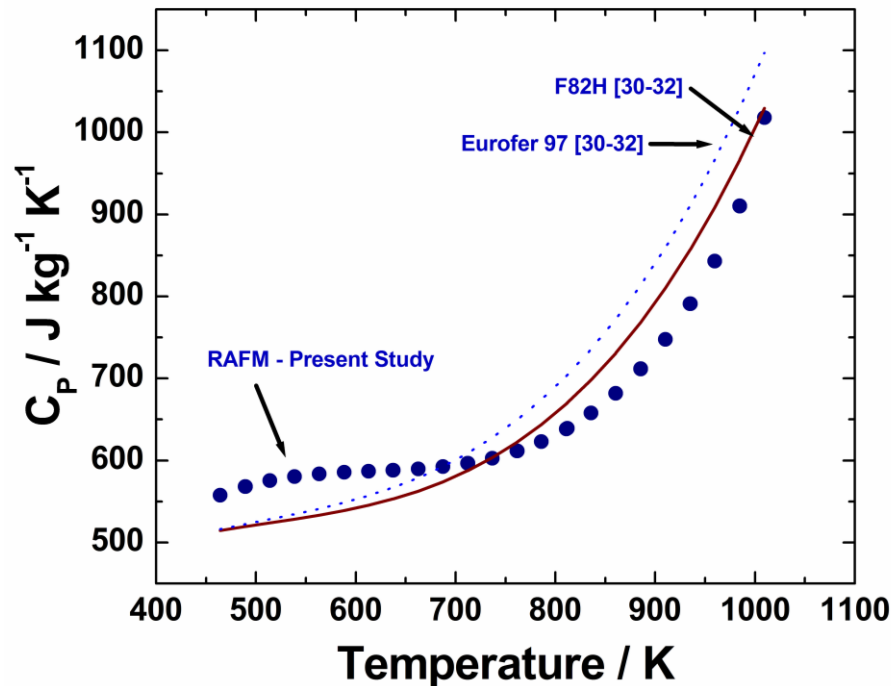


Fig. 5.4. A comparison of  $C_p$  of the reduced activation steel (RAFM) estimated in this study using the present drop calorimetry enthalpy measurements with the literature data on Eurofer 97 and F82H [30-32].

are in good accord with the reported ones.

A critical literature search for experimental phase equilibria related information in this category of alloys does not make any explicit reference to the possible magnitude of  $\alpha \rightarrow \gamma$  transformation enthalpy. However, the present estimate of about  $12 \text{ J g}^{-1}$  for this quantity appears reasonable, when a comparison is made with respect to the transformation specific heat quoted for binary Fe-Cr alloys [33]. At present, a theoretical understanding of issues concerned with phase transformation energetics and kinetics in ferritic steels is handled mostly by phenomenological or CALPHAD – based approaches [14, 26]. An adroit exploitation of this route requires

the availability of reliable thermodynamic data. In this respect, it is hoped that the transformation temperature and  $\alpha \rightarrow \gamma$  transformation enthalpy data generated in this study will be useful in the cause of building up a consistent thermodynamic dataset needed for the successful simulation studies of phase stability in high chromium ferritic steels.

## 5.0 Summary

- i. Accurate enthalpy increment data are presented on tungsten and tantalum containing low carbon reduced activation steel in the temperature range. The enthalpy increment versus temperature data for the  $\alpha$ -ferrite phase are fitted to a simple functional representation. The present study suggests a value of  $560 \text{ J kg}^{-1} \text{ K}^{-1}$  for the specific heat at 450 K.
- ii. The enthalpy data exhibited a non-linear increase with temperature; distinct inflections are found at typical phase transformation temperatures. Estimates of various on-heating transformation temperatures have been arrived at. The detectable enthalpy change due to martensite relaxation has been found at 793 K. Further, the onset of carbide precipitation is found at 930 K. The magnetic transformation temperature  $T_C$  has been measured to be 1015 K. The  $A_{e1}$  and  $A_{e3}$  transformation temperatures have been determined to be, 1063 and 1148 K respectively.
- iii. A value of  $12 \text{ J g}^{-1}$  has also been obtained for the  $\alpha \rightarrow \gamma$  phase transformation enthalpy.

## References

- [1]. S. Sharafat, G. R. Odette and J. Blanchard, *J. Nucl. Mater.*, 386-388 (2009) 896.
- [2]. A. Danon and C. Servant, *J. Nucl. Mater.*, **321** (2003) 8.
- [3]. R. L. Klueh, *Int. Mater. Rev.*, **50** (2005) 287.
- [4]. V. K. Sikka, C. T. Ward and K. C. Thomas, In: *Ferritic steels for high temperature applications, Proceedings of the ASM Conference on Production, Fabrication, Properties and Applications of Ferritic Steels for High Temperature Applications*, ASM, Metals Park, Ohio, USA (1983) p. 65.
- [5]. S. J. Sanderson, *Interrelationships between mechanical properties and microstructure in a 9Cr 1Mo steel*, in: *Ferritic Steels for fast reactor steam generators*, BNES, London (1978), p.120.
- [6]. J. Orr and S. J. Sanderson, *An examination of the potential of 9Cr1Mo steel as thick section tube plates in fast reactors*, in: *Topical Conference on ferritic alloys for use in nuclear technologies*, (eds.: J. W. Davis and D. J. Michel), Met. Soc. of AIME, Warrendale, PA (1984), pp. 261.
- [7]. W. L. Bell, T. Lauritzen, and S. Vaidyanathan, *Ferritics for breeder reactor in-core applications: A survey of alloys, properties and microstructure*, in: *Topical Conference on ferritic alloys for use in nuclear energy technologies* (eds.: J. W. Davis and D. J. Michel), ASM, Met. Soc. AIME, Warrendale, PA (1983), pp. 113.
- [8]. Manabu Tamura, Yusaku Haruguchi, Masahiro Yamashita, Yoshikazu Nagaoka, Kensuke Ohinata, Kohtaru Ohnishi, Eiki Iitoh, Hiroyuki Ito, Kei Shinozuka and Hisao Esaka, *ISIJ International*, **46** (2006) 1693.
- [9]. John Hald and Leona Korcakova, *ISIJ International*, **43** (2003) 420.

- [10]. H. Finkler and M. Schirra, *Steel Res.*, **61** (1996) 328.
- [11]. Ulrich E Klotz, Christian Solenthaler and D. J. Uggowitzer, *Mater. Sci. Engg.*, A476 (2008) 186.
- [12]. F. Abe, *Sci. Tech. Adv. Mater.*, **9** (2008) 1.
- [13]. Vaclav Foldyna, J. Purmenschky and Z. Kuban, *ISIJ International*, **41** (2001) S81.
- [14]. H. Cerjak, P. Hofer and B. Schaffernak, *ISIJ International*, **39** (1999) 874.
- [15]. R. L. Klueh and P. J. Maziasz, *J. Nucl. Mater* 155-157 (1988) 602.
- [16]. S. Raju, B. Jeyaganesh, Arun Kumar Rai, R. Mythili, S. Saroja, E. Mohandas, M. Vijayalakshmi, K. B. S. Rao and Baldev Raj, *J. Nucl. Mater.*, **389** (2009) 385.
- [17]. K. D. Maglic, A. Cezairliyan, V. E. Peletsky (Eds.), *Compendium of Thermophysical Property Measurement Techniques*, vol. **2**, Plenum Press, New York, (1992).
- [18]. Y. Zhu and J. Devletian, *J. Mat. Sci.*, **26** (1991) 6218.
- [19]. S. Raju, B. Jeyaganesh, A. Banerjee and E. Mohandas, *Mater. Sci. Engg.*, A465 (2007) 29.
- [20]. Aritra Banerjee, S. Raju, R. Divakar and E. Mohandas, *International Journal of Thermophysics*, **28** (2007) 97.
- [21]. A. Banerjee, S. Raju, R. Divakar, E. Mohandas, *Mater. Lett.*, **59** (2005) 1219.
- [22]. NIST-JANAF Thermochemical Table Series: J. Phys. and Chemical. Ref. Data Monographs, vol. 9, Malcolm Chase (Ed.), 4<sup>th</sup> edition, Springer, (1998).
- [23]. J. M. Vitek and R. L. Klueh, *Metall. Trans.*, **14A** (1983) 1047.
- [24]. L. Karmazin, *Mater. Sci. Engg.*, **100** (1988) 201.
- [25]. L. F. Alvarez, C. Garcia and V. Lopez, *ISIJ International*, **41** (2001) 599.

- [26]. Bernhard C. Schaffernak and Hornst H. Cerjak, *Calphad*, **25** (2001) 241.
- [27]. E. Gmelin and S. M. Sarge, *Thermochim. Acta*, **347** (2000) 9.
- [28]. B. Jeyaganesh, S. Raju, E. Mohandas, S. Murugesan and M. Vijayalakshmi, *Int. J. Thermo Physics*, **30** (2009) 619.
- [29]. Y. Chuang, R. Schmid and Y. A. Chang, *Metall. Trans.*, **16A**, (1985) 153.
- [30]. A.-A. F. Tavassoli *et al.* *J. Nucl. Mater.*, **329-333** (2004) 257.
- [31]. A.-A. F. Tavassoli, J. W. Rensman, M. Schirra and K. Shiba, *Fusion Engg. & Design*, **61-62** (2002) 617.
- [32]. K. Mergia and N. Boukos, *J. Nucl. Mater.*, **373** (2008) 1.
- [33]. A. S. Normanton, R. H. Moore, B. B. Argent, *Metal Sci.*, **10** (1976) 207.

## High Temperature Thermal Stability, Heat Capacity and Kinetics of $\alpha \rightarrow \gamma$ Diffusional Phase Transformation in Reduced Activation Ferritic Martensitic (RAFM) Steel: Dynamic Calorimetry Study

### 1.0. Introduction

It is well-known that low carbon medium to highly alloyed ferritic steels, especially the 9-10 wt.% Cr ferritic-martensitic steels, constitute one of the major class of structural materials in fossil fuel based conventional power plants and also in certain advanced liquid metal cooled nuclear fast reactors employing metal fuel [1-5]. Besides, some of these alloys are also under consideration for certain nuclear fusion related applications. These alloys are generally known for their good oxidation resistance, high temperature creep-rupture strength, good thermal fatigue tolerance, adequate fracture toughness under typical service conditions and a fair degree of weldability [5]. Besides, they also possess good thermal conductivity, low thermal expansion characteristics as compared to austenitic grades and high swelling resistance to fast neutrons [5]. These properties render them as the preferred candidate material for fission and fusion reactor applications [6].

#### 1.1. *Necessity to develop RAFM steels for fusion applications*

While conventional ferritic-martensitic steels designed around 9Cr-1Mo composition have met with most of the requirements that are stipulated for the in-pile applications in liquid metal cooled fast reactors, the emerging imperatives to develop fusion power have called for the development of newer grades, which can withstand neutron irradiation of higher energy and besides pose a comparatively reduced hazard from the induced radioactivity arising from transmuted transition elements (present in steel). This latter requirement on the part of fusion reactor materials has catalyzed an extensive research and development program worldwide on what are known as low or

reduced activation ferritic–martensitic steels (RAFM) [3-4,7]. The guiding metallurgical principles for the design of RAFM steels are essentially the same as that of conventional high chromium low carbon alloys, such as P91/T91; but with one important caveat that elements producing long half-life transmutants like Ni, Mo, Nb, Cu, Co, Al, N, *etc.*, are largely substituted by their comparatively low activation counterparts, such as Mn, W, V, Ta, and C, so that the RAFM steel at the end of its useful lifespan can be safely handled after a cooling period of about 100 years, rather than 1000 years, which would have been the case with conventional Cr-Mo-Ni-Nb containing ferritic steels [3,7]. It must be added that quite recently, Klueh has argued for the development of boron added newer modifications of RAFM steels from the point of view of improving its creep rupture strength to levels that are realized in the standard Nb-added modified 9Cr steels [7].

The advent of RAFM steels has ushered in a spurt of interdisciplinary research activities aimed at gathering a comprehensive understanding of relevant physical, metallurgical and mechanical properties [12-27]. In India, an elaborate research program on the development and characterization of RAFM steels has been initiated recently, as a joint collaborative activity, involving, Institute of Plasma Research (IPR), Indira Gandhi Centre for Atomic Research (IGCAR), Bhabha Atomic Research (BARC), and Mishradhatu Nigam (MIDHANI). As a first step, a RAFM steel with a nominal composition (*wt. %*) of  $9Cr-0.09C-0.56Mn-0.23V-1W-0.063Ta-0.02N$  (*see, Table 6.1*) has been produced at MIDHANI. As a part of the characterization of this first melt, it has been decided to make accurate measurements of the phase transformation temperatures and specific heat capacity of this indigenous RAFM steel, as reliable values for these material physical properties are required in enabling the knowledge based design of heat treatment and fabrication schedules.

Accordingly, an experimental investigation making use of both high temperature differential scanning calorimetry (DSC) and static isothermal drop calorimetry techniques for the purpose of characterizing high temperature thermal stability and heat capacity of RAFM has been initiated. Since this is a comprehensive study dealing with diverse aspects, the results are presented in three successive chapters devoted to specific issues of thermal stability of RAFM. Thus, the results dealing with on-heating phase transformation sequence and temperature dependent heat capacity obtained using dynamic calorimetry are presented and discussed in this chapter. The details related to the kinetic aspects displacive  $\gamma \rightarrow \alpha'$ -martensitic transformations are discussed in Chapter 7. It may be noted that this chapter is a natural continuation of the drop calorimetry (nearly equilibrium thermodynamic) presented in Chapter 5.

## 2.0. RAFM Steel Specifications

The RAFM steel used in this study is supplied by MIDHANI, Hyderabad, India. Its composition is listed in **Table 6.1**.

**Table 6.1:** The chemical composition in weight percent of the RAFM steel

Element	C	Cr	Mo	Mn	Si	V	Al	Ni	P	Co	Cu
Wt.%	0.091	9.05	0.0036	0.56	0.05	0.226	0.0036	-	-	0.0043	0.005
	W	Ti	Nb	Ta	S	N					
	1.0	0.0024	0.0039	0.063	-	0.0206					

The alloy was produced by vacuum induction melting followed by vacuum arc refining. In order to minimise the content of tramp elements, fairly pure constituents were used in alloy melting. The alloy had been remelted three or four times to ensure a high degree of homogeneity. The master ingot weighing about 300 kg had subsequently been hot forged into plates of 25 mm thickness. A small representative section of the hot forged ingot was taken up for characterization studies. Specimen of dimensions 10×10×5 mm have been sliced from the plate for individual heat

treatments and subsequent thermal stability and thermal property measurement studies.

**Table 6.2:** Heat treatment details adopted in the present study

S.No.	Treatment	Temperature/ K	Time / h	Cooling method	Designation
1	As received state	Hot Forged Condition			As received
2	Solution Treatment	1253	2	Air Cooling (AC)	N -1253
3		1453	2	AC	N-1453
4		1453	2	Water Quenching (WQ)	WQ-1453
5		1553	2	AC	N-1553
6		1553	2	WQ	WQ-1553
7		Tempering of steel normalized at 1253 K	10 33	0.25	AC
8	1033		2	AC	N-1253-T-2
9	1033		5	AC	N-1253-T-5

Since ferritic steels are known to exhibit diverse microstructural features that are in direct relation to the heat treatments adopted, certain typical normalizing temperatures are chosen in the current investigation. These were followed by suitable tempering schedules to produce the standard normalized and tempered microstructures that are characteristic of 9Cr-ferritic alloys [28]. The various heat treatments given to RAFM steel are summarized in **Table 6.2**.

The choice of the solution treatment temperatures higher than about 1253 K is made in order to realize the full dissolution of  $M_{23}C_6$  type carbides and to enhance the possible growth of austenite grains at high temperatures, which would promote the ease of formation of martensite upon subsequent air cooling. Although 9Cr –steels are generally known to be air-hardenable, few samples were also quenched in water. As a preliminary remark, it may be added that normalization treatments at 1253 and 1453 K resulted in near 100 percent martensite, while the ones quenched from 1553 K contained about 15-20 % delta ferrite. For heat capacity measurements, we have taken the steel normalized at 1253 K, which were given a tempering treatment subsequently

at 1033 K for various time durations. The relevant heat treatment details together with specimen designations are listed in **Table 6.2**.

### 3.0. Basic Microstructure Characterisation

For basic metallographic characterization, the samples were ground and polished in the standard manner. The polished samples were given a *mild* initial etching with 2 % nital to reveal the prior austenite grain boundaries and this was followed by a second etch with Vilella's reagent to reveal the normalized and tempered microstructure. The optical microscopy was done using *Leica* MeF4A, and the microhardness measurements were made using *Leitz* microhardness tester, under a load of 100 g. A total of eight hardness readings were recorded and the average Vickers hardness number (VHN) is reported here. In **Table 6.3**, the heat treatment details and corresponding microhardness values are listed.

**Table 6.3.** Microstructural and Microhardness details corresponding to various heat treatments outlined in Table 6.2.

S.No.	Designation	Microstructure	Microhardness / VHN (Load = 100 g)
1	As received	Cold rolled structure	497
2	N-1253	Martensite	429
3	N-1453	Martensite	435
4	N-1553	Martensite + $\delta$ ferrite	427
5	N-1253-T-0.25	Tempered martensite	253
6	N-1253-T-2	Ferrite + carbides	207
7	N-1253-T-5	Ferrite + carbides	195

### 4.0. Differential Scanning Calorimetry Experiments

#### 4.1. Transformation temperature measurements

The samples for DSC experiments were cut from the heat-treated plate using diamond coated wire saw. These were cleaned further and polished to regular and nearly identical shapes of mass varying from 50 to  $100 \pm 0.1$  mg. The DSC experiments were performed with *Setaram Setsys 16*<sup>®</sup> heat-flux type high-temperature

differential scanning calorimeter, employing recrystallised alumina crucibles of about  $100\mu\text{L}$  volume. The description of the equipment and the calibration procedure had been detailed in Chapter 2. Stated briefly, the experiments were performed under a constant flow ( $50\text{ ml}$  per minute) of high pure argon. For the estimation of various on-heating transformation temperatures, slow heating rates of  $1\text{--}5\text{ K min}^{-1}$  were adopted, since higher heating rates resulted in appreciable nonlinear shift of the measured thermal arrest points from their equilibrium values. In order to record the martensitic transformation start ( $M_s$ ) and finish ( $M_f$ ) temperatures, quite a few samples were cooled from  $1253\text{ K}$  at  $100\text{ K min}^{-1}$ .

For specific heat measurements, a heating rate of  $10\text{ K min}^{-1}$  is employed. The adoption of very slow heating rate such as  $1\text{ K min}^{-1}$ , for heat capacity measurements is experimentally tedious due to the difficulty in maintaining good thermal stability of the equipment for prolonged time durations. A high heating rate on the other hand is not normally recommended for specific heat study, especially due to the large thermal lag between the sample temperature and that sensed by the non-contact probe [31].

The basic output of a DSC thermogram, namely the heat flow is calibrated in terms of a reference signal obtained using pure iron reference (*Aldrich Chemicals*; with  $80\text{ wppm}$  of combined impurity). In the temperature regime that is close to the phase transitions, the recorded temperature lag in case of ferritic steel for a heating rate of  $10\text{ K min}^{-1}$  is estimated to be around  $2\text{ to }3\text{ K}$ . The sample mass is kept nearly the same for both the reference iron and steel samples in this case. Fresh samples were used for each run, and multiple runs under identical conditions were performed for calibrating the precision of the measured transformation temperature. The original temperature calibration was performed using recommended high pure melting point standards, namely, Sn, Al, Pb, In and Au. In addition, the measurement of the

enthalpy of  $\alpha \rightarrow \gamma$  allotropic transformation in pure iron (*Aldrich*, impurities less than 80 *wppm*) under identical experimental conditions was also carried out. The heat flow rate or specific heat calibration was performed using the literature data on the specific heat of pure iron [32, 33]. The measured transformation temperatures are accurate to  $\pm 3$  K; the transformation enthalpies are accurate to  $\pm 5$  % at  $10 \text{ K min}^{-1}$ . The heat capacity measurement using DSC in continuous heating mode has been made in accordance with the procedure presented in chapter 2. A typical schedule involves recording of at least three consecutive, non-stop experimental runs under identical heating, holding and cooling schedules [34]. The specific heat of sample is calculated from the three run DSC data using the following formula based on method of ratios [31, 34].

$$C_P^S = C_P^R \times (m_R/m_S) \times \{(\mu_S - \mu_b)/(\mu_R - \mu_b)\}. \quad (1)$$

In the above expression,  $C_P^S$  and  $C_P^R$  represent the specific heat of the sample and the reference whose masses are given by  $m_S$  and  $m_R$  respectively.  $\mu_S$  is the microvolt DSC signal obtained with the sample,  $\mu_R$  is the corresponding signal obtained with the reference or standard material and  $\mu_b$  is the baseline signal obtained with empty crucibles.

## 5.0. Results

### 5.1. Microstructure

In **Fig. 6.1**, typical optical microstructures of the as received (**Fig. 6.1(a)**), normalized (**Fig. 6.1(b-d)**) and tempered samples (**Fig. 6.1(e-g)**) are collated. The elongated and deformed grains arising from hot forging treatment are clearly evident in the microstructure of the as received condition (**Fig. 6.1a**). **Fig. 6(b) & (c)** show the presence of lath martensite (shown by arrows) in the steel normalized at 1253 and 1453 K. The prior austenite grain boundaries and some carbide particles (arrow in

Fig. 6.1a) are fairly well resolved, and their typical dimensions varied from 25 to 40  $\mu\text{m}$  (**Fig. 6.1(b-d)**). The presence of some  $\delta$ -ferrite (see arrow) is observed in the steel normalized at 1553 K and this is marked by the arrows in **Fig. 6.1(d)**.

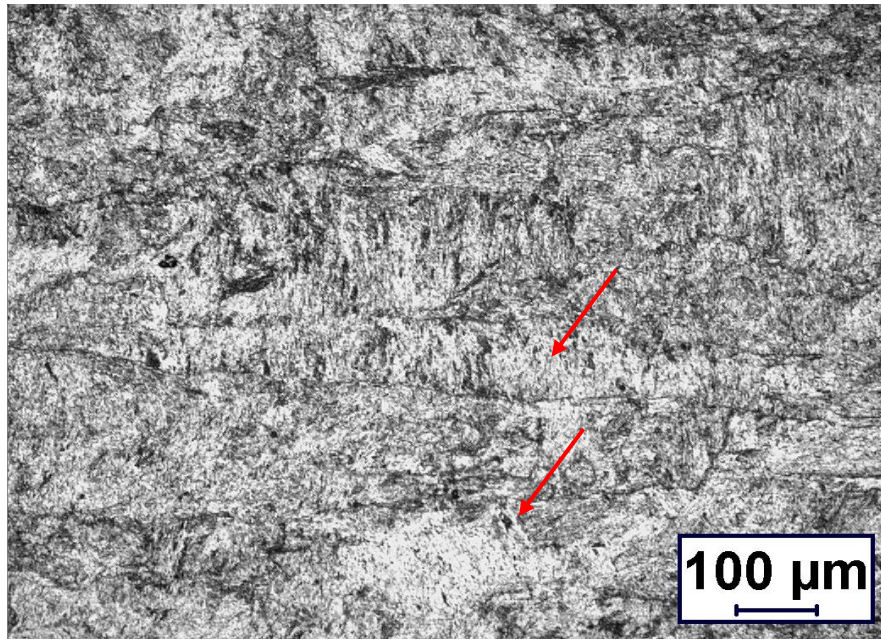


Fig. 6.1(a). Optical micrograph of the RAFM steel in the as received condition showing a highly deformed structure

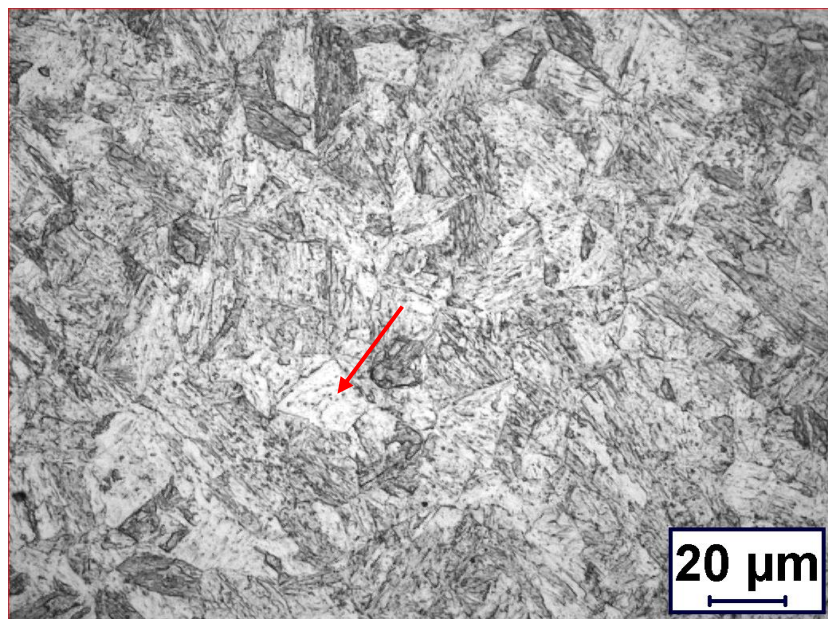


Fig. 6.1(b). Optical micrograph of the sample normalised at 1253K / 2h, showing martensite structure

As will be described in detail in the ensuing section, the  $M_{23}C_6$  type carbides which are the major ones in 9Cr-type ferritic steels do not undergo a complete dissolution at 1253 K, (in particular under dynamic continuous heating conditions). Moreover, the solvus temperature of the MX type (Ta,V)(CN) mixed carbonitrides is also higher

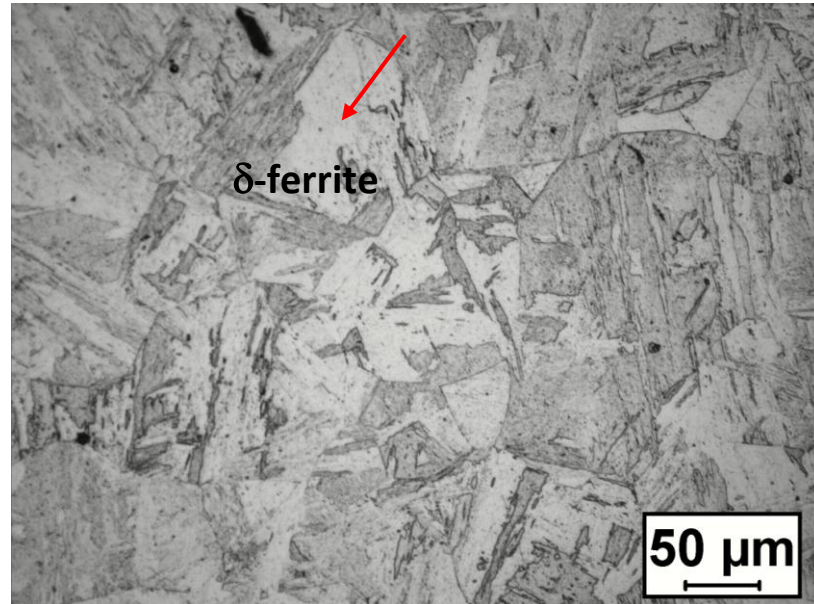


Fig. 6.1(c). Optical micrograph of the sample normalised at 1453K showing coarser austenite

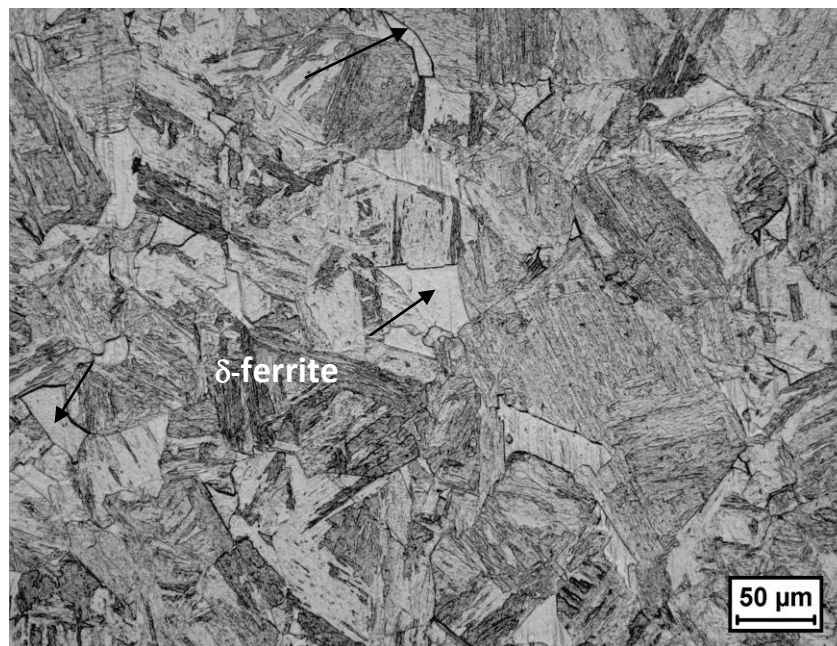


Fig. 6.1(d). Optical micrograph of the sample water quenched from 1553 K showing the presence of some  $\delta$  - ferrite (marked by arrows) in addition to martensite.

than 1253 K (*see*, **Table 6.5** for more details).

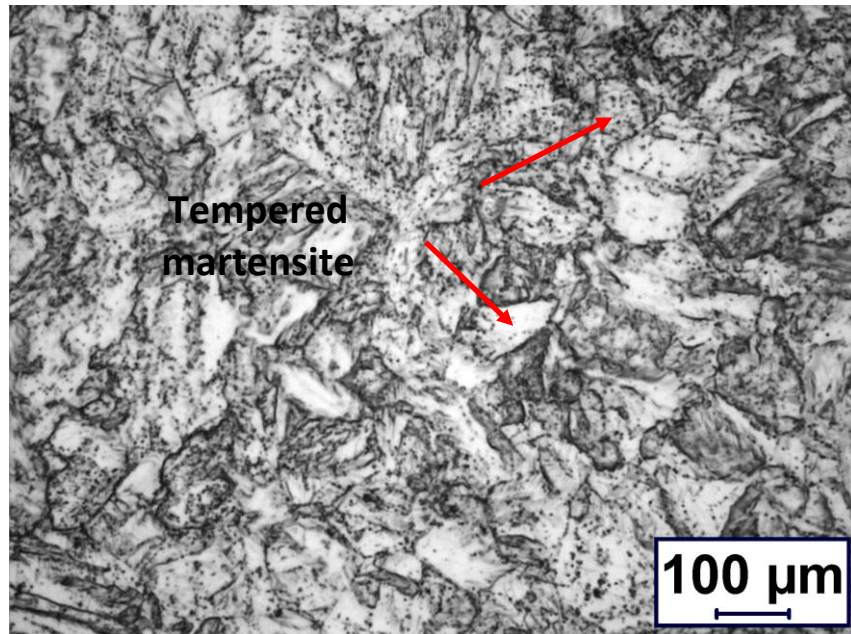


Fig. 6.1(e). Optical micrograph of the sample normalised at 1253K / 2h, followed by tempering at 1033 K for 30 min showing a tempered martensite structure

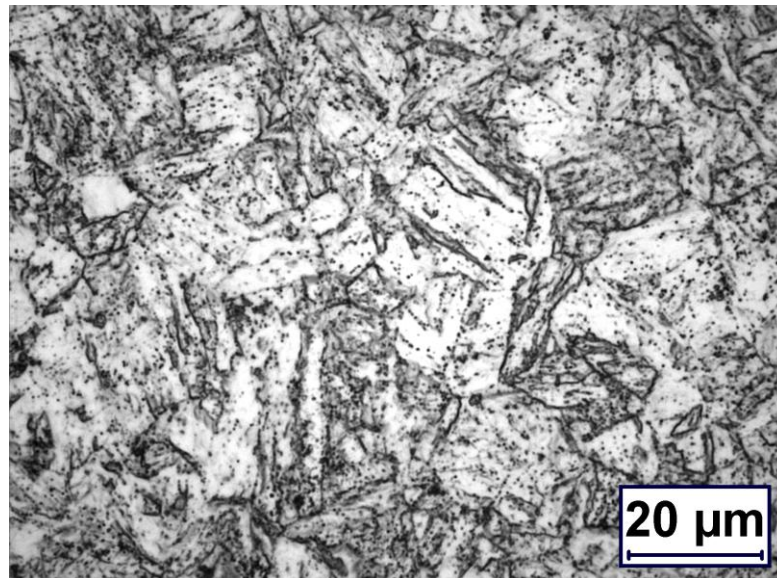


Fig. 6.1(f). Optical micrograph of the sample normalized at 1253 K followed by tempering at 1033K for 120 min showing the presence of carbides in the tempered martensite.

As a result, the presence of some undissolved  $M_{23}C_6$  and MX type carbides characterize the 1253 K normalized microstructure and these hard dispersed particles

exert a strong pinning influence on the growth of austenite grains and thereby yield a

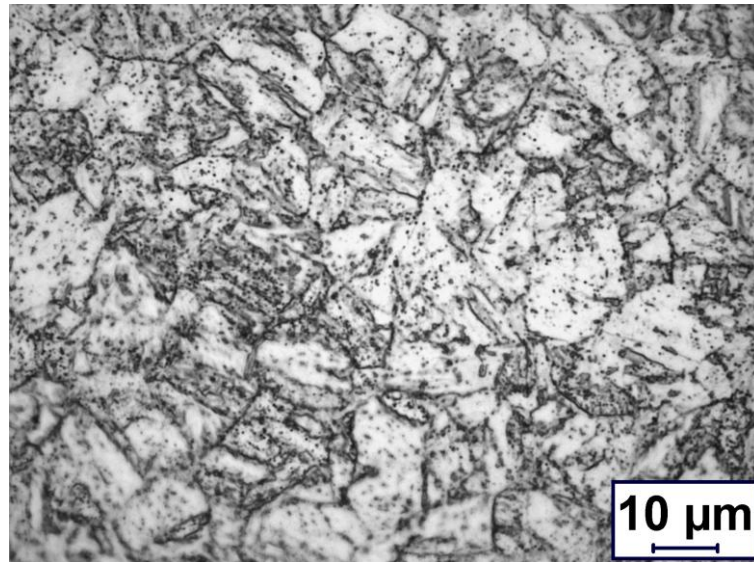


Fig. 6.1(g). Optical micrograph of the sample normalized at 1253\_K followed by tempering at 1033\_K for 300 minutes showing the presence of carbides in the ferrite matrix

fairly stable austenite grain size at these normalization conditions.

Subsequent to normalizing, the tempering treatment at 1033 K resulted in profuse carbide precipitation, both on prior austenite grain boundaries and also inside the grains, decorating thus the lath and sub-grain boundaries of the partially relaxed martensite (*Fig. 6.1(e-g)*). A longer tempering time of, up to about 5 hours in this study, had resulted in carbide coarsening at select locations (*Fig. 6.1(g)*). *Since the present study is devoted to the enumeration of phase stability and heat capacity related aspects in terms of calorimetry, the subject of microstructure evolution upon thermal treatment is not dealt with in detail in this thesis report.*

## 5.2. DSC Thermogram upon slow heating and cooling

In **Fig. 6.2(a)**, a typical DSC profile obtained during heating ( $3 \text{ K min}^{-1}$ ) and cooling ( $3 \text{ K min}^{-1}$ ) of a 1253 K normalized sample is illustrated. The presence of various thermal arrest events including the most prominent one, namely melting, is

clearly brought out in this figure. In **Fig. 6.2(b)**, an exclusive, expanded view of the high temperature region, as marked by the ellipse in **Fig. 6.2(a)** is portrayed. The values of  $A_{c1}$  and  $A_{c3}$ , the  $\alpha + \text{carbides} \rightarrow \gamma$  transformation start and finish temperatures for differently heat treated RAFM steels (with different starting microstructure) are listed in **Table 6.4**. The temperature values corresponding to different transformation arrest points obtained on 1253 K normalized samples are listed in **Table 6.5**.

Since the enthalpy effects obtained with samples of low mass (75 mg ) for various solid state phase changes are rather small, these thermal arrests are determined by taking the derivative signal of the heat flow, in which the occurrence of the inflection points are more clearly delineated. A careful inspection of **Fig. 6.2(a)** in the light of the available generic information on the phase stability of 9Cr based steels [5] highlights the following sequence of phase changes that takes place upon slow heating of the RAFM steel. It must also be remarked at this stage that in case of highly hardenable ferritic steels, it is not possible to obtain direct metallographic evidence for the actual phase constitution that exists at high temperatures by performing interrupted quenching experiments, as this would invariably yield only martensite as the end product. In view of this, we have made use of the available information generated by CALPHAD based *equilibrium* thermodynamic calculations on phase stability in related steels [36, 37]. The approximate transformation temperatures provided by these calculations correspond to equilibrium condition, where as the ones obtained in the present experiment pertain to dynamic situation. Nevertheless, the on-heating scans are performed sufficiently slowly so that the knowledge of equilibrium phase stability domains is still useful in indexing the DSC profile.

**Table 6.4.** Listing of  $Ac_1$  and  $Ac_3$  temperatures for differently treated RAFM samples

S.No.	Designation	$Ac_1$ (K)	$Ac_3$ (K)	$\Delta^{\circ}H$ for $\alpha \rightarrow \gamma$ transformation  (J g <sup>-1</sup> )	$M_s$ (K)	$M_f$ (K)	$\Delta^{\circ}H$ for $\gamma \rightarrow \alpha'$ martensite transformation  (J g <sup>-1</sup> )
1	As received	1103	1139	13	701	610	68
2	N-1253	1107	1140	11	728	621	73
3	N-1453	1105	1146	9	746	689	73
4	N-1553	1102	1145	12	717	675	63
5	N-1253-T-0.25	1106	1136	15	698	611	65
6	N-1253-T-2	1105	1140	13	714	618	63
7	N-1253-T	1108	1141	14	701	607	63

**Table 6.5.** The on-heating transformation temperatures for RAFM steel as measured by DSC. The heating rate adopted is 5 K min<sup>-1</sup>. The starting microstructure is derived from the normalisation treatment at 1253 K

Description of phase change	On-heating Transformation Temperature (K)
$\alpha$ (martensite) $\rightarrow$ $\alpha$ (ferrite) + $M_{23}C_6$ <i>Precipitation of <math>M_{23}C_6</math> on slow continuous heating</i>	937
$T_C$ , Curie temperature	1018
$\alpha + MX + M_{23}C_6 \rightarrow \alpha + \gamma + MX + M_{23}C_6$ <i>austenite transformation start</i> ( $Ac_1$ )	1104
$\alpha + \gamma + MX + M_{23}C_6 \rightarrow \gamma + MX + M_{23}C_6$ <i>austenite formation finish</i> ( $Ac_3$ )	1144

$\gamma + \text{MX} + \text{M}_{23}\text{C}_6 \rightarrow \gamma + \text{MX}$ <i>completion of <math>\text{M}_{23}\text{C}_6</math> dissolution</i>	1550
$\gamma + \text{MX} \rightarrow \delta + \gamma + \text{MX}$ <i><math>\delta</math>-ferrite formation</i>	1575
$\delta + \gamma + \text{MX} \rightarrow \delta + \gamma$ <i>completion of <math>\text{MX}</math> dissolution</i>	1681
$\delta + \gamma \rightarrow \text{Liquid} + \gamma + \delta$ <i>appearance of liquid</i>	1730
$\text{Liquid} + \gamma + \delta \rightarrow \text{Liquid} + \delta$ <i>dissolution of <math>\gamma</math> - austenite</i>	1753
$\text{Liquid} + \delta \rightarrow \text{Liquid}$ <i>completion of liquid formation</i>	1805
$\Delta^{\circ}\text{H}_m$ , enthalpy of melting $(\text{J g}^{-1})$	364
$\Delta^{\circ}\text{H}_{\alpha \rightarrow \gamma}$ , enthalpy of $\alpha \rightarrow \gamma$ transformation $(\text{J g}^{-1})$	14

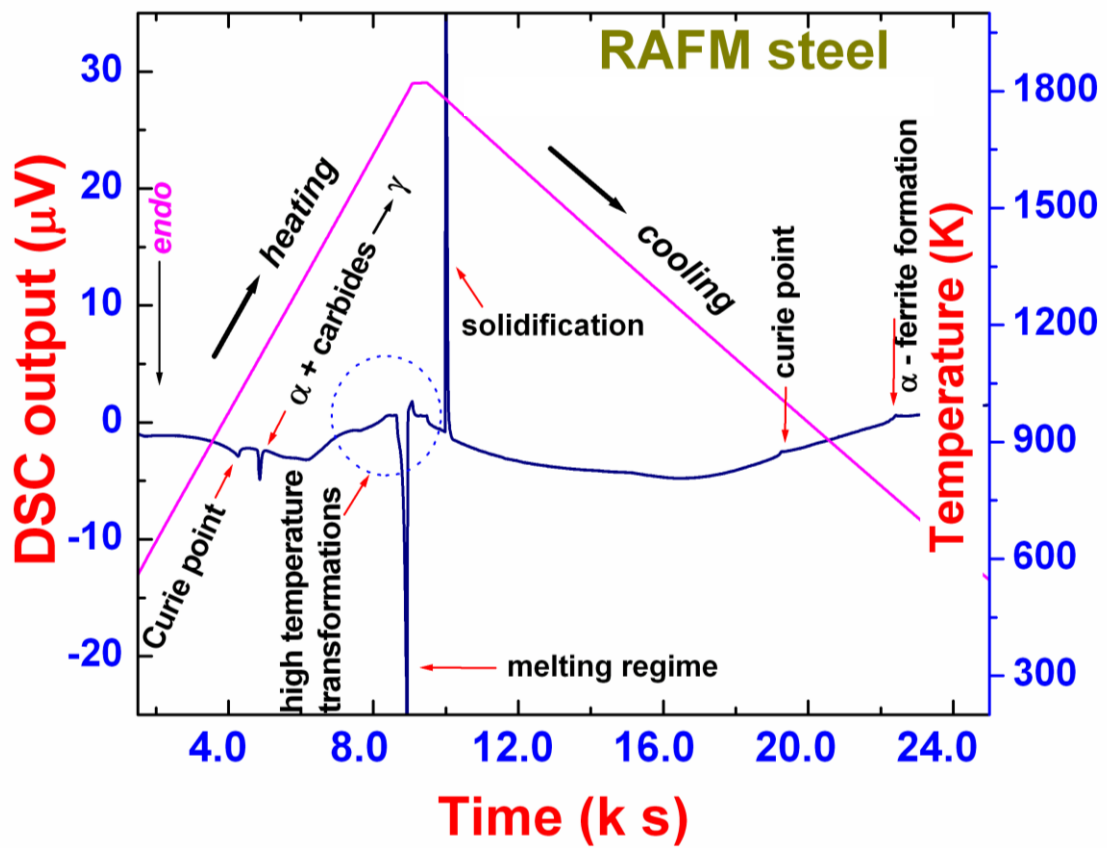


Fig. 6.2(a). Typical DSC thermogram of RAFM steel

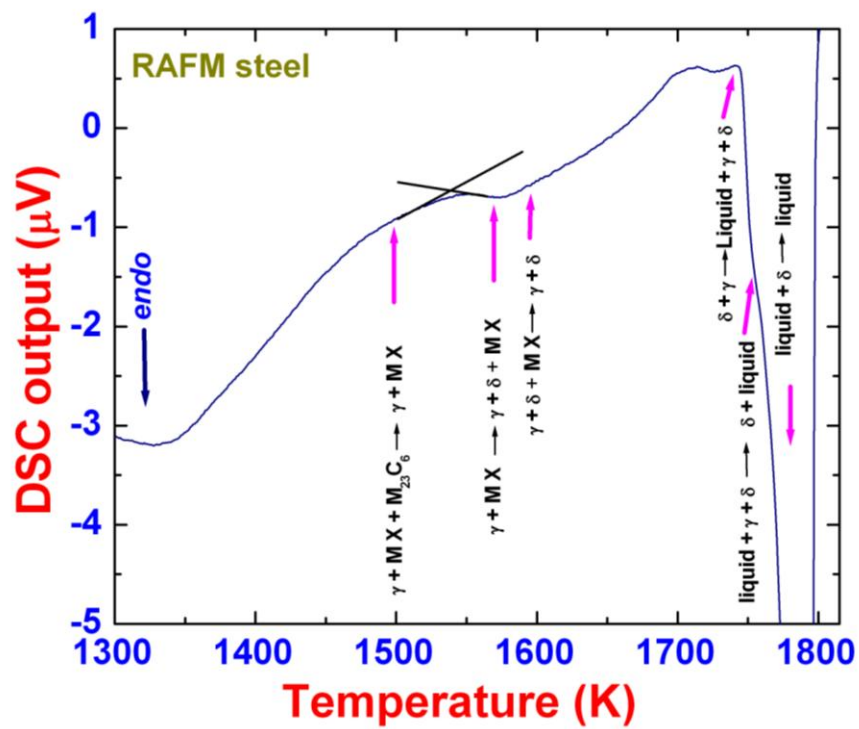


Fig.6.2(b). The expanded view of the DSC profile around the melting region

(i). Curie Temperature: The first transformation on heating is the ferromagnetic to paramagnetic ferrite taking place at  $T_C$ , the Curie point of the  $\alpha$ -ferrite phase. Depending on the composition, the  $T_C$  of 9Cr-1Mo based ferritic steels is found to vary from 1008 to 1023 K [35]. But, owing to the presence of tungsten and tantalum in RAFM steel, a slightly higher value of about  $1018 \pm 3$  K is recorded in this study. The Curie temperature,  $T_C$  is found to be more clearly attested during heating than on cooling, as the formation of martensite upon cooling just after the magnetic phase change obscures the sharpness of the magnetic transformation thermal arrest. Note that this martensite transformation during cooling occurs at about 673 K.

(ii).  $\alpha$ -ferrite +  $M_{23}C_6$  + MX  $\rightarrow$   $\gamma$ -austenite +  $M_{23}C_6$  + MX (on crossing the  $A_{c1}$  temperature); Depending on the heating rate, the austenite formation reaches a fair degree of completion at  $A_{c3}$  point - the upper critical temperature. It was earlier observed in high chromium steels, that upon reaching  $A_{c3}$ , practically very little dissolution of  $M_{23}C_6$  is realised [38], although the *Thermo Calc*<sup>®</sup> based equilibrium simulations suggest a quite a bit of dissolution (5%) by the time  $A_{c3}$  is reached [36-37]. This difference is due to the sluggish nature of the dissolution of highly cohesive alloy carbides in highly alloyed ferritic steels, as it involves the transport of substitution atoms over fairly large distances [38].

(iii).  $\gamma$  +  $M_{23}C_6$  + MX  $\rightarrow$   $\gamma$  + MX; (dissolution of  $M_{23}C_6$  carbide). Basically, the dissolution of carbide being diffusion mediated one, is a continuous process after  $A_{c3}$ . Since the enthalpy effects associated with this step is rather small due to the small volume fraction of carbides, a sharp DSC peak is not visible for carbide dissolution reaction that is progressing at a slow pace. Instead, this step is generally identified only as a shallow endothermic trough in an otherwise smooth DSC profile [29]. This is observed better only in slow heating rate scans [35].

- (iv).  $\gamma + \text{MX} \rightarrow \delta - \text{ferrite} + \gamma + \text{MX}$ ; (appearance of high temperature  $\delta - \text{bcc}$  phase)
- (v).  $\delta + \gamma + \text{MX} \rightarrow \delta + \gamma$ ; (completion of dissolution of MX phase in  $\gamma$ )
- (vi).  $\delta + \gamma \rightarrow \text{Liquid} + \delta + \gamma$ ; (appearance of liquid)
- (vii).  $\text{liquid} + \delta + \gamma \rightarrow \text{liquid} + \delta$ ; (dissolution of  $\gamma$  in liquid)
- (viii).  $\text{liquid} + \delta \rightarrow \text{liquid}$ ; (completion of melting)

The region covered by the last three thermal arrest events signifies the solidus – liquidus interval in the on-heating phase evolution diagram. In the case of 9-12%Cr-Mo steels with a nominal carbon concentration of about 0.1 wt.%, the calculated equilibrium diagram(s) using *Thermo Calc*<sup>®</sup> software and associated steel database suggests that one may encounter a very small existence domain of the (*liquid* +  $\delta$  +  $\gamma$ ) three phase field just prior to attaining the ( $\delta$  + L) two phase region on slow continued heating [36, 37]. The presence of a higher austenite stabilizing ( $Mn+Ni+N$ ) content in typical modified 9Cr-1Mo steel, such as P91 or E911 supports the possibility that a three phase (*liquid* +  $\delta$  +  $\gamma$ ) equilibrium be realized in principle during slow (1-3  $K \text{ min}^{-1}$ ) heating experiments. The actual attainment is of course dependent on kinetic factors. This aspect has been kept in mind, while annotating the high temperature region of the DSC profiles shown in **Fig. 6.2(b)**. In **Fig. 6.2(b)**, it is also interesting to note the subtle features in the nature of the DSC profiles around (*liquid* +  $\delta$ ) region. The presence of a shoulder like feature in the final melting peak is suggestive of the peritectic dissolution of  $\delta$ -ferrite in liquid, as for example taking place in dilute Fe-C binary alloys. But this observation needs further careful scrutiny.

It must also be mentioned that for a given DSC instrument and a well prescribed set of experimental conditions, the sharpness or the clearly defined nature of various transformation arrest events is a direct function of the associated enthalpy

effect. Unlike the case of  $\alpha \rightarrow \gamma$  structural transformation or melting reaction, the other continuously occurring events like the dissolution of  $M_{23}C_6$  and MX phases are accompanied by only a small change in enthalpy. This is because of the fact that the volume fractions of these phases are small in low carbon 9Cr-steels. Therefore, these changes manifest only as mild, inflections in the base line compensated DSC profile (*Fig. 6.2(b)*).

The enthalpy effects associated with  $\alpha \rightarrow \gamma$  phase change and melting are given directly in terms of the total area enclosed under the respective peak [34]. The conversion factor required for getting enthalpy in terms of  $J g^{-1}$  is obtained from the corresponding signal from pure iron [31]. The measured enthalpy values are listed in the last two rows of **Table 6.5**. As for the  $\alpha \rightarrow \gamma$  phase change is concerned, there is reasonable agreement between the transformation enthalpy  $\Delta^o H^{\alpha \rightarrow \gamma}$  values recorded for RAFM and different P91 compositions. At this point, it must be mentioned that for lower heating rates ( $1-10 K min^{-1}$ ), the  $\alpha \rightarrow \gamma$  transformation peak is found to be diffuse, contributing thereby to a higher degree of uncertainty in the measured peak area and hence enthalpy values. In addition, the low carbon concentration of about 0.09 wt.% of the present steel and the fact that solubility of carbon in ferrite is very small, support the argument that it is primarily the substitutionally alloyed ferrite matrix that is getting transformed to austenite in the  $A_{c1}-A_{c3}$  intercritical domain; any probable contribution from possible  $M_{23}C_6$  dissolution in this range is expected to be only marginal.

The measured melting enthalpy values are in the range,  $360 J g^{-1}$ . This value is estimated to be accurate to  $\pm 5 \%$ , based on similar measurements done on a iron sample with 80 ppm of impurities. Again this estimate is somewhat on the higher side as compared to the values of  $240-260 J g^{-1}$  that are reported for W, Ta free low carbon

steels [39]. This must also be viewed with the fact that the effective melting regime or the liquidus-solidus interval is rather large in high alloy ferritic steels compared to the low alloyed ones and hence the melting peak encompasses a larger area.

## 6. Specific Heat Determination

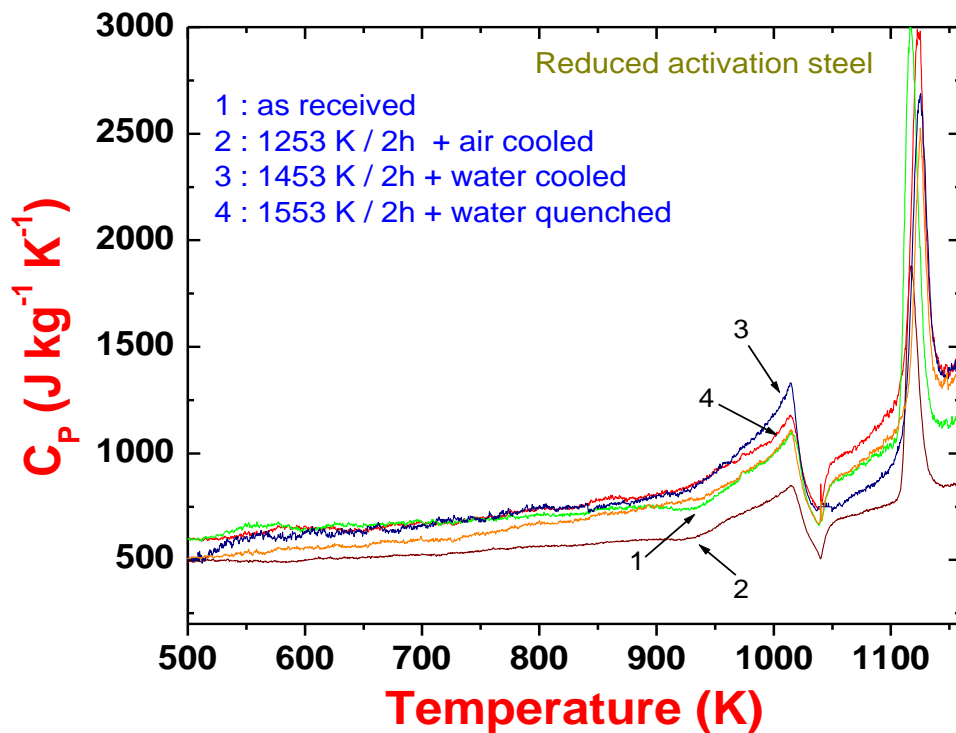


Fig. 6.3(a). Temperature variation of specific heat for RAFM steel in different normalized conditions

In Fig. 6.3(a), the measured variations in specific heat  $C_p$  with temperature for the RAFM steel in the as received and in different normalized conditions are compared. These curves are typical of untempered martensites. The presence of sharp peaks arising from magnetic and  $\alpha \rightarrow \gamma$  transformations are clearly evident in all the curves. It is also observed that no significant difference in the specific heat characteristics of different martensitic microstructures that are obtained by fast cooling from different austenitisation temperatures is noticed. This is understandable from the fact that this steel is fully hardenable upon reasonable cooling from austenite

regime. No drastic quenching is needed for getting martensite. As compared to higher austenitizing temperatures, the 1253 K normalized sample contained a higher fraction of undissolved carbides, and since the  $C_P$  of  $M_{23}C_6 + MX$  carbides is less than that of carbon lean  $\alpha$ -ferrite (solubility of carbon in bcc-iron is less), this sample shows a comparatively lower heat capacity among different normalized microstructures.

In Fig. 6.3(b), the  $C_P$ -T data are compared for tempered samples that had seen

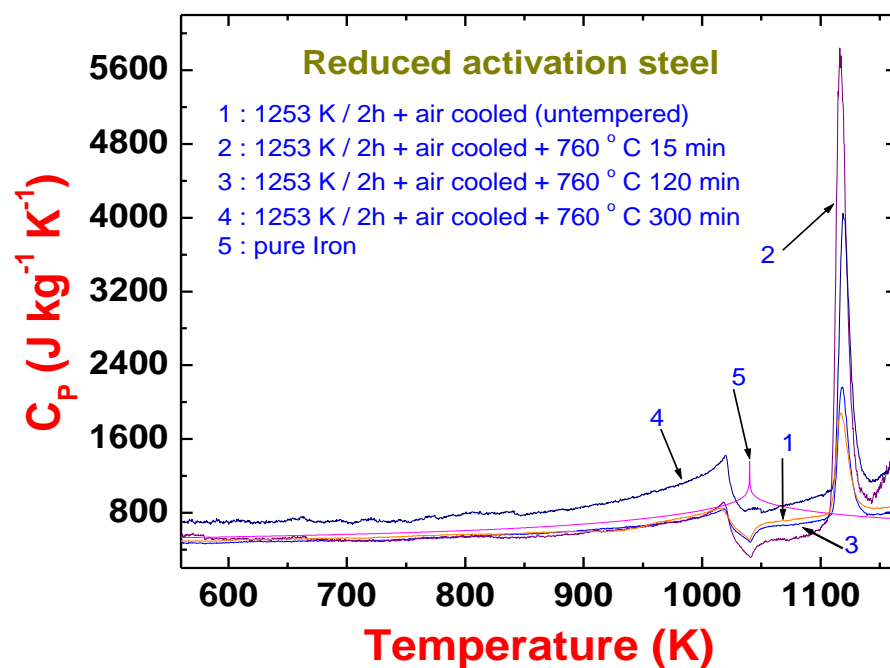


Fig. 6.3(b). The temperature variation of specific heat for RAFM steel in different tempered conditions. Note that in figure (a), the y-axis scale is compressed in order to bring out the very small differences among different martensites.

three different tempering durations (15, 120 and 300 minutes) at 1033 K. For comparison, the data on one untempered sample (1253 K + air cooling) are also co-plotted here. In accordance with our previous findings on tempered and aged 9Cr-1Mo steels [31,39], the heat capacity is expected to show a mild increase with tempering time and temperature and this is attributed to the reduction in the stored energy of martensite, following substructure reorganization upon thermal activation

[31]. In the case of W-added RAFM steel, a similar trend is observed, although in a subdued manner. This is because the presence of W and Ta, the two comparatively more cohesive substitutes for Mo slows down the rate of relaxation of martensite upon tempering. The enhanced cohesive character of the RAFM steel due to W addition may be inferred from the fact that the replacement of Mo by W enhances marginally the solid solution strengthening and thereby improves the creep properties as well [28]. Besides, the coarsening rates of carbides are also slowed down in W added steel due to reduced diffusion rates [40]. The influence of W addition is implicitly borne out in the present experimental findings in that, only for the 5-hour tempered sample, the measured  $C_p$  curve (curve 4 in Fig. 5.3b) is placed distinctly above the corresponding untempered one (curve 1 in Fig.4.3b). Note that the y-axis scales are slightly different for these two  $C_p$ -T plots, which drive home the point that tempering serves to increase the heat capacity somewhat in W added steel. However, a resolution of this issue in more quantitative terms, calls for further comparative studies with long term thermally aged samples, which are expected to have reached full thermodynamic equilibrium. These issues are scheduled for future study.

The experimental specific heat versus temperature data in the  $\alpha$  - ferrite region are fitted to the following empirical functional representation:

$$C_p / J \text{ kg}^{-1} \text{ K}^{-1} = aT + bT^2 + cT^3 + D/T + E \ln\{\text{abs}(T-T_C)/T_C\}. \quad (2)$$

The last term on the right hand side of the above expression represents the magnetic contribution to the total  $C_p$ . Although more sophisticated expressions are used in literature for representing  $\Delta C_p^{mag}$  [32], we have chosen a simple functional representation here as this captures fairly adequately the experimental scenario. The values of fit parameters in Eq. (2) are listed in **Table 6.6**.

**Table 6.6**

Listing of fitting parameters of the measured specific heat data to expression given by Eq. (2). The  $T_C$  used in fitting is 1015 K for all samples. The overall temperature range of the data chosen for fitting is 480 to 1020 K, except for three cases, for which the presence of wiggles in the low temperature region adversely affected the quality of the fit. Hence a slightly restricted temperature range is adopted for these three cases.

$C_p / \text{J Kg}^{-1} \text{K}^{-1} = AT + BT^2 + CT^3 + D/T + E \ln\{\text{abs}(T-T_C)/T_C\}$						
Steel designation	A ( $\text{J kg}^{-1}$ )	B ( $\text{J K kg}^{-1}$ )	C ( $\text{J K}^2 \text{ Kg}^{-1}$ )	D ( $\text{J kg}^{-1} \text{ K}^{-2}$ )	E ( $\text{J Kg}^{-1} \text{ K}^{-1}$ )	$R^2$
As received	$7.49 \pm 0.19$	$-0.012 \pm 0.0004$	$6.005 \times 10^{-6} \pm 1.87 \times 10^{-7}$	$-282008.08 \pm 18204.70$	$-49990.18 \pm 1603.45$	0.96
N -1253 (fitted from 502 K)	$3.62 \pm 0.12$	$-0.006 \pm 0.00002$	$2.92 \times 10^{-6} \pm 1.22 \times 10^{-7}$	$-35217.63 \pm 11363.64$	$-33741.84 \pm 1161.93$	0.97
WQ-1453 (fitted from 510 K)	$10.39 \pm 0.28$	$-0.017 \pm 0.0005$	$8.83 \times 10^{-6} \pm 2.75 \times 10^{-7}$	$-539099.68 \pm 27141.32$	$-59337.22 \pm 2292.46$	0.97
WQ-1553	$5.38 \pm 0.13$	$-0.009 \pm 0.0002$	$4.81 \times 10^{-6} \pm 1.33 \times 10^{-7}$	$-132584.48 \pm 12371.99$	$-32960.89 \pm 1261.34$	0.99
N-1253-T-0.25	$2.59 \pm 0.05$	$-0.004 \pm 0.0001$	$2.28 \times 10^{-6} \pm 25.04 \times 10^{-8}$	$13871.21 \pm 4741.66$	$-21122.24 \pm 463.56$	0.99
N-1253-T-2 (fitted from 665 K)	$10.64 \pm 0.61$	$-0.018 \pm 0.001$	$8.57 \times 10^{-6} \pm 4.58 \times 10^{-7}$	$-760670.77 \pm 69469.79$	$-30653.01 \pm 1298.51$	0.99
N-1253-T-5	$10.30 \pm 0.15$	$-0.018 \pm 0.0003$	$9.70 \times 10^{-6} \pm 1.54 \times 10^{-7}$	$-467265.84 \pm 14137.71$	$-39011.25 \pm 1454.94$	0.99

### 6.1. Discussion on Thermal Stability and Heat Capacity

At the outset, it must be mentioned that although the physical metallurgy of advanced 9Cr-steels is replete with many investigations devoted to the elucidation of microstructural development upon thermal treatment [1-27], there are not many calorimetry based studies focused on the energetics and kinetics related aspects of phase changes [29,31,39]. In this regard, the present study attempts to shed some light on the phase transformation sequence that follows as a result of continuous heating of normalized and tempered RAFM steel. It is believed that the findings of this study, especially the phase transformation temperatures and their enthalpies offer data that are useful in a simulation study of diffusional phase transformation kinetics.

The phase transformation temperatures that are obtained in this study are in general agreement with the values found for general 9Cr-1Mo based low carbon steels [39]. In case of RAFM steel, the values of  $A_{c1}$  and  $A_{c3}$  temperatures for different tempered microstructures are very similar; *in other words no appreciable microstructure sensitivity of transformation temperatures per se is apparent from this study. But in terms of absolute values, it is noted that they are slightly higher than the corresponding values obtained for tungsten and tantalum free plain 9Cr-1Mo steels [29, 39].* The clear qualitative reason for this is that the addition of tungsten and tantalum, enhances the stability of the  $\alpha$ -ferrite phase. For the same reason, it is also expected that the addition of tungsten will exert a significant influence on austenite formation kinetics upon high temperature homogenization step, since W and Ta additions will serve to decrease the diffusivity in ferrite phase, as for example they do in the bcc phase of iron [40].

Akin to the diffusional transformation onset temperature, the martensite start ( $M_s$ ) and finish ( $M_f$ ) temperatures recorded upon cooling for the RAFM steel are found to be slightly higher than that recorded for conventional 9Cr-1Mo steels [29, 39]. More importantly, they seem to be influenced by the microstructure (presence of carbides and austenite grain size) prevailing at the austenitising conditions. At about 1253 K for example, the complete dissolution of the carbide phase is not realized for reasons that are already mentioned before; and the retention of a large fraction of undissolved carbides results in an austenite phase that is not quite rich in carbon. So the  $M_s$  of this *carbon lean* austenite is expected to be somewhat higher than the *carbon rich* austenite that would have been obtained under a relatively higher austenitising temperature and prolonged annealing durations. As an added influence, the presence of some coarse  $M_{23}C_6$  and fine MX particles exert a pinning effect on the

advancement of martensitic transformation front. In view of this later effect, a higher austenitizing temperature (1453-1553 K) would obviously result in more extensive dissolution of  $M_{23}C_6$  carbides, which would in turn serve to decrease  $M_S$ . Further, systematic studies on the effect of processing variables on  $M_S$  are currently under progress.

**Table 6.7**

A comparison of  $C_P$  of martensitic with that of tempered martensite.

Temperature (K)	$C_P$ Martensite (J kg <sup>-1</sup> K <sup>-1</sup> )	$C_P$ Tempered Martensite (J kg <sup>-1</sup> K <sup>-1</sup> )
500	483	631
525	491	659
550	498	679
575	504	693
600	508	702
625	512	708
650	516	711
675	520	713
700	524	715
725	529	719
750	535	725
775	542	734
800	551	748
825	562	768
850	575	794
875	591	828
900	611	872
925	636	927
950	666	995
975	704	1081
1000	763	1197

At this stage, it may be mentioned in general terms that a full-fledged explanation of the effect of W, Ta addition on the phase transformation characteristics of RAFM steels calls for the generation of data on a range of compositions with varying W and

Ta contents. This effort must also be supplemented by a corresponding research on phase stability estimation in terms of CALPHAD methodology. The present paper, being exclusively dedicated to the generation of reliable data on one select RAFM composition, does not attempt to provide an answer on a fundamental note. Nevertheless, an attempt has been made to qualitatively explain the data using available literature information. Clearly more work is required to shed further insight on this crucial issue.

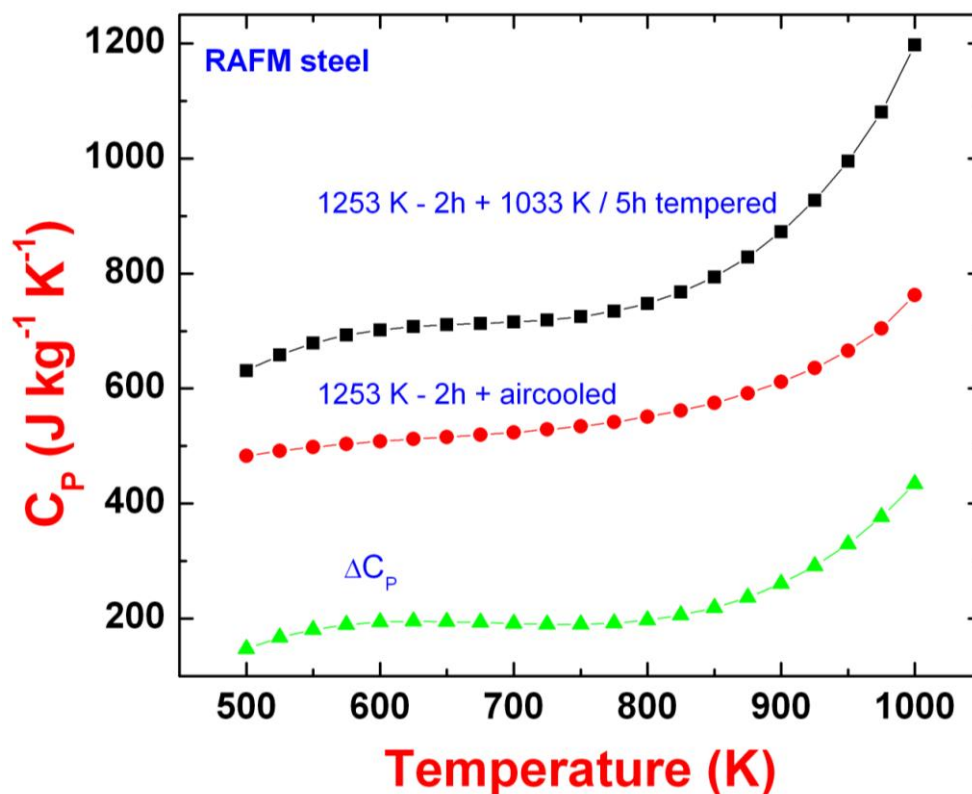


Fig. 6.4: The  $C_p$  of martensite, tempered martensite and their difference with temperature are plotted

In **Table 6.7**, the difference in  $C_p$  ( $\Delta C_p$ ) between the martensitic microstructure and the one tempered for 5 hours is tabulated at select temperature intervals. As can be seen, the heat capacity of the tempered sample is higher than that of the virgin martensite; but what is remarkable about this observation is that this difference is becoming significant at high temperatures ( $T \geq 923$  to  $973$  K), where the thermally

activated relaxation processes are poised to become active. This aspect is also nicely brought out in **Fig. 6.4**, wherein the rise in  $\Delta C_P$  is rather steep at high temperatures. One important point that must be kept in mind while interpreting this  $\Delta C_P$ , is that the martensite sample had been undergoing concurrent relaxation even as the measurement of its  $C_P$  was going on. In this sense, what is measured in the present study is not the true or exact contribution to  $C_P$  arising from the relaxation processes operating in martensite; but it is expected that at  $10\text{ K min}^{-1}$  heating rate with a minimal prior hold at 373 K for attaining thermal equilibrium, the difference in  $C_P$  estimated in this study is somewhat reflective of the contribution arising from the overall relaxation process operating in martensite.

## 7. Kinetics of $\alpha \rightarrow \gamma$ Phase Transformation

One of the important constituents of a thermokinetic database is information regarding the kinetic aspects of  $\alpha'$ -tempered martensite+carbide  $\rightarrow \gamma$ -austenite transformation, which occurs during the course of heating in a solutionising heat treatment. The kinetics of this *austenitisation* reaction, especially the extent of carbide dissolution under the actual heat treatment conditions (rate of heating, time and temperature in the  $\gamma$ -phase field etc.) is very important in deciding the compositional homogeneity and microstructural nature of high temperature austenite formed. In literature, there have been numerous studies on the austenite formation kinetics in plain carbon, low alloy microalloyed HSLA and few other steels [49-60]. As a result, a set of rich panoramic viewpoints have emerged on various mechanistic aspects of austenitisation transformation in general; yet, the situation with regard to the elucidation of the dominant or rate controlling step is not really transparent. Different mechanisms suggesting interstitial carbon to substitutional solute atom diffusion controlled ones have been proposed in literature for austenitisation in low alloy steels.

Besides, grain boundary or pipe diffusion controlled mechanisms are also thought to be plausible ones in some cases. Further, some researchers have advocated an interface controlled transformation mode for the austenite formation under fast heating conditions. In the case of high Cr-based FM steels, there is still a relative paucity of experimental data on thermodynamic and kinetic quantities associated with the formation of austenite from either virgin martensite or tempered and aged martensite upon high temperature exposure [52-54]. As compared to their low alloyed counterparts, the high solute (Cr, Mo, W, Ta, V, Nb) and low carbon(nitrogen) contents of RAFM renders austenitisation reaction somewhat sluggish. Since the austenitisation is an unavoidable step in the overall processing of these alloys, the present study is intended to provide some useful information in this regard. In particular, the evolution of austenite as a function of temperature is monitored using continuous heating differential scanning calorimetry (DSC) technique. A careful analysis of DSC results is attempted to enlist the basic kinetics aspects of the austenite formation from  $\alpha$ -ferrite + carbide phases.

In **Fig.6.5**, the stack of DSC thermal arrests for the transformation  $\alpha$ +carbides $\rightarrow\gamma$ , obtained at various heating rates are displayed. The austenite start and finish temperatures are marked as  $A_{C1}$  and  $A_{C3}$  respectively. The peak temperature corresponds to the maximum in the rate of formation of austenite. It is found that for very low heating rates ( $1 \text{ K min}^{-1}$ ), the peak profile is somewhat broad and less well resolved as well. Since austenite formation is a typical nucleation and growth phenomenon, the transformation temperatures are expected to be sensitive to the heating rate. This is shown in **Fig. 6.6**. It is clear that both  $A_{C1}$  and  $A_{C3}$  exhibit a pronounced nonlinear increase with the heating rate. In particular, the increase in  $A_{C3}$

is slightly more marked than that of  $Ac_1$ , resulting in the net effect of widening the existence domain  $\alpha$ -ferrite + carbide +  $\gamma$ -austenite phase field for higher heating rates.

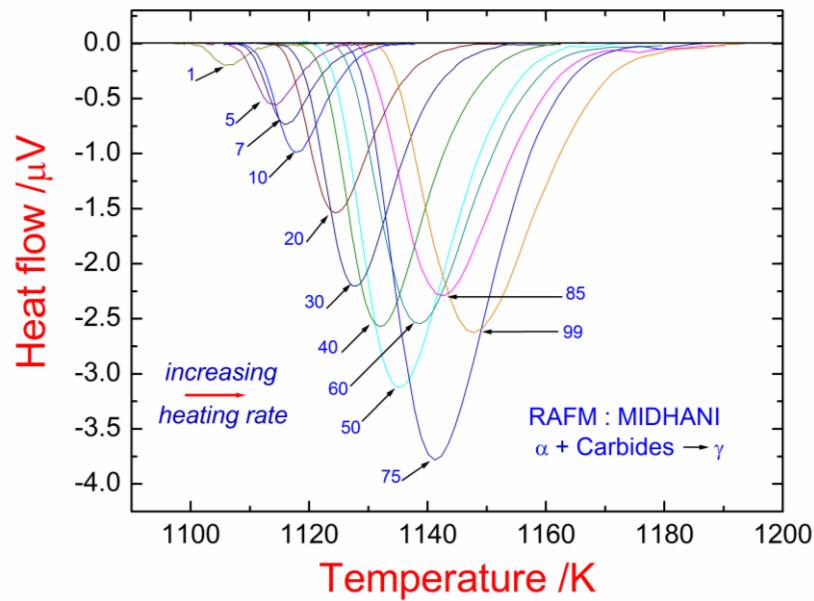


Fig. 6.5. DSC peak profiles for the  $\alpha$ + carbides  $\rightarrow$   $\gamma$  transformation in RAFM

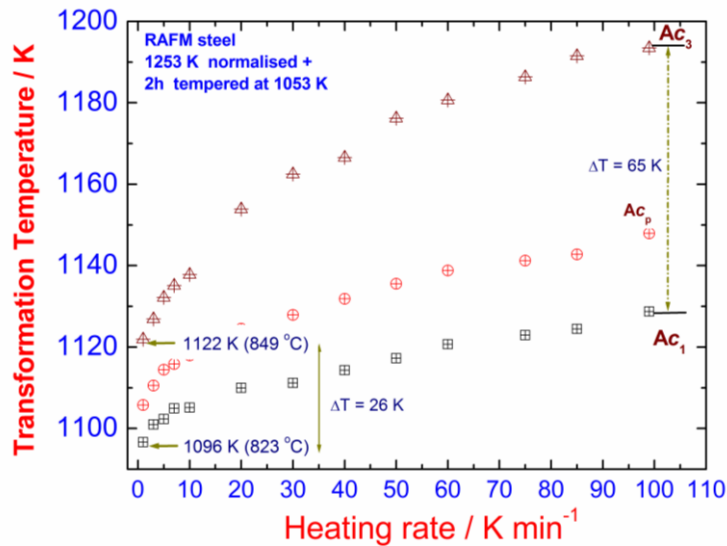


Fig. 6.6. Variation of  $\alpha$ + carbides  $\rightarrow$   $\gamma$  transformation temperature with heating rate.

The fraction of austenite ( $\gamma$ ) formed as a function of temperature ( $T$ ) in the range  $Ac_1 \leq T \leq Ac_3$  is estimated using the following expression

$$\gamma(T) = \left\{ \int_{Ac_1}^T \phi \, dT / \int_{Ac_1}^{Ac_3} \phi \, dT \right\}. \quad (3)$$

Here,  $\int_{Ac_1}^T \phi \, dT$ , is the partial area under the peak in the temperature domain  $Ac_1-T$ . The denominator  $\int_{Ac_1}^{Ac_3} \phi \, dT$  stands for the total peak area covering the entire transformation temperature range. *Eq.(3)* assumes that austenite formation and carbide dissolution is complete upon reaching  $Ac_3$ , although this is not strictly true for higher heating rates [see, drop calorimetry results]. The transformation plots obtained using *Eq. (3)* for different  $\beta$  are displayed in **Fig. 6.7**. The measured  $\gamma$  values are accurate only to about  $\pm 5\%$ .

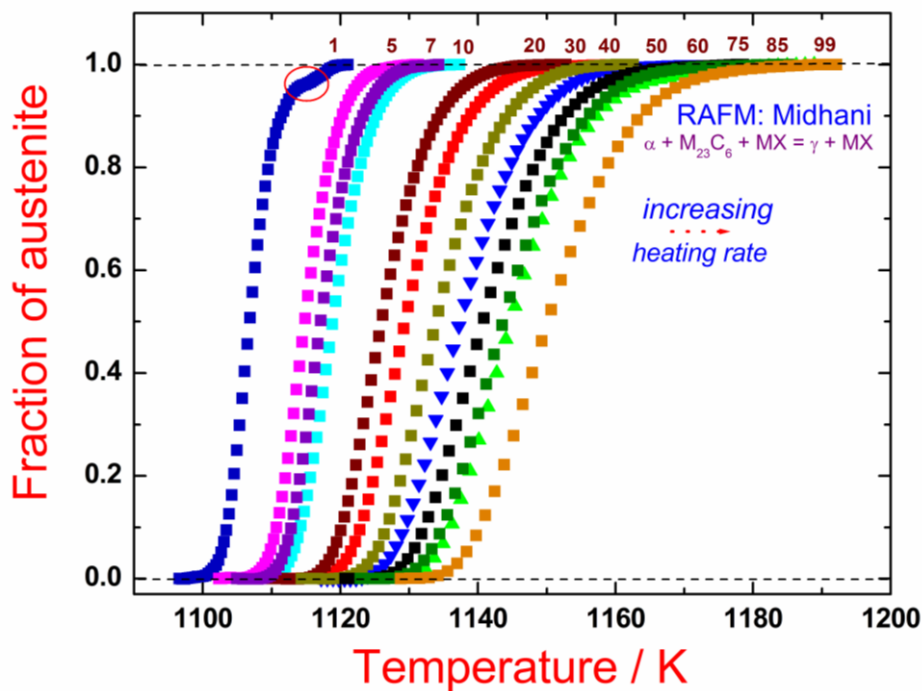


Fig. 6.7.  $\alpha \rightarrow \gamma$  transformation plots for different heating rates

As may be seen, the transformation curves are reasonably sigmoidal in character. Besides, it is also noteworthy that within a certain range of  $\gamma$  values ( $0.25 \leq \gamma \leq 0.75$ ), the slope of transformation curves, namely  $(\partial\gamma/\partial T)_\beta$  for different heating rates (1-20  $\text{K min}^{-1}$ ) is nearly the same. In other words,  $(\partial\gamma/\partial T)_\beta$  is almost independent of  $\beta$  for a small range of  $\beta$  and  $\gamma$  values. This aspect yields certain interesting insight into the kinetics of austenite formation.

In the realm of *model free isoconversional* formalism of analysing the nonisothermal transformation kinetics, the following functional form is often invoked to represent the instantaneous reaction rate [17].

$$(\partial\gamma/\partial T)_\beta = f(\gamma) k(T)(1/\beta). \quad (4)$$

where  $f(\gamma)$  is an empirical reaction model that is consistent with the observed features of the transformation studied. The empirical rate constant  $k$  is often assumed to be the of the Arrhenius form [17]

$$k = k_0 \exp(-Q/RT), \quad (5)$$

with  $Q$  being the effective or apparent activation energy for the *overall* transformation process. Since in the present case  $(\partial\gamma/\partial T)_\beta$  is found to be nearly independent of  $\beta$ , we may make use of the basic rate equation (Eq.4) in the following manner to obtain for a fixed value of transformed fraction ( $\gamma$ ) the following expressions

$$(\partial\gamma/\partial T)_{(T_1, \beta_1)} = f(\gamma) k(T_1) (1/\beta_1); \quad (6)$$

$$(\partial\gamma/\partial T)_{(T_2, \beta_2)} = f(\gamma) k(T_2) (1/\beta_2). \quad (7)$$

$(T_1, \beta_1)$  and  $(T_2, \beta_2)$  represent two arbitrary set of temperature and heating rate combinations for realising a fixed fraction of austenite  $\gamma$ . Since  $(\partial\gamma/\partial T)_{(T_1, \beta_1)} \approx (\partial\gamma/\partial T)_{(T_2, \beta_2)}$  from **Fig. 6.7**, we may obtain the following useful normalising condition namely,

$$k(T_1)/\beta_1 = k(T_2)/\beta_2. \quad (8)$$

The above deduction suggests that  $k/\beta$  is a conserved kinetic quantity in the austenite formation reaction. Thus with increasing  $\beta$ , the rate constant  $k$  should also increase, implying thereby that  $Q$  must exhibit a corresponding decrease as per Eq. (5). It is presumed that  $k_0$  the frequency factor is not affected significantly by the heating rate; but this is not true, as we shall see later. *It must however be mentioned that in reality,*

$(\partial\gamma/\partial T)_\beta$  is strictly not identical for different  $\beta$  values; but in the present case where the transformation plots evince a fair degree of scaling for different  $\beta$ , it is found that the ratio  $\{(\partial\gamma/\partial T)_{(T_1, \beta_1)} \approx (\partial\gamma/\partial T)_{(T_2, \beta_2)}\}$  for a good reasonable range of  $\beta$  values is around 0.95 to 0.98. The deduction that  $k/\beta$  is a constant can also be made use of in obtaining a crude estimate of  $Q$ . Thus, for any fixed  $\gamma$  that is realised at two arbitrary heating rates,  $\beta_1$  and  $\beta_2$ , and at respective temperatures  $T_1$  and  $T_2$ , we may write in the light of Eq. (8) the following.

$$\beta_1/\beta_2 = k_{01} \exp(-Q_1/RT_1)/k_{02} \exp(-Q_2/RT_2) \quad (9)$$

Upon regrouping of terms we get

$$R \ln[(\beta_1 k_{02}/\beta_2 k_{01})] + Q_1/T_1 = Q_2/T_2. \quad (10)$$

Assuming  $k_{01} \approx k_{02}$ , we may further simplify this expression to get

$$R \ln[\beta_1/\beta_2] + Q_1/T_1 \approx Q_2/T_2. \quad (11)$$

Eq. (11) may be used to obtain heating rate dependent  $Q_\beta$  values, provided an appropriate initial guess is made with respect to one of them, say  $Q_1$ . Even here, to start with one can assume  $Q_1=Q_2=Q$  for two closely spaced  $\beta$  values and get a rough estimate of  $Q$ . This value can then be refined in an iterative fashion by using it in a suitable transformation model  $f(\gamma)$ , and effecting an optimal fit of the experimental data. In the present case, we refrain from employing this simplification, as meaningful interpretation of  $Q$  necessitates the invocation of a suitable model for austenitisation. It is desirable that such a model is consistent with the basic nature of  $\alpha \rightarrow \gamma$  structural transformation and carbide dissolution. This is discussed below.

### 8.0. Mechanistic aspects of $\alpha$ +carbides $\rightarrow \gamma$ transformation

Admittedly, the formation of austenite from mixed  $\alpha$ -ferrite+carbide microstructure is not a simple metallurgical phenomenon. It is clear that upon

reaching  $A_{c1}$ , the lower critical temperature, both the dissolution of carbide and the structural transformation of  $\alpha$ -ferrite  $\rightarrow$  austenite begin to occur concurrently with *different* velocities. Taking a low carbon iron, we know the structural transformation of (carbon lean) ferrite to austenite is basically an interface diffusion-controlled process, while carbide dissolution is a bulk or volume diffusion controlled phenomenon. The heterogeneous nucleation of austenite is catalysed by the presence of abundant ferrite/ carbide interfaces to begin with, although at later stages, some other nucleation sites like ferrite grain boundaries, grain edges and corners *etc.*, need to get activated. This is due to the gradual dissolution of carbide particles in austenite. Thus, the nucleation rate of austenite is one of continuously decreasing with time.

However, assuming that nucleation of austenite is adequately facilitated, the issue then is one of sustaining its growth by enabling the transfer of carbon and slow diffusing substitution atoms like Cr, W, Ta *etc.*, across the growing austenite/ferrite interface. From a mechanistic point of view, the austenite growth is possible even at higher heating rates, if required diffusion is mediated somehow across the growing  $\gamma/\alpha$  interface.

For the case of carbide dissolution however, the steep concentration gradient prevailing at the carbide/austenite or ferrite interface, especially with respect to the slow diffusing substitutional elements dictates, that volume diffusion of these elements in austenite is the rate limiting one [18, 20].

Now in reality both ferrite to austenite and carbide dissolution in growing austenite are not two independent reactions. For very slow heating rates, the system can evolve with the possibility of realising local thermodynamic equilibrium at the interface. Under such circumstances, it is likely that the carbide dissolution might get initiated even at relatively lower temperatures, closer to  $A_{c1}$ , and the reaction

proceeds to a good extent, if not to completion upon reaching  $A_{c3}$ . The dissolution of carbides results in a gradual change in austenite composition and this affects subsequent austenite formation kinetics in an indirect manner by effecting a change in the activation energy for diffusion in austenite.

If on the contrary, the austenitisation is sought under very fast heating conditions, the time scales provided are simply inadequate for the successful progress of carbide dissolution [14], although the ferrite to austenite structural change can still be realised at these high rates. In any case, it is highly unlikely that transformation to austenite proceeds to completion at faster heating rates upon reaching  $A_{c3}$ . A slight superheating and or isothermal hold are often required to realise the formation of homogeneous austenite [16]. For intermediate heating rates, the carbide dissolution and  $\alpha \rightarrow \gamma$  phase change proceed to different extents.

It emerges therefore in the final analysis, that at lower heating rates the overall activation energy is influenced by the dissolution of the carbide phase, while for fast heating conditions,  $Q$  is predominantly reflective of the simple interface diffusion controlled  $\alpha \rightarrow \gamma$  structural change. In DSC, unlike in weld or thermomechanical simulators, only relatively slow heating rates are employed. 100 K/min is not really a fast heating rate, as compared to 1000 and 1000 K/min that are possible in Gleeble. During fast heating conditions, there is not much scope for change in austenite composition, as this would call for a substantial diffusion of substitutional Cr, W, Ta atoms and would therefore entail higher activation energy ( $260 \text{ kJ mol}^{-1}$ ) as compared to interfacial carbon migration. It is rather unfortunate, that extensive diffusion database is currently lacking for many heavy transition metal diffusivities in ferrite and austenite.

In the present study, the overall transformation kinetics is fitted to a simple nonisothermal version of the Kolmogorov-Johnson-Mehl-Avrami (KJMA) form [21].

$$\gamma = 1 - \exp\{-k^n (R(T-T_s)^2/\beta Q)^n\}. \quad (12)$$

It must be noted that in the above model, we have chosen  $T-T_s$  ( $T_s$  is the start onset point in DSC profile) as the independent variable as this corrects for the error incurred in precisely fixing the transformation onset temperature for slow heating rates. As discussed before the values for kinetic quantities namely  $Q$ ,  $k_0$ ,  $T_0$  and  $n$  are dependent on  $\beta$ . These are listed in **Table 6.8**.

**Table 6.8.** Listing KJMA kinetic parameters for  $\alpha \rightarrow \gamma$  transformation in RAFM steel

Heating rate (K min <sup>-1</sup> )	$n$	$Q_{eff}$ kJ mol <sup>-1</sup>	$k_0$ 10 <sup>7</sup> /s <sup>-1</sup>	$R^2$
1	1.66	278	0.57	0.997
3	1.66	278	0.57	0.997
5	1.66	263	1.3	0.997
7	1.49	263	3.7	0.997
10	1.56	265	5.1	0.997
20	1.38	267	8.3	0.997
30	1.38	267	10.1	0.997
40	1.31	265	13.4	0.997
50	1.21	264	11.9	0.997
60	1.13	267	22.5	0.997
75	1.13	268	10.6	0.997
85	1.10	265	16.2	0.997
99	1.05	262	7.6	0.998

As may be judged from this table, KJMA model is able to account for the observed transformation kinetics. There is a good convergence of  $Q$  values around 260 to 270 kJ mol<sup>-1</sup>, and that a mild decreasing tendency with increasing heating rate is noticed. The value of  $n$ , the Avrami exponent for the overall transformation kinetics, ranges about 1 to 1.6. One final point is that the measured values of  $Q_{eff}$  is of the same order as that of the activation energy for chromium diffusion in the austenite phase of a low alloy–low carbon steel ( $\sim 260$  kJ mol<sup>-1</sup>)[63].

The higher values of  $Q_{eff}$  implies that simple carbon diffusion in austenite model is not applicable for the  $\alpha \rightarrow \gamma$  reaction in high-chromium steels such as RAFM. The experimental study of Lenel [38] and the electron microscopy characterisation of austenite formation reaction in high-chromium model alloys by Shtansky *et al* [64] reinforce this viewpoint. It must be added that in a recent study on the experimental measurement of  $\alpha/\gamma$  interface mobility during austenite formation from ferrite in interstitial-free low-alloy steels, an effective activation energy of about 287 kJ mol<sup>-1</sup> is reported for the interface controlled transformation [65].

The heating rate dependence of the measured austenite formation kinetics in a fully tempered martensite steel is graphically illustrated in **Fig. 6.8**. *A review of*

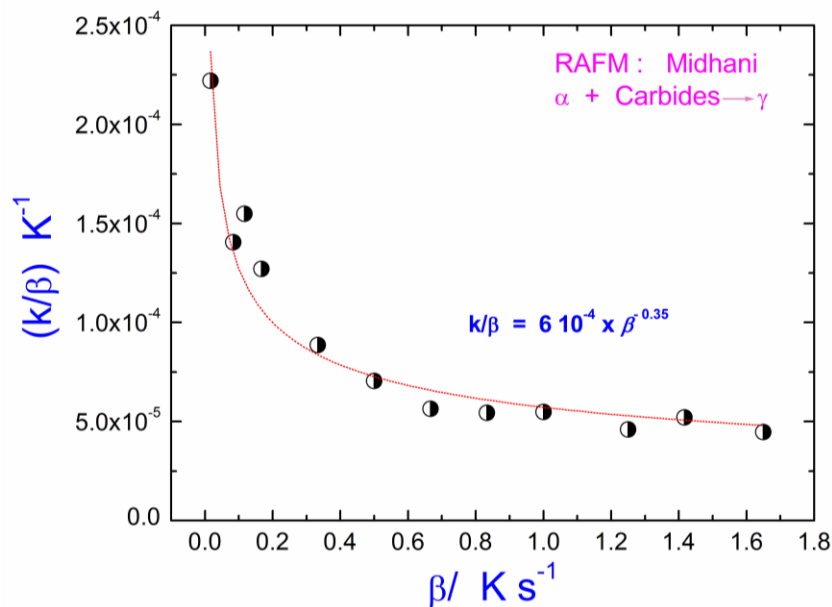


Fig. 6.8. Heating rate dependence of the kinetic constant  $k$  for the  $\alpha$ +carbide $\rightarrow\gamma$ , transformation in RAFM steel

*available literature reveals that the understanding of the kinetics of austenite formation and carbide dissolution in high-chromium steels used in both thermal and nuclear power plants is still far from complete and more studies are needed to shed further light on this important issue.*

## 9.0. Continuous Heating Transformation Diagram for RAFM Steel

The essence of dynamic calorimetry results on RAFM steel is nicely synthesized in the continuous heating transformation (CHT) diagram, shown in Fig. 6.9. Two important points emerge from this plot. The width of  $\alpha+\gamma$  two phase region (actually,

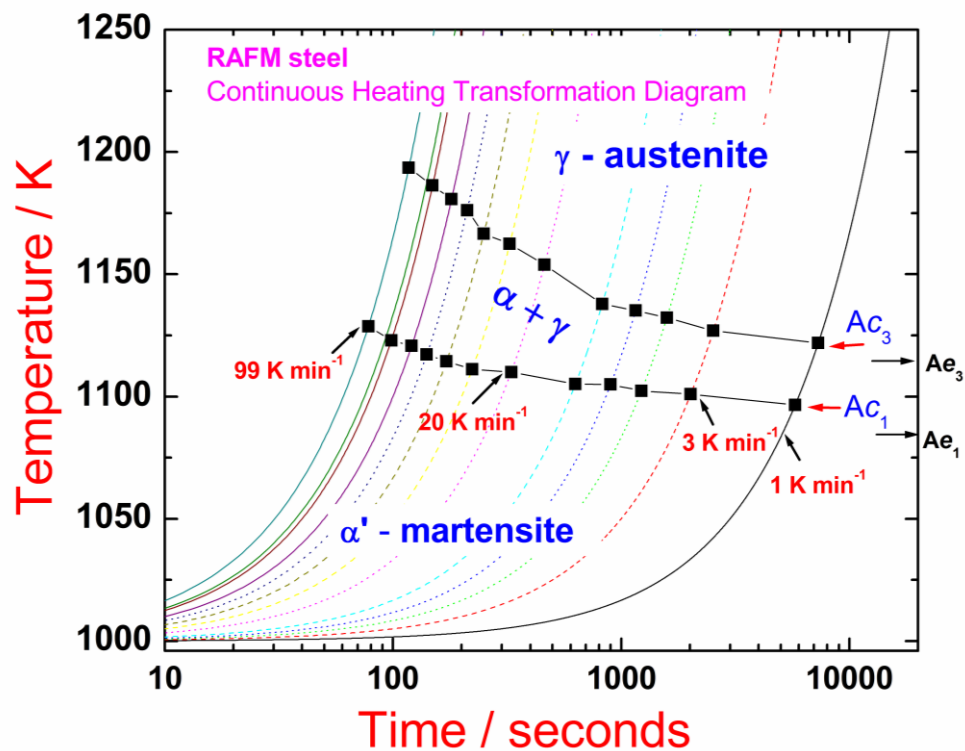


Fig. 6.9. Continuous Heating Transformation (CHT) diagram for RAFM steel

it is  $\alpha+\gamma$  carbides three phase domain) shows considerable increase with heating rate. The practical implication is that higher heating rates are not that useful in achieving a good degree of homogenization in austenite, especially since Ac<sub>3</sub> is more sensitive to heating rate. This aspect is important in post weld heat treatment of RAFM steel. Unlike the typical C-curve of TTT or CCT plots, CHT diagram is monotonous in its behavior, since both driving force and diffusivity increase as temperature increases. Although, the details are shown here, the CHT diagram is sensitive to the starting microstructure. With a 100% martensite microstructure as starting microstructure, the  $\gamma$ -austenite formation may be intercepted by tempering reaction, especially at lower heating rates. In such a case, the observed CHT will be somewhat complex, as the

measured  $Ac_1$  and  $Ac_3$  will vary somewhat nonsystematically with increasing heating rates. It must be admitted that it is rather difficult to treat these overlapping transformations as compared to austenite formation in a fully tempered martensite structure.

## 10.0 Summary

(1) A differential scanning calorimetry determination of on-heating phase transformation temperatures and specific heat have been made for normalized and tempered reduced activation ferritic / martensitic steels.

(2) The  $\alpha$ -ferrite +  $M_{23}C_6$  + MX  $\rightarrow$   $\gamma$ -austenite +  $M_{23}C_6$  + MX, transformation start and finish temperatures namely  $Ac_1$ , and  $Ac_3$ , are found to be 1104 and 1144 K respectively.

(3) The martensite transformation temperatures are mildly sensitive to the starting microstructure. For the steel normalized at 1253 K and tempered for 120 minutes at 1033 K., the martensitic start ( $M_S$ ) and finish ( $M_f$ ) temperatures are of the order of 714 and 618 K respectively

(4) The heat capacity of normalised and tempered microstructures at room temperature varies from 500 to 550  $J kg^{-1} K^{-1}$ . However, the difference between them is found to be a strong function of temperature, with the  $C_p$  of tempered microstructure turning out to be larger than the untempered martensite by about 300  $J kg^{-1} K^{-1}$  at 1000 K.

(5) The  $\alpha \rightarrow \gamma$  diffusional transformation has been studied as a function of several heating rates. The transformation kinetics is found to be well described by KJMA formalism, with an effective activation energy that is decided by Carbide diffusion step. The estimated activation barrier of about 270  $kJ mol^{-1}$  implies that slow substitutional diffusion of Cr may be rate controlling.

## References

1. T. Fujita, *ISIJ International*, **32** (1992) 175.
2. Ulrich E Klotz, Christian Solenthaler and D. J. Uggowitzer, *Mater. Sci. Engg.*, **A476** (2008) 186.
3. R. L. Klueh, *Current opinion in solid St. & Mater. Sci.*, **8** (2004) 239.
4. R. L. Klueh, K. Ehrlich and F. Abe, *J. Nucl. Mater.*, 191-194 (1992) 116.
5. J. Orr, F. R. Beckitt, G. D. Fawkes, in : Ferritic steels for fast reactor steam generators, (Eds.) S. F. Pugh and E. A. Little, BNES (1978), London, 91.
6. A. G. Ioltukhovsky, V. P. Kondratev, M. V. Leont'eva Smirnova, S. N. Votinov, V. K. Shamardin, A. V. Povstyanko and T. M. Bulanova, *J. Nucl. Mater.*, **233-237** (1996) 299.
7. R. L. Klueh, *J. Nucl. Mater.*, **378** (2008), 159.
8. R. L. Klueh and P. J. Maziasz, *J. Nucl. Mater.*, **155-157** (1988) 602.
9. M. Tamura, H. Hayakawa, A. Yoshitake, A. Hishinuma and T. Kondo, *J. Nucl. Mater.*, **155-157** (1988) 620.
10. A. Kohyama, A. Hishinuma and D. S. Gelles, *J. Nucl. Mater.*, **233-237** (1996) 138.
11. P. Fernandez, A. M. Lancha, J. Lapena, M. Hernandez-Mayoral, *Fusion Engg. Design*, **58-59** (2001) 787.
12. A. Danon and C. Servant, *J. Nucl. Mater.*, **321** (2003) 8.
13. Vaclav Foldyna, J. Purmensky and Z. Kuban, *ISIJ Int.*, **41** (2001) S81.
14. K. Sawada, M. Taneike, K. Kimura and F. Abe, *Mater. Sci. Tech.*, **19** (2003) 739
15. M. Tamura, H. Kusuyama, K. Shinozuka and H. Esaka, *ISIJ Int.*, **47** (2007) 317.
16. K. Yamada, M. Igarashi, S. Muneki and F. Abe, *ISIJ Int.*, **42** (2002) 779.
17. F. Abe, *Mater. Sci. Engg.*, **A319-321** (2001) 770.
18. M. Tamura, Y. Haruguchi, M. Yamashita, Y. Nagaoka, K. Ohinata, K. Phnishi, E. Itoh, K. Shinozuka and H. Esaka, *ISIJ Int.*, **46** (2006) 1693.
19. K. Asakura, Y. Yamashita, T. Yamada, K. Shibata, *ISIJ inter.*, **30** (190) 937.
20. A. Zielinska-Lipiec, A. Czyrska-Filemonowicz, P. J. Ennis and O. Wachter, *J. Mater. Proc. Tech.*, **64** (1997) 397.

21. M. Tamura, H. Kusuyama, K. Shinozuka and H. Esaka, *ISIJ Inter.*, **47** (2007) 317.
22. Y. Tsuchida, K. Okamoto and Y. Tokunaka, *ISIJ Inter.*, **35** (1995) 317.
23. F. Abe, T. Horiuchi, M. Taneike and K. Sawada, *Mater. Sci. Engg.*, **A378** (2004) 299.
24. F. Abe, T. Noda, H. Araki, S. Nakazawa, *J. Nucl. Mater.*, **179-181** (1991) 663.
25. S. G. Hong, W. B. Lee and C. G. Park, *J. Nucl. Mater.*, **288** (2001) 202.
26. P. Fernandez, M. Hernandez-Mayotal, J. Lapena, A. M. Lancha, G. De Diego, *Mater. Sci. Tech.*, **18** (2002) 1353.
27. T. Horiuchi, M. Igarashi and F. Abe, *ISIJ inter.*, **42** (2002) S67.
28. Kouichi Maruyama, Kota Sawada and Jun-ichi-Koike, *ISIJ Int.*, **41** (2001) 641.
29. S. Raju, B. Jeyaganesh, A. Banerjee and E. Mohandas, *Mater. Sci. Engg.*, **A465** (2007) 29.
30. S. Raju, N. S. Arun Kumar, B. Jeyaganesh, E. Mohandas and U. Kamachi Mudali, *J. Alloys Compd.*, **440** (2007) 173.
31. B. Jeyaganesh, S. Raju, E. Mohandas, S. Murugesan and M. Vijayalakshmi, *Int. J. Thermo Phys.*, accepted for publication.
32. Q. Chen and B. Sundman, *J. Phase Eq.*, **22** (2001) 631.
33. P. D. Desai, *J. Phys. Chem. Ref. Data*, **15** (1986) 967.
34. M. J. Richardson, in : K. D. Maglic, A. Cezairliyan, V. E. Peletsky (Eds.), *Compendium of Thermophysical Property Measurement Techniques*, vol. **2**, Plenum Press, New York, 1992, p.519.
35. S. Raju, unpublished research (2013).
36. A. Danon and C. Servant, **45** *ISIJ Inter.*, (2005) 903.
37. A. Kroupa, J. Havrankova, M. Coufalava, M. Svoboda and J. Vrestal, *J. Phase Eq.*, **22** (2001) 312.
38. U. R. Lenel and R. W. K. Honeycombe, *Metal. Sci.*, **18** (1984) 201.
39. B. Jeyaganesh, S. Raju, E. Mohandas and M. Vijayalakshmi, *Defect & Diffusion Forum*, **279** (2008) 85.

40. J. Cermak, J. Ruzickova and A. Pokorna, *Scripta metal. mater.*, **32** (1995) 1631-1635.
41. A. Roosz, Z. Gacsi, and E.G. Fuchs, *Acta Metall.*, **31** (1983) 509.
42. S. K. Nath, S. Ray, V.N.S. Mathur, and M. L. Kapoor *ISIJ Int.*, **34** (1994) 191.
43. H. G. Reed, *Scripta Mater.*, **37** (1997) 151.
44. C.Garcia de Andres, F.G. Caballero, C. Capdevila, and H.K.D.H. Bhadeshia, *Scripta Mater.*, **39** (1998) 791.
45. R.C. Reed, T. Akbay, Z. Shen, J.M. Robinson, J.H. Root, *Mater. Sci. Engg.*, **A256** (1998) 152.
46. F. G. Caballero, C. Capdevila and C. G. De Andres, *ISIJ Int.*, **41** (2001) 1093.
47. W. Zhang, J. W. Elmer and T. Deb Roy, *Scripta Mater.*, **46** (2002) 753.
48. F. G. Caballero, C. Capdevila and C. G. de Andres, *ISIJ Int.*, **43** (2003) 726.
49. F. L. G. Oliveira, M. S. Andrade, A. B. Cota, *Mater. Character.*, **58** (2007) 256.
50. U. R. Lenel and R.W.K. Honeycombe, *Metal Sci.*, **18** (1984) 201.
51. G. P. Krielaart, C. M. Brakman and S. Van der Zwaag, *J. Mater. Sci.*, **31** (1996) 1501.
52. J. C. Brachet, L. Gavard, C. Boussidan, C. Lepoittevin, S.Denis and C. Servant, *J. Nucl. Mater.*, **258-263** (1988) 1307.
53. A Danon, and A. Alamo, *J. Nucl. Mater.*, **307-311** (2002) 479.
54. A. Danon, C. Servant, A. Alamo, and J. C. Brachet, *Mater. Sci. Engg.*, **A348** (2003) 122.
55. S. Malinov, Z. Guo, W. Sha and A. Wilson, *Met. Mater. Trans.*, **32A** (2001) 879.
56. C. Garcia de Andres, C. Caballero, C. Capdevila, L. F. Alvarez, *Mater. Charact.*, **48** (2002) 101.
57. S. Vyazovkin, *J. Thermal Analysis and Calor.*, **83** (2006) 45.
58. R. Gullberg, *J. Iron Steel Inst.*, **211** (1973) 59.
59. M. Hillert, K.Nilsson and L.E. Torndahl, *J. Iron Steel Inst.*, **209**, (1971) 49.
60. A. Bjarbo and M. Hatterstrand, *Metall. Trans.*, **32A**, (2001) 19.
61. F. Liu, F. Sommer, and E.J. Mittemeijer, *J. Mater. Sci.*, **39** (2004) 1621.

62. J. W. Christian, *The theory of Transformations in Metals and Alloys*, Pergamon Press, Oxford, (1975) p. 542.
63. Z. Tokei, K. Hennessen, H. Viefhaus and H. J. Grabke, *Mater. Sci. Tech.*, **16** (2000) 1129.
64. D. V. Shtansky, K. Nakai and Y. Ohmori, *Z. Metallkd.*, 90 (1999) 25.
65. E. Schmidt, D. Soltesz, S. Roberts, A. Bednar and S. Sridhar, *ISIJ Int.*, **46** (2006) 1500.

## Characterisation of Martensitic Phase Transformation in RAFM steel

### 1.0. Introduction

A study of martensite formation in high chromium reduced activation ferritic-martensitic steels is of interest in both scientific and technological perspectives. The formation of hard and brittle martensite as a result of solutionising and quenching heat treatment and its subsequent tempering to achieve the desired balance between toughness and strength constitute the core physical metallurgy of modern power plant steels [1-10]. Not surprisingly therefore, numerous studies, both on experimental [11-48] and modelling–simulation fronts [49-85] have been conducted till date to understand the phase and microstructural stability of these alloys upon high temperature service-exposure and the attending changes in physical and mechanical properties in terms of simple intuitively understood metallurgical concepts. Thanks to the immense and coordinated worldwide research, the present day high-chromium power plant steels have scientifically tailored chemical compositions, melting practices and thermomechanical processing schedules that make possible the attainment of fairly stable microstructure with desired physical and mechanical properties [1, 2].

Admittedly, the bulk of the current characterisation research on modern 9Cr–based ferritic steels are at the interface of physical, mechanical and process metallurgy, with relatively few of these investigations devoted exclusively to probing the fundamental thermodynamic and kinetic aspects of phase stability [10, 26, 49, 50, 52-56,58]. It is needless to stress the fact that a fundamental study on thermodynamics

and kinetic considerations of phase stability is indeed germane to evolving a strategically transparent approach to alloy design [86]. It is amidst this background that we have undertaken a comprehensive calorimetry characterisation of various on-heating diffusional phase transformations up to melting on RAFM, the results of which are presented in previous Chapters [see also Ref. 87]. Owing to reasons of restricted scope, and to avoid unnecessary clutter in discussion, these earlier chapters did not include details of the diffusionless martensitic transformations that follow as a result of cooling from the high temperature  $\gamma$ -austenite phase field. A comprehensive understanding of the martensite formation characteristics, especially its kinetics as a function of process parameters like time and temperature of austenitisation and cooling rate from the austenite phase field is rather essential from the point of view of arriving at the optimal solutionising & tempering treatment conditions [17]. It is the purpose of the present chapter to discuss the details on the basic kinetic aspects of martensite formation in RAFM steel using dynamic calorimetry technique.

## **2.0. Experimental Plan**

All the DSC runs were carried out with fresh samples in high pure (Iolar grade 2) flowing argon (50 ml per minute) atmosphere. The Fe-80 mass ppm C alloy (Aldrich Chemicals) was used as the temperature and heat flow calibrant. The precision of temperature measurement is estimated to be  $\pm 2$  K in 673-1373 K region. The cooling rates employed were varied from 1–100 K min<sup>-1</sup> and the soaking time in the  $\gamma$ -austenite phase field was varied from 1 to 120 minutes with about 10 discrete unequal time steps.

Since the present study aims at characterising the athermal martensite formation upon controlled cooling, the following experimental plan is adopted. The starting microstructure for all our experiments is obtained by solutionising the steel at

1253 K for 15 minutes, followed by air-cooling to room temperature. Subsequent tempering at 1033 K for about 30 minutes is carried out in air. The choice of 1253 K as the solutionising temperature is quite typical of the normalising practice adopted in the case of similar high chromium reduced activation steels, such as Eurofer [89]. We have also seen earlier in this report that higher solutionising temperature is needed for getting homogeneous single phase austenite.

In one set of experiments, the normalised and tempered (N&T) samples are heated inside the DSC cell at a fixed rate of  $10 \text{ K min}^{-1}$  under flowing high pure argon atmosphere to the required solutionising temperature in  $\gamma$ -austenite regime. The samples are kept for different time periods, in the range 1 to 120 minutes at this temperature. At the end of this isothermal holding session, the samples were cooled to room temperature at a constant rate of  $99 \text{ K min}^{-1}$ . This set of experiments has been designed to monitor the effect of holding time in the austenite region on martensite transformation characteristics under constant cooling rate. In the present study, we have selected two solutionising temperatures in the  $\gamma$ -austenite region, namely 1253 and 1323 K respectively. It is found that prolonged exposures at temperatures exceeding about 1373 K resulted in some  $\delta$ -ferrite formation [87] and it is desired to avoid the formation of this phase, as this will complicate the straight-forward interpretation of the major factors that influence the martensite formation kinetics [90].

In the second set of experiments designed to estimate the critical cooling rate needed for producing martensite, an array of samples were austenitised at a fixed temperature of 1253 K for a fixed time of about 15 minutes. These samples were subsequently cooled to room temperature at different rates ranging from 1 to  $99 \text{ K min}^{-1}$ . Further, the quenched in microstructure of these samples were also

characterised by metallography and hardness measurements to assess the extent of martensite formation under different cooling conditions. For metallography studies, the specimens were ground and polished in the standard manner and for revealing the prior austenite grain boundaries, a mild initial etch with 2% nital, followed by another using Villella's reagent was carried out. The light microscopy observations were made using *Leica* MeF4A optical microscope equipped with digital image acquisition. The microhardness measurements were carried out in a *Leitz* microhardness tester using 100 g load. In general, about eight to ten hardness measurements were made and the average value is reported here. Samples for thin foil transmission electron microscopy study were obtained by the ion milling technique. The electron microscopy observations were made in a Philips CM 20<sup>®</sup> microscope operating at 200 keV. In the following section, the major experimental results are presented in a systematic fashion.

### **3.0. Results**

#### *3.1. Basic microstructure*

In **Fig. 7.1(a)**, the typical optical micrograph corresponding to 1253 K /15 minutes normalised microstructure is portrayed. The presence of nicely outlined prior austenite grain boundaries enclosing packets of lath martensite is immediately apparent. In addition, it is also evident that some undissolved carbide particles are still present after 1253 K /15 min normalisation treatment. However, their volume fraction is expected to be small as compared to tempered condition. In **Fig. 7.1(b)**, the transmission electron micrograph illustrates the typical dislocation ridden morphology of lath martensite and the stray presence of undissolved carbide particle, marked by arrow. In **Fig. 7.1(c)**, the effect of tempering at 1033 K for 30 minutes is illustrated. Copious amount of small carbide precipitates are seen to decorate prior austenite,

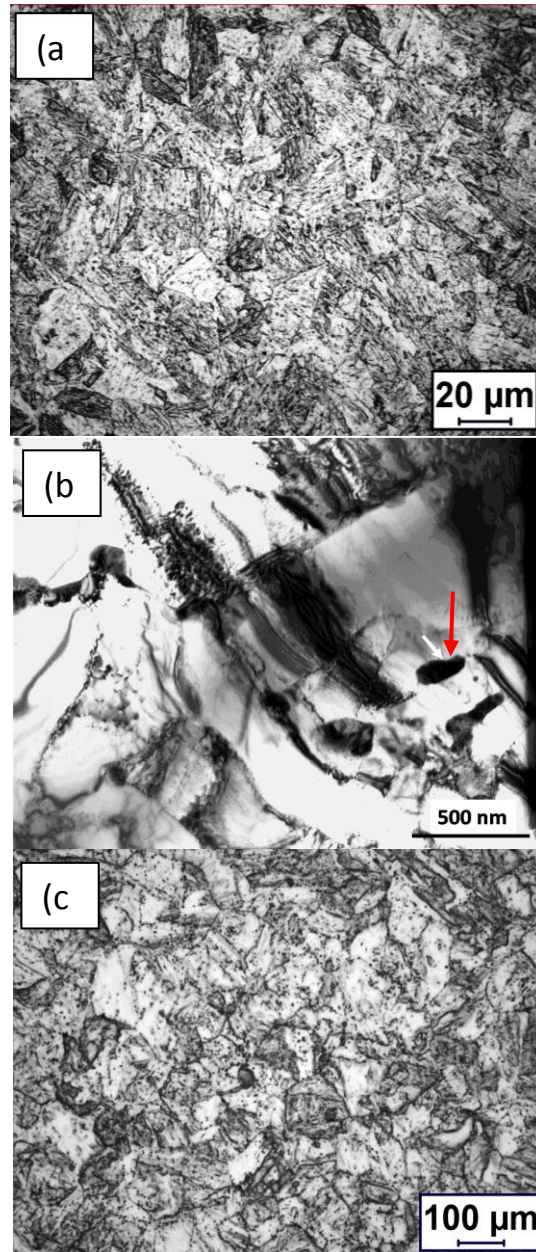


Fig. 7.1(a): The optical micrograph of the 1253 K/15 minutes normalised sample showing packets of lath martensite and well delineated prior austenite grain boundaries. (b): The bright field TEM micrograph of the 1253 K/15 minutes normalised sample showing lath martensite and a carbide particle marked by arrow; 1(c): The optical micrograph showing the effect of tempering at 1033 K for 30 minutes

interlath and intercolony boundaries of the tempered martensite matrix. The microhardness measurements revealed that the martensite produced after the normalizing treatment possessed a hardness value, in the range 425-435 VHN, and

following tempering at 1033 K for 30 minutes, the hardness tapered down to 250 VHN. These values are in expected order for the generic 9Cr-based steels [91].

### 3.2. DSC results of martensitic transformation: critical cooling rate determination

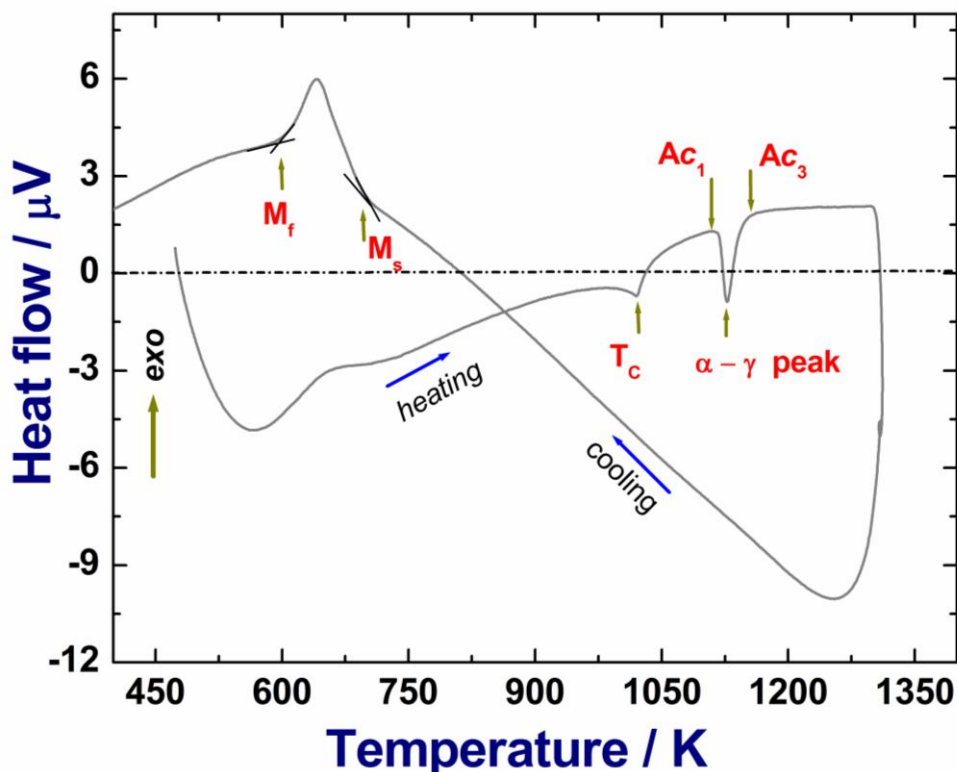
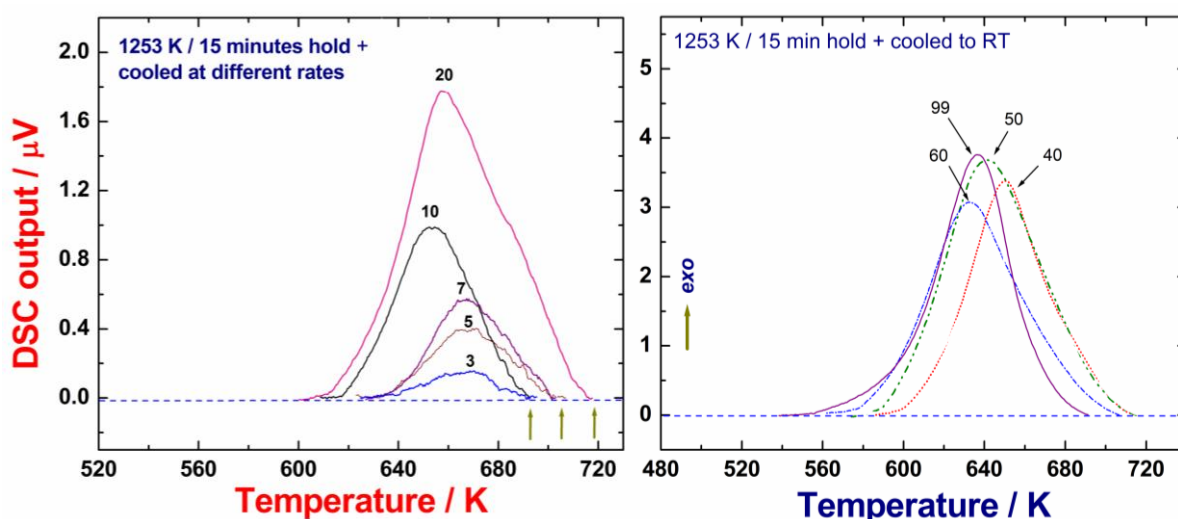


Fig. 7.2: The DSC profile recorded at  $30 \text{ K min}^{-1}$  scan rate, showing clearly marked endothermic and exothermic transformation arrests during heating and cooling cycles respectively

In Fig. 7.2, a typical DSC profile obtained during heating of the normalised and tempered sample to 1253 K and cooling thereupon at  $30 \text{ K min}^{-1}$  after 15 minutes hold, is illustrated. Apart from two distinct endothermic on-heating transformation peaks which arise respectively from the magnetic and  $\alpha$ -ferrite + carbide  $\rightarrow \gamma$ -austenite, phase changes [26, 87], the presence of a *dominant exothermic* peak in the cooling cycle due to  $\gamma$ -austenite  $\rightarrow \alpha'$ -martensite formation is also clearly evident. The on-cooling transformation onset and offset temperatures, normally designated as the martensite start ( $M_s$ ) and finish ( $M_f$ ) temperatures have also been clearly marked in

**Fig. 7.2.** In addition, it should also be noticed that the area enclosed by the martensite transformation peak and hence the net martensite transformation enthalpy ( $\Delta^{\circ}H^{\gamma \rightarrow \alpha'}$ ) is considerably larger than the corresponding value ( $\Delta^{\circ}H^{\alpha \rightarrow \gamma}$ ) obtained for its on-heating diffusional counterpart, namely  $\alpha$ -ferrite+ carbide  $\rightarrow$   $\gamma$ -austenite, transformation.

Since it is well known that the ease of martensite formation depends sensitively on the cooling rate [17], a set of different cooling rates in the range 1 to 99  $\text{K min}^{-1}$  was imposed on different, but closely identical samples to determine the



*Fig. 7.3(a):* The collage of exothermic transformation peak profiles obtained for lower range of cooling rates. The austenitising conditions are 1253 K/ 15 minutes. *Fig. 7.3(b):* Same as figure 7.3(a) with peak profiles obtained for higher range of cooling rates

critical cooling rate that is necessary to obtain nearly 100 percent martensite. In **Fig. 7.3(a) and 7.3(b)**, the peak profiles representing martensite formation that were obtained during cooling from 1253 K at different rates have been presented. Incidentally, it must be mentioned that for very slow cooling of less than about 3  $\text{K min}^{-1}$ , no discernible exothermic peak due to martensite transformation is obtained in the present study. Moreover, it is also interesting to note that although a shallow exothermic peak is observed for some moderate cooling rates, such as 3 to 5  $\text{K min}^{-1}$  (**Fig. 7.3(a)**), the quantum of martensite formed in these cases is rather meagre. With

this background information, it is clearly seen from the nature of the peak profiles shown in **Fig. 7.3(a)** that the area of the transformation peak shows a gradual increase with increasing cooling rate in the low cooling rate regime, and this attains saturation only at about  $40 \text{ K min}^{-1}$  (**Fig. 7.3b**). This indicates that in the low to moderate cooling rate regime, the extent of total martensite formed exhibits an increase with cooling rate.

In **Fig. 7.4**, the measured sensitivity of  $M_s$  and  $M_f$  temperatures to increasing cooling rate is graphically portrayed. It may be seen that notwithstanding the scatter in

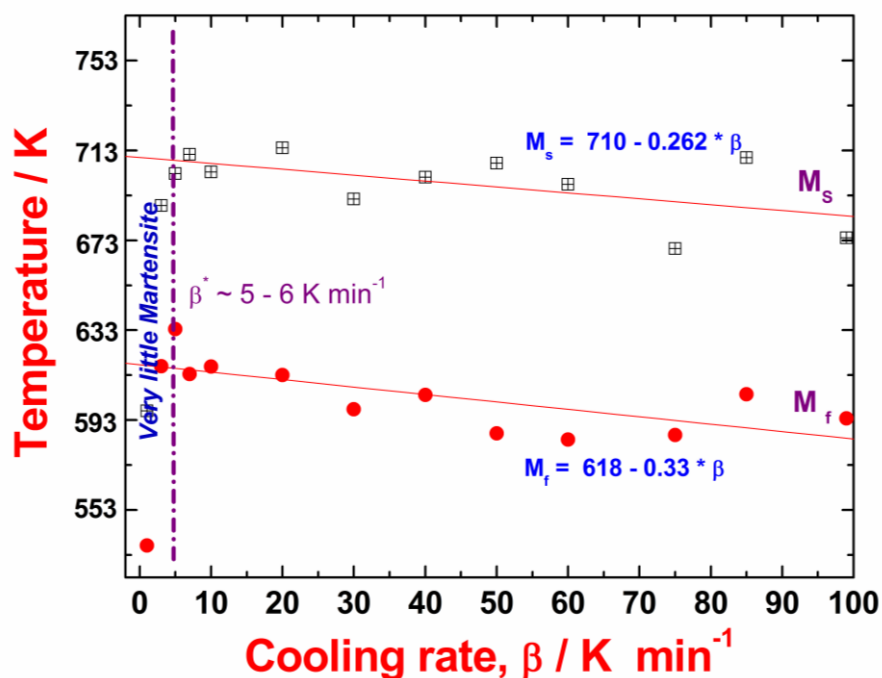


Fig. 7.4 Variation of  $M_s$  and  $M_f$  temperatures with cooling rate for 1253 K solution annealed samples

the transformation temperature data which is generally the case with martensitic transformation in high chromium ferritic steels [91], a small decrease in martensite start ( $M_s$ ) and finish ( $M_f$ ) temperatures with increasing cooling rate is readily apparent [26]. *But the important point to observe here is that for low cooling rates less than about  $5 \text{ K min}^{-1}$ , the measured onset transformation point does not correspond to the*

*martensite product, but instead to the  $M_{23}C_6$  carbide precipitation in  $\alpha$ -ferrite matrix.*

This latter fact is clearly inferred from the cooling cycle DSC profile recorded for  $1 \text{ K min}^{-1}$  and this is displayed in **Fig. 7.5**. In this figure, the broad exothermic trough that is, the hatched area seen after ferrite formation at  $833 \text{ K}$  corresponds to the continuous carbide precipitation event. In the present set of experiment, the carbide precipitation is seen to persist right down to  $592 \text{ K}$ .

Reverting our attention back to martensite formation during controlled cooling, we may say that it is only in excess of the critical cooling rate of about 5 or 6

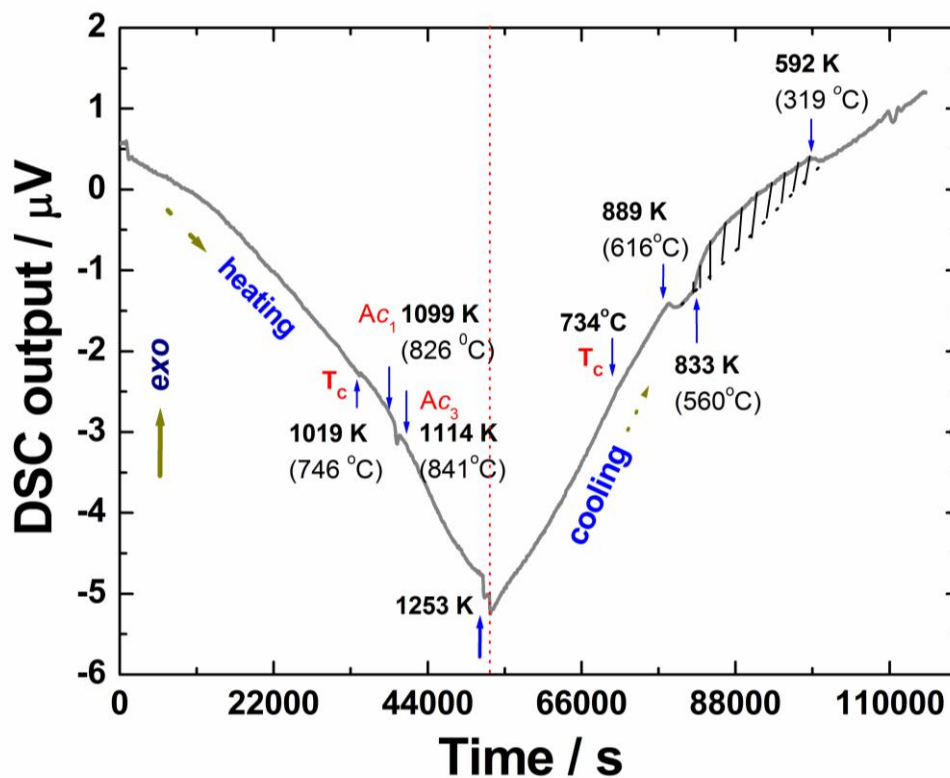


Fig. 7.5: The DSC profile pertaining to  $1 \text{ K min}^{-1}$  cooling rate. Note the absence of the highly exothermic martensitic transformation peak

$\text{K min}^{-1}$  the onset of a true martensite transformation peak becomes distinctly evident in our DSC study. This fact is even more dramatically displayed in **Fig. 7.6**, wherein the microhardness values of the martensite product are plotted against the corresponding cooling rate. The lower bound value of the hardness noted in the 1-3 K

$\text{min}^{-1}$  region corresponds to the  $\alpha$ -ferrite phase formed out of diffusional decomposition of  $\gamma$ -austenite. It is only above the  $5$  to  $6 \text{ K min}^{-1}$  threshold, the formation of martensite upon cooling is clearly attested by the pronounced increase in hardness. As a brief passing remark, it may also be added that the metallographic inspection of  $1 \text{ K min}^{-1}$  cooled sample revealed only  $\alpha$ -ferrite + carbide constituents [91]. In deference to brevity, the relevant microstructural evidence is not presented here.

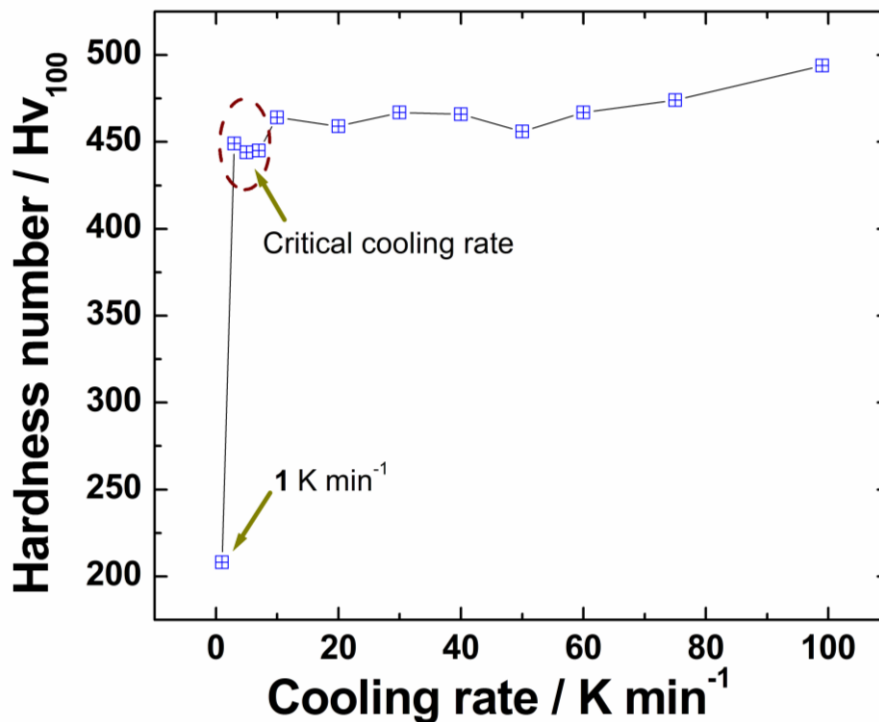


Fig. 7.6 The variation of microhardness of with cooling rate. Note the sudden increase in the hardness values at the critical cooling rate due to martensite formation

### 3.3. Effect of holding time and temperature in the $\gamma$ -austenite region on martensite formation

In **Fig. 7.7(a)** and **7.7(b)** the DSC peak profiles obtained, when the RAFM steel is cooled from 1253 K at  $99 \text{ K min}^{-1}$ , after different periods of isothermal hold are grouped together. From **Fig. 7.7(a)**, it appears that for holding time up to about 15 minutes at 1253 K, the  $M_S$  and  $M_f$  temperatures are not significantly altered. However, the longer durations of isothermal hold, up to about 120 minutes produce considerable shift in  $M_S$  temperature; in fact the  $M_S$  temperature is found to increase with the austenitising time. As a corollary of this observation, we may also infer that the nucleation of martensite is seemingly facilitated with increasing holding time in the  $\gamma$ -austenite region. In all probability this may be traced to the effect of austenite grain growth on martensite formation kinetics [77, 92]. This will be addressed in

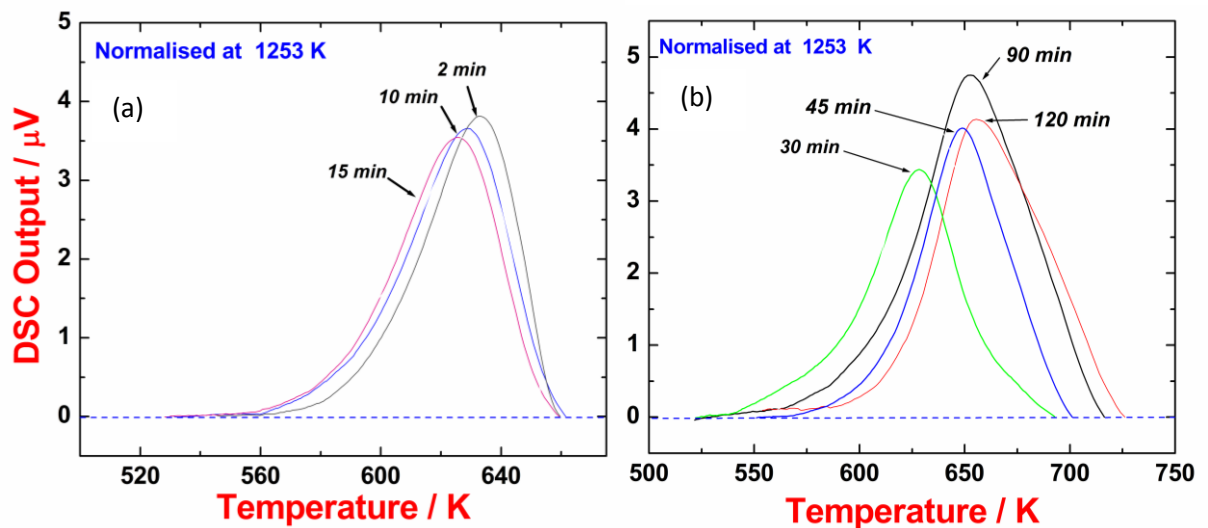


Fig. 7.7. Effect of holding time at 1253 K on martensite peak profile, for a constant cooling rate of  $99 \text{ K min}^{-1}$ . Martensite forms in all cases, but  $M_S$  increases with holding time. detail at a slightly latter point in this section.

In order to study the influence of austenitising temperature on subsequent martensite transformation upon controlled cooling, a similar set of experiments is performed by choosing a slightly higher solutionising temperature of 1323 K. The summary of results obtained is graphically presented in **Fig. 7.8**. Two important findings emerge

from a careful observation of this figure. At the outset, it is important to note that the top two curves in this figure represent the  $M_S$  temperatures for 1323 and 1253 K annealing respectively, while the bottom ones stand for their respective  $M_f$

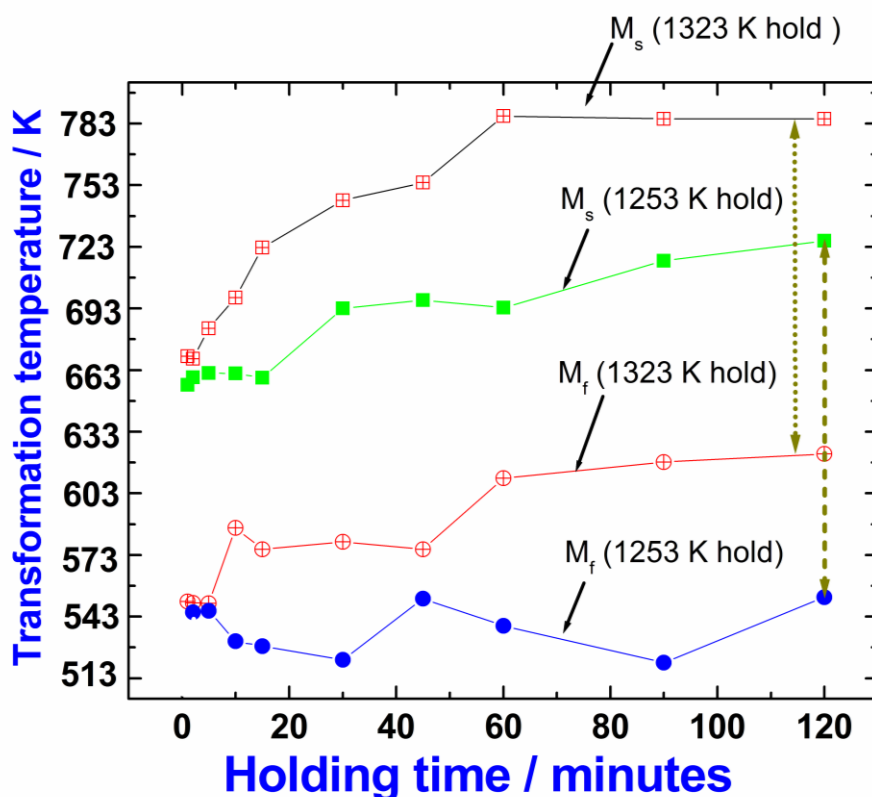


Fig. 7.8. Variation of  $M_S$  and  $M_f$  temperatures with holding time at 1253 and 1323 K. The vertical arrows placed at 120 minutes holding indicate the overall martensitic transformation temperature interval.

temperatures. The vertical dotted arrows indicate the  $M_f$ - $M_S$  temperature gap observed for the largest holding time realised in our experiment, namely 2h. In the first, it is clear that in the case of 1253 K solutionising treatment, the initial variation of  $M_S$  with holding time is rather small; it is only for time periods exceeding about 30 minutes, a gradual increase in  $M_S$  is becoming noticeable. This tendency finally tapers down to reach the saturation behaviour for larger holding times. A somewhat different trend is witnessed in the case of 1323 K solutionising anneal. In this case, a steady increase in  $M_S$  with time is noticed right from the early stages of annealing (*see upper curve in*

**Fig. 7.8).** Therefore, it is clear that the choice of the solutionising temperature plays a crucial role in deciding the initial nucleation and propagation or spreading kinetics of martensite [75-77]. The other important point that emerges from **Fig. 7.8** is that although an increase in the austenitisation temperature from 1253 to 1323 K results in an overall increase of  $M_S$ , there is not much of a change in the effective  $M_f$ - $M_S$  temperature interval, especially for longer periods of anneal in the  $\gamma$ -austenite domain. This is clearly reflected from the approximately equal length of vertical dotted arrows in **Fig. 7.8**. Thus, apart from the initial nucleation aspects of martensite formation, the overall martensite spread kinetics does not seem to be appreciably influenced by a small increase in the austenitisation temperature.

#### 3.4. Carbide dissolution in austenite and its effect on martensite formation

One of the crucial factors that affect austenite grain size, its composition and hence the martensite formation characteristics is the dissolution kinetics of carbides. It is well known that 9Cr steels depending on minor alloying additions can have both  $M_{23}C_6$  and MX type carbides after standard normalising and tempering treatment. Of these, the major  $M_{23}C_6$  carbides dissolve at the somewhat lower austenitisation temperatures of 1253 to 1323 K. Their dissolution kinetics is somewhat sluggish due to slow chromium diffusion. In case of Ta and W containing steels, the diffusivity is expected to be even little lower. On the other hand, the minor MX type carbides containing V and W partly do not dissolve appreciably at 1253 to 1323 K [87]; however, a little partial dissolution cannot be ruled out, but their completion requires a considerably higher temperature [87]. Therefore, it is expected that the progressive dissolution of carbides during isothermal holds in the austenite phase field may be qualitatively captured in the corresponding DSC traces. These results are displayed in **Fig. 7.9**.

**Fig. 7.9** depicts the base line compensated DSC traces observed during various austenitising anneals, that is isothermal holds in the high temperature  $\gamma$ -austenite region. From this figure, we bring out yet another facet of the homogenisation process taking place in RAFM steel. An array of distinctly placed small endothermic peaks is readily evident from these base line compensated DSC profiles. The first major drop in each signal signifies the default instrumental response due to the onset of an isothermal hold in the experimental schedule. It must be mentioned that although

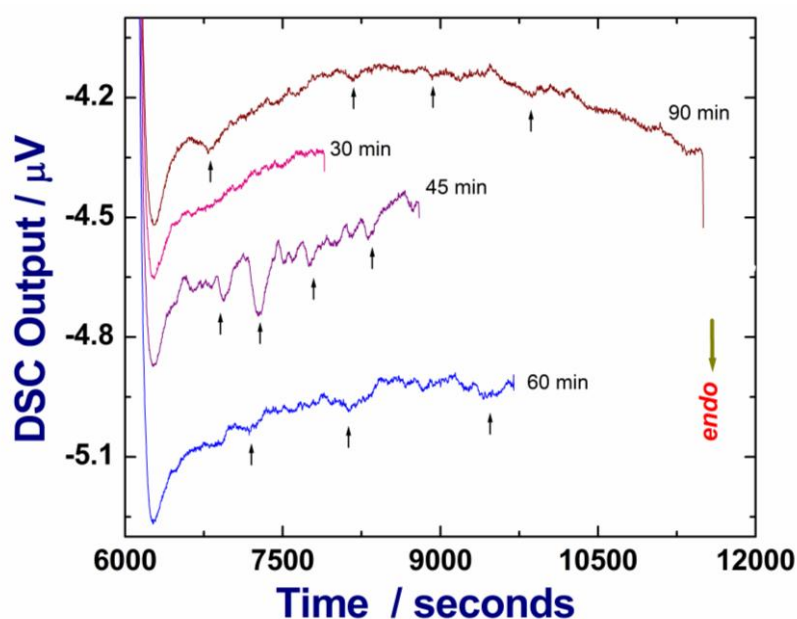


Fig. 7.9. A stack of baseline compensated isothermal DSC traces recorded at 1253 K indicating small endothermic peaks arising from discrete time dependent carbide dissolution events

these experiments were conducted with samples of similar size and mass under identical experimental conditions, the distinct attestation of carbide dissolution endothermic events occurred rather discretely in each sample. This behaviour is thus found to be statistical since samples used in different runs are not exactly microstructurally identical with respect to the spatial distribution, size and density of carbide particles. In sample with copious and large carbide particles, the dissolution events were rather more prominent. But what is noteworthy is that even after about 60

to 90 minutes of holding at 1253 K, the presence of tiny endothermic wiggles were continued to be observed.

Thus, we may infer from **Fig. 7.9** that the process of isothermal austenitisation involves certain well defined time dependent microstructural changes, such as carbide dissolution [93, 94], which as the present experimental results suggest, is progressive in nature. Depending on the homogeneity of the starting microstructure at sub-micron level, the carbide dissolution process gets initiated at different time intervals. Subsequently, these events gradually proceed to completion with a time constant that is set by the diffusivity of the slowest of diffusants in this steel. Thus the progressive carbide dissolution produces a net change in the local  $\gamma$ -austenite composition [17, 96]. Since the carbide dissolution generally involves a measurable enthalpy change, these are reflected as clearly resolved endothermic peaks or undulations in an otherwise smooth baseline compensated thermal analysis profiles that are expected for reaction free solution annealing. In **Fig. 7.9**, the thermal analysis response of isothermal carbide dissolution phenomenon is graphically illustrated, with individual arrow pointers marking well-discernible discrete carbide dissolution events. In particular, the 45 minutes isothermal hold profile presents nicely delineated carbide dissolution peaks.

A remarkable attestation of the gradual, time dependent carbide dissolution event is also found in the corresponding hardness variation of samples that are quenched ( $99 \text{ K min}^{-1}$ ) after the end of different isothermal holds in the  $\gamma$ -austenite regime. This result is graphically portrayed in **Fig. 7.10**. The curve at the top depicts the hardness drop as a function of holding time for 1323 K solution annealed samples. The bottom curve represents similar results for 1253 K annealed samples. The adoption of a higher solution anneal temperature namely, 1323 K results in a ready or

accelerated dissolution of carbides from the very beginning of the annealing process; in fact the drop in hardness values during the initial part of the curve is rather steep. This dissolution of carbides mostly of  $M_{23}C_6$  type enriches the composition of adjacent austenite in chromium and carbon as their solubility in austenite is comparatively large at high temperatures [95]. Since the diffusivity of carbon is comparatively larger than that of the substitutional chromium atoms, the local austenite region surrounding the dissolving carbide will be somewhat rich in chromium [54]. It is this new or nascent chromium rich composition of austenite prevailing at the typical solutionising conditions, which also decides the actual  $M_s$

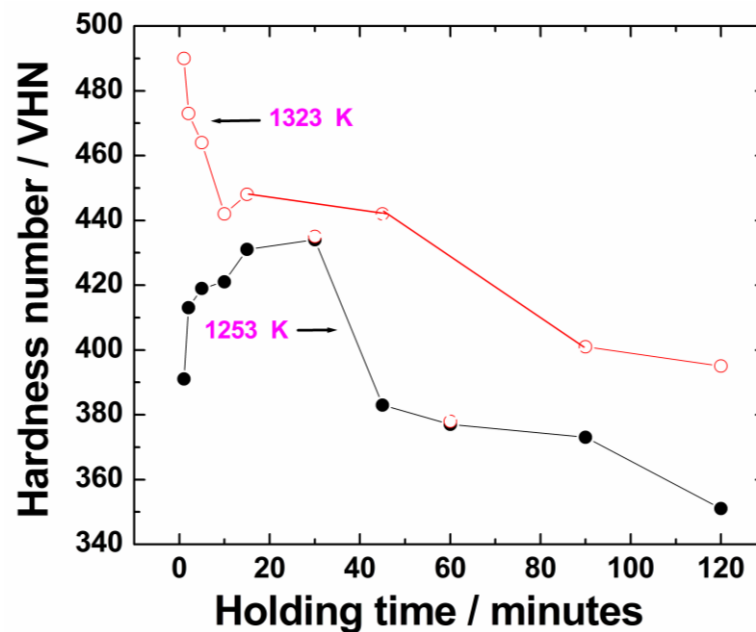


Fig. 7.10. Variation of martensite hardness with holding time in the austenite region for two different austenitising temperatures, 1253 and 1323 K respectively

temperature [63,64]. For obvious reasons, a higher chromium content of parent austenite results in an increase of  $M_s$ , as Cr is a known ferrite stabiliser.

On the kinetics front, the dissolution of carbides results in the reduction of the pinning effect that these hard particles offer to the unhindered motion of advancing martensite front [78]. On a similar note, one may also observe that the time dependent

grain growth in the  $\gamma$ -austenite phase is likewise facilitated as a concomitant or induced effect of carbide dissolution [96, 97]. Thus, the adoption of higher solutionising temperature is more effective in promoting the ease of martensite formation on two counts: namely, the enrichment of  $\gamma$ -austenite composition in chromium following carbide dissolution and the kinetic enhancement due to promoted austenite grain growth.

In stark contrast, the *initial* hardness response of martensite produced from 1253 K solution annealed samples first exhibits an increase with annealing time for up to about 30 minutes and at which point it exhibits the maximal value. This is subsequently followed by a continuous decrease in a manner that is much like the case of 1323 K austenitised samples. Obviously, this difference in the initial response of the hardness curve between these two annealing temperatures stems from the sluggish nature of carbide dissolution step at 1253 K [93, 94]. For smaller time holds at 1253 K, the parent austenite phase still contains quite an extent of undissolved carbides as compared to 1323 K. Further, the lack of carbide dissolution means that the austenite is not getting that much enriched in chromium which is a known ferrite stabiliser. Both these facts act together to give a transformation product with lower  $M_S$  temperature and which also contains some undissolved carbide (**Fig. 7.8**). The higher hardness is from the composite presence of carbides present in quenched in martensite. The lower  $M_S$  temperature is from the relatively low chromium content of the parent austenite. Unlike in low alloy steels, where the carbide dissolution kinetics is known to be fairly rapid [98], the kinetics of austenite formation and carbide dissolution in highly alloyed low to moderate carbon steels has been reported to be much sluggish, as the classical studies of Lenel and Honeycombe and that of Shtansky et al., suggest [93-95]. Moreover, the slow carbide dissolution kinetics which is

compounded by the sluggish transportation of the dissolved chromium away from the carbide/matrix interface into the bulk causes appreciable solute build up near the reaction front, which could also manifest as a sort of solute drag effect on the overall solutionising kinetics. Thus, the kinetics of  $\alpha$ -ferrite+carbides $\rightarrow\gamma$ -austenite transformation which is taking place in the high temperature austenite domain during homogenisation treatment is crucially dependent on the choice of the austenitising temperature, in addition to time.

*A slightly higher solutionising temperature may be advised if complete dissolution is desired, while on the contrary, adoption of a lower austenitization temperature results in the retention of pinning carbide particles that might affect the rapid mobility of martensite interfaces.*

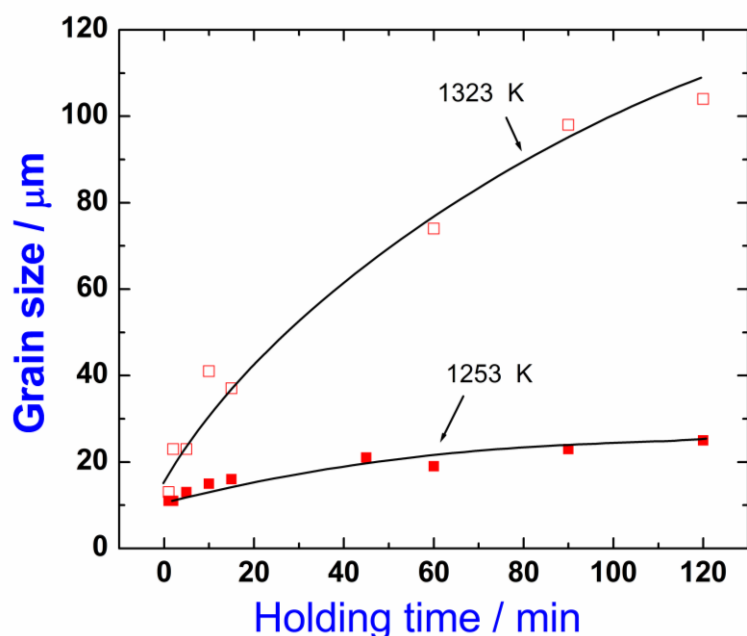


Fig. 7.11 Variation of austenite grain size with holding time at 1253 and 1323 K respectively

As an additional point, we may also add that measurement of parent  $\gamma$ -austenite grain size (martensite colony size) has been made as a function holding time for both 1323 K and 1253 K solution annealed samples. These results are displayed in **Fig. 7.11**.

From this figure, it is clearly seen that the adoption of a slightly higher annealing temperature of 1323 K promotes grain growth in austenite to a much greater extent. It is in order to avoid this excessive grain growth, a relatively low normalising temperature of about 1253 K is chosen for present RAFM. As stated before, an enquiry into the mechanistic aspects of austenite grain growth must take into account the concurrent occurrence of carbide dissolution and thereby the reduction in their pinning potential of the growing austenite grain boundaries against the intrinsic interface energy driven grain coarsening tendency [97]. Since the present discussion is oriented more towards the elucidation of martensite formation based on calorimetry experiments, a detailed discussion of austenite grain growth kinetics is not taken up here. An in-depth study of carbide dissolution characteristics, with electron microscopy support would be of great help in offering further insight into this important issue.

#### **4.0. Discussion**

##### *4.1. General remarks*

Although the field of martensitic transformation, especially in ferrous alloy systems has been an extensively researched one, the application of calorimetric techniques to elucidate its kinetic characteristics has not been that extensively pursued, as compared to microscopy or dilatometry, for example. To the best of the author's knowledge, there were relatively few studies devoted exclusively to measuring the martensite transformation kinetics as a function of composition, grain size, cooling rate etc., in ferrous alloys using calorimetry [26, 91]. In the case of reduced activation steels meant for fusion reactor applications, such studies were even fewer. It must be added that careful calorimetry measurements are a boon for obtaining vital thermodynamic and kinetic data on martensitic transformation. These

data are of immense value in thermodynamic modelling of martensitic phase transformations in general [98-107]. It is amidst this backdrop, the theme of the present study has been framed. In what follows, we present a brief discussion of the major findings of our study in the light of the currently held viewpoints on athermal martensite formation in Fe-based alloys.

#### 4.2. *Enthalpy of martensite formation, $M_S$ temperature and grain size effect*

The  $M_S$  and  $M_f$  temperatures obtained in this study for the RAFM steel are 714 and 614 K respectively. Since  $M_S$  is as much a kinetic quantity as it is thermodynamic in origin, the present values are slightly sensitive to the specifics of the heat treatment, besides actual austenite composition at the austenitisation temperature [90,98]. Notwithstanding such a caveat, the measured values are found to be in fair degree of agreement with the reported values for 9Cr-based low carbon power plant steels [42, 91]. The enthalpy for the  $\gamma \rightarrow \alpha'$ -martensite transformation  $\Delta^{\circ}H^{\gamma \rightarrow \alpha'}$ , as estimated from the measured transformation peak area after appropriate calibration is found to be in the range 64-75 J g<sup>-1</sup>. There are not many recent estimates of this quantity in the metallurgical literature, almost none for advanced nuclear power plant steels [91]. Therefore the present discussion derives heavily from some of the classical calorimetry studies.

In a classical study using isoperibol type drop calorimeter, Lee et al have measured martensite formation enthalpy for some Fe-Ni, Fe-Ni-Mn, Fe-Ni-C, Fe-Ni-Cr-C stainless steel alloys [109]. They found that  $\Delta^{\circ}H^{\gamma \rightarrow \alpha'}$ , in addition to deriving a contribution from composition, is also substantially influenced by the nature of martensite substructure. Thus for example, a twin martensite with a higher amount of stored energy is found to possess relatively lower transformation enthalpy than the dislocation laden lath type martensite. This difference is attributed to the increased

stored energy in case of twin martensite, which is not released as a part of the transformation heat during phase change [109]. The reason for bringing this fact into present discussion is to stress the viewpoint that the enthalpy effects as detected by calorimetry for a nonequilibrium phase change like martensite formation is generally subject to a larger degree of scatter, which *per se* is intrinsic to the nature of phase change, in addition to the limitations of the sensing technique. As shown in **Fig. 7.1(b)**, the martensite in RAFM is basically of lath type with high dislocation density. In this light, the present experimental estimate  $64\text{--}75 \text{ J g}^{-1}$  for the transformation enthalpy is expected to be a little high by virtue of the large amount of stored energy. In a sense, this also borne out by our earlier DSC based measurement of the specific heat of martensite [87]. In their study on Fe-11.9Cr-1.53Mn-0.6C-0.02Si-0.02Co (wt.%) alloy, Lee *et al* obtain an estimate of  $2740 \text{ J mol}^{-1}$  for  $\Delta H^{\gamma \rightarrow \alpha'}$ , the net martensite transformation enthalpy estimated at 510 K [109]. This is lath martensite with a different composition from our RAFM steel. Assuming an average atomic weight of about 55 for the present RAFM steel, the present experimental estimates for  $\Delta^{\circ} H^{\gamma \rightarrow \alpha'}$  translate to  $3520\text{--}4125 \text{ J mol}^{-1}$ . If a stored energy contribution of  $1400 \text{ J mol}^{-1}$ , which is typical of lath martensites is discounted from this total value [109], we then get a value in the range  $2725\text{--}2120 \text{ J mol}^{-1}$  for the chemical contribution to the overall martensite transformation enthalpy of RAFM steel. This estimated value for the formation of hypothetical strain free martensite is certainly greater than the experimental enthalpy obtained for the diffusional on-heating  $\alpha$ -ferrite + carbide  $\rightarrow$   $\gamma$ -austenite transformation [87]. Thus in a nutshell, the microstructure or strain contribution to martensite transformation is quite appreciable for highly alloyed ferrous martensites and this is also supported by present findings. But we hasten to

add that more experimental work on many controlled alloy compositions is needed to throw further insight on this interesting basic issue.

#### 4.3. *Critical cooling rate, carbide dissolution and grain size effect*

In the present study, the critical cooling rate to form nearly 100 percent martensite is found to be of the order of 5-6 K min<sup>-1</sup>, for the 1253 K normalising treatment. This value is slightly higher than the corresponding estimate of about 1 K min<sup>-1</sup> reported for modified 9Cr-steel [87]. As discussed in the previous section, M<sub>S</sub> is essentially decided by the austenite composition prevailing at the solutionising temperature. In addition, it is also dependent on austenite grain size and the presence of any external stress [90, 104]. Ignoring the influence of stress in the present discussion, it emerges from the results obtained here, that both the effective austenite composition and its grain size are the two deciding factors and these are controlled by the austenitisation temperature and time.

To begin with, it is instructive to recall that RAFM steel is almost free of Mo and Nb, which are invariably present in a typical modified 9Cr –steel composition, such as P91 or T91. The substitution of these elements by more cohesive *bcc* neighbours like W and Ta raises in general all the diffusive transformation temperatures, which include M<sub>23</sub>C<sub>6</sub>, MX carbide dissolution solvii, the temperature of austenite and δ-ferrite formation etc [87]. The major effect of the increased cohesion brought about by W and Ta addition is that for a relatively low normalising temperature of 1253 K adopted in this study, the carbide dissolution is never realised to its completion in the usually adopted solutionising time of about 30 minutes. This is found to be true even with our *small specimen* studies, in which almost nil or only a minimal thermal gradient is expected across the entire cross section. A CALPHAD simulation done using Thermo Calc® software and critically assessed multi-

component thermodynamic database for Fe-based systems, also suggests higher solution temperatures for W and Ta containing carbides that are encountered in this steel [49-50]. Therefore, it is clear that for most part of the time during shallow austenitisation anneal, there will be a definite presence of some undissolved carbides, which are quite conducive to restraining the growth of austenite grains through the mechanism of Zener pinning [111]. In addition, the sluggish carbide dissolution would not serve to enrich the austenite composition in Cr, Ta and W, if the solution anneal were to be carried out at lower temperatures in the  $\gamma$ -austenite phase field. The net effect in such a situation is the achievement of relatively small austenite grain sizes (**Fig. 7.11**) with not much change in  $\gamma$ -austenite composition from the starting base composition.

Since athermal martensite nucleation is known to be heterogeneous in nature [103, 106], and further the austenite grain boundaries are not known to serve as potential nucleating sites for martensite [77], the fine grained austenite do not necessarily promote martensite transformation [92,112]. Since martensite propagation in ferrous alloys is one of mainly through bursts, the austenite grain boundaries only serve to impede the growth of martensite plates. A larger austenite grain size on the other hand facilitates laths of larger linear dimensions which by virtue of the strain field at its tips serve to nucleate another cluster in a neighbour grain [75-77]. Thus from kinetics point of view, larger austenite grain size promotes martensite nucleation and growth. In **Fig. 7.12**, the present experimental findings of grain size effect on  $M_S$  temperature is graphically summarised.

In the light of this simple picture, it is now clear as to why the  $M_S$  and  $M_f$  temperatures are relatively depressed for 1253 K normalised samples. It is also interesting to note that the prior austenite grain sizes enclosing the martensite colony

are also small in this case (**Fig. 7.11 & 7.12**), which is why this annealing temperature is selected for the RAFM steel. The adoption of 1323 K as the annealing temperature

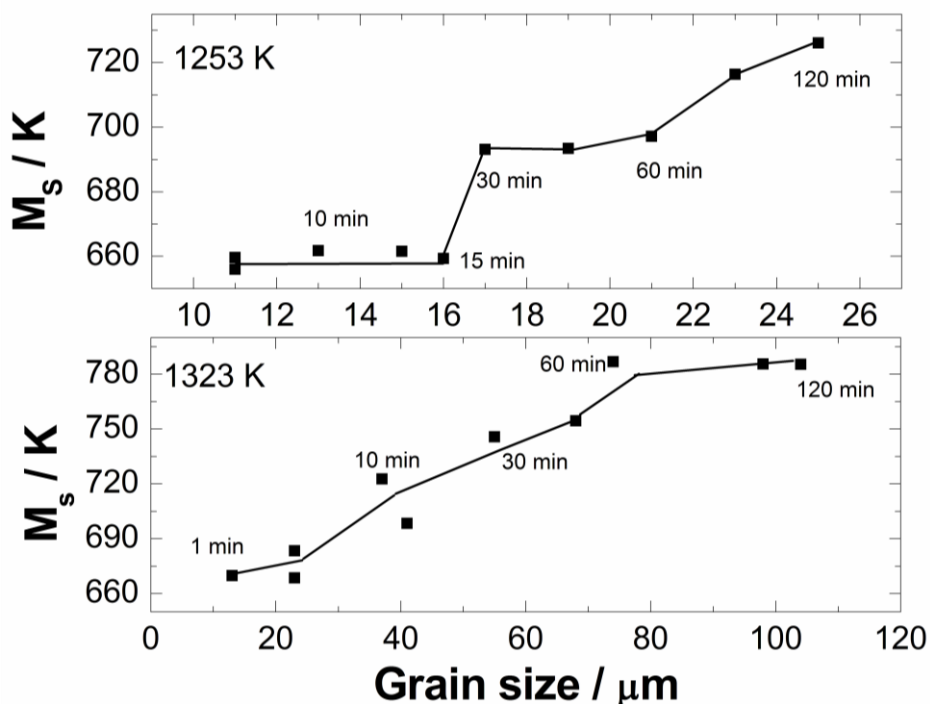


Fig. 7.12. Variation of  $M_s$  temperature with austenite grain size at 1253 and 1323 K respectively

on the contrary promotes rapid grain growth, which serves to increase the  $M_s$  and  $M_f$  temperatures (**Fig. 7.12**), but results in a reduction of its strength, as reflected by the drop in hardness (**Fig. 7.10**).

#### 4.4. Martensitic transformation kinetics

In **Fig. 7.13(a)** and **7.13(b)**, the fraction of martensite formed as a function of temperature is plotted for different samples that have undergone different extents of austenitisation at 1253 K. For reasons of space and brevity, only results pertaining 1253 K austenitising treatment are discussed here. It must be added that all these samples are cooled at a uniform rate of  $99 \text{ K min}^{-1}$  to room temperature. Assuming that the total area under the transformation peak corresponds to 100 percent

martensite formation, the fraction transformed at any intermediate temperature  $T$ , such that  $M_S < T < M_f$ , can be estimated from the following relation

$$f(T) = \frac{\int_{M_S}^T \phi \, dT}{\int_{M_S}^{M_f} \phi \, dT} \quad (1)$$

The integral in the numerator stands for the partial peak area measured in the

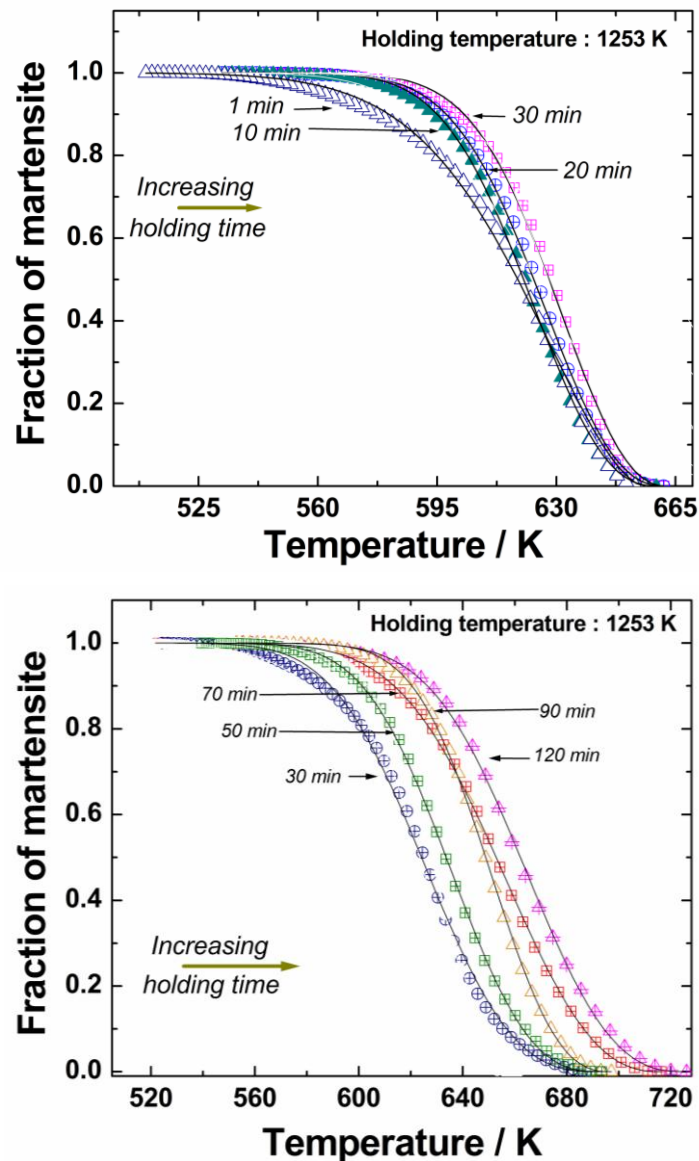


Fig. 7.13 Fraction of martensite formed as a function of undercooling below  $M_S$  for samples that are subject to austenitisation treatment at 1253 K for (a): 1-30 minutes (top panel) and (b) 30 – 120 minutes (bottom panel). The line through the curves represents the Koistinen-Marburger fit (Eq. 2) to the transformation data

temperature range  $M_S$  to  $T$ , while that in the denominator stands for the full peak area spanning from  $M_f$  to  $M_S$ . The discrete points in **Fig. 7.13** denote the actual experimental data obtained using *Eq. (1)*, while the continuous line passing through them represents the Koistinen-Marburger (K-M) fit given by the expression [113].

$$f_{\alpha}(T) = 1 - \exp \{ [C/\beta (M_S - T)]^n \}. \quad (2)$$

In *Eq. (2)*,  $f_{\alpha}(T)$  is the fraction of martensite formed as a function of temperature  $T$ , below  $M_S$ ,  $C$  is an empirical rate constant and  $n$  is the transformation exponent, again assumed in the empirical sense. In order to incorporate the cooling rate effect in Koistinen-Marburger relation, *Eq. (2)* is written in a modified form by absorbing in the prefactor the cooling rate  $\beta$  in an explicit manner [114]. As judged from **Fig. 7.13**, the K-M relation fits the present experimental data rather well and the fit parameters are listed in **Table 7.1**. It emerges from **Fig. 7.13(a)**, that for holding times up to about 30 minutes, the different transformation curves are closely overlapping, suggesting thereby that martensite transformation kinetics is not very much differentiated in this regime. The average value of  $C/\beta$  as listed in **Table 7.2** turns out to be about 0.001, which incidentally agrees well with the original proposition of Koistinen-Marburger [113].

**Table 7.1**

Listing of the parameters of the Koistinen - Marburger fit (*Eq. 2*) to the experimental data

Holding time at 1253 K (min.)	$M_s$ (K)	$M_f$ (K)	$C$	$n$	$R^2$ value
1	656	508	$0.03752 \pm 0.00011$	$1.71145 \pm 0.01343$	0.99777
2	660	545	$0.04342 \pm 0.00007$	$2.14442 \pm 0.01005$	0.99956
5	662	546	$0.04087 \pm 0.00012$	$2.18828 \pm 0.01966$	0.99839
10	662	531	$0.03702 \pm 0.00006$	$2.32103 \pm 0.01306$	0.99936
15	659	528	$0.03636 \pm 0.00006$	$2.39268 \pm 0.0136$	0.99935

30	693	522	$0.02109 \pm 0.00004$	$2.92995 \pm 0.0229$	0.99862
45	697	551	$0.02962 \pm 0.00004$	$2.60108 \pm 0.01118$	0.9997
60	694	538	$0.02415 \pm 0.00003$	$2.78195 \pm 0.01154$	0.99971
90	716	522	$0.02243 \pm 0.00003$	$2.49416 \pm 0.01137$	0.99961
120	726	553	$0.02253 \pm 0.02253$	$2.70304 \pm 0.0175$	0.99943

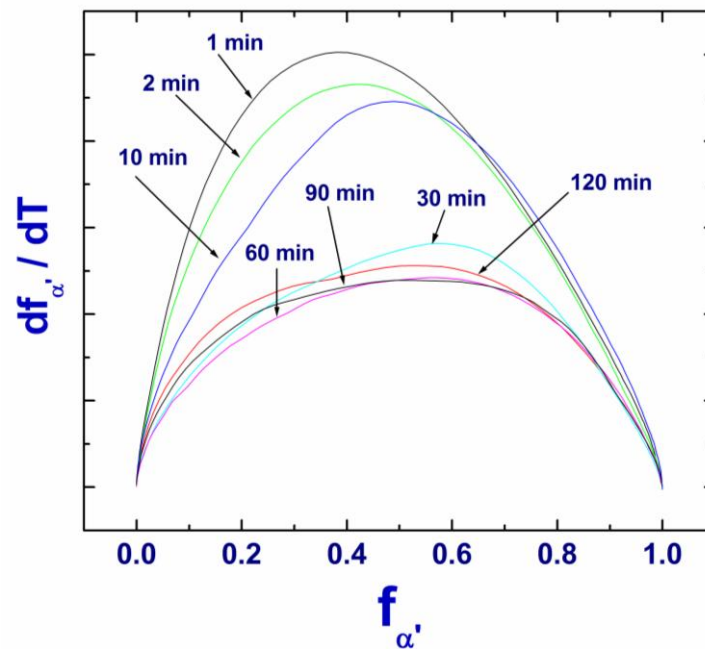


Fig. 7.14. The rate of martensite formation is plotted as a function of martensite fraction for samples that are solution treated at 1253 K for different durations

In **Fig. 7.14**, another interesting manifestation of the holding time effect on martensitic transformation kinetics is illustrated. It emerges from this figure that in samples which had seen only smaller durations of austenitising anneal, the maximum in the rate of martensite formation, that is the quantity  $df_{\alpha'}/dT$  is realised at a value of about 0.2 to 0.4 for  $f_{\alpha'}$ , the fraction of martensite formed. However for longer anneals, which is synonymous with larger austenite grain size, the maximum transformation rate is realised at  $f_{\alpha'} \sim 0.6$ . This is again supportive of the deduction that austenite grain growth catalyses martensite spread kinetics.

## 5.0. Summary

- i. A comprehensive characterisation of the kinetics of martensitic transformation phenomenon in RAFM steel has been carried out using differential scanning calorimetry. The effects of holding temperature and time in the  $\gamma$ -austenite phase field and also the cooling rate on the martensite start temperature  $M_S$  have been precisely quantified.
- ii. The  $M_S$  and  $M_f$  temperatures for 1253 K/15 minutes normalised samples are found to be 714 and 614 K respectively. The transformation enthalpy for martensite formation is estimated to be  $64 - 75 \text{ J g}^{-1}$ . The critical cooling rate for the austenitisation temperature 1253 K is found to be between  $5 - 6 \text{ K min}^{-1}$ .
- iii. The  $M_S$  temperature exhibited a continuous increase with increasing holding times for 1323 K austenitisation treatment. The corresponding martensite hardness values exhibited a systematic drop. In case of 1253 K austenitisation anneal, the  $M_S$  temperature did not evince much of a change with holding time for the initial region. However, for annealing periods exceeding 30 minutes, the  $M_S$  has started showing a steady increase. For both 1253 and 1323 K austenitisation anneals, the martensitic transformation interval  $M_f - M_S$ , do not exhibit any substantial difference for the longer annealing periods.
- iv. The large prior austenite grain size which is obtained for longer annealing durations is found to promote the kinetics of martensite formation. The slow carbide dissolution phenomenon which co-occurs during the initial phase of annealing at lower solutionising temperature is found to have an indirect influence on  $M_S$  temperature, by slowing down the austenite grain coarsening.
- v. The kinetics of martensite formation is found to follow the empirical Koistinen-Marburger relation.

## References

- [1]. Fujio Abe, *Sci. Tech. Adv. Mater.*, **9** (2008) 1.
- [2]. H. K. D. H. Bhadeshia, *ISIJ International*, **41** (2001) 626.
- [3]. Fujimitsu Masuyama, *ISIJ International*, **41** (2001) 612-625.
- [4]. Ulrich E. Klotz, Christian Solenthaler and D. J. Uggowitzer, *Mater. Sci. Engg.*, **A76** (2008) 186.
- [5]. H. Cerjak, P. Hofer and B. Schaffernak, *ISIJ International*, **39** (1999) 874.
- [6]. J. W. Morris, Jr., Z. Guo, C. R. Krenn and Y.-H. Kim, *ISIJ International*, **41** (2001) 599.
- [7]. J. M. Vitek and R. L. Klueh, *Metall. Trans. A*, **14A** (1983) 1047.
- [8]. J. Hald, *Int. J. Pr. Vessel & Piping*, **85** (2008) 30.
- [9]. G. Krauss, *ISIJ International*, **35** (1995) 349.
- [10]. V. Knezevic, G. Sauthoff, J. Vilk, G. Inden, A. Schneider, R. Agamennone, W. Blum, Y. Wang, A. Scholz, C. Berger, J. Ehlers and L. Singheiser, *ISIJ International*, **42** (2002) 1505.
- [11]. V. Thomas Paul, S. Saroja and M. Vijayalakshmi, *J. Nucl. Mater.*, **378** (2008) 273.
- [12]. M. Igarashi, S. Muneki, H. Hasegawa, K. Yamada and F. Abe, *ISIJ International*, **41** (2001), supplement, S101.
- [13]. X. Y. Liu and T. Fujita, *ISIJ International*, **29** (1989) 680.
- [14]. M. Tamura, H. Kusuyama, Kei Shinozuka and H. Esaka, *ISIJ International*, **47** (2007) 317.
- [15]. K. Maile, *Int. J. Pr. Vessel & Piping*, **84** (2007) 62.
- [16]. F. Abe, M. Tabuchi, M. Kondo and S. Tsukamoto, *Int. J. Pr. Vessel & Piping*, **84** (2007) 44.
- [17]. L. F. Alvarez, C. Garcia, and V. Lopez, *ISIJ International*, **34** (1994) 516.
- [18]. P. Hofer, M. K. Miller, S. S. Babu, S. A. David and H. A. Cerjak, *ISIJ International*, **42** (2002); supplement S62.
- [19]. T. Hasegawa, Y. R. Abe, Y. Tomita, N. Maruyama and M. Sugiyama, *ISIJ International*, **41** (2001) 922.

- [20]. M. Tamura, H. Hayakawa, A. Yoshitake, A. Hishinuma, T. Kondo, *J. Nucl. Mater.*, **155-157** (1988) 620.
- [21]. R. Kishore, R. N. Singh, T. K. Sinha and B. P. Kashyap, *J. Nucl. Mater.*, **195** (1992) 198.
- [22]. M. Tamura, H. Iida, H. Esaka and K. Shinozuka, *ISIJ International*, **43** (2003) 1807.
- [23]. S. G. Hong, W. B. Lee and C. G. Park, *Scripta Mater.*, **43** (2000) 181.
- [24]. S. G. Hong, W. B. Lee and C. G. Park, *J. Nucl. Mater.*, **288** (2001) 202.
- [25]. F. Abe, T. Noda, H. Araki and S. Nakazawa, *J. Nucl. Mater.*, **179-181** (1991) 663.
- [26]. S. Raju, B. Beyaganesh, A. Banerjee and E. Mohandas, *Mater. Sci. Engg.* **A465** (2007) 29.
- [27]. F. Abe, T. Horiuchi, M. Taneike and K. Sawada, *Mat. Sci. Engg.*, **A378** (2004) 299.
- [28]. A. Zielinska-Lipiec, A. Czyrska-Filemonowicz, P. J. Ennis and O. Watcher, *J. Mater. Proc. Tech.*, **64** (1997) 397.
- [29]. K. Kaneko, S. Matsuyama, A. Sadakata, K. Fujita, W. J. Moon, S. Ozaki, N. Nishimura and Y. Tomokiyo, *Mater. Sci. Engg.*, **A374** (2004) 82.
- [30]. K. Yamada, M. Igarashi, S. Muneki and F. Abe, *ISIJ International*, **42** (2002) 779.
- [31]. F. Abe, *Mater. Sci. Engg.*, **A319-321** (2001) 770.
- [32]. K. Yamada, M. Igarashi, S. Muneki and F. Abe, *ISIJ International*, **41** (2001) supplement; S116.
- [33]. M. Tamura, Y. Haruguchi, M. Yamashita, Y. Nagaoka, K. Ohinata, K. Ohnishi, E. Itoh, H. Ito, K. Shinozuka and H. Esaka, *ISIJ International*, **46** (2006) 1693.
- [34]. Y. Murata, M. Kamiya, T. Kuneida, A. M. Abdel-Daiem, T. Koyama, M. Morinaga, and R. Hashizume, *ISIJ International*, **45** (2005) 101.
- [35]. K. Iwanaga, T. Tsuchiyama and S. Takai, *Key Engg. Mater.*, **171-174** (2000) 477.
- [36]. T. K. Kim, J. H. Baek, C. H. Han, S. K. Kim and C. B. Lee, *J. Nucl. Mater.*, **389** (2009) 359.

- [37]. R. Jayaram and R. L. Klueh, *Metall. Mater. Trans.*, **29A**, (1998) 1551.
- [38]. J. M. Koo, S. Y. Kim, K. Shin, Y. G. Jung and S. K. Hur, *Key Engg. Mater.*, **345-346** (2007)465.
- [39]. V. Homolova, J. Janovec, P. Zahumensky and A. Vyrostkova, *Mater. Sci. Engg.*, **A349** (2003) 306
- [40]. M. Yoshino, Y. Mishima, Y. Toda, H. Kushima, K. Sawada and K. Kimura, *ISIJ International*, **45** (2005) 107.
- [41]. K. Sawada, T. Ohba, H. Kushima and K. Kimura, *Mater. Sci. Engg.*, **A394** (2005) 36.
- [42]. H. Finkler and M. Schirra, *Steel Research*, **67** (1996) 328.
- [43]. Y. Tsuchida, K. Okamoto and Y. Tokunaka, *ISIJ International*, **35** (1995) 317.
- [44]. H. D. Kim and I. S. Kim, *ISIJ International*, **34** (1994) 198.
- [45]. V. Foldyna, J. Purmensky and Z. Kuban, *ISIJ International*, **41** (2001) S81.
- [46]. V. Fodarek and A. Strang, *Mater. Sci. Tech.*, **16** (2000) 1207.
- [47]. S. Kobayashi, K. Toshimori, K. Nakai, Y. Ohmori, H. Asahi and T. Muraki, *ISIJ International*, **42** (2002) S72.
- [48]. K. Maruyama, K. Sawada and Jun -ichi- Koike, *ISIJ International*, **41** (2001) 641.
- [49]. A. Danon and C. Servant, *J. Nucl. Mater.*, **321** (2003) 8.
- [50]. A. Danon and C. Servant, *ISIJ International*, **45** (2005) 903.
- [51]. J.-O. Andersson, *Metall. Trans.*, **14A** (1988) 627.
- [52]. V. A. Yardley and Y. de Carlan, *J. Phase Eq. & Diff.*, **27** (2006) 102.
- [53]. A. Kroupa, J. Havrankova, M. Coufalova, M. Svoboda and J. Vrestal, *J. Phase Eq. & Diff.*, **22** (2001) 312.
- [54]. A. Bjarbo and M. Hatterstrand, *Metall. Trans.*, **32A** (2001) 19.
- [55]. B. C. Schaffernak and H. Cerjak, *Calphad*, **25** (2001) 241.
- [56]. J. D. Robson and H. K. D. H. Bhadeshia, *Calphad*, **20** (1996) 447.

- [57]. F. G. Caballero, C. Capdevila and C. Garcia de Anders, *ISIJ International*, **41** (2001) 1093.
- [58]. A. Schneider and G. Inden, *Acta Mater.*, **53** (2005) 519.
- [59]. R. G. Thiessen, I. M. Richardson and J. Sietsma, *Mater. Sci. Engg.*, **A427** (2006) 223.
- [60]. M. Perez and A. Deschamps, *Mater. Sci. Engg.*, **A360** (2003) 214.
- [61]. M. Sob, A. Kroupa, J. Pavlu and J. Vrestal, *Solid St. Phenomena*, **150** (2009) 1.
- [62]. Y. Murata, T. Koyama, M. Morinaga and T. Miyazaki, *ISIJ International*, **42** (2002) 1423.
- [63]. T. Sourmail and C. Garcia-Mateo, *Comp. Mater. Sci.*, **34** (2005) 323.
- [64]. T. Cool and H. K. D. H. Bhadeshia, *Mater. Sci. Tech.*, **12** (1996) 40.
- [65]. L. Gavard, H. K. D. H. Bhadeshia, D. J. C. MacKay and S. Suzuki, *Mater. Sci. Tech.*, **12** (1996) 453.
- [66]. Q. Li, *Mater. Sci. Engg.*, **A361** (2003) 385.
- [67]. R. G. Faulkner, *Acta Metall.*, **35** (1987) 2905.
- [68]. You Ya Fin and R. G. Faulkner, *Mater. Sci. Engg.*, **A344** (2003) 92.
- [69]. P. Maugis, D. Gendt, S. Lanteri and P. Barges, *Def. Diff. Forum*, **194-199** (2001) 1767.
- [70]. J. Miettinen, *Calphad*, **22** (1988) 275.
- [71]. F. Masuyama, *Mater. Sci. Engg.*, **A510-511**, (2009) 158.
- [72]. M. Y. He, G. R. Odette, T. Yamamoto and D. Klingensmith, *J. Nucl. Mater.*, **367-370** (2007) 556.
- [73]. C. Kocer, T. Abe and A. Soon, *Mater. Sci. Engg.*, **A505**, (2009) 1.
- [74]. J. Agren, *ISIJ International*, **32** (1992) 291.
- [75]. J. R. C. Guimaraes and A. Saavedra, *Mater. Sci. Engg.*, **62** (1984) 11.
- [76]. J. R. C. Guimaraes, *Mater. Sci. Engg.*, **A476** (2008) 106.
- [77]. J. R. C. Guimaraes and J. C. Gomez, *Acta Metall.*, **26** (1978) 1591.

- [78]. S. Kustov, J. Pons, E. Cesari and J. Van Humbeeck, *Acta Mater.*, **52** (2004) 3075.
- [79]. R. G. Faulkner, *Acta Metall.*, **35** (1987) 2905.
- [80]. D. Gaude – Fugarolas and Y. de Carlan, *J. Nucl. Mater.*, **374** (2008) 109.
- [81]. J.-B. Leblond, G. Mottet, J. Devaux and J.-C. Devaux, *Mater. Sci. Tech.*, **1** (1985) 815.
- [82]. J. Agren, *Scand. J. Metall.*, **19** (1990) 2.
- [83]. S. G. E. teVelthuis, N. H. Van Dijk, M. Th. Rekveldt, J. Sietsma and S. Van der Zwaag, *Mater. Sci. Engg.*, **A277** (2000) 218.
- [84]. S. Denis, D. Farias and A Simon, *ISIJ International*, **32** (1992) 316.
- [85]. W. Xu, D. San Martin, P. E. J. Rivera Diaz del Castillo and S. Van der Zwaag, *Mater. Sci. Engg.*, **A467** (2007) 24.
- [86]. S. Sharafat, G. R. Odette and J. Blanchard, *J. Nucl. Mater.*, **386-388** (2009) 896.
- [87]. S. Raju, B. Jeyaganesh, A. K. Rai, R. Mythili, S. Saroja, E. Mohandas, M. Vijayalakshmi, K. B. S. Rao and Baldev Raj, *J. Nucl. Mater.*, **389** (2009) 385.
- [88]. R. L. Klueh, *Int. Mater. Rev.*, **50** (2005) 287.
- [89]. R. Lindau, A. Moslang and M. Schirra, *Fusion Engg., & Design*, **61-62** (2002) 659.
- [90]. E. Hornbogen, *Acta Metall.*, **33** (1985) 595.
- [91]. B. Jeyaganesh, S. Raju, A. K. Rai, R. Mythili, E. Mohandas, M. Vijayalakshmi, K. B. S. Rao and Baldev Raj, *Mater. Sci. Tech.*, **27** (2011) 500.
- [92]. A. Garcia Junceda, C. Capdevila, F. G. Caballero, and C. Garcia de Andres, *Scripta Mater.*, **58** (2008).
- [93]. U. R. Lenel and R. W. K. Honeycombe, *Metal Sci.*, **18** (1984) 201-205.
- [94]. U. R. Lenel, *Scripta Metall.*, **17** (1983) 471.
- [95]. D. V. Shtansky and G. Inden, *Acta Mater.*, **45** (1997) 2879.

- [96]. A. Danon, C. Servant, A. Alamo and J. C. Brachet, *Mater. Sci. Engg.*, **A348** (2003) 122.
- [97]. M. Shome, D. S. Sarma, O. P. Gupta and O. N. Mohanty, *ISIJ International*, **43** (2003) 1431.
- [98]. M. Palumbo, *Calphad*, **32** (2008) 693.
- [99]. G. N. Haidemenopoulos, M. Grujicic, G. B. Olson and M. Cohen, *J. Alloys Comp.*, **220** (1995) 142.
- [100]. G. N. Haidemenopoulos and A. N. Vasilakos, *J. Alloys Comp.*, **247** (1997) 128.
- [101]. Zhao Jicheng and Jin Zhanpeng, *Acta metal. mater.*, **38** (1990) 425.
- [102]. J. Kunze and B. Beyer, *Z. Metallkd.*, **91** (2000) 10.
- [103]. A. Borgenstam and M. Hillert, *Acta mater.*, **45** (1997) 2079.
- [104]. H. Kato and S. Miura, *Acta metall. mater.*, **43** (1995) 351.
- [105]. P. Wollants, M. De Bonte and J. R. Roos, *Z. Metallkd.*, **70** (1979) 113.
- [106]. G. Ghosh and G. B. Olson, *Acta metall. mater.*, **42** (1994) 3361.
- [107]. G. Ghosh and G. B. Olson, *Acta metall. mater.*, **42** (1994) 3371.
- [108]. J. Kunze and B. Beyer, *Z. Metallkd.*, **91** (2000) 106.
- [109]. B. Lee, S. Millman, I. L. MacDougall, S. R. Keown and B. B. Argent, *Metal Sci.*, **11** (1977) 261.
- [110]. A. Paul, A. Beirante, N. Franco, E. Alves and J. A. Odrizolo, *Mat.Sci. Forum*, **514-516** (2006)500.
- [111]. C. R. Hutchinson, H. S. Zurob, C. W. Sinclair and Y. J. M. Brechet, *Scripta mater.*, **59** (2008) 635.
- [112]. J. R. C. Guimaraes, *Scripta mater.*, **57** (2007) 237.
- [113]. D. P. Koistinen and R. E. Marburger, *Acta metall.*, **7** (1959) 59.
- [114]. A. K. Rai, S. Raju, B. Jeyaganesh, E. Mohandas, S. Sudha and V. Ganesan, *J. Nucl. Mater.*, **383** (2009) 215.

## High Temperature Phase Stability, Thermal Properties and Metallurgical Compatibility of Ferroboron with SS 304L

### 1.0. Introduction

The successful commercialisation of fast reactor technology for clean and economical power generation amidst a highly competitive energy market entails a persistent quest for continuous design innovations. This involves implementing functionally more efficient design options, besides exploring the possible deployment of cheaper material inventory in future fast reactor designs. It is in view of the latter imperative, that an indigenously developed ferroboron alloy containing about 15 to 17 wt.% of *unenriched* boron in combined form, has been under active consideration as alternate shielding material in India's forthcoming fast (breeder) reactors. Towards this cause, Sunil Kumar and Keshavamurthy have recently analysed the feasibility of using ferroboron (herein designated as Fe-B) alloy as a probable shielding candidate from the point of view of providing adequate neutron and gamma shielding [1]. The results of this study suggested that it is indeed possible to use ferroboron as a potential and economical shield material, provided its metallurgical and chemical compatibility with the stainless steel clad and liquid sodium at typical operating conditions are satisfactorily ensured. In this regard, it must be mentioned that the proposed shielding subassembly design using ferroboron in place of B<sub>4</sub>C consists of vibropacking of Fe-B powder of appropriate size fraction(s) and chemical composition inside a twin clad SS 304L sheath, which experiences a normal in-reactor service temperature of about 723 K [1]. *Since it is well known that boron exhibits considerable tendency to interact with boride forming elements like Ni, Cr, Fe, Mo etc., that are present in nuclear*

*grade austenitic stainless steel [2-14], it is necessary to characterise the thermal stability and the nature of the metallurgical interaction between Fe-B alloy and the SS 304L clad, at typical service and also at higher temperatures.* It is in this perspective that a comprehensive metallurgical characterisation study of the indigenously developed Fe-B alloy has been initiated. The results of this investigation are presented in this chapter.

Since in general, not much information on the physical metallurgy and thermal properties of high boron containing Fe-B alloys is available in open literature [15-23], measurements of high temperature phase stability along with heat capacity and volume thermal expansion have also been taken up as a part of this characterisation study. It is believed that such comprehensive database on material physics and chemistry aspects of new as well as potential alternate shielding material will greatly facilitate the process of knowledge driven reactor design [24-26].

## 2.0. Chemical composition and characterisation

Element	B	Si	Al	C	S	P	O	Fe
Weight percent	15.24	0.89	0.169	0.29	0.061	0.0046	0.03	balance

The Fe-B alloy used in the present study is manufactured at MINEX metallurgical corporation, Nagpur, India from classified Fe-B source material and also commercial boron oxide lumps through proprietary pyrometallurgical process. In view of the requirement of boron atom density of about  $0.7 \text{ g cc}^{-1}$  from shielding point of view [1], an Fe-B alloy having a nominal composition of 15 to 17 wt.% B, with an overall material density of about 4 to  $4.2 \text{ g cc}^{-1}$  has been selected. This specification amounts to achieving about 60% of the theoretical density with Fe-15 wt.% B alloy. In Table 7.1, the compositional details of the Fe-B alloy used in the present study are listed.

The material has been received in the form of small, hard lumps, which are mechanically crushed and ball milled into powders of size approximately in the range 100 to 200 microns for further characterisation. The coarse fraction of the powder sample as well as small chips that are sliced out of the bulk material have been mounted onto an epoxy mould for optical (Leica MeF4A) and scanning electron microscopy (SEM Philips XL-30) observation. The Vickers microhardness measurements are taken in Leitz microhardness tester under a static load of 100 g. About eight independent hardness indentations are made and the average of the resulting hardness values has been taken as the representative value. The powder x-ray diffraction analysis has been carried out in Philips X'pert Pro powder diffractometer using Cu-K $\alpha$  radiation in the  $\theta$ - $\theta$  geometry, with a  $2\theta$ -scan step of 0.01 degrees [27]. Pure Silicon powder obtained from the National Physical Laboratory (NPL) New Delhi, India has been used for  $\theta$ -calibration. The high temperature x-ray diffraction analysis was performed in the same machine under a vacuum of about  $10^{-6}$  torr, using Buehler's high temperature stage. The temperature measurement and diffraction angle calibration procedures for the high temperature x-ray study have already been presented in detail in chapter 2.

### **3.0. Experimental measurements**

#### *3.1. Thermal stability of Fe-B alloy and combined Fe-B + 304L SS reaction couple*

The high temperature thermal stability of Fe-B alloy has been investigated using *Setaram Setsys 1600*<sup>®</sup> heat-flux type high resolution differential scanning calorimeter (DSC) operated under flowing high purity argon (99.9 percent by volume) atmosphere [26,28]. Basically, two types of experiments are conducted using scanning calorimetry. In the first set, the mechanically milled Fe-B alloy powder has been

investigated for its thermal stability, up to its melting point. This experiment yielded typical on-heating and on-cooling phase transformation temperatures of Fe-B alloy. In the second set of experiment, small milligram quantities of compacted Fe-B powder together with a small centrally located cylindrical piece of SS304L are co-heated as a single cohesive mass in calorimeter cell, up to the melting point of 304L. The aim of this second set of experiment, which has been conducted with different mass ratios of Fe-B and 304L is to explore quantitatively the nature of pre-melting reaction of 304L SS in molten Fe-B. **As explained in the latter sections of this chapter, these experiments yield useful data on the possible dissolution of stainless steel in liquid ferroboration, even before the equilibrium melting point of clad is reached** (in any accidental excursions of temperature). The principal aim of this experiment is to obtain data on the nature of the fused product of Fe-B alloy with the stainless steel sheath that might form under hypothetical high temperature conditions. It may be mentioned that similar experiments were earlier performed with B<sub>4</sub>C control rod material and SS clad combination [7, 29]. This co-melting experiment has been augmented by supplementary x-ray diffraction and metallographic characterisation of the solidified Fe-B+304L SS composite product in order to establish the nature of complex intermetallic borides that form as a result of interaction between molten Fe-B and stainless steel at high temperatures.

### 3.2. *Enthalpy, heat capacity and lattice thermal expansion measurements*

As mentioned before, there exists in open literature little experimental data on thermal properties of high boron containing Fe-B alloys [15, 18, 22]. In view of this, we have also carried out static isothermal drop calorimetry measurements which yield accurate estimates of enthalpy or total heat content as a function of temperature [26, 30].

### 3.3. Estimation of the high temperature metallurgical compatibility between 304L stainless steel and Fe-B alloy

Based on the experience gained from SS 316 or 304 diffusion couple with boron carbide ( $B_4C$ ) control rod material at high temperatures [3-5,7,8,29], it emerges that the Fe-B/SS304L combination is also thermodynamically unstable at high temperatures. There is an inherent tendency for the B atoms in ferroboration to diffuse into the stainless clad and chemically interact with some of the transition elements like, Fe, Cr, Ni, Mo etc that are present in steel [11-13]. Moreover, the presence of some carbon in both 304L and in the Fe-B, can lead to the formation of stable borocarbides through mutual chemical interaction. These complex intermetallic phases formed at the steel/ceramic interface are usually very hard and brittle, and results in the reduction of interfacial ductility of stainless steel/Fe-B combination. In view of such strong high temperature metallurgical interaction between Fe-B alloy and stainless steel, it is considered essential to measure the '*clad penetration thickness*' or the '*reaction layer depth*' that would form at the interface of Fe-B/304L SS couple, as a function of time and temperature [7]. Since the primary concern of this study is to evaluate Fe-B alloy with regard to its suitability as economical shielding candidate rather than as control rod material which forms part of the highly active core, the range of temperatures that the Fe-B shielding subassembly is likely to see inside the reactor under normal operating conditions is also rather restricted in comparison [1]. Nevertheless, keeping in mind the long envisaged life span of about 60 years for the outer shielding subassembly in the current design considerations of commercial Indian fast reactors, it has been decided to perform the metallurgical compatibility tests in an extended temperature range of 823-1073 K and with an interaction time of up to about 5000 h. It is believed that such accelerated testing at

high temperatures for reasonably long time durations would by the way of offering more stringent reacting conditions will more than compensate for the highly time consuming and costly experimentation of conducting the tests at typical lower operating temperature of 823 K for longer durations (60 years) time. It must be added as a passing remark that to the best of our knowledge, there exist in open nuclear metallurgy literature not much data on the metallurgical compatibility between high boron containing Fe-B alloy and austenitic 304L stainless steel in the temperature range of our interest. The experimental details concerning the investigation of high temperature metallurgical interaction of Fe-B with 304L SS are given below.

#### *3.4. Reaction couple experiments*

The schematic of the diffusion jig that is used for investigating the high temperature metallurgical interaction between Fe-B and 304L SS is shown in **Fig. 8.1**. As may be seen, the experimental setup consists of a cylindrical cavity made of 304L stainless steel into which the Fe-B alloy powder is loaded and firmly compacted by the 304L plunger that is screwed down from the top. The height of the Fe-B powder column and that of the plunger are so adjusted that by forcing the plunger down and into the powder filled cavity by the top screw, the entire diffusion jig assembly forms one hermetically sealed reaction chamber (**Fig. 8.1**). A number of such Fe-B loaded diffusion jigs has been made, which are then exposed to different temperatures in a muffle furnace under argon cover for different durations of time. At the end of the diffusion experiment, the jig is taken out of the furnace, allowed to cool in air to room temperature, and subsequently sectioned for microscopic characterisation of the reaction layer formed between the stainless steel plunger and Fe-B powder bed. In the following section, the results of different set of experiments described above are systematically presented.

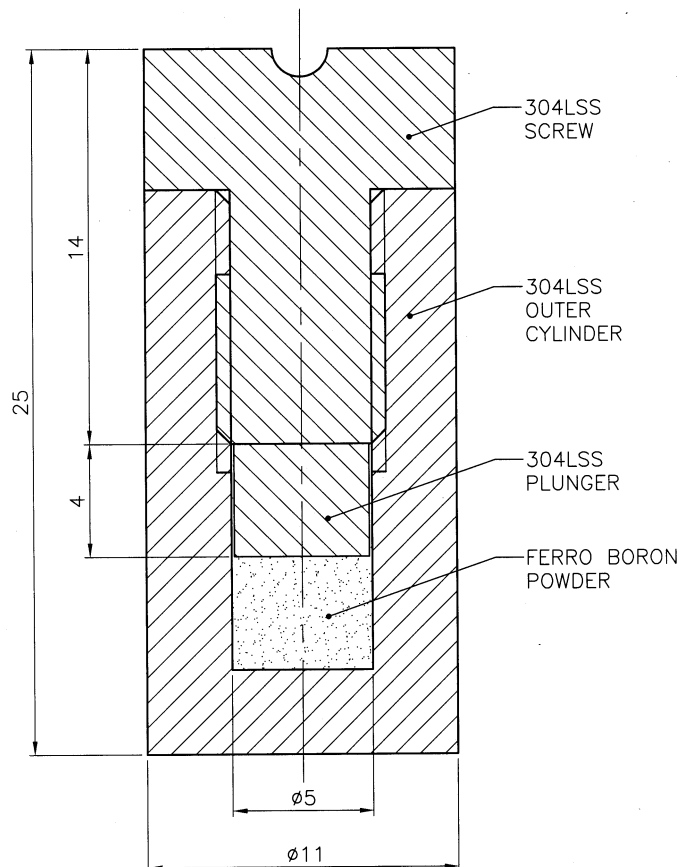


Fig. 8.1. Schematic diagram of the diffusional jig used for simulating the high temperature metallurgical interaction between ferroboron powder and 304L stainless steel. Dimensions are given in mm.

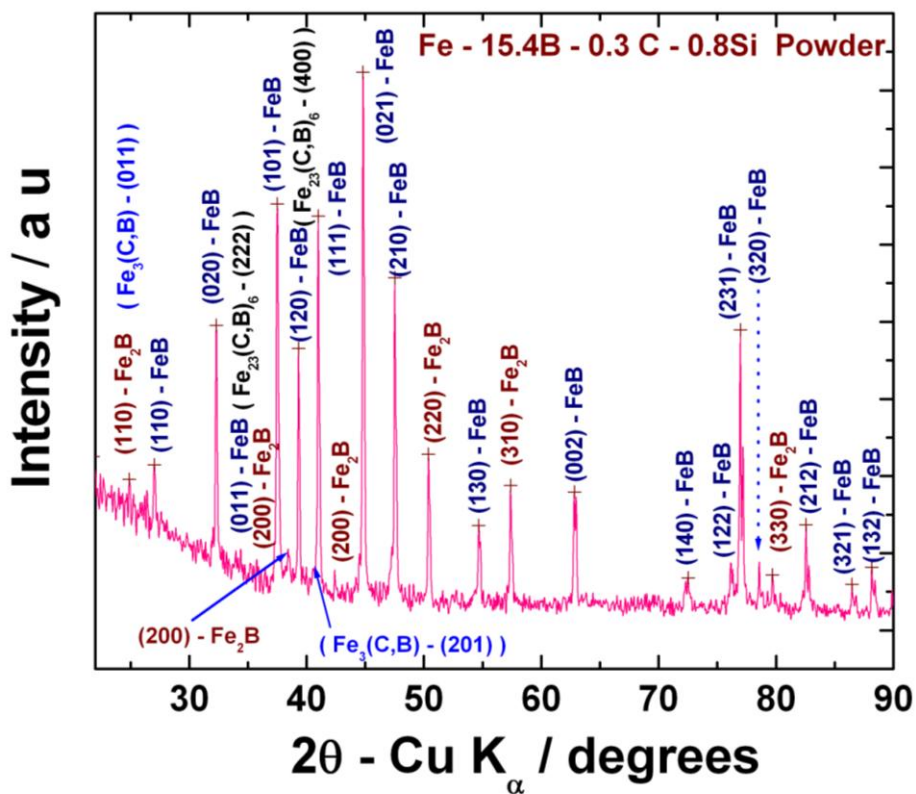


Fig. 8.2. XRD pattern of the as-received Fe-B alloy powder

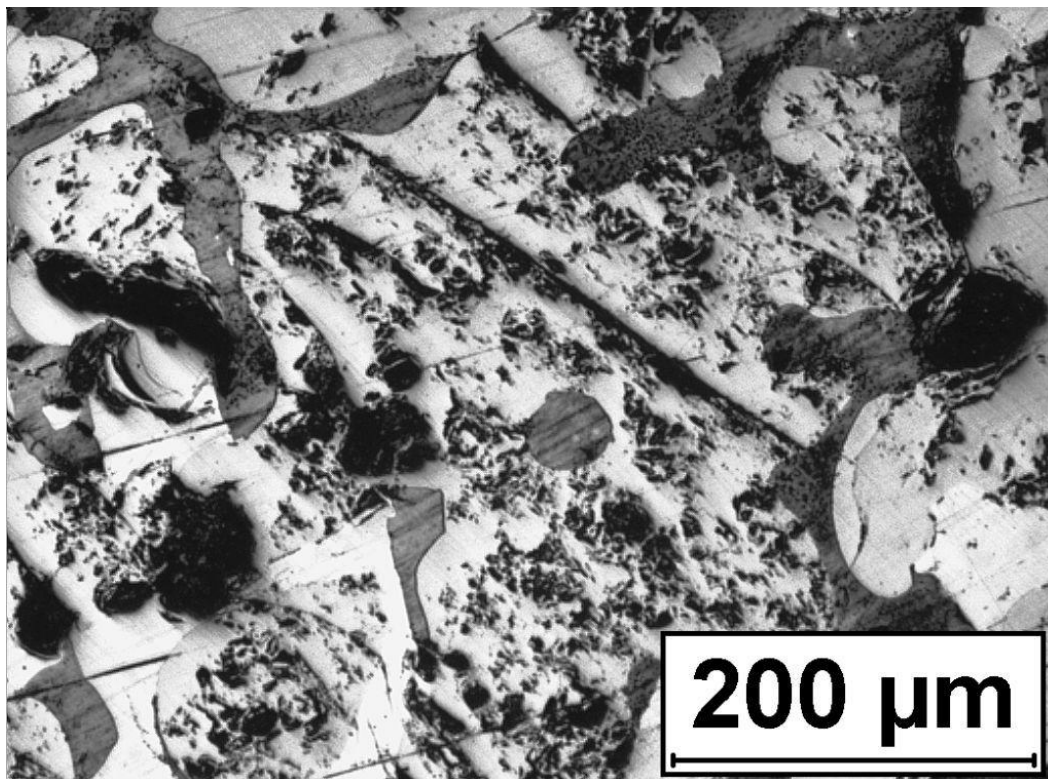


Fig. 8.3. Optical micrograph of the as received Fe-B alloy. The irregular shape and size of the individual powder particle mounted onto the epoxy base is worth noting.

#### 4.0. Results

##### 4.1. Basic structural and microstructural characterization

In Fig. 8.2, the powder x-ray diffraction pattern of Fe-B alloy powder taken using Cu-K $\alpha$  radiation is shown. As can be seen, the XRD profile bears clear testimony to the presence of two boride phases, namely tetragonal lower boride Fe<sub>2</sub>B phase with I4/mcm symmetry and the major orthorhombic FeB phase. The room temperature lattice parameters of these two phases have been estimated using standard procedures and are found to be:  $a = 0.529$  nm;  $b = 0.553$  nm and  $c = 0.29788$  nm for the orthorhombic FeB phase and  $a = 0.5093$  nm and  $c = 0.42413$  nm for the tetragonal Fe<sub>2</sub>B phase. These values are in good agreement with those reported in literature [31-33] for the phase pure Fe<sub>2</sub>B and FeB phases. Since the Fe-B alloy used in this study

contains about 0.3 wt.% C, the presence of additional phases like borocementite of  $\text{Fe}_3(\text{B,C})$  stoichiometry and cubic  $\text{Fe}_{23}(\text{B,C})_6$  type carbides is also witnessed in the XRD profile. Judged by the weak intensity of their respective x-ray diffraction peaks, it can be concluded that these phases are present only in small quantities. The presence of FeB and  $\text{Fe}_2\text{B}$  type borides as a two phase mixture with the former being the major component in an alloy of Fe-15 wt.% B, is readily understood from the currently accepted version of Fe-B binary phase diagram [20, 34]. However, it must be added that the owing to the non negligible presence of Si and C (Table 6.1), the present Fe-B alloy is actually a multicomponent system.

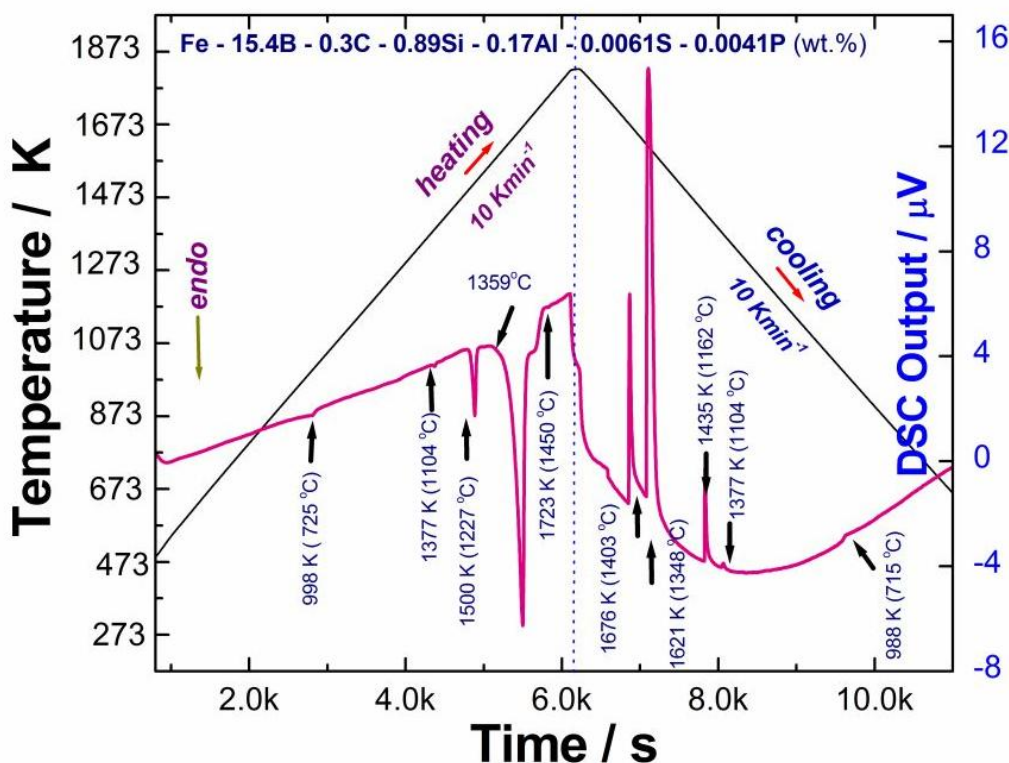


Fig. 8.4. DSC thermogram of Fe-B alloy obtained during heating and cooling at  $10 \text{ K min}^{-1}$  in pure argon atmosphere. The occurrence of phase transformation events are marked by arrows.

In Fig. 8.3, the optical micrograph of the as received Fe-B alloy is shown. The microstructure is one of containing an assembly of discrete and irregularly shaped Fe-

B particles. The energy dispersive X-ray analysis carried out in a scanning electron microscope on a few randomly chosen particles did not reveal the presence of free unbound iron particle; but on the other hand, suggested the presence of small amount of Si in each particle. The presence of free boron, being a low atomic number element could not be however detected using this technique.

#### 4.2. Thermal stability of Ferroboron alloy

In **Fig. 8.4**, the DSC thermogram obtained during heating of Fe-B alloy to its melting range, followed by cooling to room temperature in controlled argon atmosphere is shown. The DSC profile exhibits distinct peaks or thermal arrests at characteristic temperatures that are associated with distinct phase transformation

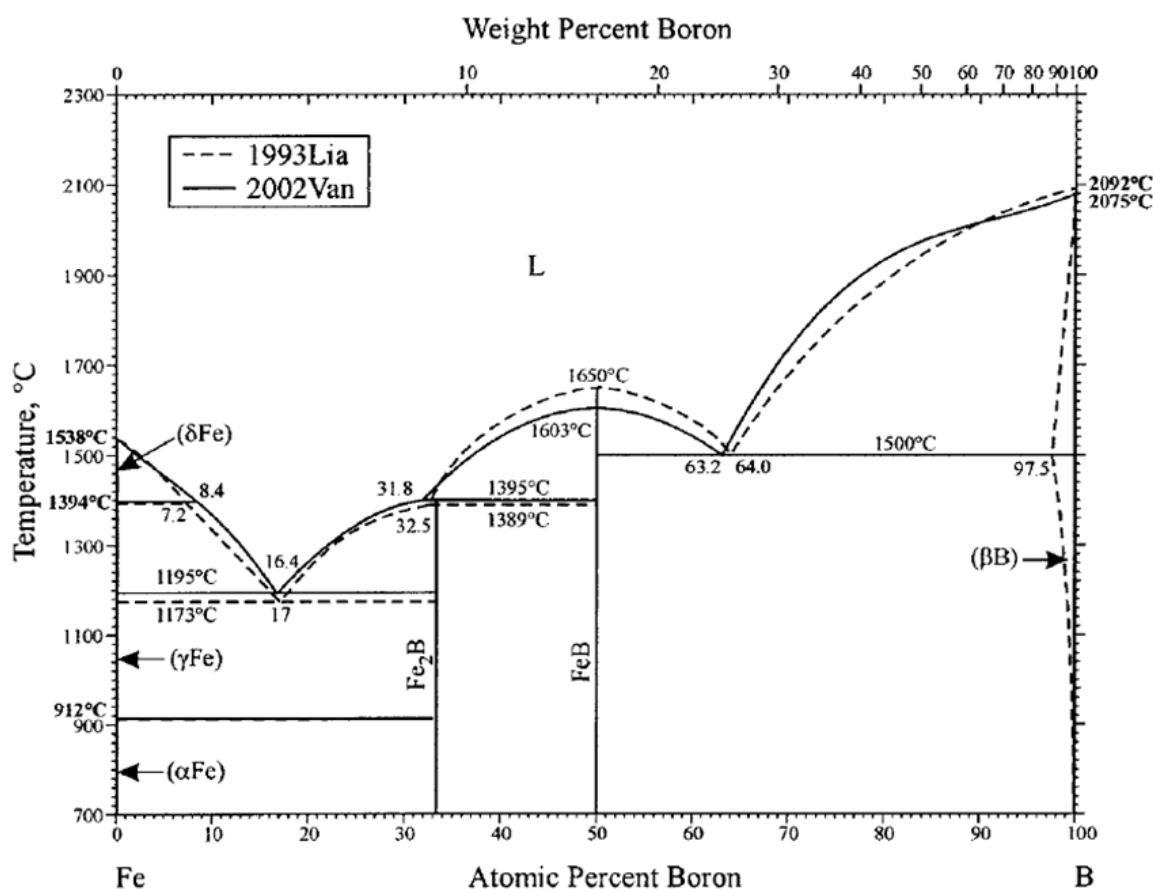


Fig. 8.5. Fe-B binary phase diagram taken from the recent assessment of Okamoto [34].

events. With a view to facilitate the understanding of temperature induced phase instability of Fe-B alloy, the binary Fe-B phase diagram is presented in **Fig. 8.5** [20, 34]. It must however be mentioned that the Fe-B alloy used in the present study is actually a multicomponent system, containing especially about 0.3 wt.% C and 0.89 wt.% Si. At present, very few experimental high temperature phase equilibrium data exist on Fe-B-Si-C quaternary system, especially around high boron and low carbon side [21]. Nevertheless, the available phase stability assessments suggest that the presence of 0.3 wt.% C results in the formation of boron containing cementite phase  $\text{Fe}_3(\text{B,C})$ , besides possible cubic  $\text{Fe}_{23}(\text{B,C})_6$  mixed borocarbide phase [17]. This is also supported by our XRD result shown in **Fig. 8.2**.

It is also likely that the presence of 0.89 wt.% Si will have some influence in governing the phase evolution behaviour especially through the formation of some complex borosilicides, although we could not get concrete evidence for the definite presence of separate silicide particles. It is possible that FeB and  $\text{Fe}_2\text{B}$  boride phases which are the major constituents of present Fe-B alloy may contain some amount of silicon dissolved in solid solution form. With this background and with the help of Fe-B binary phase diagram shown in **Fig. 8.5**, the different thermal arrests witnessed in **Fig. 8.4** may be interpreted in the following manner.

- (i) Curie temperature ( $T_c$ ) signifying magnetic to nonmagnetic transformation of  $\text{Fe}_2(\text{B,Si})$  phase is found to be 988 K. The  $T_c$  of phase pure  $\text{Fe}_2\text{B}$  is listed as 1015 K [32].
- (ii) Dissolution of borocementite  $\text{Fe}_3(\text{B,C})$  and cubic  $\text{Fe}_{23}(\text{B,C})_6$  mixed borocarbide phases in matrix occurs at about 1377 K. Since their phase fractions are small, the corresponding enthalpy changes are also found to be small, accounting for the feeble thermal arrests, witnessed in **Fig. 8.4**.

- (iii) Dissolution of the lower boride phase,  $\text{Fe}_2(\text{B},\text{Si})$  and the formation of the first traces of liquid is found to occur at 1500 K. This is similar to the  $\text{Fe}_2\text{B} + \text{FeB} \rightarrow \text{FeB} + \text{L}$  invariant reaction encountered in Fe-B binary at 1389 °C (see, **Fig. 8.5**). However, it must be remembered that in the present case of multicomponent Fe-B alloy, the dissolution of lower boride occurs over a narrow temperature range and besides is also initiated at a *lower* temperature.
- (iv) Finally, the full melting of higher boride  $\text{Fe}(\text{B},\text{Si})$  begins at 1632 K. The dissolution is almost complete at 1723 K. This reaction can again be considered analogous to the  $\text{FeB} + \text{L} \rightarrow \text{L}$  transition associated with pure Fe-B binary system, as illustrated in **Fig. 8.5**.

The phase changes that are witnessed during heating are essentially repeated in the cooling cycle, with some undercooling effects. *Thus, the first traces of  $\text{Fe}(\text{B},\text{Si})$  solid phase formation through solidification begins at 1676 K. This temperature can be taken as representing the liquidus point of present Fe-B alloy.* The precipitation of lower boride namely,  $\text{Fe}_2(\text{B},\text{Si})$  and the complete disappearance of liquid phase is found at 1621 K. A certain degree of asymmetry associated with the enthalpy effects of each of these reactions during heating and cooling cycles is also evident in **Fig. 8.4**. This is due to the fact that unlike in the case of polymorphic structural transformations involving no compositional changes, the phase changes in Fe-B-C-Si multi component system involves significant partitioning of alloying elements between the coexisting phases. This solute re-partitioning during heating and cooling seldom occurs in a reversible manner due to kinetic reasons and because of this fact the enthalpy of forward and reverse transformations as encountered in a thermal analysis experiment are not always identical. In simple terms, the reaction goes to slightly

differing degrees of completion and gives rise to products with different compositions upon cooling.

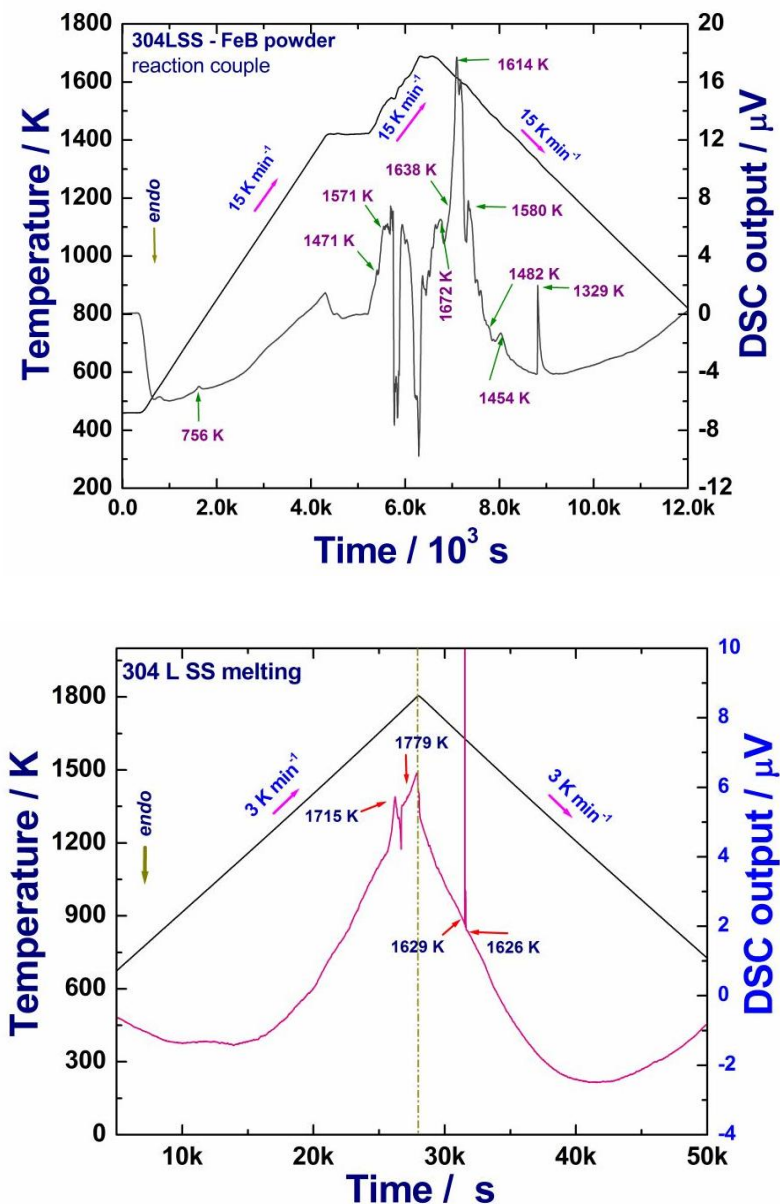


Fig. 8.6(a). DSC profile obtained during heating of SS 304L + Fe-B alloy composite. The gradual time dependent pre-melting of SS304L in molten Fe-B is clearly evident. The series of thermal arrests witnessed during cooling is due to the formation complex boride phases.

Fig. 8.6(b). DSC profile of SS 304L showing thermal arrests due to melting and solidification.

The uncertainty in the quoted transformation temperature values is estimated to be  $\pm 2$  K [26, 27, 35]. It may also be added that a few additional heating experiments are conducted at a slightly lower heating rate of  $3 \text{ K min}^{-1}$ . The values of various transformation temperature recorded at lower heating or cooling rate are found to be lower by about 2 to 3 K. An estimate of the latent heat associated with melting is made by conducting a calibration experiment under identical conditions with pure iron [35]. After such calibration procedures, the total melting enthalpy estimated for Fe-B alloy is found to be  $1115 \pm 20 \text{ kJ.kg}^{-1}$ .

#### 4.3. Thermal stability of Fe-B + 304L SS composite mixture

In order to investigate the nature of the composite product that might form under hypothetical very high temperature scenario leading to the eventual possibility of fusion of Fe-B alloy and SS304L clad together, it is decided to perform few co-melting experiments of Fe-B alloy powder and 304L steel inside the controlled ambience of the calorimeter. This set of experiment also yielded useful data on the variety of various intermetallic phases that might form upon solidification of the co-melted product. Towards this cause, small reaction couples consisting of cylindrical pieces of 304L stainless steel that are centrally compacted together with varying amounts of Fe-B alloy

**Table 8.2**

Details regarding the co-melting experiments of Fe-B alloy powder with SS 304L. Four different reaction couples with the following Fe-B to 304L mass ratios: 1:1/4, 1:2/5, 1:2 and 1:3 are melted, at  $15 \text{ K min}^{-1}$  heating rate with the exception of couple I which is melted at  $3 \text{ K min}^{-1}$ . The corresponding data set obtained with separate experiments carried out on SS 304L and Fe-B powder is given for comparison

Thermal arrest event details	SS304 L $3 \text{ K min}^{-1}$	Ferro boron $3 \text{ K min}^{-1}$	Couple I $3 \text{ K min}^{-1}$	Couple II $3 \text{ K min}^{-1}$	304 L Stainless steel $15 \text{ K min}^{-1}$	Couple III $15 \text{ K min}^{-1}$	Couple IV $15 \text{ K min}^{-1}$
Mass of reaction couple & mass ratio ( $10^6 \text{ kg}$ )	32.2	74.7	Fe-B = 128.8 304 L = 32.2	Fe-B = 253.12 304 L = 100.2 $\sim (1:2/5)$	36.6	Fe-B = 155.8 304 L = 275 $\sim (1:2)$	Fe-B = 126.30 304 L = 389.9

			~ (1:1/4)				~ (1:3)
Maximum temperature (K)	1848	1833	1833	1833	1848	1743	1673
Liquation or pre-melting temperature (K)	----	---	1471	1471	--	1471	1471
Regular melting onset temperature (K)	1715	1568	1606	1608	1700	1581	1558
Melting finish temperature (K)	1779	1658	1781	1779	1743	1672	Not obtained Melting not finished
Total area recorded for the melting peak ( $\text{mV s mg}^{-1}$ )	4.37 (250 $\text{kJ kg}^{-1}$ )	19.45 (1115 $\text{kJ.kg}^{-1}$ )	21.63 (1240 $\text{kJ.kg}^{-1}$ )	19.69 (1129 $\text{kJ.kg}^{-1}$ )	11.28	18.53 (1062 $\text{kJ.kg}^{-1}$ )	14.67 (841 $\text{kJ.kg}^{-1}$ )
Solidification onset temperature during cooling (K)	1629	1724	1782	1781	1704	1638	1474
Solidification finish temperature (K)	1626	(1592)	1544	1524	1605	1482	1367
Total area under the solidification peak ( $\text{mV s mg}^{-1}$ )	4.38 (250 $\text{kJ.kg}^{-1}$ )	23.38	16.63	12.29	11.04	14.82	13.28
First solid product formation temperature (K)	--	1468	1511	1353		--	-
Area under the Peak ( $\text{mV s mg}^{-1}$ )	--	1.138	0.62	0.09		--	-
Second Product formation temperature (K)	--		1390	1324		1454	-
Area under the Peak ( $\text{mV s mg}^{-1}$ )	--	-	0.58	0.2509		0.5484	
Third product formation temperature (K)	--	-	1318	1278		1329	
Area Under the Peak ( $\text{mV s mg}^{-1}$ )	--	-	0.17			1.29	

powder in a small alumina crucible. These are heated to about 1873 K at controlled rates (3 & 15 K min<sup>-1</sup>) in the thermal analysis apparatus under flowing high pure argon atmosphere. The DSC thermogram recorded during one such heating and cooling cycle is shown in **Fig. 8.6(a)**. For the sake of comparison, the DSC profile recorded with 304L stainless steel is also presented in **Fig.8.6(b)**.

*It is clear from **Fig. 8.6(a) and 8.6(b)** that detectable pre-melting of stainless steel or its dissolution in liquid Fe-B sets in at temperatures, of the order of 1400 K. This premelting or liquid formation temperature is lower than the melting onset temperature of 304L steel (**Fig. 8.6(b)**). Further, the presence of two distinct endothermic peaks seen at 1471 and 1571 K in **Fig. 8.6(a)** and the nearly horizontal nature of the temperature-time (T, t) profile in this small temperature interval suggests that *gradual and incremental dissolution of SS304L occurs in molten ferroboron*. It is found that this melting proceeds up to a temperature of 1672 K with considerable enthalpy effects, the magnitude of which depends on the actual Fe-B to 304L mass ratio (see, **Table 8.2**).*

In the cooling cycle, the individual identity of both Fe-B and 304L stainless steel being completely lost as they have now fused together to form a multicomponent composite mass, we see only the thermal arrests that are characteristic of the solidification thermal history of this fused product. Thus, during the cooling part, clearly detectable exothermic thermal events at several successively lower temperatures, such as 1614 K, 1580 K, 1482 K, 1454 K and 1329 K are seen (**Fig. 8.6(a)**). These events correspond to phase evolution behaviour of stainless steel+ Fe-B composite melt product, which is in principle a multi component system constituted among others by the following principal elements: Fe-Cr-Ni-Si-B-C. The nature of the solidification phase equilibria is dependent on the actual composition of the fusion

composite, which in turn is decided by the mass ratio of Fe-B powder to stainless steel, in addition to the extent of dissolution of 304L in molten Fe-B alloy during heating. Since this is an intricate and cumbersome experimental issue to be addressed in its entirety, we have simulated the co-melting experiments by varying the mass ratio of 304L SS to Fe-B alloy. Qualitatively similar results are found and in deference to brevity, the individual DSC thermograms obtained with different reaction couples are not presented here; instead these details are presented in **Table 8.2**. It must also be stated that a few additional co-melting experiments have been repeated at  $3 \text{ K min}^{-1}$  heating/cooling rate and again similar results are found with the noteworthy observation that the progressive dissolution event of stainless steel in molten Fe-B is rather well spread at lower rates of heating, signifying thereby the possibility of its complete dissolution, when slowly heated.

In addition, as is evident from **Table 8.2**, a systematic change in the transformation thermal arrest temperatures and associated enthalpy effects are noticed with respect to the progressive increase in the 304L Fe-B alloy mass ratio. However, one important finding that is contrary to this trend is the near *constant nature* of the pre-melting onset temperature during heating, which we denote in the present study as the *liquation* temperature, meaning thereby the premature liquid phase formation at temperatures below the individual melting point of 304L steel and Fe-B alloy. This near constancy of the liquation temperature is graphically shown in **Fig.8.7** for different reaction couples that had different mass ratios of Fe-B to 304L steel.

The important physical implication of this set of results is *that 304L stainless steel/Fe-B reaction couple is prone to strong metallurgical interaction at high temperatures, by the way of formation of a liquid phase at a temperature of about 1471 K.*

In **Fig. 8.8**, the X-ray diffraction profile of the co-melted product taken at room temperature is illustrated. As can be seen from this figure, the fused product consists of mixed borides or possibly mixed borocarbides of Fe, Cr and Ni. Most of the reflections shown in **Fig.8.8** can be satisfactorily indexed to  $(\text{Fe,Cr})_2\text{B}$  phase *vide* PDF card No. 35-1180,  $(\text{Fe,Ni})_3\text{B}$  phase *vide* PDF card No. 36-0979 and  $(\text{Fe,Cr})\text{B}$

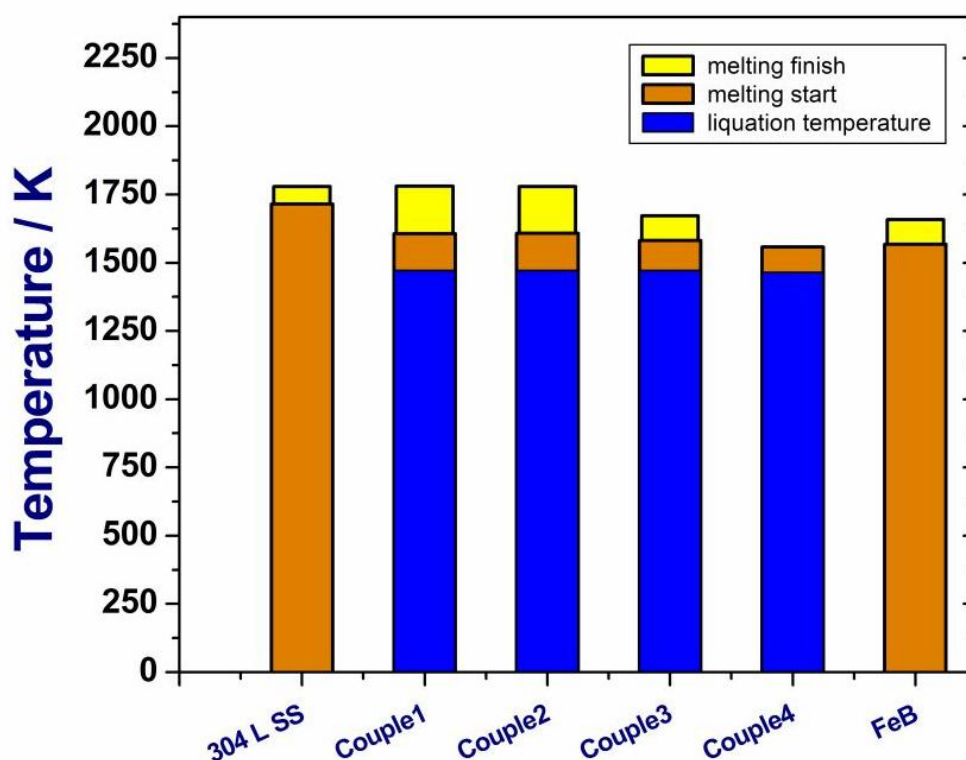


Fig. 8.7. Variation in the onset of pre-melting or liquation temperature as a function Fe-B to 304L mass ratio: Couple (1):1:1/4; Couple (2): 1:2/5; Couple (3): 1:2 and Couple (4): 1:3. Note that independent of the mass ratio, the pre-melting of 304L in Fe-B is initiated at a constant temperature of 1471 K.

phase *vide* PDF card No. 51-1410 phases. These powder diffraction details are listed in **Table 8.3**.

$2\theta$ (Cu-K $\alpha$ )	Normalized Intensity	d spacing ( $\text{\AA}$ )	PDF Card No 35-1180	PDF Card No 36-0979	PDF Card No. 51-1410

degrees)	(%)				
26.89	60.71	3.31295	(120) – (Cr, Fe) <sub>2</sub> B		
28.77	80.79	3.10059			
29.63	89.30	3.01253			
31.11	100.00	2.8725	(311) – (Cr, Fe) <sub>2</sub> B		(311) – (Fe, Cr)B
34.75	41.16	2.57949	(420) – (Cr, Fe) <sub>2</sub> B		
36.23	49.30	2.47744	(600) – (Cr, Fe) <sub>2</sub> B		
39.65	35.56	2.27128	(511) – (Cr, Fe) <sub>2</sub> B	(112) – Fe <sub>3</sub> Ni <sub>3</sub> B	(511) – (Fe, Cr)B
41.29	46.33	2.18477		(121) – Fe <sub>3</sub> Ni <sub>3</sub> B	
43.37	34.76	2.08469	(131) – (Cr, Fe) <sub>2</sub> B	(022) – Fe <sub>3</sub> Ni <sub>3</sub> B	(131) – (Fe, Cr)B
45.13	36.29	2.00739	(202) – (Cr, Fe) <sub>2</sub> B		(620) – (Fe, Cr)B
47.63	31.44	1.9077	(331) – (Cr, Fe) <sub>2</sub> B		
48.77	28.46	1.86574		(113) – Fe <sub>3</sub> Ni <sub>3</sub> B	
50.69	28.58	1.79948	(240) – (Cr, Fe) <sub>2</sub> B		
51.29	27.98	1.77983	(222) – (Cr, Fe) <sub>2</sub> B		
56.57	85.96	1.62559	(440) – (Cr, Fe) <sub>2</sub> B		(422) – (Fe, Cr)B
60.79	22.73	1.52246			
63.79	14.35	1.4579	(622) – (Cr, Fe) <sub>2</sub> B		(911) – (Fe, Cr)B
67.55	15.34	1.3856	(113) – (Cr, Fe) <sub>2</sub> B	(311) – Fe <sub>3</sub> Ni <sub>3</sub> B	(113) – (Fe, Cr)B
77.41	12.24	1.23187	(060) – (Cr, Fe) <sub>2</sub> B	(042) – Fe <sub>3</sub> Ni <sub>3</sub> B	
79.89	40.22	1.19975		(313) – Fe <sub>3</sub> Ni <sub>3</sub> B	(333) – (Fe, Cr)B
87.95	10.88	1.10939			

In **Fig. 8.9**, the back scattered electron image of the Fe-B+304L SS fusion product is presented together with a collage of pseudo coloured x-ray images obtained using characteristic x-ray lines of Fe, Cr and Ni respectively. It is clear from **Fig. 8.9**, that the high temperature interaction between Fe-B and 304L SS results in the formation of a heterogeneous reaction product. Thus, the matrix consists of predominantly Fe

rich  $(\text{Fe,Cr})_2\text{B}$  and  $(\text{Fe,Cr})\text{B}$  phases, into which fairly big particles of Cr-rich carbides or probably borocarbides are embedded. Besides these, films of nickel rich  $(\text{Ni,Fe})_3\text{B}$  borides are also seen to envelope intergranular or interdendritic regions of previously liquid phase that was present in the initial stages of solidification.

This description of the melt product is accordance with the x-ray diffraction

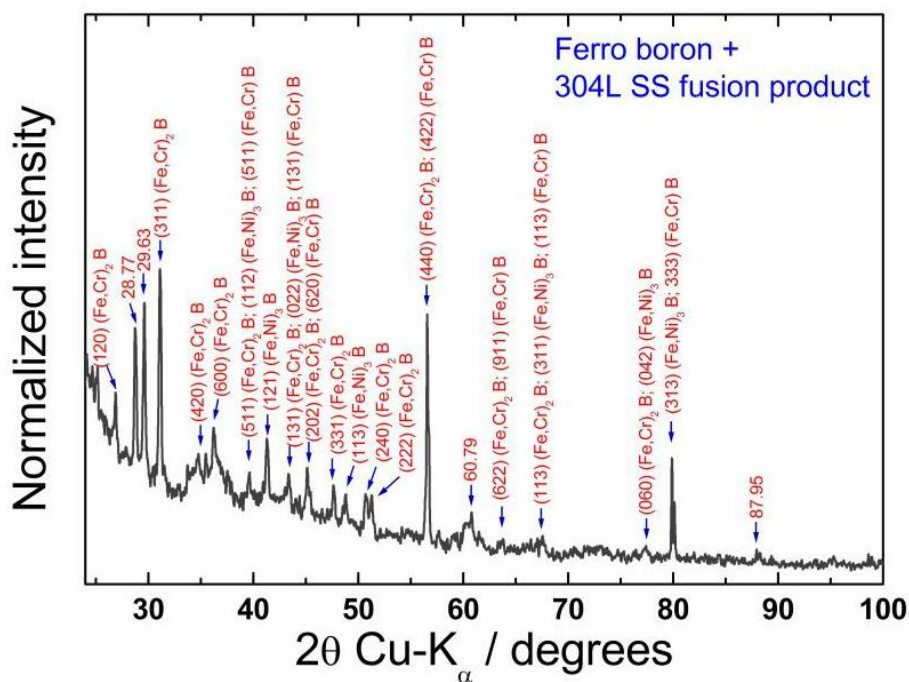


Fig. 8.8. XRD profile of the fused product of Fe-B alloy powder and 304L stainless steel

findings (See, **Fig. 8.8 & Table 8.3**). The possibility of formation of different transition metal borides upon high temperature metallurgical interaction of Fe-B with austenitic or ferritic stainless steels is amply supported in literature [5, 24, 36, 37].

#### 4.4. 304L stainless steel-Ferroboron reaction couple: microstructural characterisation of the reaction interface

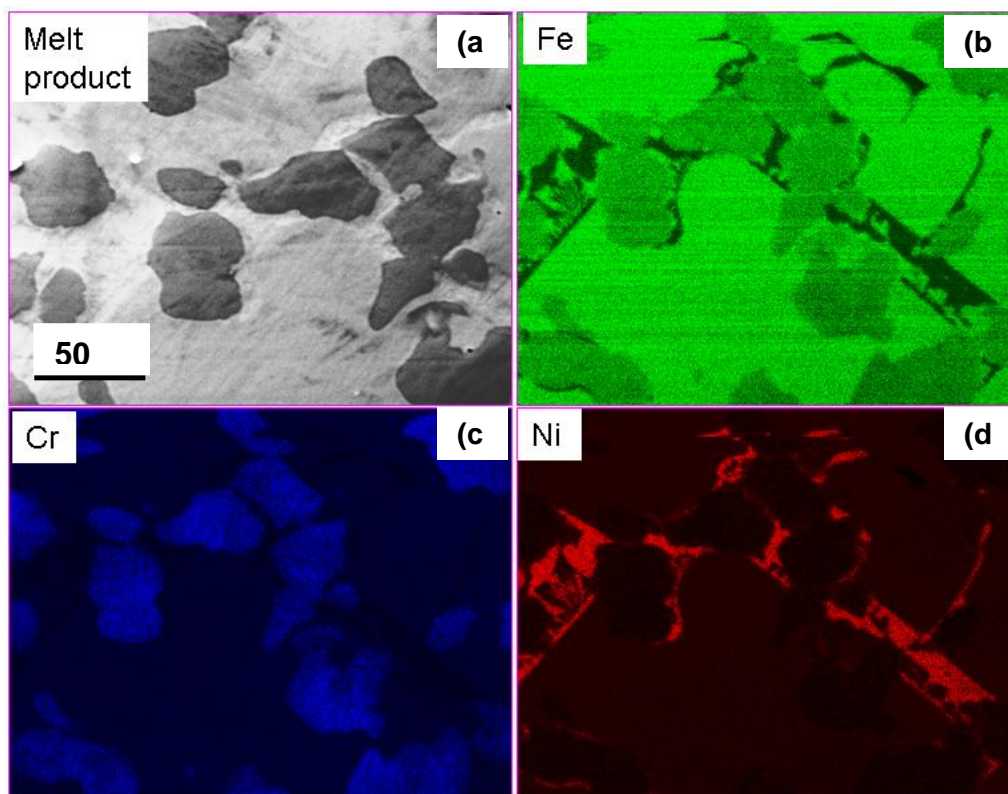


Fig. 8.9.(a). Back scattered electron image of the high temperature Fe-B+304L stainless steel melt product. (b). Pseudo colour image obtained by x-ray mapping represents the matrix region rich in Fe; (c). Cr-rich boride phase embedded in matrix, and (d) the Ni-rich intergranular phase.

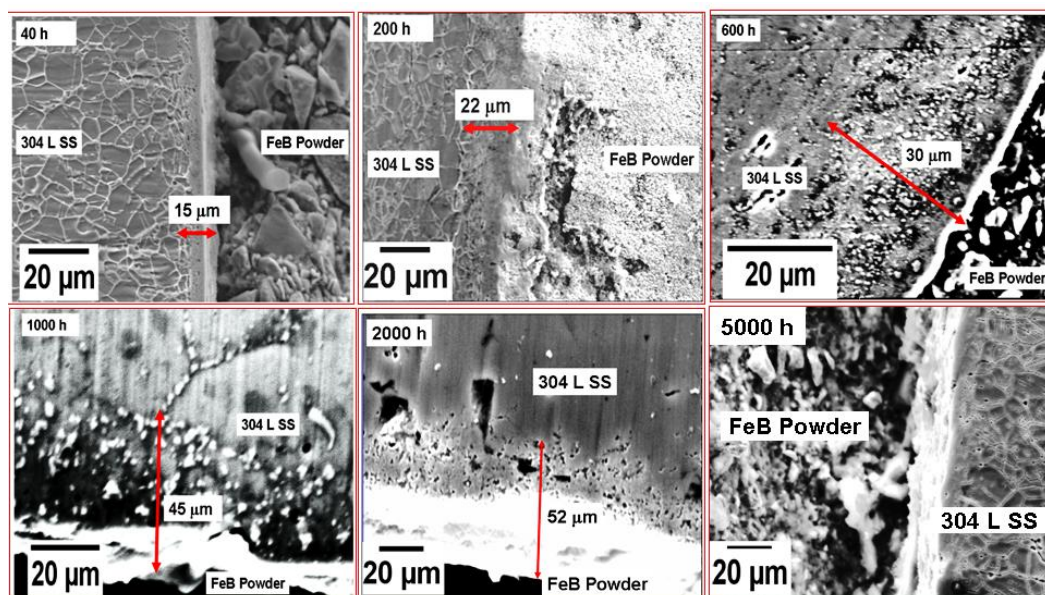


Fig. 8.10. Microstructural collage of the reaction layer formed at the interface between 304L stainless steel and Fe-B powder for various time durations at 973 K.

In **Fig. 8.10**, the microstructural development across the reaction interface for various time durations at a typical test temperature of 973 K is illustrated. In **Fig. 8.11**, the influence of reaction temperature on interfacial microstructure, for a fixed annealing time of 600 h is depicted. In both cases, the reaction layer is clearly delineated so that fairly accurate measurements of its thickness as a function of time and temperature could be made using microscopy measurements. In general, the diffusion layer consists of parallel tracks of fine intermetallic boride particles, embedded in the steel matrix whose composition is progressively modified as one moves away from the central line of the reaction interface.

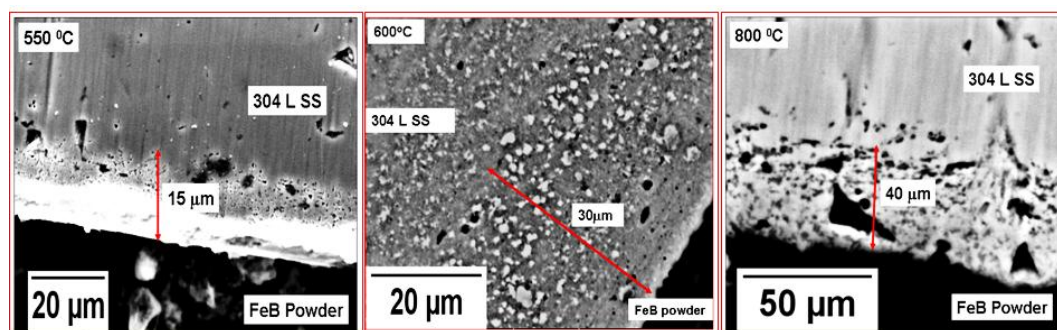


Fig. 8.11. Microstructural collage of the reaction layer formed at the interface between 304L stainless steel and Fe-B powder at various temperatures for 600 h exposure.

This latter aspect is illustrated in **Fig. 8.12**, wherein, the characteristic X-ray EDS spectra obtained at different locations on either side of the interface clearly suggest that as one moves away from the bulk of 304L SS and into the Fe-B region traversing thus across the interface, there is a slight but definite *differential* enrichment of Ni and Cr, seen in the Fe-B region that is immediately adjacent to the reaction interface. Of these, the Cr-enrichment is restricted to a small zone adjacent to the interface. In this region, appreciable Ni-enrichment is however not found. On the contrary, the Ni-intensity seems to be enhanced in regions that are located a little further from the

interface and is next to the Cr-rich zone. Thus Cr and Ni rich zones appear to exclude each other. In an analogous manner, it is indeed possible that boron diffusion into the stainless steel taking place at a much accelerated pace, but since the solubility of boron in  $\gamma$ -austenite is restricted even at high temperatures [20, 34] and further owing to the presence of Fe, Ni and Cr in 304L steel, one witnesses copious formation of grain boundary transition metal borocarbides on the interior of stainless steel side. The hardness of the borided layer region on 304L stainless steel is found to be very high, of the order of 1600 VHN.

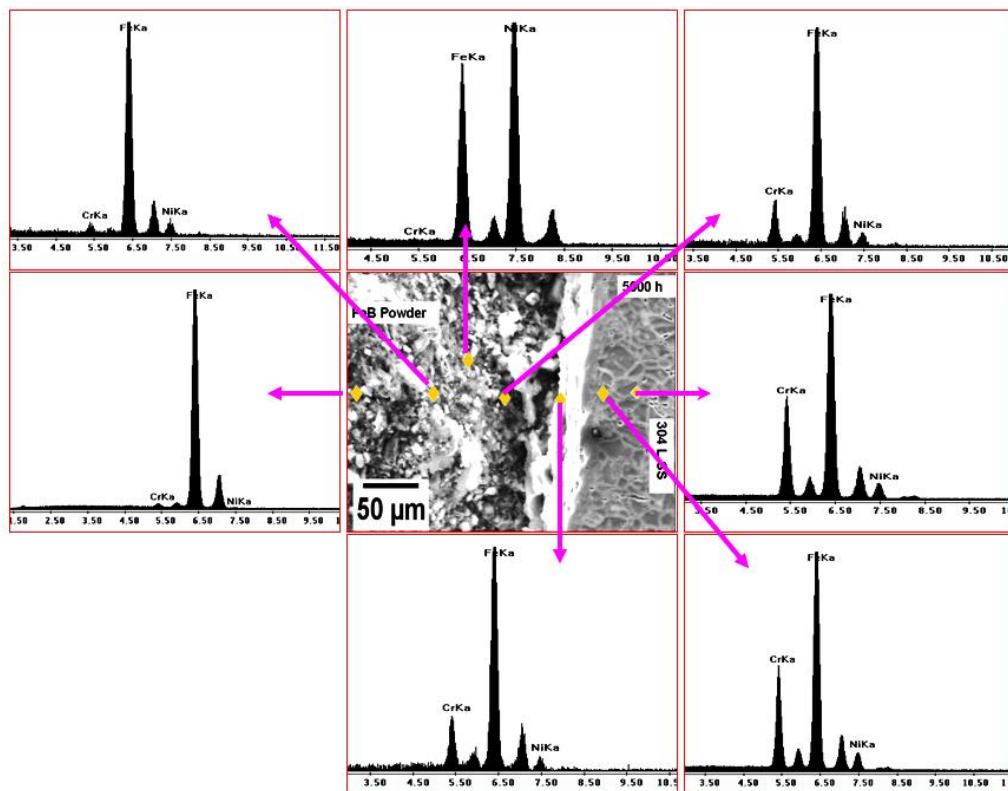


Fig. 8.12. The progressive variation in the Ni and Cr concentration across the reaction interface for 1073 K/5000h diffusion anneal

4.5. 304L stainless steel-Ferroboron reaction couple: estimation of reaction layer formation kinetics

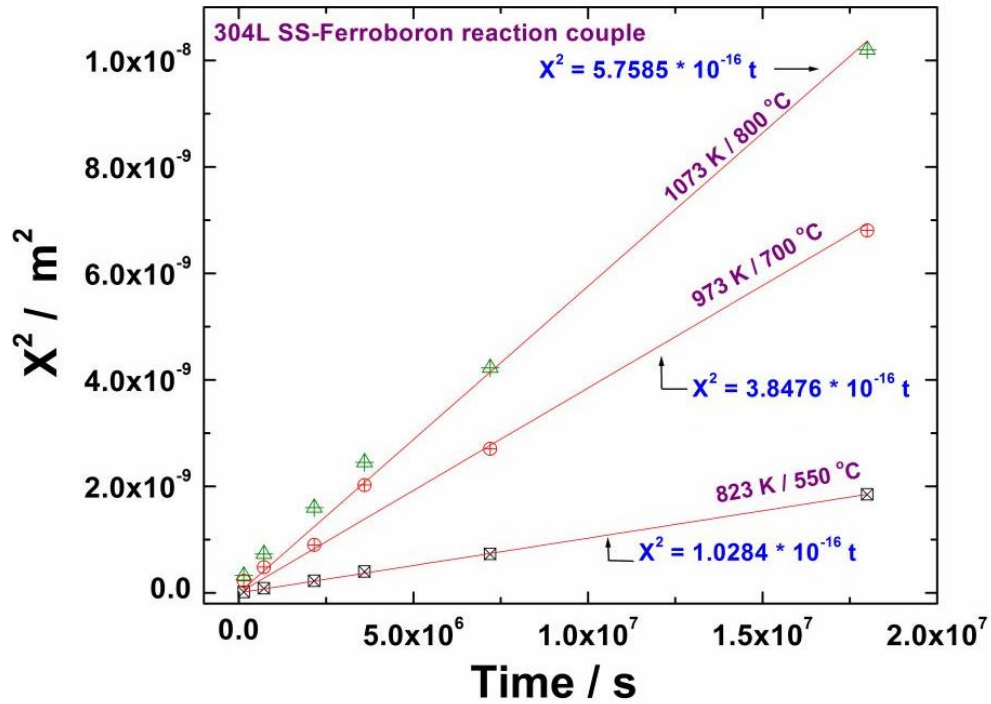


Fig. 8.13. Time temperature variation of the penetration layer depth.

In **Fig. 8.13**, the variation of the reaction layer depth with temperature and time is presented in the form as  $\sqrt{x^2}$  versus time (t) plot. Here,  $x$  stands for the reaction layer depth given in metres and time  $t$ , is given in seconds. As can be seen, good linear correlation is observed for the temperature range, 823–1073 K and time up to 5000 h.

$$x^2 = kt. \quad (1)$$

The rate constant  $k(T)$  is a function of temperature. The linear behaviour given in Eq. (1) is usually interpreted as supportive of the operation of bulk diffusion as the probable rate controlling step. The temperature dependence of  $k$  is usually represented by the Arrhenius form.

$$k(T) = k_o \exp(-Q/RT). \quad (2)$$

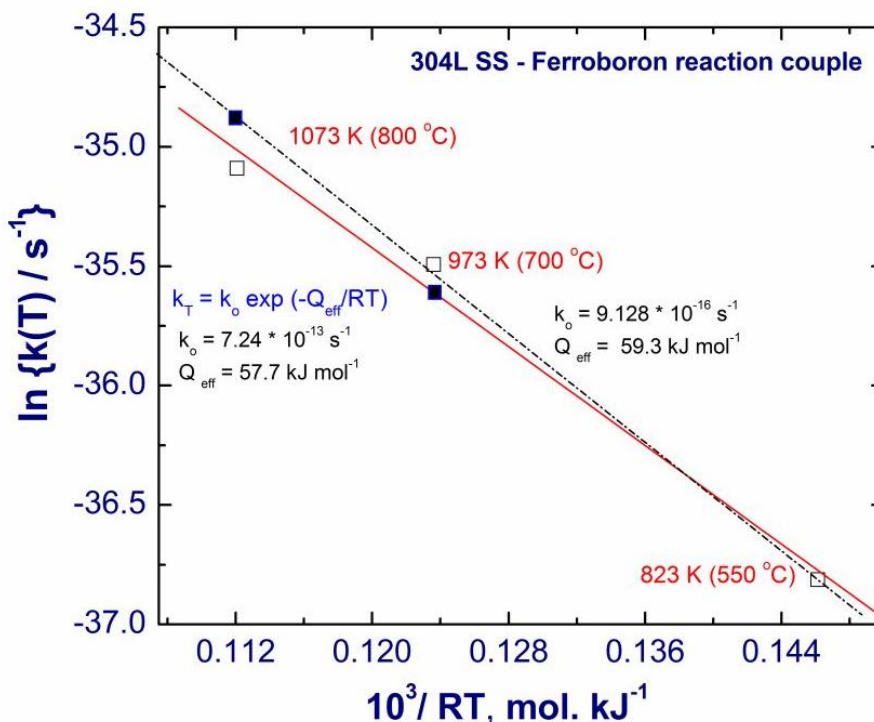


Fig. 8.14. Variation of reaction rate constant  $k(T)$  with temperature in the range 823-1073 K.

$k_o$  is the pre-exponential factor and  $Q$  is the apparent activation energy for the *overall* reaction occurring at the interface. In **Fig. 8.14**, the measured variation of  $\ln\{k(T)\}$  with  $1/T$ , is presented. The activation energy  $Q$  estimated from the slope of the linear correlation is  $57.7 \text{ kJ}\cdot\text{mol}^{-1}$ . Considering the possible intrinsic experimental uncertainty associated with our experiments, especially with regard to the penetration layer depth estimation using microscopy techniques, another set of data, which is within  $\pm 5\%$  of the standard deviation has been used to cross check the consistency of  $Q$  value obtained in this study. This second fit obtained with another independent data

set is shown as dotted line in **Fig. 8.14**. The value for  $Q$  obtained in the latter case is found to be  $59.3 \text{ kJ mol}^{-1}$ . Thus, in summary, it may be said that an effective or apparent  $Q$  value in the range, 57 to  $60 \text{ kJ mol}^{-1}$  may be estimated for the overall diffusional interaction between Fe-B alloy and 304L stainless steel in the temperature range 823–1073 K (550–800 °C).

4.6. *Thermal Property Measurement: Enthalpy and specific heat versus temperature data*

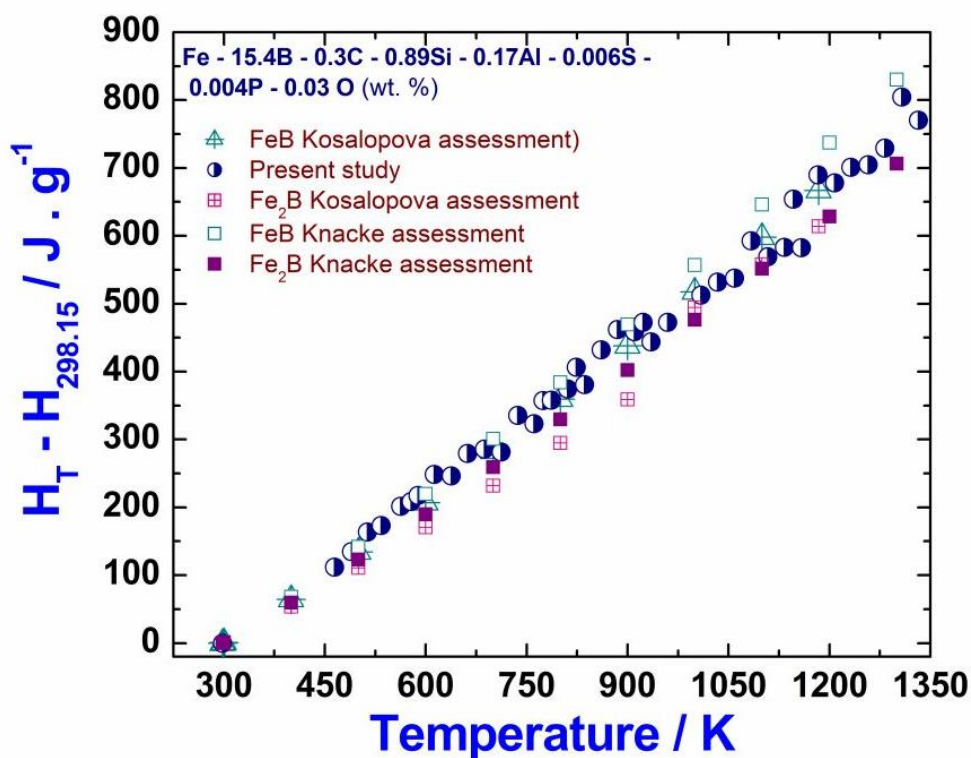


Fig. 8.15. Enthalpy increment values as a function of temperature obtained in this study are compared with literature assessments for Fe<sub>2</sub>B and FeB phases (Kosalopova, 1990; Knacke, 1991).

In **Fig. 8.15**, the variation of measured enthalpy increment  $H_T - H_{298}$  values with temperature is compared with the available literature data for phase pure Fe<sub>2</sub>B and FeB compounds [18, 22, 38]. It is clear that the current measurements are located in between the Fe<sub>2</sub>B and FeB data points, which is in accordance with the fact that the

Fe-B alloy used in this study is basically a mixture of FeB and Fe<sub>2</sub>B phases. The present enthalpy data are fitted by the method of nonlinear least squares regression to the following functional representation.

$$\Delta^{\circ}H = H_T - H_{298} / \text{J.g}^{-1} = a (T-298) + b/2(T^2-298^2) - c(1/T-1/298). \quad (3)$$

The values of fit coefficients are:

$$a = 0.62094;$$

$$b = 0.00012 \pm 0.00002; \text{ and}$$

$$c = 10685.80827 \pm 3910.76779.$$

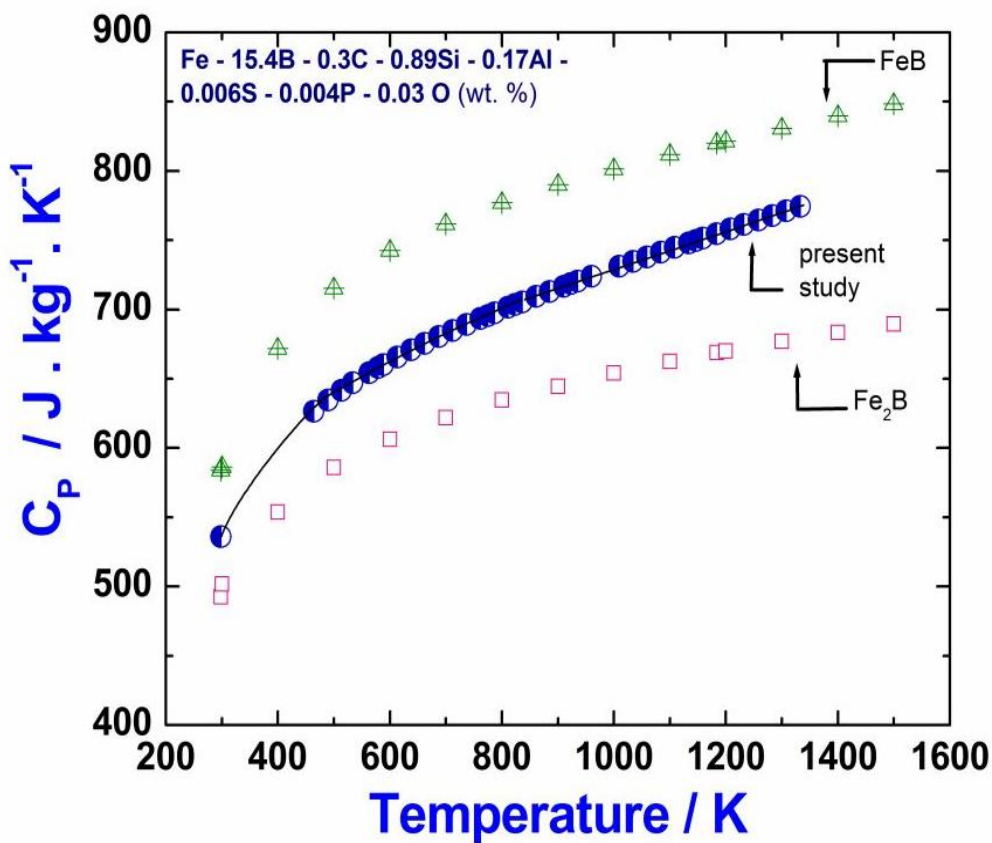
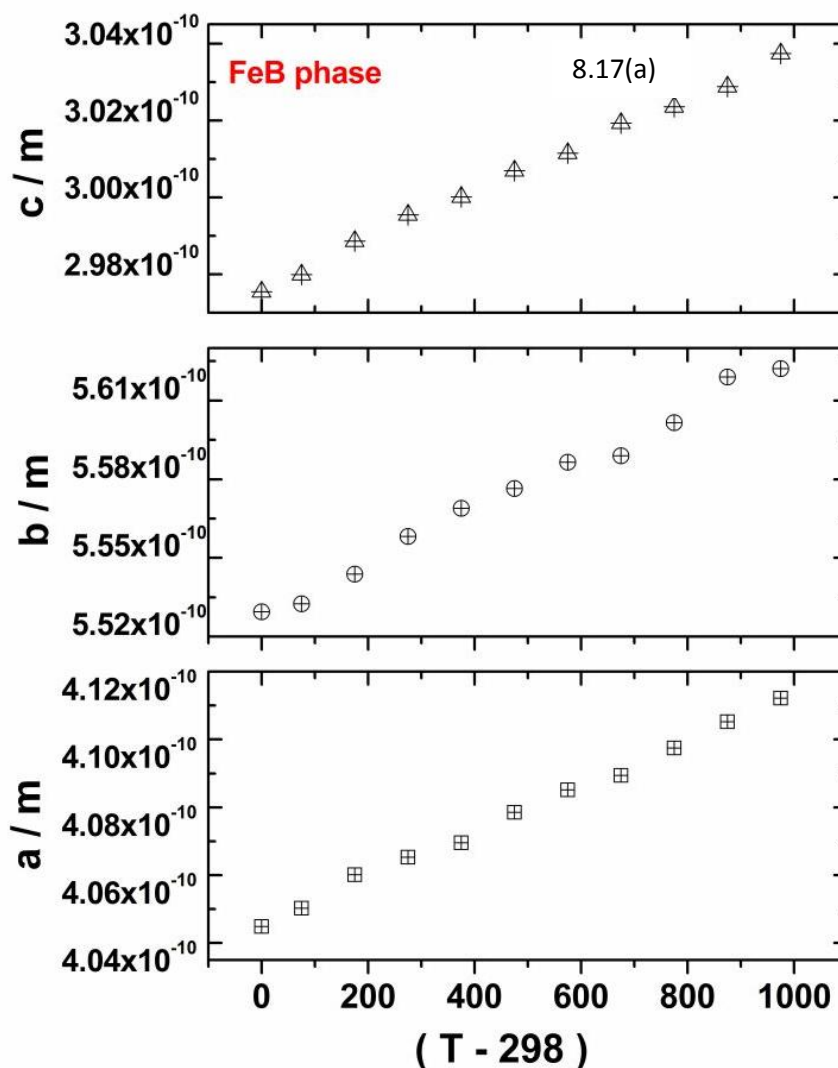


Fig. 8.16. Specific heat for Fe-B alloy obtained in this study is compared with literature estimates for FeB and Fe<sub>2</sub>B borides (Kosolapova, 1990).

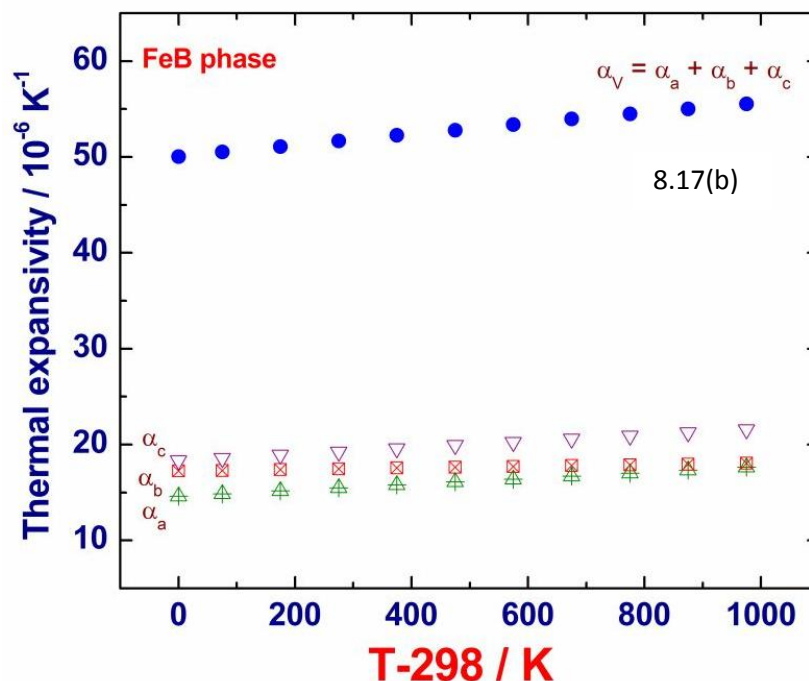


In the above expression, temperature  $T$  is given in Kelvin. The  $R^2$  value of the fit is 0.99. The above functional form is chosen so that the specific heat  $C_p$  is directly given by the most often used form which is given as

$$C_p = a + bT + cT^2. \quad (4)$$

In **Fig. 8.16**, the calculated  $C_p$  data are displayed together with the assessed values for FeB and Fe<sub>2</sub>B borides, taken from literature [18, 22, 38]. As can be seen, the measured  $C_p$  curve for the Fe-B shielding alloy falls in between that of phase pure Fe<sub>2</sub>B and FeB phases, which is only expected from the two phase nature of Fe-B alloy. At this juncture, it can be stated that to the best of author's knowledge, not much published data exist on the thermal properties of high boron containing Fe-B

alloys. Hence, the comparison could be made only with respect to assessed estimates for phase pure Fe<sub>2</sub>B and FeB borides.



#### 4.7. High temperature lattice thermal expansion of Fe-B alloy

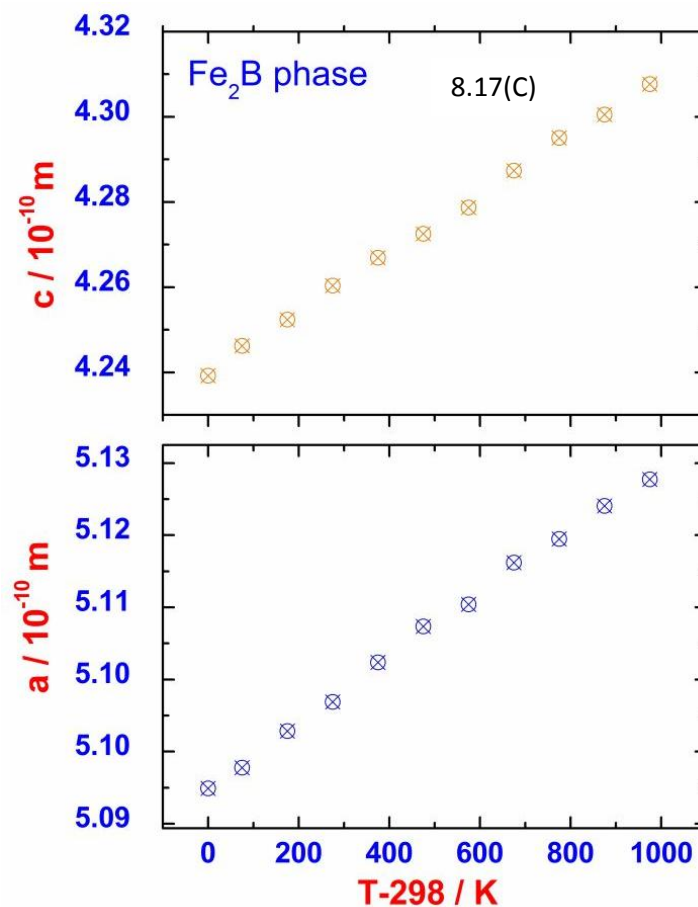
In Fig. 8.17(a) to (d), the lattice thermal expansion data obtained by high temperature powder x-ray diffraction technique of Fe-B alloy powder are graphically summarised. The high temperature XRD profiles are analysed by standard procedures and the lattice parameter versus temperature data after due calibration are fitted to the following functional form. For the orthorhombic FeB phase, which constitutes the major fraction of present Fe-B material, the relevant expressions are as follows.

$$a(\text{T/K})/\text{m} = 5.529 \times 10^{-10} + 9.5312 \times 10^{-15} (\text{T}-298) + 3.1713 \times 10^{-19} (\text{T}-298)^2. \quad (5)$$

$$b(\text{T/K})/\text{m} = 2.9788 \times 10^{-10} + 5.4553 \times 10^{-15} (\text{T}-298) + 5.6077 \times 10^{-19} (\text{T}-298)^2. \quad (6)$$

$$c(\text{T/K})/\text{m} = 5.53 \times 10^{-10} + 9.4723 \times 10^{-15} (\text{T}-298) + 1.1315 \times 10^{-19} (\text{T}-298)^2. \quad (7)$$

In Fig. 8.17(a), the variation of  $a$ ,  $b$  and  $c$  lattice parameters of the FeB phase with temperature is illustrated. The coefficients of linear thermal expansion or axial



thermal expansivity along ‘*a*’, ‘*b*’ and ‘*c*’ directions are easily computed from the above expressions by the standard definition,

$$\alpha_i = 1/i \times [di/dT]; i= a, b \text{ and } c. \quad (8)$$

The bulk thermal expansion coefficient  $\alpha_v$  is estimated by the following expression

$$\alpha_v = \alpha_a + \alpha_b + \alpha_c \quad (9)$$

In **Fig. 8.17(b)**, the calculated values of  $\alpha_i$  and  $\alpha_v$  are plotted for different temperatures. For ease of representation, the calculated thermal expansivity data are fitted to following analytical expressions in the temperature range 300-1273 K.

$$\alpha_a \text{ (T/K)/K}^{-1} = \{ 13.7866 + 0.00283 T + 1.5522 \times 10^{-7} T^2 \} \times 10^{-6}. \quad (10)$$

$$\alpha_b \text{ (T/K)/K}^{-1} = \{ 17.0105 + 0.00078 T + 2.4501 \times 10^{-8} T^2 \} \times 10^{-6}. \quad (11)$$

$$\alpha_c \text{ (T/K)/K}^{-1} = \{ 17.3916 + 0.00318 T + 8.447 \times 10^{-8} T^2 \} \times 10^{-6}. \quad (12)$$

In a similar manner, the estimated lattice parameter data for the lower boride phase  $\text{Fe}_2\text{B}$  are presented in **Fig. 8.17(c)**. These data are fitted to the following functional form.

$$a(T/\text{K})/\text{m} = 5.09299 \times 10^{-10} + 3.0 \times 10^{-5} (T-298) + 1.0271 \times 10^{-9} (T-298)^2. \quad (13)$$

$$c(T/\text{K})/\text{m} = 4.24134 \times 10^{-10} + 7.0 \times 10^{-5} (T-298) + 2.77 \times 10^{-9} (T-298)^2. \quad (14)$$

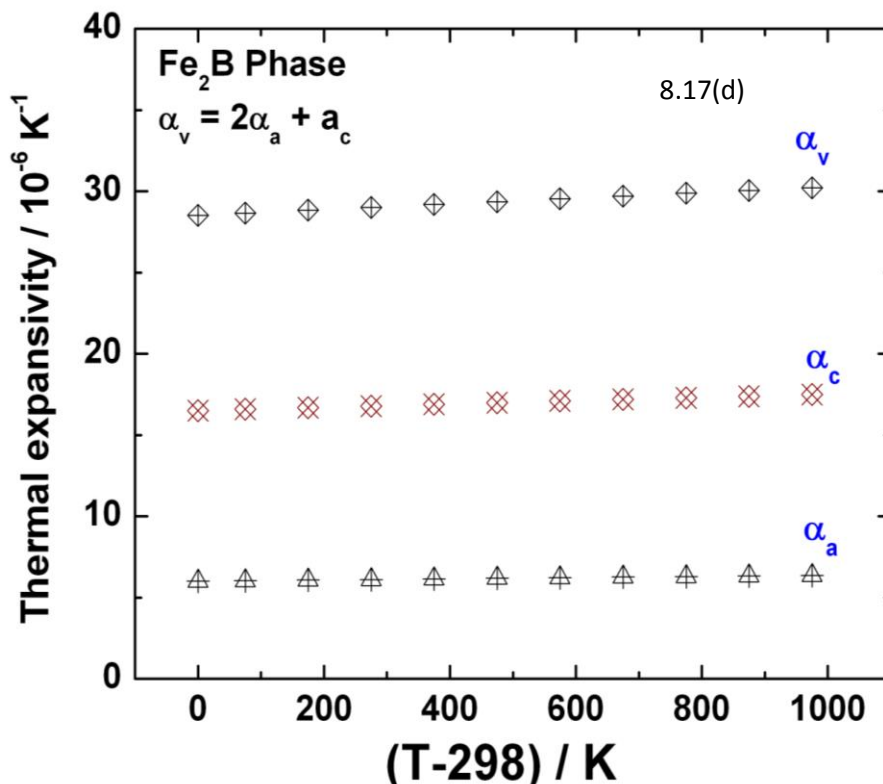


Fig. 8.17(a). Variation of the lattice parameter of orthorhombic  $\text{FeB}$  phase with temperature. (b). Thermal expansivity along ‘a’ ‘b’ and ‘c’ directions are plotted with estimated volume thermal expansivity. (c). Lattice parameter variation with temperature of tetragonal  $\text{Fe}_2\text{B}$  phase (d). Thermal expansivity variation with temperature along ‘a’, and ‘c’ axes along with computed

The axial thermal expansion coefficients,  $\alpha_a$  and  $\alpha_c$  are estimated from the above expressions and these data are graphically presented in **Fig. 8.17(d)**. For the tetragonal  $\text{Fe}_2\text{B}$  phase, the calculated temperature dependencies of thermal expansivity along ‘a’ and ‘c’ directions are:

$$\alpha_a (T/\text{K})/\text{K}^{-1} = \{5.91469 + 0.00033 T + 1.9448 \times 10^{-8} T^2\} \times 10^{-6}. \quad (15)$$

$$\alpha_c (T/K)/K^{-1} = \{ 16.22346 + 0.00097 T + 2.0964 \times 10^{-8} T^2 \} \times 10^{-6}. \quad (16)$$

The bulk thermal expansivity for the tetragonal Fe<sub>2</sub>B phase is given by the following relation,

$$\alpha_v = 2\alpha_a + \alpha_c \quad (17)$$

## 5.0. Discussion

At the outset, it is clear that a critical analysis of the suitability of a new alternate shielding material such as Fe-B for fast reactor applications needs to be undertaken from multiple perspectives; of which the comprehensive characterisation of intrinsic thermal stability, thermal properties and the propensity to strongly interact with the clad material constitutes one important component. The present characterization study is an attempt in this direction.

The comprehensive scanning calorimetry studies on Fe-B alloy shed light on two fundamental issues. In the first, it established the phase transformation sequence of multicomponent Fe-B-C-Si based shielding alloy both as a function of heating and cooling, up to its fusion regime. The present study clearly revealed that the first traces of liquid appears in the Fe-B alloy at a temperature of about 1500 K, which is considerably lower than the melting point of the SS 304L clad (see, **Table 8.2**). It should also be noted that melting is complete only after a fairly long temperature interval, namely at 1723 K. This rather large temperature domain of liquid phase coexistence with solid is generic to high boron containing Fe-B alloy systems and can lead to solidification cracking arising out of lack of accommodation of strains due to solid phase formation.

In the second it is also demonstrated that the Fe-B+304L stainless steel reaction couple as a single cohesive mass exhibits a premature dissolution reaction at temperature at 1471 K, which is lower than the melting onset of virgin Fe-B shielding

alloy. The finding suggests that 304L stainless steel can undergo complete dissolution in molten ferroboron to form a fused product which is a mixture of complex intermetallic borides. These borides are brittle in character and hence their formation at the Fe-B/stainless steel clad interface during accidental high temperature scenarios will result in *clad embrittlement*, the severity of which is a function of the clad penetration depth.

This leads us to the third important issue namely the nature of metallurgical interaction between Fe-B alloy and 304L stainless steel taking place in the solid state. The experimental results obtained in this study with regard to solid state diffusional interaction between Fe-B and 304L stainless steel clearly point to the possibility of strong interfacial interaction taking place at the diffusional zone. In the temperature range of present study, namely 823-1073 K, the *attack layer* thickness or the so-called reaction layer depth is found to vary with square root of time, as given by *Eq. 1*. This suggests that for longer time durations, there is a gradual reduction creeping in with respect to *attack layer* thickening kinetics. The tendency to attain asymptotically the saturation limit for the clad attack layer thickness is in fact advantageous, as compared to the linearly increasing growth behaviour of the clad penetration depth with time.

There are extensive studies in metallurgical literature on boriding kinetics of steel and also with regard to the high temperature interaction of  $B_4C$  with stainless steel, which support qualitatively the present experimental findings [4, 7, 11-14]. With regard to surface boriding of stainless steel done for tribological applications by paste boriding or other related techniques, it is found that the reaction interface is highly heterogeneous in its metallurgical character. It is constituted of multiple borides like  $Fe_2B$ ,  $Ni_2B$ ,  $FeB$ ,  $CrB$  etc [see, for example, Ref. 4]. However, there seems to be some variation with regard to the kinetic parameters associated with their formation,

as estimated by different authors from the boride layer growth. Thus, for example Dunner et al [4] obtain a value of about  $97.2 \text{ kJ mol}^{-1}$ , probably for the B-atom diffusion in the  $\gamma$ -austenite iron matrix. Ozdemir et al., [14] on the other hand report a value of  $199 \text{ kJ mol}^{-1}$  for the effective activation energy involved in the boriding kinetics of austenitic stainless steels. Recently, Campos et al [11-14] in a series of experiments conducted a systematic study of the kinetics of boriding of different steels. They list a varying activation energy spectrum ranging from 179 to  $79 \text{ kJ mol}^{-1}$ , depending on the fact that whether the analysis is made for  $\text{Fe}_2\text{B}$  phase formation or for the entire diffusion zone formation.

To the best of author's knowledge, the most comprehensive investigation that has been carried out and reported so far with regard to the diffusional interaction between  $\text{B}_4\text{C}$ /stainless steel combination, is that of Hofman et al [7, 13]. The temperature range and time period of their experiments vary from 1073–1473 K and 5–300 h. Subsequently, Nagase et al., [39] have extended the range of temperatures up to 1623 K. However, in the present study carried out with Fe-B alloy, higher temperatures could not be adopted due to the fear of pre-melting reaction setting in at 1400 K itself. However, our experiments have been conducted for more extended time durations, of the order of 5000 h. The basic microstructural features of the diffusion zone that are found immediately adjacent to the  $\text{B}_4\text{C}$  layer in the case of Hofman et al's investigation are remarkably similar to the observations made in the present study with respect to Fe-B alloy. But the principal difference between our study and that of  $\text{B}_4\text{C}$  combination with austenitic stainless steel is that in case of Fe-B alloy, there is *per force* no necessity to form  $\text{Fe}_2\text{B}$  type  $(\text{Fe,Cr})_2\text{B}$  boride phase at the interface. This is because of the fact that the Fe-B alloy used here already contained a small fraction of this lower boride phase. Therefore, the interfacial reaction that is taking place in the

present case is one of simple bulk boron transfer from boride phase into the austenitic clad by diffusional processes. We must also note that the solubility of boron in the fcc-austenite phase of 304L steel even at high temperatures is somewhat restricted (below 9 ppm for temperatures less than 1273 K in 304L; (see, Ref. 40), and this fact coupled with the strong exothermic interaction of B with Fe, Cr, Ni etc., present in steel, result in copious formation of hard boride particles on the grain boundaries of stainless steel. The apparent activation energy estimated in the present study for the diffusional interaction therefore corresponds to the reactive boride formation reaction, which is decided by the bulk mobility of B-atoms in the Fe-Cr-Ni-Mo- austenitic matrix. At the of time of this research, We could not gather extensive information with regard to the B-diffusion coefficient in highly alloyed austenitic matrix; but considering the fact that boron may be treated as an interstitial in fcc-matrix, the measured activation energy, which is in the range 57-60 kJ mol<sup>-1</sup>, can be taken to represent the chemical diffusion of B-in austenitic steel. The activation energy estimated in this study is somewhat lower than the spectrum of values reported by Campos et al for AISI 1045 steel [13]. However, Hofmann et al reports a value of 37.8 kJ mol<sup>-1</sup> for B<sub>4</sub>C/SS1.4919 combination in the temperature range 1073-1473 K [7]. In general there is considerable spread noticed in the reported apparent activation energy values for the boriding kinetics of steel. We believe that this high degree of variance is due to different processing conditions including temperature and the changes in the base composition of steel.

As compared to the data that are available with regard to high temperature metallurgical interaction of Fe-B with austenitic stainless steel, the available information on the thermal property scenario of Fe-B alloys is rather meagre. Vatolin et al. [16], have measured certain physicochemical characteristics of boron containing

ferro alloys. For an alloy of nominal composition, Fe-15 wt.% B, a solidification temperature of 1813 K is quoted by Vatolin et al [16]. As compared to this, the measured solidification onset in the present study ( $3 \text{ K min}^{-1}$ ) is 1724 K, which is lower by about 90 K. But it must be added that the composition of our Fe-B alloy is not the same as that of the ferroboration studied by Vatolin et al [16]; besides our measured solidification onset for 304 L stainless steel (1629 K) is in good agreement with the standard quoted fusion point of 1673 K. Therefore, it is believed that our measured transformation temperatures are accurate and reliable. The measured melting enthalpy for the Fe-B alloy is about  $1115 \text{ kJ kg}^{-1}$ , which is in good agreement with the values quoted by Vatolin et al [16]. However, we notice a systematic change in the melting temperature and enthalpy values recorded for the reaction couples 1 to 4 that have different Fe-B/304L mass ratio (See, **Table 8.2** for details). It is obvious that the extent of dissolution of 304L into Fe-B decides the final composition of the alloy melt and hence their melting characteristics. However, it is worth noting that independent of the mass ratio of Fe-B to 304L, the liquation or pre-melting sets in at a relatively constant temperature of about 1471 K (Fig. 7.7). *This in all probability is due to the development of a eutectic type of reaction in the complex multi-component phase equilibria involving (Fe, Cr, Ni, Mo)-B-C system.* Such a possibility had earlier been observed with the  $\text{B}_4\text{C}/304$ , 316 stainless steel reaction couple at about 1473 K [10, 21]. *The practical significance of this finding is that the metallurgical and mechanical integrity Fe-B/304L combination cannot be sustained for temperatures exceeding 1400 K.*

The enthalpy, specific heat and lattice thermal expansion measurements that are obtained in this study for Fe-B-Si-C alloy appear to constitute in all probability the first open literature data on high boron containing Fe-base alloy. In agreement with

the presence of both  $(\text{Fe,Cr})_2\text{B}$  and  $(\text{Fe,Cr})\text{B}$  phases in Fe-B-Si-C alloy, the measured enthalpy increment and specific heat values can be approximated as the weighted average contribution of the two boride phases. This is supported by the  $C_P - T$  curve shown in **Fig. 8.16**. Only meagre published information is available with regard to high temperature thermal expansion characteristics of ferroboron alloy [18, 41]. In their study, Abenojar et al. [21], have carried out high temperature x-ray diffraction characterisation of Fe-10 wt.% B alloy up to 1673 K; but these authors have not reported the lattice thermal expansion data. In the present investigation, we have used the high temperature x-ray diffraction technique for characterising the axial expansivity of both tetragonal and orthorhombic boride phases, from their respective reflections de-convoluted from the whole pattern. It emerges that on a comparative basis, the bulk thermal expansion of orthorhombic FeB phase is slightly larger than the tetragonal  $\text{Fe}_2\text{B}$  boride phase. According to the comprehensive compilation of Kosolapova [18], the average linear thermal expansion coefficient of orthorhombic FeB phase in the temperature range, 700-1300 K (427 to 1027°C), is of the order of  $12 \times 10^{-6} \text{ K}^{-1}$ , which compares favourably with our present x-ray based estimates. From **Fig. 8.17(b)**, it is clear, that the axial thermal expansion along the  $c$ -axis for the orthorhombic FeB phase is comparatively more than that along  $a$  and  $b$ -axes. On the other hand, it is found that the disparity among axial thermal expansivities is more pronounced in the case of tetragonal  $\text{Fe}_2\text{B}$  phase (**Fig. 6.17d**). The tetragonal  $\text{Fe}_2\text{B}$  phase suffers more expansion along the  $c$ -axis. In addition, it is also interesting to note that the thermal expansivity of  $\text{Fe}_2\text{B}$  increases only marginally with temperature (**Fig. 8.17d**). According to the compilation of Kosolapova [18], the average linear thermal expansion coefficient of  $\text{Fe}_2\text{B}$  in the temperature range, 700-1300 K (427-1027 °C) is about  $8 \times 10^{-6} \text{ K}^{-1}$ . Since in the case of present Fe-B alloy, FeB constitutes the major

phase, the overall thermal expansivity is decided by the increasing thermal expansion behaviour of the FeB phase. From the perspective of practical engineering applications, it is desirable to obtain dilatometric estimates of the thermal expansion of Fe-B alloy, as this would incorporate in an implicit manner the effect of porosity and other defects. In this regard, efforts to compact and sinter Fe-B alloy with minimal or no organic binder are currently underway, and the results of property characterisation of sintered product will be reported separately.

## 6.0. Summary

The comprehensive characterisation of thermal stability, high temperature metallurgical compatibility with 304L stainless steel and measurements of heat capacity and lattice thermal expansion of indigenously developed Fe-15B-0.3C-0.89Si alternate shielding material have been carried out. The essential findings of this study are:

- Fe-B/304L stainless steel combination is thermodynamically unstable and there is a strong propensity for the boron atom to diffuse into the austenitic stainless steel clad and form complex intermetallic borides in the thick diffusion zone. This tendency increases with increasing temperature.
- The thickness of the reaction layer is found to follow a parabolic rate law in the temperature range of this study, namely 823-1073 K. The temperature dependence of the kinetic rate constant is adequately described by the Arrhenius equation. The apparent activation energy for the overall reaction occurring in the diffusion zone is estimated to be 57-60 kJ mol<sup>-1</sup>. This corresponds approximately with the activation barrier for the diffusion of boron in austenitic iron matrix.

- The diffusion interface is found to be heterogeneous and consists of hard boride particles embedded in ductile stainless steel matrix, whose composition in the immediate vicinity of the interface is found to vary in Cr and Ni with distance.
- The melting range of the Fe-B alloy is estimated to be 1500-1723 K. The melting enthalpy is estimated to be  $1115 \text{ kJ kg}^{-1}$ .
- 304L stainless steel is found to dissolve extensively in molten Fe-B and experiments performed with different mass ratios of Fe-B to 304L steel revealed that at a temperature of about 1471 K, the pre-melting or liquation starts setting in Fe-B+304L reaction couple. The fused product resulting from complete dissolution of stainless steel in Fe-B consists of a mixture of complex intermetallic borides. *The practical significance of this finding is that the metallurgical integrity Fe-B/304L combination cannot be sustained for temperatures exceeding 1400 K.*
- The enthalpy and heat capacity of Fe-B alloy have been measured up to 1300 K. The specific heat of Fe-B alloy is found to be approximated well by the weighted average of the values of  $\text{Fe}_2\text{B}$  and FeB type boride phases.
- The thermal expansivity of both orthorhombic FeB and tetragonal  $\text{Fe}_2\text{B}$  are found to be anisotropic, in that the *c*-axis thermal expansivity is found to be larger than the *a*-axis and *b*-axis expansion coefficients.

## References

1. Sunil Kumar, D., Keshavamurthy, R. S., Mohanakrishnan, P., Chetal, S. C., 2010, *Nucl. Engineering and Design*, (2010)
2. Leitten, Jr., C. F., Beaver, R. J., Richt, A. E., *J. Nucl. Mater.*, 2, (1959) 136.
3. Ihara, S., Tanaka, K., Kojima, M., Akimoto, Y., 1973. Study on the compatibility between B<sub>4</sub>C and stainless steel, IAEA-IWGFR Specialists meeting on Development and Application of Absorber materials, Dimitrovgrad, USSR, June 3-8, (1973) pp. 201.
4. Dunner, Ph., Heuvel, H.-J., Horle, M., 1984. *J. Nucl. Mater.*, 124, (1984) 185.
5. Hans – Joachen Heuvel, Peter Holler, Phillip Donner, *J. Nucl. Mater.*, 130, (1985) 517.
6. Badini, C., Gianoglio, G., Pradelli, G., *J. Mater. Sci.*, 21, (1986) 1721.
7. Hofmann, P., Markiewicz, M., Spino, J., 1989. Reaction behaviour of B<sub>4</sub>C absorber rod material with stainless steel and zircaloy in severe LWR accidents, *KfK report 4598*, CNEA NT-10/89, (1989) pp.1-20.
8. Veshchunov, M. S., Hofman, P., *J. Nucl. Mater.*, 226, (1995) 72.
9. Kyu, S., Sang, I., *J. Korean Inst. Met. Mater.*, 34, (1996) 174.
10. Hofmann, P., *J. Nucl. Mater.*, 270, (1999) 194.
11. Campos, I., Oseguera, J., Figueroa, U., Garcia, J. A., Bautista, O., Kelemenis, G., *Mater. Sci. Engg.*, A352, (2003) 261.
12. Campos, I., Bautista, O., Ramirez, B., Islas, M., De La Parra, J., Zuniga, L., *Appl. Surf. Sci.*, 243, (2005) 429.
13. Campos, I., Ramirez, G., Figueroa, U., Martinez, J., Morales, O., *Appl. Surf. Sci.*, 253, (2007) 3469.
14. Ozdemir, O., Omar, M. A., Usta, M., Zeytin, S., Bindal, C., Ucisik, 2009. A. H., *Vacuum*, 83, 175.
15. Voitovich, R. F., 1971. Thermodynamic characteristics of refractory compounds, *Naukova Dumka, Kiev*. (as cited in Kosolapova, T. Ya., (1990)).
16. Vatolin, N. A., Zavalov, A. L., Zhuchkov, V. I., *J. Less Common Metals*, 117, (1986) 91.
17. Hiroshi Ohtani, Mitsuhiro Hasebe, Kiyohito Ishida, Taiji Nishizawa, *Trans. ISIJ*, 28, 91988) 1043.

18. Kosolapova, T. Ya., Handbook of high temperature compounds: properties, production and application, Hemisphere Publications, (1990) New York.
19. Halleman, B., Wollants, P., Roos, J. R., *Zeits. Metallkd.*, 85, (1994) 676.
20. Van Rompaey, T., Harikumar, K. C., Wollants, P., *J. Alloys Compd.*, 334 (2002), 173.
21. Abenojar, J., Velasco, F., Martinez, M. A., *J. Mater. Processing Technology*, (2003) 143-144, 28.
22. Zaitsev, A., Zaitseva, N, Kodenkov, A., *J. Mater., Chem.*, 13, (2003) 943.
23. Liu Zhong-Li, Chen Xiang, Li Yan Xiang, Hu Kai hua, *J. Iron & Steel Res.*, 16, (2009) 37.
24. Simnad, M. T., Zumwalt, L. R., 1964. Materials and fuels for high temperature nuclear energy applications, Chapter 13, MIT press, (1964) Cambridge, Mass.
25. Sharafat, S., Odette, G. R., Blanchard, J., *J. Nucl. Mater.*, 386-388, (2009) 896-900.
26. Raju, S., Jeya Ganesh, B., Rai., A. K., Saroja, S., Mohandas, E., Vijayalakshmi, M., Baldev Raj, *Int. J. Thermophysics.*, 31, (2010) 399.
27. Raju, S., Sivasubramanian, K., Divakar, R., Panneerselvam, G., Banerjee, A., Mohandas, E., Antony, M. P., *J. Nucl. Mater.*, 325 (2004) 18.
28. Jeya Ganesh, B., Raju, S., Murugesan, S., Mohandas, E., Vijayalakshmi, M., 2009. *Int. J. Thermophysics*, 30,(2009) 619.
29. Steinbruck, M., *J. Nucl. Mater.*, 400 (2010) 138.
30. Banerjee, A., Raju, S., Divakar, R., Mohandas, E., *Int. J. Thermophys.*, 28, (2007) 97.
31. Fernandez Barquin, L., Gomez Sal, J. C., Gorria, P., Garitaonandia, J. S., Barandiaran, J. M., *J. Phys. Cond. Matter*, 10, (1998) 5027.
32. Chen, B., Penwell, D., Nguyen, J. H., Kruger, M. B., *Solid State Commn.*, 129, (2004) 573.
33. Tadahito Kanaizuka, *J. Solid State Chem.*, 41 (1982) 195.
34. Okamoto, H., *J. Phase Equilibria & Diffusion*, 25, (2004) 297.
35. Raju, S., Jeya Ganesh, B., Rai., A. K., Mythili, R., Saroja, S., Mohandas, E., Vijayalakshmi, *J. Nucl. Mater.*, 389, (2009) 385.

36. Dybkov, V. I., Lengauer, W., Barmak, K., 2005. *J. Alloys & Compd.*, 398, (2005) 113.
37. Dybkov, V. I., Goncharuk, L. V., Khoruzha, V. G., Meleshevich, K. A., Samelyuk, A. V., Samelyuk, A. V., Sidorko, V. R., 2008. *Soild St. Phenomena*, 138, (2008) 181.
38. Knacke, O., Kubaschewski, O. Hesselmann, K., Thermochemical properties of inorganic substances, II edition, (1991) Springer -Verlag, Berlin.
39. Nagase, F., Uetsuka, H., Otomo, T., *J. Nucl. Mater.*, 245 (1997) 52.
40. Elen, J. D., Glas, A., *J. Nucl. Mater.*, 34, (1970) 182.
41. Barinov, V. A., Dorofeev, G. A., Ovechkin, L. V., Elsokov, E. P., Ermakov, A. E., *Phys. Stat. Solidi*, 123(a),(1991) 527.

## AVENUES FOR FURTHER RESEARCH

- The present study has addressed the high temperature phase stability, and thermal properties of RAFM steel & Ferroboron using calorimetry as the prime experimental technique, and yielded valuable data on thermokinetic stability. However, it must be admitted that only the tip of the phase stability issue has been just scratched. A lot more needs to be done for building up a comprehensive Thermophysical database on INRAFM, especially as a function of varying W and Ta concentration
- In the first, supplementing calorimetry with in situ high temperature x-ray diffraction and or dilatometry on RAFM steel will yield a more rounded data, especially since, quantitative estimates of thermal expansion and its jump at phase transition can be obtained. Both XRD and dilatometry data can also be gainfully used to model kinetics
- A proper study of thermodynamic stability of RAFM steel requires that the effect of Ta and W on  $Ac_1$ ,  $Ac_3$ ,  $M_s$ , liquidus and solidus temperature be studied. These data together with corresponding phase change enthalpy constitute valuable input to CALPHAD based phase stability assessment.
- Likewise, thermal diffusivity data on RAFM steel is highly appreciated, as it is an important design input parameter. Further, an accurate measurement of thermal diffusivity change with tempering would also serve as a novel measure of characterising the microstructure evolution.
- There are hardly any data on sound velocity in RAFM steel. The measurement of average acoustic velocity, if carried out over a range of temperatures, will yield information about elastic properties, which together with enthalpy and molar volume data can be used to make a critical assessment of internal thermodynamic consistency. Besides, ultrasonic velocity can precisely herald the onset of phase instabilities as well.
- In addition to what has been mentioned above, reliable values of atomic diffusivity parameter are lacking for many alloying elements in RAFM steel. These data are extremely important, if meaningful simulation of carbide dissolution upon heating, and tempering transformation during aging have to be performed. Some key diffusion experiments, followed by modelling can be initiated for this purpose.
- Role of magnetism in influencing the phase stability needs critical evaluation
- Ferroboron's compatibility with SS 304L clad has been established for up to about 1140 °C. From a UZr metal fuel reactor point of view, it would be necessary to generate out of pile data on the metallurgical compatibility between Ferroboron and Gr. 91 ferritic steel. Although B solubility in ferritics is normally small, any stray free boron can cause havoc to the ferritic clad, if clad temperature shots up accidentally and locally. In this respect, the boronising kinetics of ferritic clad also needs to be studied.

## LIST OF PUBLICATIONS

1. **S. Raju**, Arun Kumar Rai, B. Jeya Ganesh, M. Vijayalakshmi, T. Jayakumar and Baldev Raj, Characterisation of High Temperature Phase Stability and Evaluation of Metallurgical Compatibility with SS 304L, of Indigenously Developed Alternate Shielding Material Ferro-Boron for Fast Reactor Applications, *Energy Procedia*, **7** (2011) 264-272.
2. **S. Raju**, Arun Kumar Rai, , B. Jeya Ganesh, G. Panneerselvam, M. Vijayalakshmi, T. Jayakumar and Baldev Raj , Investigation of high temperature phase stability, thermal properties and evaluation of metallurgical compatibility with 304L stainless steel, of indigenously developed ferroboration alternate shielding material for fast reactor applications, *Nucl. Engg. Design*, **241** (2011) 2787–2801.
3. **S. Raju**, B. Jeyaganesh, Arun Kumar Rai, R. Mythili, S. Saroja and Baldev Raj, A study on martensitic phase transformation in 9Cr-1W-0.23V-0.063Ta- 0.56Mn-0.09C-0.02N reduced activation steel using differential scanning calorimetry, *J. Nucl. Mater.*, **405** (2010) 59-69.
4. **S. Raju**, B. Jeya Ganesh, Arun Kumar Rai, S. Saroja, E. Mohandas, M. Vijayalakshmi and Baldev Raj, Drop Calorimetry Studies on 9Cr–1W–0.23V–0.06Ta–0.09C Reduced Activation Steel, *Int. J. Thermophys.*, **31** (2010) 399-415.
5. **S. Raju** and E. Mohandas, Kinetics of solid state phase transformations: Measurement and Modelling of some basic Issues, *J. Chem. Sci.*, **122** (2010) 83-89.
6. **S. Raju**, B. Jeya Ganesh, Arun Kumar Rai, R. Mythili, S. Saroja, E. Mohandas, M. Vijayalakshmi, K.B.S. Rao and Baldev Raj, Measurement of transformation temperatures and specific heat capacity of tungsten added reduced activation ferritic–martensitic steel, *J. Nucl. Mater.*, **389** (2009) 385-393.